



Numerical modelling and analysis of a room temperature magnetic refrigeration system

Petersen, Thomas Frank

Publication date:
2008

Document Version
Publisher's PDF, also known as Version of record

[Link back to DTU Orbit](#)

Citation (APA):
Petersen, T. F. (2008). *Numerical modelling and analysis of a room temperature magnetic refrigeration system*. Danmarks Tekniske Universitet, Risø Nationallaboratoriet for Bæredygtig Energi. Risø-PhD No. 33(EN)

General rights

Copyright and moral rights for the publications made accessible in the public portal are retained by the authors and/or other copyright owners and it is a condition of accessing publications that users recognise and abide by the legal requirements associated with these rights.

- Users may download and print one copy of any publication from the public portal for the purpose of private study or research.
- You may not further distribute the material or use it for any profit-making activity or commercial gain
- You may freely distribute the URL identifying the publication in the public portal

If you believe that this document breaches copyright please contact us providing details, and we will remove access to the work immediately and investigate your claim.

Numerical modelling and analysis of
a room temperature magnetic
refrigeration system

Thomas Frank Petersen

Report number: Risø-PhD-33(EN)

Author: Thomas Frank Petersen
Title: Numerical modelling and analysis of a room temperature magnetic refrigeration system
Department: Fuel Cells and Solid State Chemistry Department

This thesis is submitted in partial fulfillment of the requirements for the Ph.D. degree at The Technical University of Denmark.

Abstract (max. 2000 char.): This thesis presents a two-dimensional mathematical model of an Active Magnetic Regenerator (AMR) system which is used for magnetic refrigeration at room temperature. The purpose of the model is to simulate a laboratory-scale AMR constructed at Risø National Laboratory. The AMR model geometry comprises a regenerator made of parallel plates, which are separated by channels of a heat transfer fluid. The time-dependent model solves the momentum and continuity equations of the flow of the heat transfer fluid and the coupled energy equations of the heat transfer in the regenerator and the fluid. The AMR performs a cyclic process, and to simulate the AMR refrigeration cycle the model starts from an initial temperature distribution in the regenerator and fluid channel and takes time steps forward in time until the cyclical steady-state is obtained. The model can therefore be used to study both transient and steady-state phenomena. The AMR performance can be evaluated in terms of the no-load temperature span as well as the refrigeration capacity and the COP. The AMR model was verified extensively and it was concluded that the model has energy conservation and that the solution is independent of the chosen grid and time step. Initial results from the model showed significant temperature differences in both the regenerator and the fluid channel during the AMR cycle. This justifies the use of two-dimensional methods when an AMR with a parallel-plate regenerator is modelled. The model is flexible and was used to perform several parametric studies of the AMR performance for different design choices and operating conditions. The results of these studies are presented and the implications for optimal AMR operation are discussed. Finally, the AMR model was validated by comparing the model result to measurements from the experimental AMR constructed by Risø. The validation shows good agreement between the model and the experiments and it is possible to predict both the trends as well as the temperature span of the experimental AMR. In addition, the model can estimate the optimal operating conditions with good accuracy. The ability to provide good results of both the behavior and the performance of the experimental AMR shows that the developed model is a useful tool, which may be used for analysis, design and optimization of the laboratory AMR.

Report number: Risø-PhD-33(EN)
Publication date: September 2007

ISBN 978-87-550-3632-1

Contract no.:

Group's own reg. no.:
(Fønix PSP-element)
1940006-00

Sponsorship:
Risø National Laboratory

Cover :

Pages: 186
Tables: 20
References: 67

Information Service Department
Risø National Laboratory
Technical University of Denmark
P.O.Box 49
DK-4000 Roskilde
Denmark
Telephone +45 46774004
bibl@risoe.dk
Fax +45 46774013
www.risoe.dk

Numerical modelling and analysis of a room temperature magnetic refrigeration system

Thomas Frank Petersen

Technical University of Denmark

Risø National Laboratory
Fuel Cells and Solid State Chemistry Department

&

Department of Mechanical Engineering
Energy Engineering Section
September 2007

Published by:
Risø National Laboratory

Copyright © Thomas Frank Petersen.
All rights reserved

*Fuel Cells and Solid State Chemistry Department
Risø National Laboratory
The Technical University of Denmark - DTU
Building 228, P.O. Box 49
DK-4000 Roskilde
Denmark
Tel +45 4677 5800
Fax +45 4677 5858
web: <http://www.risoe.dk>*

Publication Reference Data:

*Petersen, T.F
Numerical modelling and analysis of a room temperature magnetic refrigeration system.
Ph.D. Thesis
Risø National Laboratory, Fuel Cells and Solid State Chemistry Department
The Technical University of Denmark - DTU
September 2007
Report number. Risø-PhD-33(EN)
ISBN 978-87-550-3632-1
Keywords: magnetic refrigeration, Active Magnetic Regenerator (AMR), 2-D mathematical model, numerical simulation, cyclical steady state, experimental validation.*

Preface and acknowledgements

This thesis was prepared at the Fuel Cells and Solid State Chemistry Department at Risø National Laboratory, the Technical University of Denmark (DTU) and submitted in partial fulfillment of the requirements for obtaining the Ph.D. degree at DTU. The work was financed by Risø National Laboratory and lasted from October 2004 to September 2007. The Ph.D. project was supervised by Dr. B. Elmegaard, and Dr. H. J. H. Knudsen from the Department of Mechanical Engineering, DTU, Dr. N. H. Pryds, Dr. A. Smith, and Prof. S. Linderoth from the Fuel Cells and Solid State Chemistry Department, Risø, DTU.

This thesis describes the development of a mathematical model for simulation of an Active Magnetic Regenerator (AMR) system, which is used for magnetic refrigeration. The thesis consists of a report on the development of the AMR model and the results obtained by application of the model as well as a collection of four research papers.

I owe my supervisors Dr. Brian Elmegaard, Dr. Hans-Jørgen Høgaard Knudsen, Dr. Nini Pryds, Dr. Anders Smith and Prof. Søren Linderoth a dept of gratitude for their constant guidance, support and encouragement throughout the past three years. I would also like to thank my friends and colleagues at Risø. In particular, I would like to thank Anders Dinesen, Søren Linderoth, Stinus Jeppesen, Christian Bahl, Luise Theil Kuhn, Kristian Nim Sørensen, Jens Borchsenius, Toke Henriksen and the magnetic refrigeration group at the Neutron house. I am also very grateful to Jesper Hattel and Henrik Schmidt from the Department of Manufacturing Engineering and Management, DTU for their invaluable assistance in the development of the AMR model and their help in preparing the subsequent paper. Thure Ralfs and Lars Gregersen from COMSOL A/S are gratefully acknowledged for allowing me to run the COMSOL Multiphysics software on a Linux Cluster. Kurt Engelbrecht from the University of Wisconsin-Madison is thanked for his assistance with the comparison of the two AMR models. I would also like to thank Frank Petersen for helping with the preparation of this manuscript. Finally, I would like to extend my deepest gratitude to my family and friends for believing in me throughout this project and for being very understanding and patient during the stressed periods of the past three years.

Thomas Frank Petersen
Roskilde, September 2007

This page was intentionally left blank.

Abstract

This thesis presents a two-dimensional mathematical model of an Active Magnetic Regenerator (AMR) system which is used for magnetic refrigeration at room temperature. The purpose of the model is to simulate a laboratory-scale AMR constructed at Risø National Laboratory. The AMR model geometry comprises a regenerator made of parallel plates, which are separated by channels of a heat transfer fluid. The time-dependent model solves the momentum and continuity equations of the flow of the heat transfer fluid and the coupled energy equations of the heat transfer in the regenerator and the fluid. The AMR performs a cyclic process, and to simulate the AMR refrigeration cycle the model starts from an initial temperature distribution in the regenerator and fluid channel and takes time steps forward in time until the cyclical steady-state is obtained. The model can therefore be used to study both transient and steady-state phenomena. The AMR performance can be evaluated in terms of the no-load temperature span as well as the refrigeration capacity and the COP. The AMR model was verified extensively and it was concluded that the model has energy conservation and that the solution is independent of the chosen grid and time step. Initial results from the model showed significant temperature differences in both the regenerator and the fluid channel during the AMR cycle. This justifies the use of two-dimensional methods when an AMR with a parallel-plate regenerator is modelled. The model is flexible and was used to perform several parametric studies of the AMR performance for different design choices and operating conditions. The results of these studies are presented and the implications for optimal AMR operation are discussed. Finally, the AMR model was validated by comparing the model result to measurements from the experimental AMR constructed by Risø. The validation shows good agreement between the model and the experiments and it is possible to predict both the trends as well as the temperature span of the experimental AMR. In addition, the model can estimate the optimal operating conditions with good accuracy. The ability to provide good results of both the behavior and the performance of the experimental AMR shows that the developed model is a useful tool, which may be used for analysis, design and optimization of the laboratory AMR.

This page was intentionally left blank.

Resumé (Summary in Danish)

Magnetisk køling ved stuetemperatur er en teknologi på udviklingsstadiet, der giver mulighed for et energieffektivt og miljøvenligt alternativ til konventionelle kompressorbaserede kølesystemer. Denne afhandling beskriver udviklingen af en todimensional matematisk model af en Aktiv Magnetisk Regenerator (AMR), som anvendes til magnetisk køling. Formålet med modellen er at simulere en eksperimentel AMR på laboratorieskala, som er konstrueret på Forskningscenter Risø. Modelgeometrien omfatter en magnetisk regenerator, der består af flade, parallelle plader adskilt af kanaler med kølevæske, samt to varmevekslere. AMR-modellen er tidsafhængig og løser bevægelsesligningerne for væskestrømningen i regeneratorens kanaler og de koblede energiligninger for varmetransmissionen i regeneratoren og kølevæsken. En AMR udfører en cyklisk proces, og modellen simulerer denne proces ved at starte med en given temperatur profil i regeneratoren og væskekanalen som begyndelsesbetingelser. Herefter tager modellen skridt frem i tiden indtil den cykliske stationære løsning er fundet. Modellen kan derfor anvendes til analyse af transiente og stationære fænomener og kan bestemme både temperaturløftet i AMR-systemet såvel som kølekapaciteten og COP. AMR-modellen blev verificeret igennem en række tests, som viste, at modellen har energibevarelse og, at løsningen er uafhængig af det valgte beregningsnet og tidskridt. Endeligt blev modellen valideret ved at sammenligne målinger fra den eksperimentelle AMR med modellens resultater. Sammenligningen viste god overensstemmelse mellem de to sæt resultater. Modellen er i stand til at bestemme det eksperimentelle AMR-systems opførsel, det opnåede temperaturløft, samt at forudsige de optimale driftsbetingelser med god nøjagtighed. AMR-modellen kræver en lang beregningstid, og modellen blev derfor implementeret på en beregningscluster, således at flere parallelle simuleringer kan udføres samtidigt. AMR-modellen er fleksibel, og blev anvendt til at udføre en række parameterstudier, hvor geometri, materialevalg og driftsbetingelser alle blev varieret. Resultaterne fra disse studier præsenteres, og deres betydning for optimal drift af en AMR diskuteres. Blandt andet viser resultaterne, at der er signifikante temperaturgradienter internt i regeneratoren og væskekanalerne. Dette betyder, at det er nødvendigt at anvende todimensionale metoder til at modellere en AMR med en regenerator af parallelle plader. Endelig viser modellen at det er muligt at opnå et højt temperaturløft i en AMR med et magnetisk felt på 1 T men, at der stadig er brug for forbedringer før magnetisk køling kan konkurrere med konventionel køling. Den udviklede model kan simulere det eksperimentelle AMR-systems opførsel med god nøjagtighed, og kan bruges til at bestemme systemets ydelse for en lang række driftsbetingelser. Resultaterne viser, at den udviklede model er et nyttigt værktøj til analyse, design og optimering af den eksperimentielle AMR.

This page was intentionally left blank.

Nomenclature

List of symbols

Symbol	Meaning	Units
A_c	Cross section area	m^2
a_s	Specific heat transfer area	m^{-1}
C	Volumetric heat capacity	Jm^{-3}
c_{ele}	Electronic specific heat capacity	$Jkg^{-1}K^{-1}$
c_{lat}	Lattice specific heat capacity	$Jkg^{-1}K^{-1}$
c_{mag}	Magnetic specific heat capacity	$Jkg^{-1}K^{-1}$
c_p	Specific heat capacity	$Jkg^{-1}K^{-1}$
D_h	Hydraulic diameter	m
ΔT_{ad}	Adiabatic temperature change	K
ΔT	Temperature span	K
Δx	Piston stroke	m
f	Friction factor	
\mathbf{F}	Force	N
g	Landé factor	dimensionless
h	Heat transfer coefficient	$Wm^{-2}K^{-1}$
H_{fl}	Height of the fluid channel	m
H_{reg}	Height of the regenerator plate	m
H	Magnetic field strength	Am^{-1}
J	Total angular momentum	In units of \hbar
k	Thermal conductivity	$Wm^{-1}K^{-1}$
L	Length	m
L_0	Characteristic length	m
m	Mass of the regenerator	kg
\dot{m}	Mass flow	kgs^{-1}
p	Pressure	Pa
q'_c	Absorbed energy per unit width	Jm^{-1}
\dot{q}''_c	Absorbed heat flux	Wm^{-2}
\dot{q}'_c	Refrigeration capacity per unit width	Wm^{-1}
q'_r	Rejected energy per unit width	Jm^{-1}
\dot{q}''_r	Rejected heat flux	Wm^{-2}

Continued on the next page

Continued from the previous page

Symbol	Meaning	Units
\dot{q}'_r	Rejected heat per unit width	Wm^{-1}
Δs_M	Isothermal entropy change	$\text{Jkg}^{-1}\text{K}^{-1}$
s	Specific entropy	$\text{Jkg}^{-1}\text{K}^{-1}$
s_{ele}	Electronic specific entropy	$\text{Jkg}^{-1}\text{K}^{-1}$
s_{lat}	Lattice specific entropy	$\text{Jkg}^{-1}\text{K}^{-1}$
s_{mag}	Magnetic specific entropy	$\text{Jkg}^{-1}\text{K}^{-1}$
t	Time	s
T	Temperature	K
T_C	Temperature at the cold heat exchanger	K
T_H	Temperature at the hot heat exchanger	K
T	Temperature	K
U_P	Piston velocity	ms^{-1}
U_0	Characteristic velocity	ms^{-1}
\bar{U}	Mean velocity	ms^{-1}
u	x-direction velocity	ms^{-1}
v	y-direction velocity	ms^{-1}
w'	Work	Jm^{-1}
\dot{w}'	Work	Wm^{-1}
W	Width	m

List of Greek symbols

Symbol	Name	Unit
α	Thermal diffusivity	m^2s^{-1}
δ	Relative difference	%
ϵ	Porosity	%
η	Carnot efficiency	%
μ_f	Viscosity	$\text{kgm}^{-1}\text{s}^{-1}$
γ_e	Sommerfeld constant	$\text{Jkg}^{-1}\text{K}^{-2}$
Φ	Utilization	Dimensionless
ρ	Density	kgm^{-3}
τ	AMR cycle length	s
τ_1	Length of the magnetization	s
τ_2	Length of the cold blow	s
τ_3	Length of the demagnetization	s
τ_4	Length of the hot blow	s
σ	Specific magnetization	$\text{Am}^2\text{kg}^{-1}$
Θ_C	Curie temperature	K
Θ_D	Debye temperature	K

Sub- and superscripts

Subscript or superscript	Name
f	Fluid
fl	Fluid channel
hex	heat exchanger
mag	Magnetic work
piston	Piston work
reg	regenerator
s	Solid
dm	Demagnetization
m	Magnetization

Physical constants

Symbol	Name	Value	Unit
k_B	The Boltzmann constant	$1.38 \cdot 10^{-23}$	Jkg^{-1}
μ_0	Vacuum permeability	$4\pi \cdot 10^{-7}$	NA^{-2}
μ_B	Bohr magneton	$9.27 \cdot 10^{-24}$	Am^2
N_A	Avogadro's number	$6.02 \cdot 10^{23}$	mol^{-1}

Glossary of abbreviations

Abbreviation	Meaning
AMR	Active Magnetic Regenerator
COP	Coefficient Of Performance
CHEX	Cold Heat Exchanger
Gz	Graetz number
HHEX	Hot Heat Exchanger
Nu	Nusselt number
Pr	Prandtl number
Re	Reynolds number
RMSE	Root mean square error

This page was intentionally left blank.

Contents

Preface and acknowledgements	i
Abstract	iii
Resumé (Summary in Danish)	v
Nomenclature	vii
1 Introduction	1
1.1 Outline of this thesis	3
2 The magnetocaloric effect and magnetic refrigeration	5
2.1 Introduction	5
2.2 The magnetocaloric effect	5
2.2.1 Thermodynamic theory	6
2.2.2 Magnetocaloric materials	8
2.2.3 Modelling the magnetocaloric effect	8
2.3 Magnetic refrigeration	9
2.3.1 The magnetic Carnot refrigeration cycle	10
2.3.2 The magnetic Ericsson refrigeration cycle	11
2.3.3 The Active Magnetic Regenerator	13
2.4 Previously developed mathematical models of the AMR	16
3 Development of a 2-D model of a room-temperature AMR	23
3.1 Modelling geometry	24
3.2 Governing equations of the AMR model	25
3.2.1 Stage 1 - The velocity distribution in the fluid	26
3.2.2 Stage 2 - Magnetization and cold blow	27
3.2.3 Stage 3 - Demagnetization and hot blow	28
3.2.4 Stage 4 - Evaluation of AMR performance	30
3.3 Modelling the piston displacement	31
3.4 Modelling the flow in the fluid channels	32
3.5 Model implementation	34
3.6 Model verification	37

3.6.1	Verification of the coordinate transformation method	38
3.6.2	Grid sensitivity analysis of the velocity distribution in the fluid channel	41
3.6.3	Grid and time step sensitivity analysis	43
3.6.4	Independence of initial conditions	44
3.7	Implementation of the AMR model on a cluster	45
3.8	Summary and final remarks	46
4	Numerical analysis of an Active Magnetic Regenerator	47
4.1	Initial results	47
4.2	Introduction to the AMR parameter studies	52
4.3	Influence of the piston stroke	52
4.3.1	Results and discussion	53
4.4	Influence of the fluid channel height	55
4.4.1	Results and discussion	56
4.5	Combined influence of the piston stroke and the fluid channel height	58
4.5.1	Results and discussion	58
4.6	Influence of the heat transfer fluid	60
4.6.1	Results and discussion	60
4.7	Influence of the frequency of the refrigeration cycle	66
4.7.1	Results and discussion	66
4.8	Pressure loss in a parallel-plate AMR regenerator	69
4.8.1	Results and discussion	70
4.9	Summary and final remarks	73
5	Experimental validation of the AMR model	75
5.1	The Experimental Active Magnetic Regenerator	75
5.2	Numerical modelling of the experiment	78
5.3	The parameter studies	79
5.3.1	Piston stroke variation	80
5.3.2	Cycle timing variation	80
5.4	Results and discussion	81
5.4.1	Piston stroke variation	81
5.4.2	Refrigeration cycle variation	83
5.5	Summary and final remarks	85
6	Comparison of the 2-D AMR model to a 1-D AMR models	87
6.1	Description of the one-dimensional AMR model	87
6.1.1	Governing equations	88
6.1.2	Heat transfer between the regenerator and the fluid	89
6.1.3	Solution method of the 1-D model	90
6.1.4	Evaluation of the AMR performance	90
6.1.5	Key modeling differences between the 1-D and the 2-D model	91
6.2	Implementation of the two models	91
6.2.1	The implementation of the magnetocaloric effect in the two models .	92

6.3	Comparison of the 1-D and 2-D model	93
6.4	Results and discussion	94
6.4.1	Refrigeration capacity, rejected heat and the COP	94
6.4.2	Fluid temperature profiles, RMSE and temperature gradients	96
6.5	Summary and final remarks	98
7	Conclusion	101
	References	103
A	Modelling the magnetocaloric effect	109
A.1	The Weiss mean field theory	109
A.2	The Debye theory	110
A.3	The Sommerfeld theory	110
A.4	The magnetocaloric effect of gadolinium	110
B	Further verification of the AMR model	115
B.1	Implementation and test of the coordinate transformation method	115
B.1.1	Basic test of the coordinate transformation method	115
B.1.2	Implementation of the coordinate transformation method in COMSOL Multiphysics	116
B.1.3	Results	117
B.1.4	Implementation of moving boundaries using the coordinate transfor- mation method	119
B.2	Verification of the solution of the fluid channel flow	122
B.3	Cyclical steady-state of the flow in the fluid channel	123
C	Paper presented at the Danske Køledage Conference, 2006	125
D	Paper published in the International Journal of Refrigeration	139
E	Paper presented at the Nordic Comsol Conference, 2006	153
F	Paper presented at The Second IIF-IIR International Conference on Mag- netic Refrigeration at Room Temperature, 2007	161

This page was intentionally left blank.

Chapter 1

Introduction

This thesis presents a two-dimensional mathematical model of an Active Magnetic Regenerator (AMR) system for magnetic refrigeration. Magnetic refrigeration at room temperature is an emerging technology with the potential to become an energy efficient and environmentally friendly alternative to conventional refrigeration. Today, almost all refrigeration is based on vapour-compression that was introduced more than 120 years ago and, which today is a mature, reliable and low-cost technology. However, improvements to conventional refrigeration will be incremental due to the technological limitations of the present refrigeration systems. As concern for the global climate grows, the demand for clean, energy efficient technologies increases and this makes magnetic refrigeration attractive. In experiments, magnetic refrigeration have obtained a Coefficient Of Performance (COP) ranging from 3 to 10, corresponding to Carnot efficiencies ranging from 15% to 75% [1]. With energy efficiencies in this range, magnetic refrigeration has the potential to reduce the energy consumption of household refrigerators significantly [2]. Refrigeration consumes a large fraction of our society's energy supply. For example, refrigeration in the US account for 25% of the residential electricity demand and 15% of the commercial electricity demand [3]. Thus magnetic refrigeration has the potential to significantly reduce the global energy consumption and as a result limit the CO₂ emissions. Secondly, magnetic refrigeration is an environmentally friendly technology. Conventional refrigeration is widely based on hydrofluorocarbon (HFC) gasses that have a large Global Warming Potential (GWP) and are controlled substances under the Kyoto Protocol. However, because magnetic refrigeration uses a solid material as the refrigerant, the use of HFCs is eliminated.

Magnetic refrigeration is based on the magnetocaloric effect which manifests itself as a temperature change when a magnetic material is subjected to a magnetic field. The magnetocaloric effect is virtually reversible and when the magnetic field is removed the material reverts to its initial temperature. The magnitude of the temperature change depends on the strength of the magnetic field. To obtain maximum energy efficiency and minimize costs room temperature magnetic refrigeration systems will be based on permanent magnets which does require to power to produce the magnetic field unlike electromagnets and superconducting magnets. Permanent magnets typically produces magnetic fields ranging from 0.5 T to 2 T where the magnetocaloric effect results in temperature changes from

0.5 K to 8 K [4]. Such temperature changes are too small for practical purposes and modern magnetic refrigeration utilizes heat recovery in the form of regeneration in order to obtain temperature spans comparable to conventional refrigeration.

The magnetocaloric effect was discovered by Warburg [5] in 1881 and explained theoretically in 1918 by Weiss & Piccard [6]. In 1933, Giauque and MacDougall used the magnetocaloric effect to cool a sample of gadolinium sulphate from 1.5 K to 0.25 K using a method known as adiabatic demagnetization, which was originally proposed in 1926-27 by Debye and Giauque [7, 8, 9]. For this research Giauque was awarded the Nobel prize in 1949. Continuous magnetic refrigeration systems were first demonstrated in 1953-1954 by Collins & Zimmermann and Heer et al. who built a magnetic refrigerator that operated between approximately 1 K and 0.73 K and approximately 1 K and 0.2 K, respectively [10, 11]. In 1976 Brown constructed the first room-temperature magnetic refrigeration system and obtained a no-load temperature difference of 47 K between the hot end (46 °C) and the cold end (-1 °C) [12]. In 1983, Barclay & Steyert introduced the Active Magnetic Regenerator (AMR) concept that almost all modern magnetic refrigeration systems are based on [13]. Ten years later, there was a breakthrough on room-temperature magnetic refrigeration when the Ames Laboratory and the Astronautics Corporation in 1998 presented an AMR system with a refrigeration capacity of 500 W and a COP of 6.6 obtained at a temperature span of about 12 K. The results were obtained with a magnetic field of 5 T [1]. Using a magnetic field of 1.5 T, the same AMR obtained a COP of 4 at a temperature span of 12 K, but the refrigeration capacity at these operating conditions was not specified [1]. The maximum temperature span of the machine was 23 K at 5 T and 14 K at 1.5 T. The same year the material $\text{Gd}_5\text{Si}_2\text{Ge}_2$ was discovered [14] which has a magnetocaloric effect much greater than previously known and therefore the potential to make magnetic refrigeration even more effective [1]. Another important development occurred in 2001 when the Astronautics Corporation unveiled an AMR that used permanent magnets to provide the magnetic field. This showed that magnetic refrigeration does not require superconducting or electromagnets, which are unsuitable for household applications [15]. These three developments demonstrated that magnetic refrigeration is a serious candidate for commercial room-temperature refrigeration.

Risø National Laboratory has since 2003 performed research on the magnetocaloric effect and magnetic refrigeration and has recently constructed an experimental, laboratory-scale AMR. The purpose of the present study is to aid this project by developing a mathematical model of the experimental AMR. The model will then be used to perform tests and analysis of the AMR, which would be too expensive or time-consuming to perform experimentally. Mathematical models have been used to understand, analyze and optimize the AMR since its invention [13] and previous work on AMR models has mainly used one-dimensional methods. However, to increase the amount of detail that may be obtained from such models and to avoid some of the inherent simplifications of the 1-D approach, the present work has focused on the development of a two-dimensional AMR model.

1.1 Outline of this thesis

This thesis is structured as follows: Chapter 2 gives a general introduction to the magnetocaloric effect and magnetic refrigeration as well as an overview of the present status of AMR models. Chapter 3 describes the development and validation of the AMR model. Chapter 4 presents the results of a series of parameter studies performed with the AMR model. Chapter 5 presents an experimental verification of the AMR model performed by comparing the results from the model to the results from the experimental AMR. In chapter 6, the developed two-dimensional AMR model is compared to a one-dimensional AMR model. Finally, Chapter 7 gives a conclusion. Appendix A describes a physical model of the magnetocaloric effect and Appendix B gives additional detail of the development of the AMR model. Appendices C to F contains the four research papers written during this Ph.D. project.

This page was intentionally left blank.

Chapter 2

The magnetocaloric effect and magnetic refrigeration

2.1 Introduction

The first part of this chapter gives a general introduction to the magnetocaloric effect (MCE) and presents the underlying thermodynamic theory. The second part explains the concept of magnetic refrigeration (MR) and describes two basic magnetic refrigeration cycles before explaining the AMR concept for MR in detail. The third and final part of the chapter presents a literature study of the present status of mathematical model of AMRs.

Parts of this chapter was published in a paper presented in 2006, at the "Danske K oledage" conference in Odense, Denmark [16]. This paper is included in Appendix C.

2.2 The magnetocaloric effect

The MCE is intrinsic to all magnetic materials and manifests itself as a temperature change when a magnetic material is subjected to a time-varying magnetic field [17]. The magnetocaloric effect is a result of the coupling between the magnetic energy reservoir and the thermal energy reservoir of a magnetic material. The two reservoirs are closely coupled and exchange energy fast and without losses. The result is that the MCE occurs within milliseconds of the application of a magnetic field [18]. The magnetic energy reservoir is associated with the spins of the electrons in the material and Fig. 2.1 shows the magnetization of a randomly ordered magnetic material by an external magnetic field. The field aligns the spins of the electrons along the direction of the magnetic field and if hysteresis is neglected¹ the material returns to its initial state when the magnetic field is removed. The magnetization can therefore be regarded as a reversible process and as a consequence the MCE may also be considered to be reversible [19]. This assumption will be used for the remainder of this thesis. The total specific entropy (s) of a magnetic material can to

¹Hysteresis is an effect, which occurs when a magnetic material retains some remnant magnetization even when removed from the magnetic field.

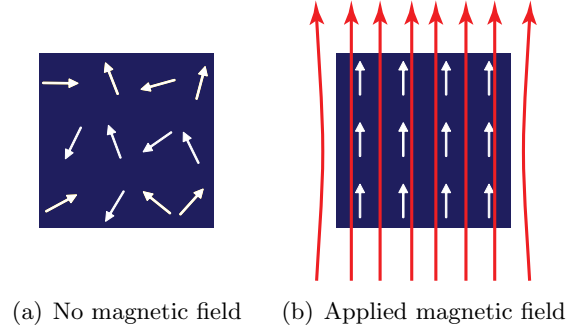


Figure 2.1: The alignment of a randomly ordered magnetic spin system by an external magnetic field. (a) Without an external magnetic field the spin system has a random alignment. (b) When the external magnetic field is applied, the magnetic spin system becomes aligned with the field thus magnetizing the material.

a good approximation be split into three sources [20]; (1) the magnetic specific entropy from the degrees of freedom of the electronic spin system, (2) the lattice specific entropy from the lattice vibrations of the material and (3) the electronic specific entropy from the free electrons of the material (denoted s_{mag} , s_{lat} and s_{ele} respectively). The lattice and the electronic specific entropies are independent of the magnetic field (H) and depends only on the temperature (T), whereas the magnetic specific entropy depends on both the magnetic field and the temperature [20]:

$$s_{\text{tot}} = s_{\text{mag}}(H, T) + s_{\text{lat}}(T) + s_{\text{ele}}(T) \quad (2.1)$$

During an adiabatic application of the magnetic field, the total entropy remains constant since the MCE is reversible. The magnetization reduces the degrees of freedom in a magnetic material and as a result decreases the associated entropy. Consequently, the lattice and electronic entropy increase by an equal and opposite amount to the decrease in the magnetic entropy. The result is that the temperature of the material increases by the *adiabatic temperature change* (ΔT_{ad}). Similarly, during an isothermal magnetization the lattice and electronic entropy remains constant but the magnetic entropy is reduced by the *isothermal entropy change* (Δs_{M}). The relationship between Δs_{M} and ΔT_{ad} is illustrated in the T-S diagram shown in Fig. 2.2.

2.2.1 Thermodynamic theory

The infinitesimal change in the specific entropy of a magnetic material in terms of temperature and magnetic field at constant pressure can be written as [21]:

$$ds = \left(\frac{\partial s}{\partial T} \right)_H dT + \left(\frac{\partial s}{\partial H} \right)_T dH. \quad (2.2)$$

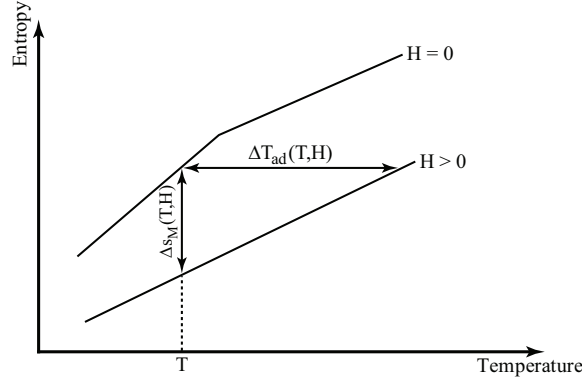


Figure 2.2: The relationship between ΔT_{ad} and Δs_{M} . The former occurs when the entropy is constant during magnetization, and the latter occurs when the temperature is constant during magnetization. The bend on the curve for $H = 0$ denotes the Curie temperature (explained later).

The relationship between entropy and the magnetic field can be expressed in terms of the thermodynamic Maxwell equation [22]

$$\left(\frac{\partial s}{\partial H}\right)_T = \mu_0 \left(\frac{\partial \sigma}{\partial T}\right)_H, \quad (2.3)$$

where μ_0 is the vacuum permeability and σ is the specific magnetization. The dependence of the entropy on the temperature is determined from the 2nd law of thermodynamics [21]

$$\left(\frac{\partial s}{\partial T}\right)_H = \frac{c_p}{T}, \quad (2.4)$$

where c_p is the specific heat capacity at constant magnetic field (and pressure), which is also the sum of a magnetic, a lattice and an electronic contribution [20]

$$c_p = c_{\text{mag}}(H, T) + c_{\text{lat}}(T) + c_{\text{ele}}(T). \quad (2.5)$$

By substitution of Eq. 2.3 and 2.4 into Eq. 2.2 a final expression for the specific entropy as a function temperature and the magnetic field is obtained:

$$ds = \frac{c_p}{T} dT + \mu_0 \left(\frac{\partial \sigma}{\partial T}\right)_H dH \quad (2.6)$$

Using Eq. 2.1 Δs_{M} is determined by setting dT equal to zero and integrating over the change in the magnetic field:

$$\Delta s_{\text{M}} = \mu_0 \int_{H_i}^{H_f} \left(\frac{\partial \sigma}{\partial T}\right)_H dH, \quad (2.7)$$

where H_i is the initial field and H_f is the final field. Likewise, ΔT_{ad} is determined from Eq. 2.1 by setting ds equal to zero and integrating over the change in the magnetic field:

$$\Delta T_{\text{ad}} = -\mu_0 \int_{H_i}^{H_f} \frac{T}{c_p} \left(\frac{\partial \sigma}{\partial T}\right)_H dH. \quad (2.8)$$

The magnetization usually decreases with temperature meaning that the derivative of the specific magnetization with respect to the temperature ($\partial\sigma/\partial T$) is negative. As a result, an applied magnetic field produces a negative Δs_M and a positive ΔT_{ad} ; both as expected. From Eq. 2.7 and Eq. 2.8 it follows that the absolute value of the MCE is large when:

- The change in the magnetic field is large ($H_f - H_i$).
- The magnetization varies rapidly with temperature i.e. when $|\partial\sigma/\partial T|$ is large.
- The specific heat capacity is small (only applies to ΔT_{ad}).

2.2.2 Magnetocaloric materials

All magnetic materials exhibit the MCE to a greater or lesser degree but some materials display a significantly enhanced MCE that makes them potential candidates for MR. In general, room temperature MR uses ferromagnetic materials which have a large MCE near the Curie temperature (Θ_C) where the material undergoes a magnetic phase transition from an ordered ferromagnetic spin system to a random paramagnetic spin system. The magnetic phase transition is associated with a large reduction in magnetization over just a few kelvin and as a result a large $|\partial\sigma/\partial T|$ is obtained. Fig. 2.3 illustrates the behavior of the MCE near the Curie temperature. The MCE peaks at the magnetic phase transition and is rapidly reduced above and below the Curie temperature, which can be varied depending on the material composition. Because of the behavior shown on Fig. 2.3, room temperature

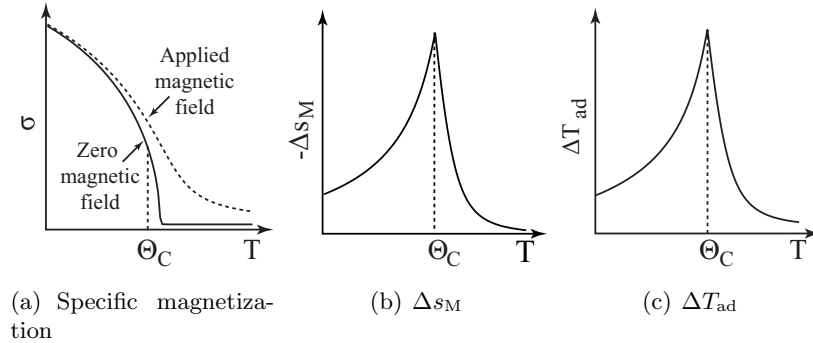


Figure 2.3: The relationship between the specific magnetization, σ , and the MCE in a ferromagnetic material. The MCE is largest around the Curie temperature where σ changes rapidly.

MR uses materials with a Curie temperature close to the operating temperature interval of the MR system. The benchmark material for MR is gadolinium (Gd) because of its high MCE near room temperature.

2.2.3 Modelling the magnetocaloric effect

It is possible to model the magnetocaloric effect using a combination of physical models. The specific magnetism, the magnetic specific heat capacity and the specific entropy can

be determined with the Weiss mean field model [22], the lattice specific heat capacity and specific entropy can be determined with the Debye model [23] and the electronic specific heat capacity and specific entropy can be determined using the Sommerfeld model [23]. These models are collectively known as the WDS model in this thesis and gives a reasonable estimate of the MCE and is often used to analyze magnetocaloric material and MR systems, see [24, 25, 26] for examples of the former and [27] for an example of the latter. As an example the WDS model was used to determine the specific heat capacity, Δs_M and ΔT_{ad} of gadolinium and the results are shown in Fig. 2.4. The Weiss, Debye and Sommerfeld models are presented in more detail in Appendix A.

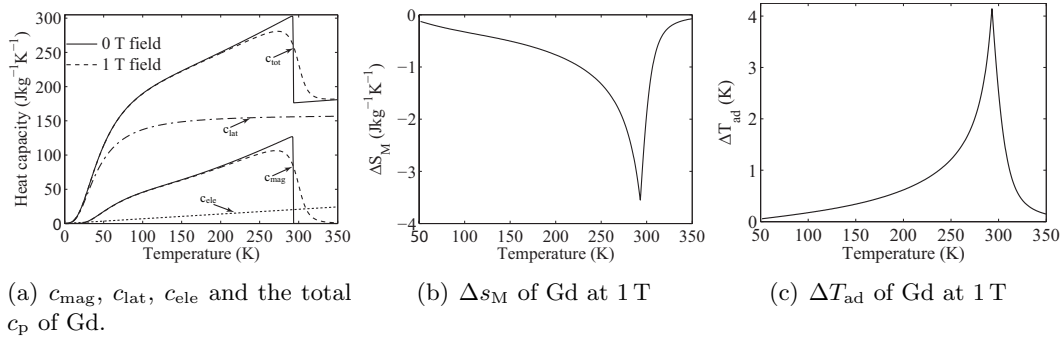


Figure 2.4: The specific heat capacity, Δs_M and ΔT_{ad} for Gd in magnetic fields of 0 T and 1 T.

2.3 Magnetic refrigeration

Magnetic refrigeration uses the MCE by bringing a solid, magnetocaloric refrigerant through repeated "heat pump" cycles thereby transporting heat from from a cooling load to the surroundings by supplying work through the repeated magnetization and demagnetization of the refrigerant. The general principle is comparable to conventional vapour-compression refrigeration where the magnetization of the solid is analogue to the compression of a vapour and the demagnetization is analogue to the expansion of the vapour. Because the refrigerant is solid, the heat transfer to the cooling load and the surroundings is facilitated by an inert *heat transfer fluid* like helium, water or alcohol in direct contact with the refrigerant. Fig. 2.5 shows a simple cycle, which illustrates the principle of MR. The magnetic field used for MR can be produced by superconducting magnets, electromagnets or permanent magnets. For practical applications superconducting magnets are unrealistic since they require liquid helium or nitrogen to function, and electromagnets require a high electrical current to produce a usable magnetic field. Permanent magnets are thus of central importance to magnetic refrigeration because they require no energy input to produce the magnetic field. Current state-of-the-art permanent magnets are limited to about 2 T where ΔT_{ad} typically is no greater than 8 K [4]. This is significantly below the 30 K to 50 K temperature spans required for conventional refrigeration. As a consequence the simple magnetic refrigeration cycle shown in Fig. 2.5 cannot be used for practical refrigeration and modern MR utilizes

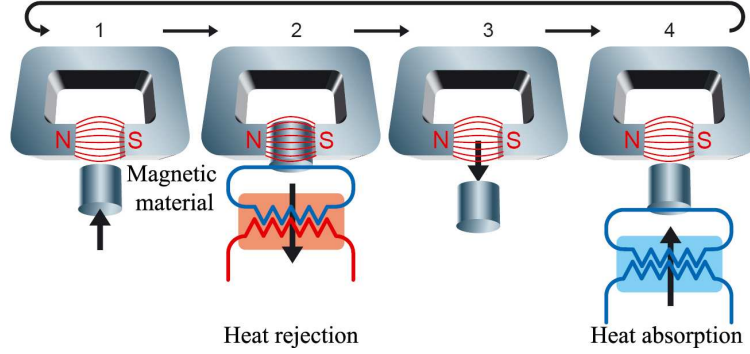


Figure 2.5: Schematic representation of simple magnetic refrigeration cycle. The solid refrigerant is initially at the temperature of the surroundings and with no applied magnetic field. The cycle is then performed in four steps: (1) the solid refrigerant is magnetized and heated above the temperature of the surroundings, (2) the heat is then rejected to the surroundings, (3) the refrigerant is demagnetized and as a result, cooled below the temperature of the surroundings, and (4) the cooled refrigerant absorbs heat from a cooling load. The figure was adapted from ref. [28].

heat recovery in the form of regeneration to span a wider temperature range than that produced by the MCE. In the following two basic thermodynamic cycles used for MR are described before going into the details of modern MR based on the AMR.

2.3.1 The magnetic Carnot refrigeration cycle

In MR the Carnot cycle is considered as the reference cycle since it can obtain the highest effectiveness. The Carnot cycle consists of two isothermal and two isentropic processes and is illustrated in the T - S^2 diagram shown on Fig. 2.6 between two isofield³ lines. For a cyclic process the 1st law of thermodynamics is written as

$$\oint du = \oint dw + \oint dq = 0, \quad (2.9)$$

where du is the internal energy, dw is the external work and dq is the amount of heat transfer. Using the 2nd law of thermodynamics the cyclic work can also be written as

$$w = - \oint T ds. \quad (2.10)$$

From Eq. 2.10 The work (the area ABCD) can be calculated as

$$w = - \oint T ds = - \int_A^B T ds - \int_C^D T ds = T_{\text{hot}}(s_A - s_B) - T_{\text{cold}}(s_D - s_C). \quad (2.11)$$

²Contrary to conventional refrigeration where the refrigeration cycles are shown in S - T diagrams, MR illustrate the refrigeration cycle in T - S diagrams. This makes it easy to illustrate the cycle between the entropy curves at different magnetic fields like those shown in Fig. 2.2.

³An isofield refer to constant magnetic field.

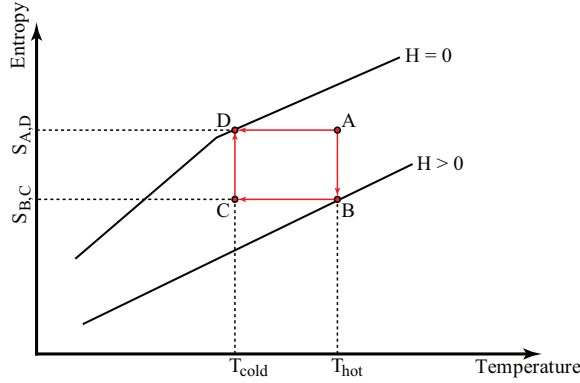


Figure 2.6: The magnetic Carnot cycle consists of four steps; isothermal magnetization from A to B, adiabatic demagnetization from B to C, isothermal demagnetization from C to D and finally adiabatic magnetization from D to A.

The cooling load is the heat absorbed during process CD, which can be calculated as

$$q_c = \int_C^D T ds = T_{\text{cold}}(s_D - s_C). \quad (2.12)$$

The COP can now be determined from Eqs. 2.11 and 2.12:

$$COP = \frac{q_c}{w} = \frac{T_{\text{cold}}(s_D - s_C)}{T_{\text{hot}}(s_A - s_B) - T_{\text{cold}}(s_D - s_C)}. \quad (2.13)$$

Since process AB and CD have the same entropy difference, Eq. 2.13 can be further simplified to the following well known result for the COP of a Carnot cycle:

$$COP = \frac{T_{\text{cold}}}{T_{\text{hot}} - T_{\text{cold}}} = \frac{T_{\text{cold}}}{\Delta T}, \quad (2.14)$$

where ΔT is the temperature span between the source and the sink. The Carnot cycle is unsuitable for commercial refrigeration for the following reasons: The temperature span (AD or BC) between the hot and cold sink is limited by the ΔT_{ad} , which can be obtained between the high and lowest magnetic fields of the cycle (the two isofield curves). For example, if T_{H} is known then T_{C} cannot be chosen freely but is limited by ΔT_{ad} . In addition, as ΔT approaches ΔT_{ad} the refrigeration capacity and COP goes towards zero as the entropy difference between AB and CD becomes smaller. Finally, the cycle requires a varying magnetic field, which can only be produced by an electromagnet or superconducting magnet where the field can be manipulated.

2.3.2 The magnetic Ericsson refrigeration cycle

For practical refrigeration, it is necessary to make the ΔT independent of ΔT_{ad} . This can be accomplished by the magnetic Ericsson cycle which utilizes regeneration to achieve this

purpose. The Ericsson cycle consists of two isothermal and two isofield processes and is illustrated in the S-T diagram shown on Fig. 2.7⁴.

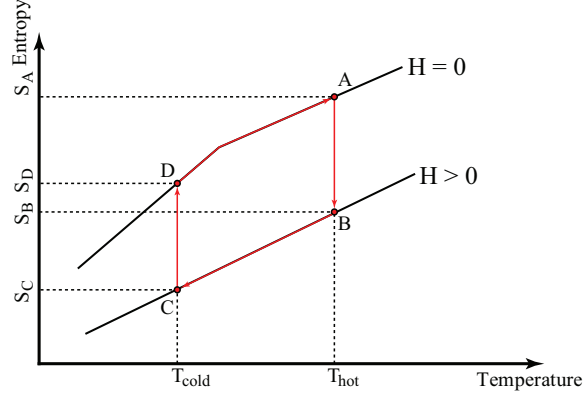


Figure 2.7: The magnetic Ericsson cycle. Process A to B consists of isothermal magnetization and heat rejection, from B to C isofield cooling and regeneration by rejection of heat to a storage medium, from C to D isothermal demagnetization and heat absorption and from D to A isofield heating with regeneration by absorption of heat from a storage medium.

The absorbed heat can be determined as:

$$q_c = \int_C^D T ds = T_{\text{cold}}(s_D - s_C) \quad (2.15)$$

The rejected heat can likewise be determined as:

$$q_r = \int_A^B T ds = T_{\text{hot}}(s_B - s_A) \quad (2.16)$$

The work is then determined as:

$$w = -q_r - q_c = T_{\text{hot}}(s_A - s_B) - T_{\text{cold}}(s_D - s_C) \quad (2.17)$$

Finally, the COP can be calculated as:

$$COP = \frac{T_{\text{cold}}(s_D - s_C)}{T_{\text{hot}}(s_A - s_B) - T_{\text{cold}}(s_D - s_C)} \quad (2.18)$$

Brown [12] constructed the first room temperature magnetic refrigerator based on the Ericsson cycle⁵. Browns design is illustrated on Fig. 2.8, and used in the following to describe regeneration and the practical realization of a magnetic refrigerator in more detail. The

⁴Equation 2.17 show above, can only be used to determine the magnetic work of a reversible cycle. However, if the Curie temperature lies within the temperature span of the cycle as shown on Fig. 2.7 the cycle becomes irreversible. In this case Eq. 2.17 is only an approximation of the magnetic work.

⁵Notice Brown refers to the cycle as a magnetic Stirling cycle. Here the refrigeration cycles are named according to ref. [17]

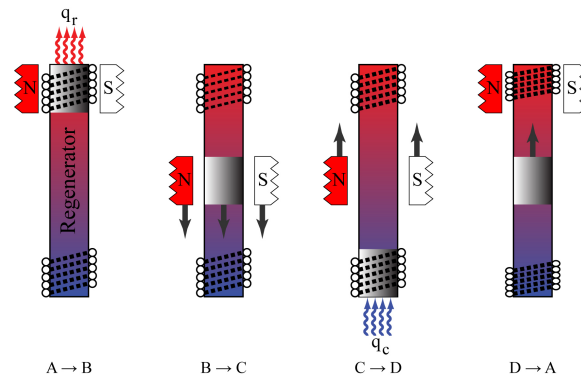


Figure 2.8: Browns room temperature magnetic refrigerator based on the Ericsson cycle. The position of the magnet and refrigerant inside the regenerator during the four steps of the Ericsson cycle shown on Fig. 2.7 is illustrated on the four figures from left to right.

regenerator of Browns machine consisted of a vertical cylinder filled with a water/alcohol mixture and the refrigerant was Gd in the form of parallel plates. The refrigerant slides up and down the length of the regenerator allowing the regenerator fluid to pass between the Gd plates. In each end of the regenerator a heat exchanger was placed to provide isothermal conditions. One heat exchanger was connected to the surroundings while the other was connected to the cooling load. At steady-state there is a temperature gradient along the regenerator and the machine starts with the refrigerant and the magnet positioned at the hot end of the regenerator. The refrigerant is magnetized and rejects heat to the hot heat exchanger. The refrigerant and the magnet are then simultaneously moved down through the regenerator during which the refrigerant rejects heat to the regenerator until it is cooled to the temperature at the cold end. The magnet is then moved up to the hot reservoir thereby demagnetizing the refrigerant, which then absorbs heat from the cold reservoir. Finally, the refrigerant is moved up through the regenerator where it absorbs heat from the fluid until it is heated to the temperature of the hot end. The regenerator functions as a heat recovery storage where heat is stored as the refrigerant moves from the hot end to the cold end. Part of this heat is then reabsorbed as the refrigerant moves from the cold end to the hot end. Using this design and a superconducting magnet with a field of 7 T, Brown was able to produce a no-load ΔT of 47 K between the hot end (46 °C) and the cold end (−1 °C). This is approximately 3 times larger than ΔT_{ad} at 7 T [12].

2.3.3 The Active Magnetic Regenerator

Barclay & Steyert presented and patented the Active Magnetic Regenerator (AMR) refrigeration cycle in 1982 [29, 13]. Chen et al. subsequently determined that except for the Carnot cycle, the AMR is the most efficient refrigeration cycle for MR at room temperature [30]. The AMR is based on a solid regenerator of a magnetocaloric material (the refrigerant) that allows an inert fluid to flow through. The fluid acts as a medium for heat transfer between the solid refrigerant and the cooling load and the surroundings. Exam-

ples of regenerator geometries are parallel plates, perforated plates and packed beds [31]. The regenerator is situated within an enclosure, which also contains the heat transfer fluid. Pistons or valves are mounted in both ends of the enclosure and move the fluid out from the regenerator and into two heat exchangers placed in both ends. One heat exchanger (the CHEX) is connected to the cooling load and the other heat exchanger (the HHEX) is connected to the surroundings. The MCE is typically generated by moving the AMR enclosure in and out of a static magnetic field. The AMR refrigeration cycle consists of four steps: (1) Magnetization, which increases the temperature of the regenerator with a subsequent heat transfer to the fluid, (2) the cold blow where hot fluid is displaced from the regenerator and into the HHEX where the fluid rejects heat to the surroundings, (3) demagnetization, which decreases the temperature of the regenerator which results in heat absorption from the fluid and (4) the hot blow which displaces cold fluid from regenerator towards the CHEX where the fluid absorbs heat from the cooling load [19]. There are two main AMR designs: the reciprocating AMR and the rotating AMR, as shown on Fig. 2.9. The difference between the two designs is that the rotating AMR consists of a wheel with

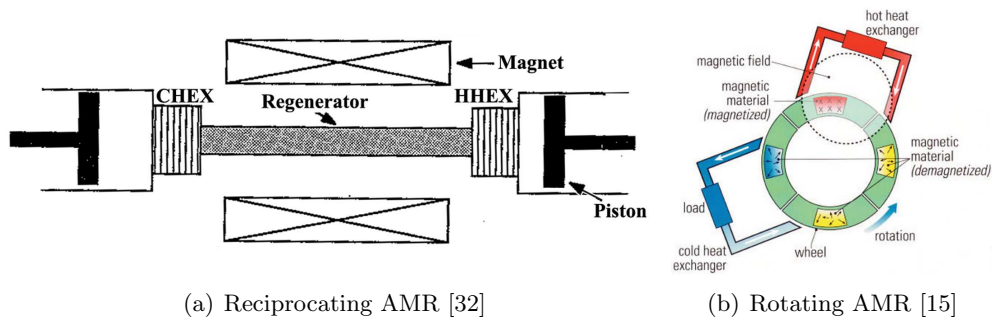


Figure 2.9: A schematic illustration of the reciprocating and rotating AMR designs.

multiple regenerators that rotates such that one regenerator enters the magnetic field and rejects heat while another regenerator is removed from the magnetic field and absorbs heat. This design allows the rotating AMR to continuously produce cooling. Compared to this configuration, the reciprocating AMR typically only has a single regenerator and perform each step of the AMR cycle sequentially and thus only produces cooling during the cold blow. During the cyclical steady-state, there is a nearly linear temperature profile through the regenerator going from T_C at the CHEX to T_H at the HHEX [33, 34]. Fig. 2.10 shows a simplified temperature profile in a reciprocating AMR, during the four steps of the refrigeration cycle. The figure also shows the positions of the pistons and the magnetic field during the cycle. The regeneration occurs during the blow periods, where the regenerator acts as a heat storage that heats or cools the fluid flowing out of the regenerator [34]. During the cold blow the regeneration heats the exiting fluid to a temperature equal to or above T_H and during the hot blow the regeneration cools the exiting fluid to a temperature equal to or below T_C . However, if an excessive amount of fluid is displaced from the regenerator there is insufficient heat stored in the regenerator to heat or cool the fluid sufficiently. It is therefore important that the fluid only moves a specific fraction of the regenerator length.

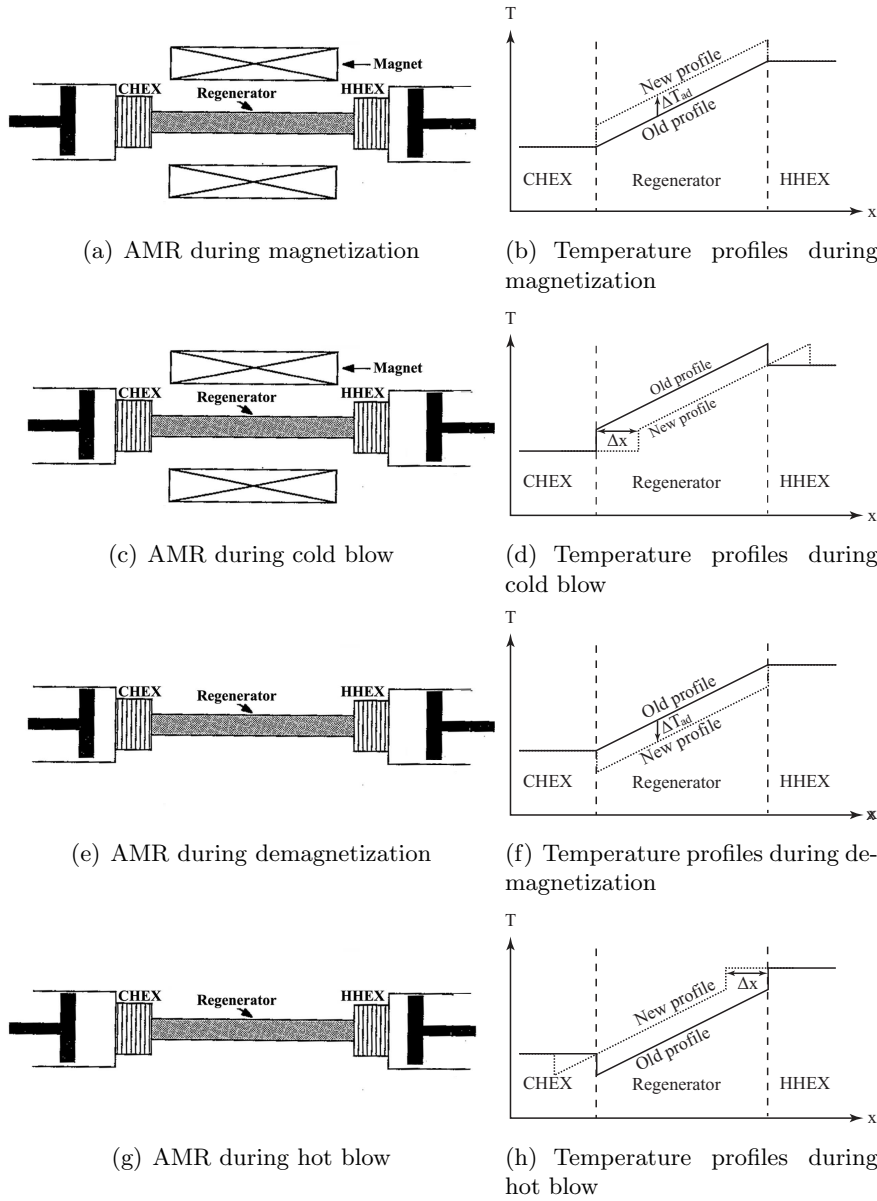


Figure 2.10: The position of the pistons and the magnet (left column) and the temperature profiles in the regenerator (right column) during the AMR cycle. For simplicity it is assumed that ΔT_{ad} is constant in the illustration of the temperature profiles. Figs. (a-b) During the magnetization the temperature of the regenerator increases above that of the fluid by ΔT_{ad} and the fluid is heated by heat transfer from the regenerator. Figs. (c-d) During the cold blow, fluid at T_C flows from the CHEX into the regenerator and displace all the fluid with a temperature above T_H and the hot fluid, which flows into the HHEX rejects heat to the surroundings. Figs. (e-f) During the demagnetization, the temperature profile increases by ΔT_{ad} and the fluid in the regenerator is cooled by heat transfer to the regenerator. Figs. (g-h) During the hot blow, fluid at T_H from the HHEX flows into the regenerator and displaces all the fluid with a temperature below T_C and the cold fluid, which flows into the CHEX absorbs heat from the cooling load. Figs. a,c,e,g were adapted from [32].

2.4 Previously developed mathematical models of the AMR

The AMR constitutes a thermodynamic system, which can neither be represented by analogies to regenerative vapour-compression refrigeration cycles nor as a multiple-stage refrigeration cycle [35]. Each infinitesimal element of the AMR regenerator experiences a unique thermodynamic cycle where a solid produces the refrigeration while the heat transfer fluid transfers heat between the regenerator elements [34]. In addition, there is a possible overlap between the thermodynamic cycles of adjacent elements. These issues and the coupled physical effects of fluid flow, heat transfer and magnetism make analytical analysis of AMRs difficult if not impossible. To overcome these issues, numerical models are used for design and optimization of AMRs. This section presents examples of previously developed AMR models and shows selected model.

The first model of the AMR was presented in 1983 by Barclay for a reciprocating AMR which operated in the temperature range from 20 K to 77 K [29]. The AMR regenerator consisted of a porous bed of particles of an unspecified magnetocaloric material and the heat transfer fluid was hydrogen or helium. The model was one-dimensional and based on a model of heat transfer in a porous prism originally presented by Schumann in 1929 [36]. Because the model is one-dimensional, it only considers the temperature distribution along the length of the regenerator (the x-direction) and assumes that the temperature differences across the bed (the y-direction) can be neglected due to the small diameter of the particles in the regenerator. The governing equations were a coupled set of partial differential equations of the temperatures in the regenerator and fluid and the MCE of the regenerator is implemented as a heat source. The original model by Barclay is detailed and accounts for conduction and convection, heat loss to the surroundings and heat generation due to viscous dissipation and a large majority of later AMR models are based on this model.

One such model was presented by Schroeder et al in 1990 who developed the first model of a room temperature AMR [27]. The regenerator was made of a porous bed of Gd, compressed nitrogen was used as the heat transfer fluid and the magnetic field was assumed to be produced by a superconducting magnet with a strength of 7 T. The model was based on the schematic shown on Fig. 2.11(a). The governing equations for the regenerator (Eq. 2.19a) and the fluid (Eq. 2.19b) were expressed as:

$$\rho_s c_{p,s} \frac{\partial T_s}{\partial t} = k_s \frac{\partial^2 T_s}{\partial x^2} + \frac{A_s h}{V_s} (T_f - T_s) \quad (2.19a)$$

$$\rho_f c_{p,f} \frac{\partial T_f}{\partial t} = k_f \frac{\partial^2 T_f}{\partial x^2} - \rho_f c_{p,f} u \frac{\partial T_f}{\partial x} + \frac{A_s h}{V_f} (T_s - T_f) + \frac{A_w h}{V_f} (T_w - T_f) + \dot{Q} \quad (2.19b)$$

where the terms from left to right in Eq. 2.19a represent heat storage in the regenerator, conduction in the regenerator and heat transfer from the regenerator to the fluid and the terms in Eq. 2.19b represent heat storage in the fluid, conduction in the fluid, convection in the fluid, heat transfer from the fluid to the regenerator, heat loss to the surroundings and a heat source. In Eq. 2.19a and Eq. 2.19b ρ_s , ρ_f are the solid and fluid densities

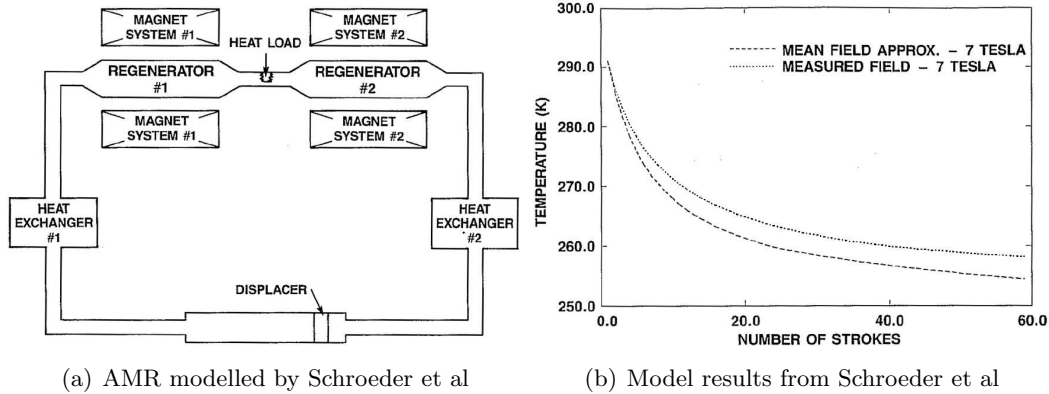


Figure 2.11: (a) Schematic illustration of the AMR modelled by Schroeder et al. which shows a double acting reciprocating AMR with two independent regenerators, magnet systems and hot heat exchangers connected to a common cooling load. (b) The predicted temperature span with a 7 T field using both model and experimental data of the heat capacity and the MCE of Gd. The figures were adapted from ref. [27].

respectively, $c_{p,s}$, $c_{p,f}$ are the solid and fluid heat capacities, respectively, T_s , T_f are the temperature of the solid and fluid, respectively, k_s , k_f are the thermal conductivities of the solid and fluid, respectively, h is the heat transfer coefficient for the heat transfer between the fluid and solid, A_s, A_w are the surface areas between the regenerator and fluid and the fluid and AMR enclosure walls, respectively, V_s, V_m are the volumes of the regenerator material and fluid, respectively, u is the velocity of the fluid and \dot{Q} is a heat source. Schroeder et al does not explicitly state how the MCE is implemented but assumes adiabatic magnetization in the AMR. This implies that the MCE is implemented as a temperature change. The boundary conditions are a prescribed temperature for the fluid entering the regenerators and the cooling load was implemented as a prescribed heat source. Furthermore, during the magnetization and demagnetization periods the temperature of the fluid is equal to the temperature of the regenerator. This simplification is justified by the fact that the superconducting magnet takes several seconds to apply or remove the magnetic field, which is assumed to be enough time for heat transfer so that the temperature differences between the solid and the fluid are negligible [27]. The model was implemented with both experimental values and mean field model data of the specific heat capacity and the MCE of Gd. The AMR performance using both kinds of properties is presented on Fig. 2.11(b). Using the experimental data the AMR reaches a temperature of 258 K at the cold end of the regenerators and using the mean field model data the AMR obtains a temperature of 254 K at the cold end, which shows that there is little difference in the results of the model with either type of material properties.

The majority of subsequent models are simpler than the models presented by Schroeder et al. and Barclay, see for example [37, 38, 39, 40]. For instance, the model developed by Shir et al [39] was based on the reciprocating AMR design illustrated on Fig. 2.12(a). The regenerator is made of a packed bed of Gd particles, the heat transfer fluid was a non-

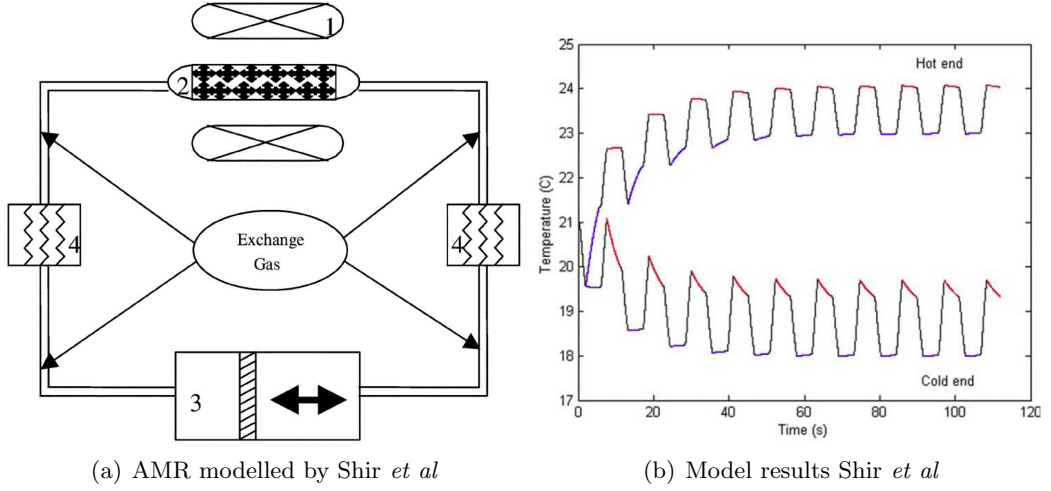


Figure 2.12: (a) Schematic illustration of the AMR modelled by Shir *et al.*, where (1) is a permanent magnet, (2) is the regenerator, (3) is a piston-cylinder displacer and (4) are the heat exchangers. (b) The predicted temperatures at the hot and cold end of the regenerator with a 2 T field where the temperature of the fluid entering the regenerator from both heat exchangers was equal to the temperature of the surroundings. The figures were adapted from ref. [39].

specific gas and the magnetic field was 2 T. Compared to the model by Schroeder *et al.*, Shir *et al.* does not account for axial conduction in the regenerator and fluid and neglects losses to the surroundings. With these approximations the governing equations for the solid (Eq. 2.20a) and the fluid (Eq. 2.20b) can be expressed as:

$$\frac{\partial T_s}{\partial t} = \frac{A_s h}{\rho_f c_{p,s}(1 - \epsilon)} (T_f - T_s) \quad (2.20a)$$

$$\frac{\partial T_f}{\partial t} + u \frac{\partial T_s}{\partial x} = \frac{A_s h}{\rho_s c_{p,f} \epsilon} (T_s - T_f), \quad (2.20b)$$

where ϵ is the porosity of the regenerator. To implement the MCE Shir *et al.* assumes that the temperature of both regenerator change as:

$$\frac{dT}{dt} = -\mu_0 \frac{T}{c_{p,s}} \left(\frac{\partial \sigma}{\partial T} \right)_H \frac{dH}{dt}, \quad (2.21)$$

Eq. 2.21 allows the magnetic field to be a function of time which make the AMR model fully time dependent. The boundary conditions for the flow entering the regenerator are a prescribed temperature. Fig. 2.12(b) presents selected results from the model. The simplifications of the governing equations for the AMR used by Shir *et al.* results in that the model does not account for the conduction from heat from the hot end to the cold end, referred to as the back flow. In Eq. 2.20b the simplifications may be justified by that convection in a fluid is normally much greater than the conduction and also because a gas was used as the heat transfer fluid, which has a thermal conductivity much lower than

the regenerator material. These factors makes such approximations reasonable. However, AMRs operating at room temperature commonly use liquids as the heat transfer fluid where the values of the thermal conductivity is high compared to a gas. These two factors makes such approximations less appropriate in AMR operating at room temperature. The consequence of the above simplifications and the neglect of losses to the surroundings may be that the AMR model may overestimate the performance of the AMR.

The governing equations of the AMR can be further simplified by using the approach presented by Matsumoto & Hashimoto [41] and DeGregoria [32] which was originally developed to model AMRs operating in the cryogenic regime. This type of AMR model does not account for the thermal conductivity of the fluid and regenerator nor any other losses and further neglects the mass of the fluid entrapped in the regenerator. Using this approach the governing equations for the solid (Eq. 2.22a) and the fluid (Eq. 2.22b) are expressed as [42, 43]:

$$m_s c_{p,s}(H, T) \frac{\partial T_s}{\partial t} = hAL(T_f - T_s), \quad (2.22a)$$

$$\dot{m}_f c_{p,f} \frac{\partial T_f}{\partial x} = hA(T_s - T_f), \quad (2.22b)$$

where m_s is the mass of the regenerator, L is the length of the regenerator and A is in this case the heat transfer area per unit length of the regenerator. These simplifications allow the governing equations to be expressed in dimensionless numbers where the temperature of the regenerator and fluid only depend on two parameters: the Number of heat Transfer Units (NTU) and the utilization (Φ) which are defined as

$$NTU = \frac{hAL}{\dot{m}_f c_{p,f}}, \quad (2.23)$$

$$\Phi = \frac{\dot{m}_f c_{p,f} P}{m_s c_{p,s}}, \quad (2.24)$$

where P is the time period of either blow and $c_{p,s}$ is the average specific heat capacity of the regenerator material during the cycle. These two parameters are convenient because they have a physical meaning as both the NTU and the utilization are used in traditional heat transfer. The use of the dimensionless variables allows the AMR to be characterized in terms of only NTU and Φ in a performance map similar to the one shown on Fig. 2.13. The additional simplifications result in that the fluid instantaneously obtains the same temperature as the solid, which again may be justified by the use of a gas as heat transfer fluid. The high thermal diffusivity ($k/(c_p \cdot \rho)$) of a gas compared to the regenerator material means that the gas responds quickly to temperature changes in the surroundings [44]. However, using a liquid instead of a gas as the heat transfer fluid may invalidate this simplification since the thermal diffusivity of a liquid is much lower than that of a gas.

Comparisons between modelling and experimental results have been published and selected results are shown in Fig. 2.14. Generally, these results show that the models are able to reproduce the general shape of the transient temperatures at the hot and cold ends of the regenerator and generally provides a reasonable estimate of the trends in the experimental results of AMR behavior. However, the models tend to over-estimate the temperature span

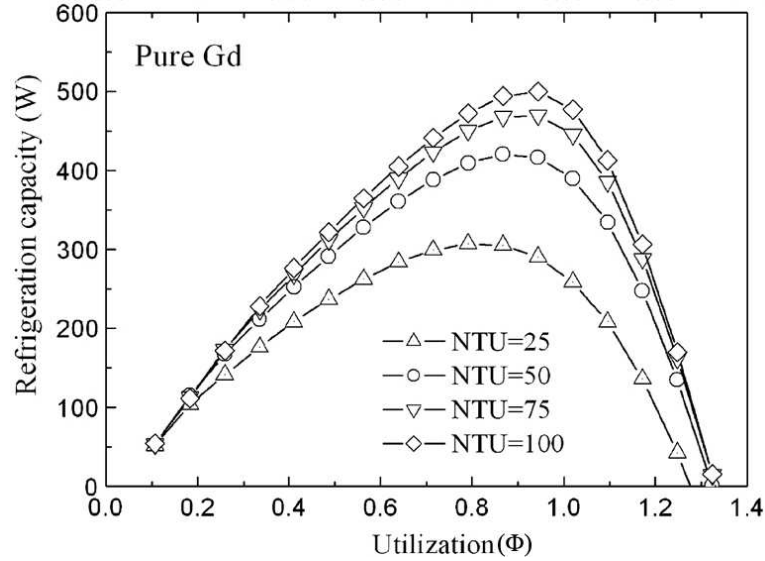
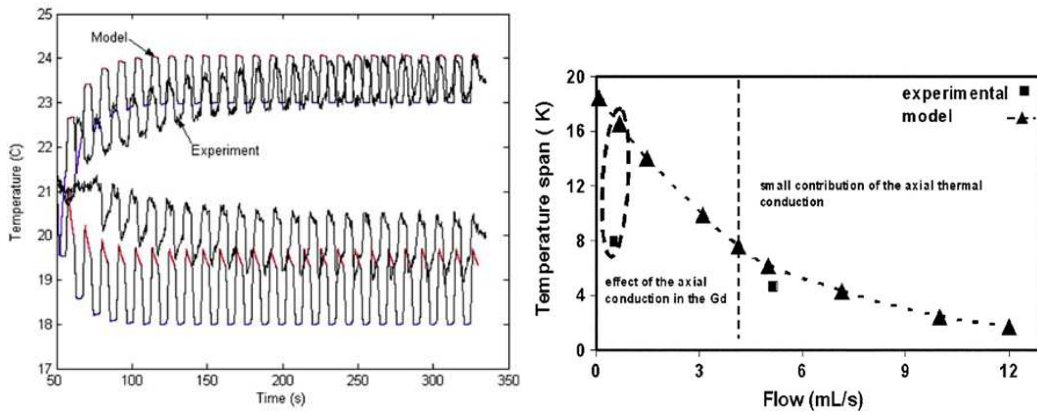


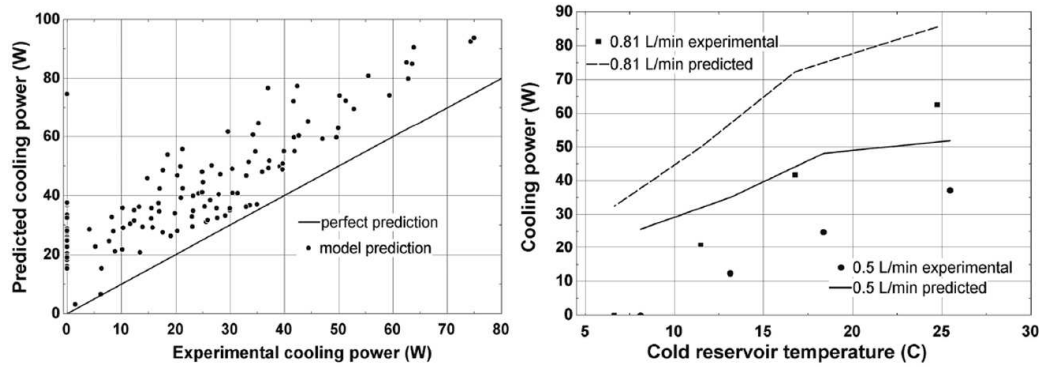
Figure 2.13: The refrigeration capacity of a reciprocating AMR in terms NTU and Φ predicted with the model developed by Li et al. The figure was adapted from ref. [43].

between the heat exchangers and the refrigeration capacity. These discrepancies are attributed to the neglecting of axial conduction and because parasitic losses are not included in the model [38, 45]. It has also been suggested that the tangential temperature gradient should be taken into consideration [46].

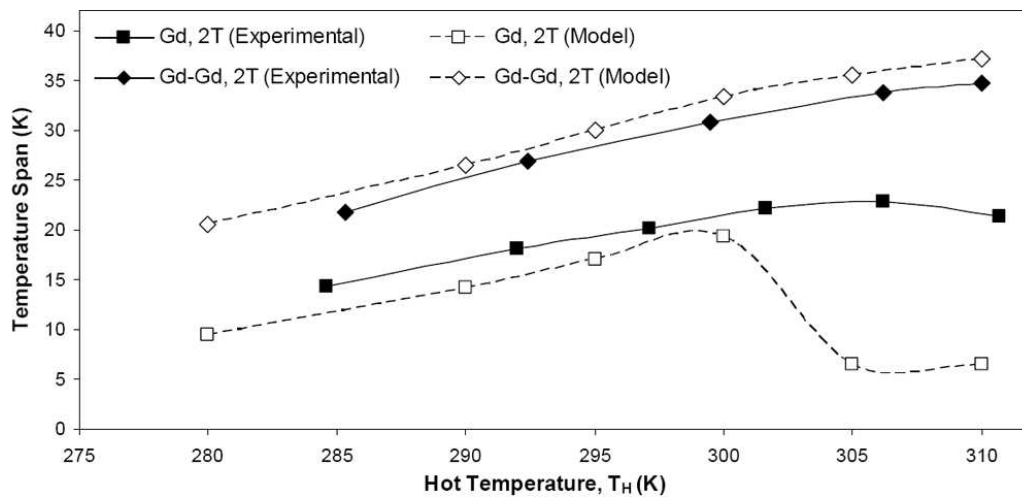
All the models described above are very similar and the main differences are the types of heat transfer in the models and which types of losses are accounted for. The 1-D AMR model is attractive because it is relatively simple to implement and gives reasonably accurate results. However, the 1-D approach was originally developed for a porous regenerator, where it can be assumed that the temperature gradient across the bed is negligible. This may not apply for other types of regenerator geometries. In addition, the one-dimensional approach is highly dependent on an accurate estimate of the heat transfer coefficient for the heat transfer between the regenerator and fluid. Empirical or theoretical correlations are normally used to estimate the heat transfer coefficient. However, such correlations are general in nature and often assumes that the temperature or heat flux of the solid is constant [44]. This does not apply in an AMR. In addition, many of the correlations for heat transfer coefficients were developed on the basis of a gas as heat transfer fluid. This may not be appropriate since many room temperature AMRs use liquids [46]. In a 2-D model the heat transfer between the regenerator and the fluid is calculated explicitly from the temperature gradients at the interface between the two and this is one of the strengths of the 2-D model approach compared to the 1-D approach.



(a) Comparison between experimental and simulated AMR performance from Shir et al. [45] (b) Comparison between experimental and simulated AMR performance from Allab et al. [38]



(c) Comparison between experimental and simulated AMR performance from Engelbrecht et al. [47]. The solid line of the left figure shows where the model results would be if there was perfect agreement between the experimental and the model.



(d) Comparison between experimental and simulated AMR performance from Dikeos et al. [48]

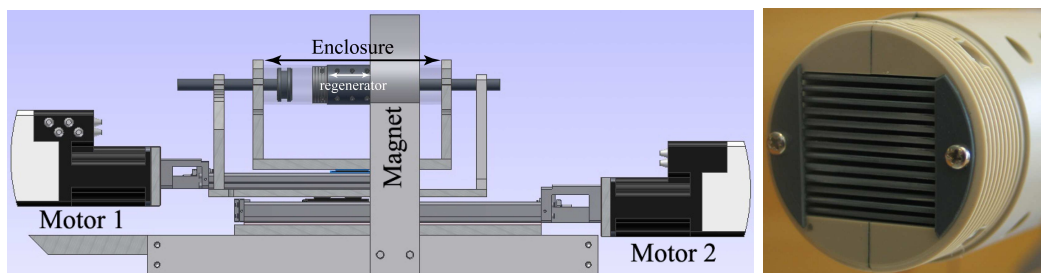
Figure 2.14: Comparisons between the experimental and the simulated performance for an AMR from selected studies.

This page was intentionally left blank.

Chapter 3

Development of a two-dimensional mathematical model of a reciprocating room-temperature Active Magnetic Regenerator

The mathematical model described in this chapter was developed in order to simulate the behavior and performance of an experimental AMR designed and constructed at Risø National Laboratory. The experimental AMR features a reciprocating design and is based on a regenerator, which consists of parallel plates arranged in a stack configuration and separated by channels of heat transfer fluid. The regenerator is placed inside a cylindrical enclosure, which also holds the pistons that move the heat transfer fluid through the channels of the regenerator. The design of the experimental AMR and a close-up of the regenerator are shown on Fig. 3.1. The magnetic field will be produced by a ring shaped



(a) Experimental reciprocating AMR design.

(b) Cross section of the regenerator.

Figure 3.1: (a) The design of the experimental AMR constructed at Risø National laboratory shown without heat exchangers. The pistons inside the enclosure is moved by motor number 1 and the enclosure is moved in and out of the magnetic field by motor number 2. (b) The regenerator consists of a stack of flat, parallel plates.

permanent magnet (Hallbach array) with a central hole where the magnetic field is concentrated. A motor moves the enclosure in and out of the permanent magnet and a second motor move the pistons inside the enclosure. Fig. 3.2(a) shows a schematic of the interior of the enclosure including the proposed positions of the two heat exchangers and Fig. 3.2(b) shows an illustration of the regenerator.

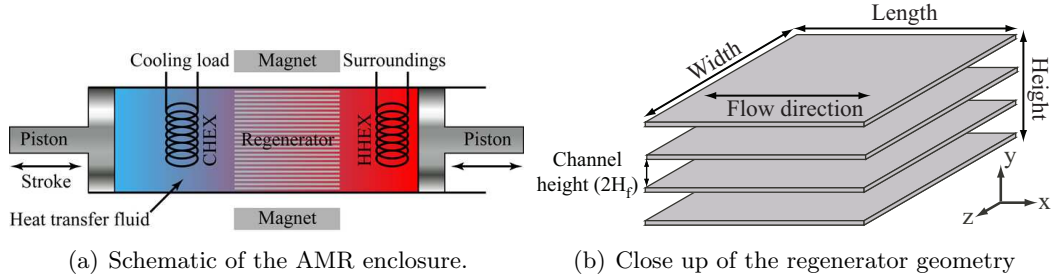


Figure 3.2: The AMR enclosure and regenerator geometry considered in the development of the mathematical model.

The parallel-plate regenerator is rarely used compared to the more common packed bed regenerator. A recent review shows that out of 10 recently constructed AMRs, only two uses parallel-plates whereas 7 uses a porous bed [49]. However, a study by Barclay & Sarangi [31] showed that a parallel-plate regenerator can achieve a higher performance compared to the packed bed. Furthermore, the parallel-plate regenerator has a more controlled flow (i.e. laminar) of the fluid which results in a lower pressure loss. In addition, the shape and the dimensions of the regenerator can be controlled to obtain a better heat transfer and therefore a better performance.

3.1 Modelling geometry

By neglecting boundary effects in the transversal direction (the z -direction in Fig. 3.2(b)) the AMR can be confined to two dimensions. Fig. 3.3(a) shows a schematic of the full 2-D geometry considered in the development of the mathematical model. It is reasonable to neglect the transversal heat transfer since a well-insulated AMR has little heat loss to the surroundings and therefore a small temperature gradient in the z -direction. The heat exchangers are modelled as plates, which are placed at both ends of the regenerator. The gap between the regenerator and the heat exchangers ensure that the heat transfer to and from the regenerator only occurs through the fluid. This gap is considered to be thermally insulated and therefore omitted from the model geometry. This is a reasonable assumption since the gap either consists of heat transfer fluid, which has a thermal conductivity much lower compared to that of the regenerator material (see Table 3.2 for typical values) or is made of a material specially chosen to ensure thermal insulation between the heat exchangers and the regenerator. However, the gap is included in the modelling of the fluid flow to obtain pure channel flow between the regenerator plates. Likewise, the pistons are also

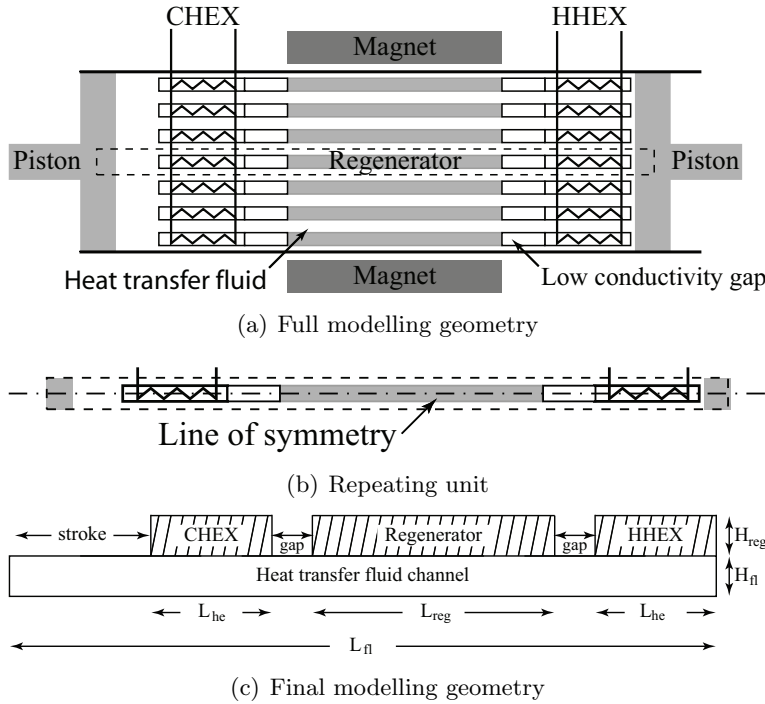


Figure 3.3: (a) Schematic illustration of the full modelling geometry considered in the development of the AMR model. (b) The repeating design of the AMR allows the model geometry to be reduced to a single repeating unit, which consists of a single regenerator plate surrounded by half a channel of fluid on either side with heat exchangers and pistons at both end of the regenerator plate. (c) The line (- · - ·) on Fig. (b) illustrates the symmetry line of the repeating unit that allows the repeating unit to be simplified to the final modelling geometry which consists of half a repeating unit.

omitted from the model geometry since the heat conduction through the pistons is negligible. By neglecting boundary effects, the repetitive design of the regenerator allows the full geometry to be reduced to a repeating unit as illustrated on Fig. 3.3(b). The geometry of the repeating unit can be further simplified due to symmetry as illustrated on Fig. 3.3(c). Note, the pistons on Fig. 3.3 are in their leftmost position as shown on Fig. 3.2(a).

3.2 Governing equations of the AMR model

The governing equations of the AMR mathematical model consists of a set of coupled partial differential equations (PDE), which were solved with the commercial software COMSOL Multiphysics. COMSOL uses the weak formulation of the Finite Element (FE) method to solve the PDEs on integral form and the time-dependent terms are solved with an implicit backwards differentiation method (BDF) [50]. The governing equations of the channel flow and the heat transfer were solved with the standard COMSOL implementation of these PDEs. However, during the development of the AMR model it was necessary to develop

specialized methods to model some of the unique characteristics of the AMR and to solve the model itself. These methods will be described in more detailed in the following description of the AMR model. The simulation of the AMR cycle is performed in four stages which are illustrated on the schematic diagram in Fig. 3.4, and in the following, each stage is described in detail.

1. The initial stage determines the velocity profile in the fluid.
2. The second stage models the magnetization and the cold blow.
3. The third stage models the demagnetization and the hot blow.
4. The final post-processing stage evaluates the performance in terms of temperature span, cooling capacity, work input and COP.

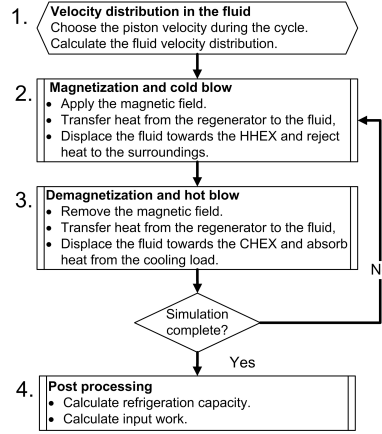


Figure 3.4: The AMR cycle is modelled by grouping the four physical steps into two repeating stages: (2) magnetization and the cold blow and (3) the demagnetization and the hot blow. The two stages are repeated until convergence. The AMR simulation is preceded by an initialization stage (1) which determines the fluid flow and the simulation is concluded with an post processing stage (4) which evaluates the AMR performance.

3.2.1 Stage 1 - The velocity distribution in the fluid

The velocity distribution in the fluid is determined by solving the momentum (Eq. 3.1a) and continuity equations (Eq. 3.1b) as implemented in COMSOL for an incompressible fluid (subscript f) with constant (temperature independent) properties.

$$\rho_f \left(\frac{\partial \mathbf{U}}{\partial t} + (\mathbf{U} \cdot \nabla) \mathbf{U} \right) - \mu_f \nabla^2 \mathbf{U} + \nabla p = 0, \quad (3.1a)$$

$$\nabla \cdot \mathbf{U} = 0, \quad (3.1b)$$

where ρ_f is the density of the fluid, μ_f is the dynamic viscosity of the fluid, \mathbf{U} is the two-dimensional velocity field (u, v) of the fluid, where u is the velocity in the x-direction and v is the velocity in the y-direction, p is the pressure and t is the time. Using a predetermined piston movement, the transient velocity distribution in the fluid is determined by solving Eq. 3.1a and Eq. 3.1b with the boundary conditions described in Section 3.4 until a cyclical steady-state is reached. Since the viscosity and the density are constants, the momentum and continuity equations are independent of the energy equation. The flow can therefore be solved, before the temperatures in the AMR are determined, without any impact on the solution of the flow. The resulting velocity field is then used as input to stage 2 and 3 of the AMR model. The approach used to solve Eq. 3.1a and 3.1b is described in Section 3.4.

3.2.2 Stage 2 - Magnetization and cold blow

During the magnetization, the MCE occurs almost instantaneously and increases the temperature throughout the entire regenerator [17, 18], which is followed by heat transfer from the hot regenerator to the fluid. During the cold blow, part of the fluid heated by the regenerator is removed by the pistons and the hot fluid rejects its heat to the HHEX. The two processes are illustrated on Fig. 3.5.

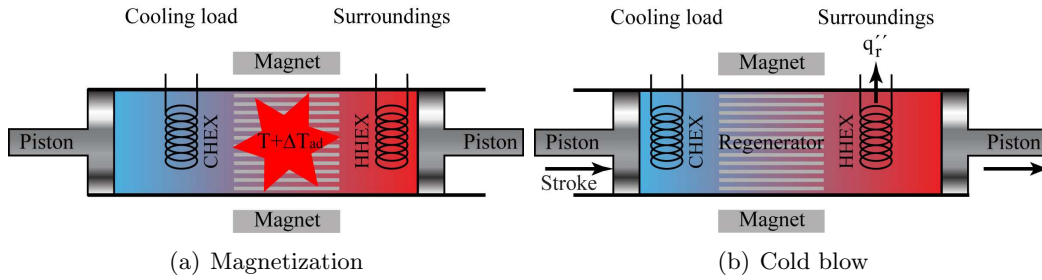


Figure 3.5: The second stage models the magnetization and the cold blow.

The magnetization can be assumed adiabatic [51] and is modelled by increasing the temperature in the regenerator by ΔT_{ad}

$$T = T_i + \Delta T_{ad}^m(T_i, H_0), \quad (3.2)$$

where T is the local temperature of the regenerator bed after the magnetization, T_i is either the initial temperature of the regenerator or the temperature in the regenerator at the end of stage 3 and $\Delta T_{ad}^m(T, H_0)$ is a function that describes ΔT_{ad} as the magnetic field is increased from zero to H_0 , where H_0 is the magnetic field applied to the AMR. To determine the temperature distribution in the AMR after the magnetization and during the cold blow, the coupled heat transfer equations for the solid domains (the regenerator and the two heat exchangers) and the fluid are solved. For the solid domains (subscript s) the temperature distribution is determined by the standard heat transfer equation implemented in COMSOL

$$\rho_s c_{p,s} \frac{\partial T_s}{\partial t} - k_s \nabla^2 T_s = 0, \quad (3.3)$$

where $c_{p,s}$ is the specific heat capacity of the solid, T_s is the temperature of the solid and k_s is the thermal conductivity of the solid. For compactness the generic subscript s is used for all the solid domains, however each domain is modelled with unique thermal properties. The temperature distribution in the fluid is determined by the heat transfer equation implemented in COMSOL for an incompressible fluid with convective terms

$$\rho_f c_{p,f} \left(\frac{\partial T_f}{\partial t} + (\mathbf{U} \cdot \nabla) T_f \right) - k_f \nabla^2 T_f = 0, \quad (3.4)$$

where $c_{p,f}$ is the specific heat capacity of the fluid, T_f is the temperature of the fluid and k_f is the thermal conductivity of the fluid. The velocity field previously determined from Eq. 3.1a and Eq. 3.1b is used in Eq. 3.4 to determine the convective heat transfer. All thermodynamic properties, except the specific heat capacity of the magnetocaloric material, which is temperature dependent, are evaluated at T_H . The solids and the fluid are assumed in perfect thermal contact with the following boundary condition

$$\left(k_f \frac{\partial T_f}{\partial y} \right) \Big|_{y=H_H} = \left(k_s \frac{\partial T_s}{\partial y} \right) \Big|_{y=H_H}. \quad (3.5)$$

Note, when Eq. 3.5 is used as the boundary condition between the solid and fluid, Eq. 3.1a and Eq. 3.1b must be solved with a sufficiently fine mesh to determine the development of the velocity boundary layer accurately. The boundary condition of the HHEX is a prescribed temperature¹:

$$T = T_H, \quad (3.6)$$

where T_H is temperature of the surroundings. This boundary conditions represents an ideal coupling between the HHEX and the surroundings, which may be obtained by having a large mass flow in the external circuit connecting the HHEX to the surroundings. The temperature distribution and the rate of rejected heat are determined by solving Eq. 3.2 – Eq. 3.4 with the described boundary conditions. The temperature distribution at the end of stage 2 is then used as the initial conditions in stage 3.

3.2.3 Stage 3 - Demagnetization and hot blow

In stage 3 the MCE reduces the temperature of the regenerator during the adiabatic demagnetization and the regenerator absorbs heat from the fluid. During the hot blow part of the cooled fluid is then removed by the pistons and absorbs heat from the cooling load. The two processes are illustrated on Fig. 3.6. The demagnetization is modelled by decreasing the temperature in the regenerator by the adiabatic temperature change

$$T = T_i + \Delta T_{ad}^{dm}(T_i, H_0), \quad (3.7)$$

¹The AMR model was described in a paper previously published in the International Journal of Refrigeration [52]. However, the version of the AMR model described in this paper uses a convective boundary. The change is due to that a prescribed temperature results in more accurate calculation of the refrigeration capacity and the COP. However, the solution of the temperatures in the AMR does not change. In addition, a prescribed temperature boundary condition also results in a shorter solution time of the model.

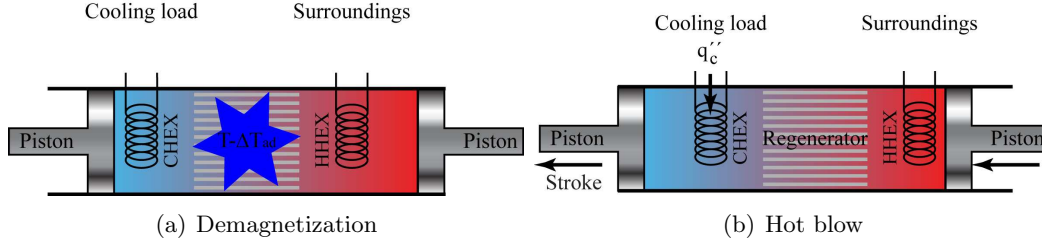


Figure 3.6: The third stage models the demagnetization and the hot blow.

where $\Delta T_{ad}^{dm}(T, H_0)$ describes ΔT_{ad} when the magnetic field is decreased from H_0 to zero and T_i is the initial temperature in the regenerator just after the end of stage 2. The two functions ΔT_{ad}^{dm} and ΔT_{ad}^m are related by the following equation:

$$\Delta T_{ad}^m(T_i, H_0) = -\Delta T_{ad}^{dm}(T_i + \Delta T_{ad}^m(T_i, H_0), H_0). \quad (3.8)$$

The boundary condition of the CHEX is either a prescribed temperature

$$T = T_C, \quad (3.9a)$$

or a prescribed heat flux

$$\dot{q}'' = \dot{q}_c'', \quad (3.9b)$$

where T_C is the temperature of the cooling load and \dot{q}_c'' is the prescribed cooling load per area of the CHEX. Eq. 3.9a is used when T_C is known and the corresponding refrigeration must be determined. Eq. 3.9b is used as a boundary condition for the CHEX when the applied cooling load is known, and the corresponding T_C must be determined. The two equations represents different options for specifying known or desired boundary conditions of the AMR. The remaining boundaries are considered adiabatic as they are either insulated or a symmetry line² in the model geometry:

$$\dot{q}'' = 0. \quad (3.10)$$

The overall boundary conditions for the heat transfer equations are illustrated in Fig. 3.7. The temperature distribution and the rate of absorbed heat is determined by solving Eqs. 3.3 to Eq. 3.9b with the described boundary conditions. The temperature distribution at the end of stage 3 is used as the initial conditions for stage 2 in the following cycle.

To determine the behavior in the AMR as a function of time, the model starts from an initial temperature distribution in the regenerator and fluid and then takes time steps forward in time by repeating stage 2 and 3 until the cyclical steady-state is obtained. In numerical terms, the cyclical steady-state occur when the difference between the solutions of two subsequent cycles are below a specified tolerance. In practice, the average T_C during the refrigeration cycle or the amount of absorbed heat from the cooling load or the COP are used as criteria to determine when the cyclical steady-state is obtained.

²There is no heat flux through a symmetry line in heat transfer as the temperatures on either side of the line are equal [44]

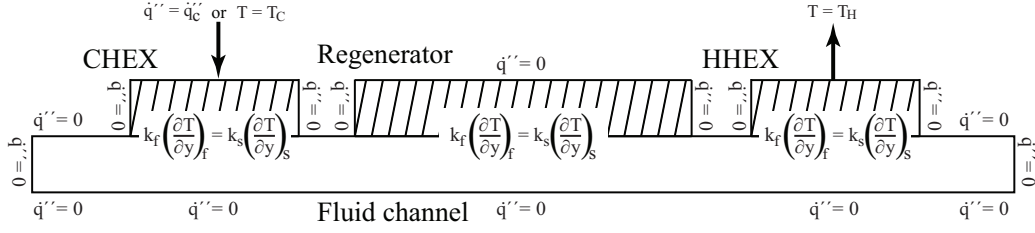


Figure 3.7: The boundary conditions of the heat transfer equations used in the AMR model.

3.2.4 Stage 4 - Evaluation of AMR performance

The amount of cooling per cycle absorbed per unit width of the CHEX in the z -direction is determined by integration of the heat flux through the outer boundary of the CHEX:

$$q'_c = \int_0^\tau \int_0^{L_{\text{HEX}}} \dot{q}'' dx dt, \quad (3.11)$$

where τ is the cycle period and L_{HEX} is the length of the heat exchanger. The corresponding refrigeration capacity is determined as

$$\dot{q}'_c = \frac{q'_c}{\tau}. \quad (3.12)$$

The rejected heat per cycle per width of the HHEX is similarly determined by integration of heat flux through the outer boundary of the HHEX:

$$q'_r = \int_0^\tau \int_0^{L_{\text{HEX}}} \dot{q}'' dx dt. \quad (3.13)$$

The total work input per width of the AMR is the sum of the work required to magnetize the regenerator and the work required to move the pistons:

$$w'_{\text{tot}} = w'_{\text{mag}} + w'_{\text{piston}}. \quad (3.14)$$

The work required to magnetize and demagnetize the regenerator bed cannot be calculated directly. However, there are no losses in the AMR model and the piston work is decoupled from the magnetic work. Therefore the 1st law of thermodynamics can be used during the cyclical steady-state to determine the magnetic work input per cycle as

$$w'_{\text{mag}} = q'_r + q'_c. \quad (3.15)$$

In Eq. 3.15 the plus sign (+) is due to the fact that q'_c is negative. Notice that the work required to move the fluid is not included in Eq. 3.15, because of the decoupling between the momentum and continuity equations and the heat transfer equations. The piston work

required to displace the fluid during the two blow periods is evaluated as the product of the pressure difference between the ends of the pistons and the volume flow of the fluid [44]:

$$w'_{\text{piston}} = \int_0^{\tau} \left(U_p \cdot H_{\text{fl}} \Delta p dy \right) dt, \quad (3.16)$$

where U_p is the velocity of the pistons, H_{fl} is the height of the fluid channel and Δp is the pressure difference between the two pistons. The COP of the AMR is determined as

$$COP = -\frac{q'_c}{w'_{\text{tot}}} \quad (3.17)$$

The Carnot efficiency of the AMR is determined as:

$$\eta = \frac{COP}{COP_{\text{Carnot}}}, \quad (3.18)$$

where COP_{Carnot} is determined by Eq. 2.14.

3.3 Modelling the piston displacement

The displacement of the heat transfer fluid constitutes a moving boundary problem, since the pistons move during the cycle, which cannot be solved directly by COMSOL³. To model the movement of the pistons a special procedure was developed for the AMR model, referred to as the coordinate transformation method. To model the stroke of the pistons, the model geometry is divided into a solid domain (the two heat exchangers and the regenerator) and a fluid domain. The situation where the pistons displace the fluid below the solid domain is equal to a situation where the fluid domain is stationary while the solid domain slides along the upper boundary of the fluid. This is illustrated on Fig. 3.8a. This approach allows both the solid and fluid domains to be modelled as stationary, while the relative movement is modelled using the coordinate transformation methods. This is illustrated on Fig. 3.8b. To implement the coordinate transformation let x_s be the x-coordinate of the solid domain boundary, let x_f be the x-coordinate of the fluid domain boundary, and let Δx denote the displacement of the solid domain relative to the fluid (the stroke of the pistons). The two coordinates are related by the following expression:

$$x_f = x_s + \Delta x(t). \quad (3.19)$$

Since Δx is equal to the movement of the pistons during the cycle it can be determined by integration of the piston velocity

$$\Delta x(t) = \int_0^t U_p(t') dt'. \quad (3.20)$$

³Moving boundaries have since become a standard part of COMSOL but this addition to COMSOL occurred after the development of solution method described here. Therefore it was decided to keep the model in the form described here since the model was already developed and verified.

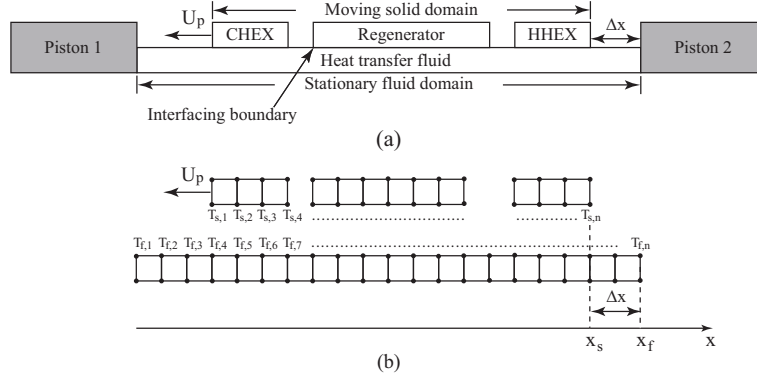


Figure 3.8: The conceptual approach of the coordinate transformation method, which is used to model the thermal conduction between a moving and the stationary domain. (a) The piston displacement of the fluid is converted to a situation where the solid domain slides along the top of the fluid domain. (b) The solid and the fluid domains are modelled separately and the piston movement is modelled with a coordinate transformation of the temperature along the interface. As an example, consider the situation in (b) where the solid domain has moved a distance (Δx) relative to the fluid. In this case, the part of the solid domain with the temperature $T_{s,1}$, is in contact with $T_{f,4}$, $T_{s,2}$, is in contact with $T_{f,5}$ and so on. This relation is used to implement the boundary condition given by Eq. 3.5.

If $T_s(x_s)$ is the temperature of the solid and $T_f(x_f)$ is the temperature of the fluid along the interfacial boundary, then the two temperatures must be identical since x_f and x_s represents identical positions in the AMR. Using Eq. 3.19, x_s can be substituted by Eq. 3.19 and $T_s(x_s)$ can be expressed in terms of x_f

$$T_s(x_f - \Delta x(t)) = T_f(x_f). \quad (3.21)$$

The corresponding temperatures determined by Eq. 3.21 are used in Eq. 3.5 to couple the two domains. The implementation of the coordinate transformation method in COMSOL is described in more detail in Appendix B.

3.4 Modelling the flow in the fluid channels

To solve the velocity field in the fluid, the momentum and continuity equations shown in Eq. 3.1a and Eq. 3.1b are formulated using dimensionless variables to obtain a consistent grid and good numerical accuracy of the solution. The following dimensionless variables are used:

Dimensionless time:

$$t^* = \frac{t}{\tau_0} \quad (3.22)$$

Dimensionless velocity vector:

$$\mathbf{U}^* = \frac{\mathbf{U}}{U_0} \quad (3.23)$$

Dimensionless x- and y-coordinate:

$$x^* = \frac{x}{L_0} \quad y^* = \frac{y}{L_0} \quad (3.24)$$

Dimensionless derivative with respect to position:

$$\nabla^* = L_0 \nabla \quad (3.25)$$

Dimensionless pressure:

$$p^* = \frac{p}{\rho_f U_0^2} \quad (3.26)$$

Dimensionless force:

$$\mathbf{F}^* = \frac{\mathbf{F} L_0}{\rho_f U_0^2} \quad (3.27)$$

Except for t^* these dimensionless variables are commonly used in fluid mechanics [53]. In the above equations τ_0 is a characteristic time scale, L_0 is a characteristic length and U_0 is a characteristic velocity. Introducing Eqs. 3.22 to 3.27 into Eq. 3.1a and multiplying by $L_0/(\rho U_0^2)$ on both sides yields the following result:

$$\left(\frac{L_0}{U_0 \tau_0} \frac{\partial \mathbf{U}^*}{\partial t} + (\mathbf{U}^* \cdot \nabla^*) \mathbf{U}^* \right) - \frac{1}{Re_f} \nabla^{*2} \mathbf{U}^* + \nabla p^* = \mathbf{F}^*, \quad (3.28)$$

where Re_f is the Reynolds number:

$$Re_f = \frac{\rho_f L_0 U_0}{\mu_f} \quad (3.29)$$

Inserting Eq. 3.23 and Eq. 3.25 into Eq. 3.1b yields the dimensionless continuity equation:

$$\nabla^* \cdot \mathbf{U}^* = 0. \quad (3.30)$$

In the present formulation the cycle period is used as the characteristic time, the piston velocity is used as the characteristic velocity and the characteristic length is half the height of the fluid channel (H_{fl}), see Fig. 3.3(c). Note, the Reynolds number is normally determined using the hydraulic diameter as the characteristic length. For a channel between parallel plates the hydraulic diameter is defined as four times H_{fl} [54]. This means that the Reynolds number determined by Eq. 3.29 is four times lower than the standard Reynolds number for flow between two infinite parallel plates. The difference has no impact on the solution and H_{fl} was chosen as the characteristic length because it results in a dimensionless y-coordinate, which goes from zero at the middle of the fluid channel (bottom of the repeating unit) to one at the top of the fluid channel. The solution of the velocity distribution in the fluid must also account for the coordinate transformation. This is done by specifying the appropriate boundary conditions for Eq. 3.1a and Eq. 3.1b in dimensionless form. The interface between the fluid and the pistons is a no-slip boundary where

$$\begin{pmatrix} u^* \\ v^* \end{pmatrix} = \begin{pmatrix} 0 \\ 0 \end{pmatrix}. \quad (3.31)$$

The interface between the fluid and the solid has a prescribed velocity equal to the velocity of the pistons as shown in Fig. 3.9 where

$$\begin{pmatrix} u^* \\ v^* \end{pmatrix} = \begin{pmatrix} U_p(t)/U_0 \\ 0 \end{pmatrix}. \quad (3.32)$$

where U_p is the piston velocity. The symmetry line is modelled as a slip boundary where the normal component of the velocity is zero

$$v^* = 0, \quad (3.33)$$

and the tangential component of the viscous force is zero

$$\left(\frac{\partial u^*}{\partial y^*} \right) = 0. \quad (3.34)$$

The boundary conditions for the solution of the fluid flow are illustrated in Fig. 3.9.

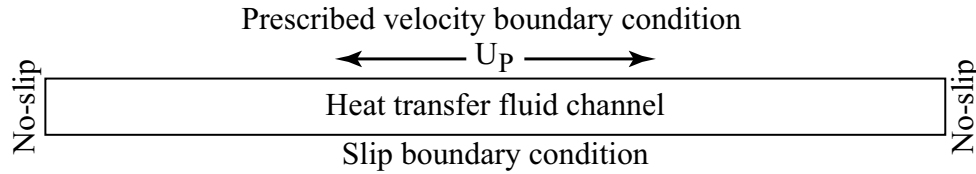


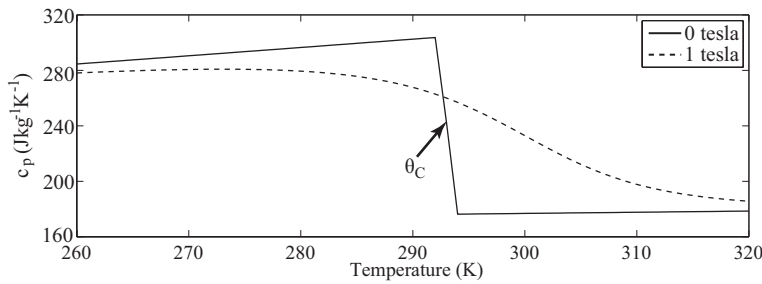
Figure 3.9: The boundary conditions of the momentum and continuity equations.

Appendix B shows a comparison of the results obtained with the dimensionless and non-dimensionless formulations of the momentum and continuity equations. The flow in the fluid channel reaches a cyclical steady-state within a single cycle. Thus only the flow in the first cycle is solved and the resulting velocity profiles are simply reused in every subsequent cycle when the temperature distribution in the AMR is determined. In Appendix B results of the flow during the initial two cycles are presented, which show that the cyclical steady-state of the flow is obtained within the first cycle.

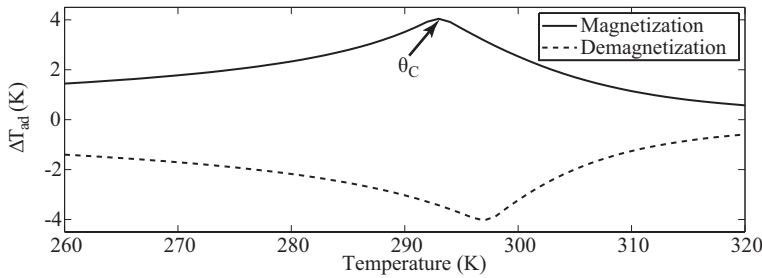
3.5 Model implementation

The geometrical dimensions were chosen on the basis of the original design of the prototype AMR constructed at Risø National laboratory. This AMR design features a regenerator made of approximately 25, 1 mm parallel plates separated by 1 mm channels, which are enclosed in a 16 cm long cylinder. Gadolinium was used as the regenerator material, the heat transfer fluid is water and the heat exchangers are assumed to be made of copper. The gap between the regenerator and the heat exchangers in the AMR model correspond to the proposed placement of the heat exchangers in the experimental AMR. The repeating unit of the AMR model was implemented with the geometry shown in Table 3.1 and the material

properties shown in Table 3.2. Fig. 3.10 shows the specific heat capacity and ΔT_{ad} of Gd in the temperature range where the AMR is expected to operate, which were evaluated with the WDS model. Fig. 3.11 illustrated the variation of the velocity of the pistons and the application of the magnetic field during the AMR cycle. The process parameters of the AMR cycle used in the initial simulations are shown in Table 3.3. The cycle period was chosen on the basis on the AMR description in ref. [19]. The length of the cycle into magnetization, demagnetization and blow periods was chosen to facilitate adequate heat transfer between the regenerator and the fluid before the blow periods. The 1 T was chosen since a magnetic field of this magnitude can easily be obtained by permanent magnets [4].



(a) The specific heat capacity of Gd at 0 and 1 T



(b) ΔT_{ad} of Gd at 1 T

Figure 3.10: (a) The specific heat capacity of Gd at 0 T and 1 T. (b) The ΔT_{ad} of Gd during magnetization and demagnetization. During magnetization ΔT_{ad} peaks at the Curie temperature, but during demagnetization ΔT_{ad} peaks at a higher temperature, in agreement with Eq. 3.8.

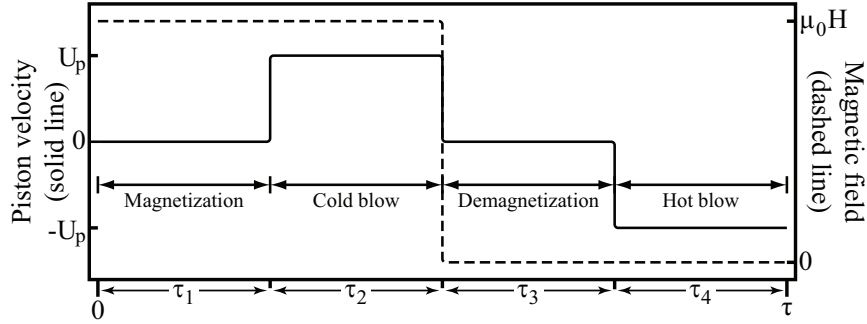


Figure 3.11: The variation of the piston velocity and the magnetic field during the AMR cycle. The pistons are stationary during the magnetization period (τ_1) and demagnetization period (τ_3) and move with a constant velocity during the cold blow (τ_2) and hot blow (τ_4). The magnetic field is applied at the beginning of the cycle (0 and τ) and removed at the end of the cold blow.

Table 3.1: Geometrical data used to validate the AMR model. Note, the dimensions corresponds to those of the modelling geometry, i.e. half a repeating unit.

Part	Material	Length (cm)	Height (mm)
Regenerator	gadolinium	5	0.5
Heat exchangers	copper	2	0.5
Fluid channel	water	16	0.5
Insulating gap	-	1	0.5

Table 3.2: Material properties evaluated at 298 K [55, 56]. In some of following validation tests the specific heat capacity of Gd is regarded as constant using the value below.

Material	c_p ($\text{Jkg}^{-1}\text{K}^{-1}$)	k ($\text{Wm}^{-1}\text{K}^{-1}$)	ρ (kgm^{-3})	μ ($\text{kgm}^{-1}\text{s}^{-1}$)
Gadolinium	235	10.5	7900	n.a.
Copper	385	401	8933	n.a.
Water	4183	0.595	997	$8.91 \cdot 10^{-4}$

Table 3.3: Initial process parameters for the AMR cycle

Parameter	Value	Unit
Piston stroke	2	cm
Cycle period (τ)	6	s
τ_1 and τ_3	2	s
τ_2 and τ_4	1	s
$\mu_0 H$	1	T

3.6 Model verification

The Comsol Multiphysics code has previously been validated and verified in a number of NAFEMS⁴ benchmark studies [57]. However, because the presented model uses an uncommon method to solve the moving boundary problem the model is further validated through a series of tests. The following tests are performed:

1. Validation of the coordinate transformation method.
2. A grid sensitivity analysis of the solution of the flow in the fluid channel.
3. Verification that the model has energy conservation.
4. A grid and time step sensitivity analysis of the AMR model.
5. Validation that the steady-state solution is independent of the initial conditions.

The spatial discretization of the geometry consists of a grid of rectangular elements. The spatial grid is illustrated on Fig. 3.12 where N_x is the number of elements in the x-direction and N_y is the number of elements in the y-direction. The grid sensitivity analysis is per-

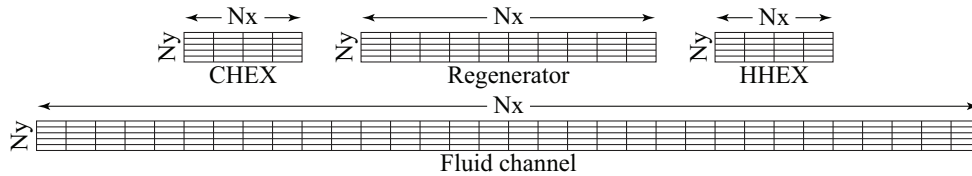


Figure 3.12: Schematic illustration of the rectangular grid used to discretize the AMR geometry.

formed on three grids where each grid has at least 50% more elements in each direction than the previous [58]. The number of elements in each of the three grids are shown in Table 3.4. It is important that the velocity distribution is determined accurately to ensure sufficient detail of the velocity boundary layer as discussed previously. The velocity field in the fluid channel is therefore solved on a finer grid than the grid used to determine the temperature distribution. In addition, the grid used to determine the flow is refined near the ends of the channel in order to get a good resolution of any vortices near these boundaries. The refinement increases the amount of grid elements in the x-direction by a factor of ten compared to the basic grid in the bulk of the fluid. The grids used to perform the grid sensitivity analysis of the fluid channel flow are shown in Table 3.4.

The temporal discretization of the AMR cycle consists of time steps of equal length and the time step sensitivity analysis is performed using the three different number of time steps shown in Table 3.5. However, the BDF method used by COMSOL uses an implicit scheme with variable order and variable time step to ensure that an accurate solution is achieved by adapting the time step to actual problem. This means that both the size and number of

⁴National Agency for Finite Element Methods and Standards.

Table 3.4: The grids used for the grid sensitivity analysis of the AMR model. The normal grid correspond to an element size of $1 \text{ mm} \times 0.05 \text{ mm}$ in all parts of the geometry. For simulation of the fluid flow the normal grid corresponds to an element size of $0.5 \text{ mm} \times 0.025 \text{ mm}$.

	Coarse grid	Normal grid	Fine grid
	$N_x \times N_y$	$N_x \times N_y$	$N_x \times N_y$
Regenerator	33×6	50×10	75×15
Heat exchangers	13×6	20×10	30×15
Fluid channel	106×6	160×10	240×15
Fluid channel (flow)	213×13	320×20	480×30

Table 3.5: The time steps used for the time step sensitivity analysis.

Time step	Number of time steps
Fine	240
Normal	120
Coarse	60

time steps used during the simulation may be somewhat different from the specified time step. COMSOL does solve the model at the specified time steps but may take additional time steps in between in order to achieve a proper solution when fast processes or transient impulses occur. This means that the model should be relatively independent of the number of time steps. However, during the post-processing the number of time steps are important since numerical integration is used to evaluate the amount of absorbed and rejected heat. The grid sensitivity analysis is performed using the normal time step, and the time step sensitivity analysis is performed using the normal grid.

3.6.1 Verification of the coordinate transformation method

Using the coordinate transformation method to couple the temperatures of two interfacing boundaries in order to solve the moving boundary problem is non-trivial and uses a specialized solution developed specifically for the 2-D AMR model. A test was therefore designed to determine the validity of the method and test whether the method obeys energy conservation. The test was performed by using the AMR model to simulate a single refrigeration with the above dimensions and material properties. In this test both the CHEX and the HHEX were kept thermally insulated (i.e. zero heat flow) to ensure that the amount of energy in the system remains constant. The MCE was not implemented in the test and the specific heat capacity of Gd was constant. The initial temperature of the heat exchangers and the fluid was 298 K and the initial temperature of the regenerator was 308 K. The normal grid and the normal time step shown in Table 3.4 and Table 3.5 was used for the discretization. The absolute tolerance on the temperatures was $1 \times 10^{-2} \text{ K}$ and the relative tolerance was 10^{-10} . The energy conservation of the model was tested by determining the

absolute residual of the sum of the energy content in the different parts of the AMR:

$$\delta_{abs} = \left| \sum_{j=1}^N c_{p,j} \rho_j \Omega_j T_{i,j} - T_{f,j} \right|, \quad (3.35)$$

where N is the number of domains, $c_{p,j}$ is the specific heat capacity of the j^{th} domain, ρ_j is the density of the j^{th} domain, Ω_j is the area of the j^{th} domain, $T_{i,j}$ is the initial temperature of the j^{th} domain and $T_{f,j}$ is the final temperature of the j^{th} domain and. The relative residual is determined as:

$$\delta_{rel} = \frac{\left| \sum_{j=1}^N c_{p,j} \rho_j \Omega_j T_{i,j} - T_{f,j} \right|}{\left| \sum_{j=1}^N c_{p,j} \rho_j \Omega_j |T_{i,j} - T_{ref}| \right|} \quad (3.36)$$

where T_{ref} is the reference temperature of 298 K. If the model obeys energy conservation both residuals should be approximately zero. The test was performed for three cases where each test increases the complexity of the model. (1) No piston displacement and no velocity in the fluid. (2) Piston displacement but no velocity in the fluid. (3) Both piston displacement and velocity distribution in the fluid. The results of the test cases are shown in Table 3.6. The low absolute and relative residuals in the first test case show that the

Table 3.6: The results of the energy conservation test of the coordinate transformation method.

Test case	$\delta_{abs}(J)$	$\delta_{rel}(\%)$
1	$2.39 \cdot 10^{-7}$	$5.14 \cdot 10^{-8}$
2	$1.08 \cdot 10^{-3}$	$2.34 \cdot 10^{-4}$
3	$2.06 \cdot 10^{-3}$	$4.45 \cdot 10^{-4}$

coordinate transformation method obeys energy conservation. Using the coordinate transformation method to simulate the relative movement between the domains increases the residuals by four orders of magnitude and the addition of the flow of the fluid increases the residuals by a factor of ≈ 2 . However, the relative residuals are in all the test cases low enough to conclude that the coordinate transformation method obeys energy conservation. In addition to the above tests, Appendix B presents a basic test, where the coordinate transformation method is used to solve a standard heat transfer problem which is then compared to the analytical solution to the problem. The comparison showed no difference between the analytical solution and the numerical solution and serves as further verification of the coordinate transformation method. Appendix B also describes the implementation of the coordinate transformation method in COMSOL in more detail. Fig. 3.13 shows the temperature in the different parts of the AMR geometry and the temperature profile at the interface between at the interface between the solid and fluid ($y = H_{fl}$). The figure show the results at different times during the AMR refrigeration cycle. As the figure shows, there is virtually no difference between the temperature of the solid and the fluid at the interface and it can be concluded the coordinate transformation method is valid to model a relative movement between the solid and the fluid domain.

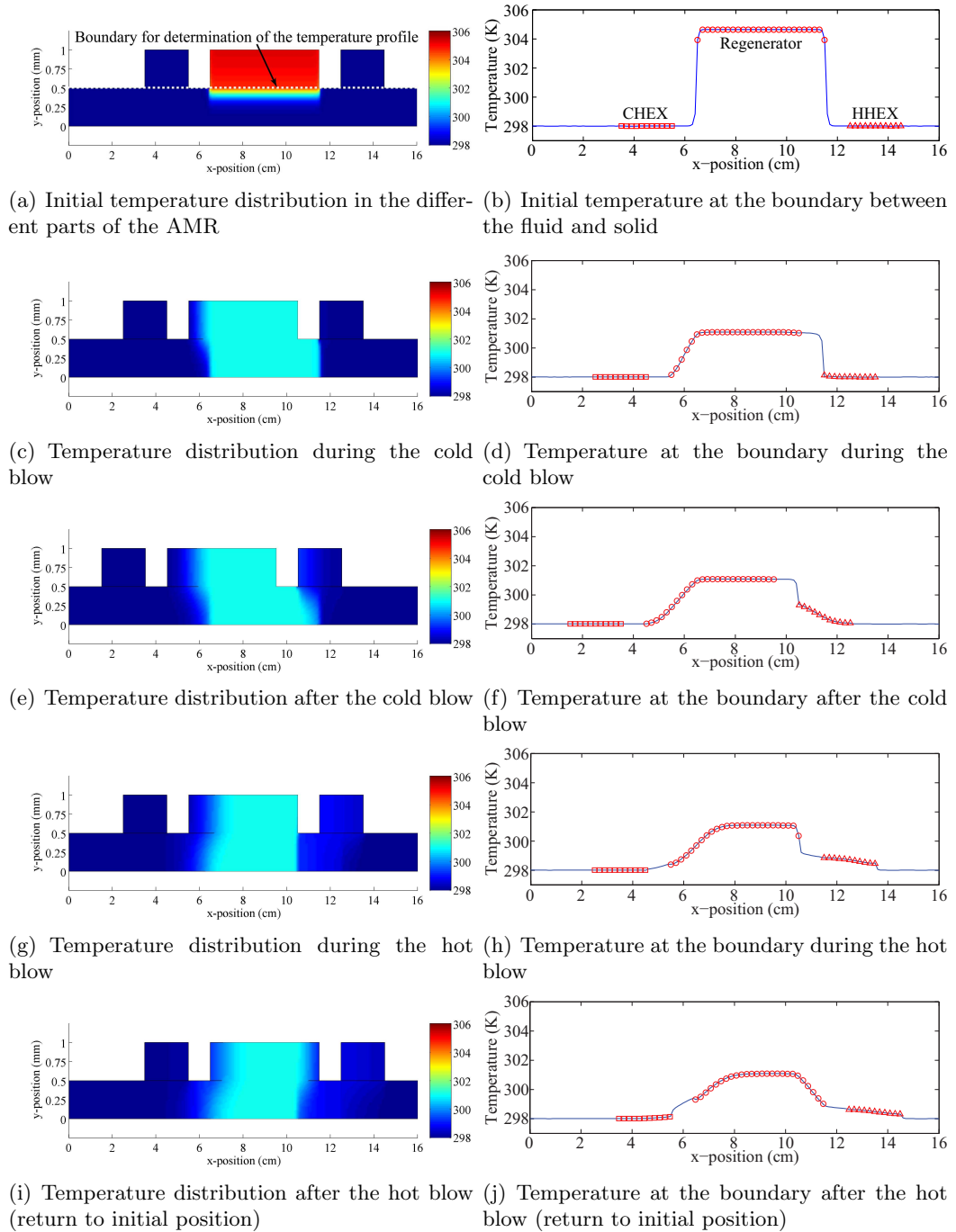


Figure 3.13: Test of the coordinate transformation method. The left column shows the 2-D temperature distribution in the different parts of the AMR and the right column shows the 1-D temperature profile at the boundary between the solids and the fluid. In the right column the solid blue line correspond to the the fluid channel, the red triangles correspond to the CHEX, the red circles correspond to the regenerator and the red squares correspond to the HHEX.

3.6.2 Grid sensitivity analysis of the velocity distribution in the fluid channel

The grid sensitivity analysis of the velocity distribution in the fluid channel was determined with the parameters and properties shown in Table 3.2 and Table 3.3 and on each of the three grids shown in Table 3.4. The resulting velocity profiles, at selected times during the cycle, are presented in the following figures. Fig. 3.14 shows the variation of the u -velocity in the y -direction, Fig. 3.15 shows the variation of the u -velocity in the x -direction and Fig. 3.16 shows the variation of the v -velocity in the x -direction. The results in Fig. 3.14 was determined at the middle of the fluid channel ($x = L_{fl}/2$) in the x -direction and Fig. 3.15 and Fig. 3.16 was determined in the middle of the fluid channel in the y -direction ($y = H_{fl}/2$) at the left boundary. Note, the figure shows the solution of the flow in the simplified repeating unit, which means that the velocity profiles in the y -direction is only a half parabola. The figures shows that there is almost no difference between the solutions near the lower boundary using either grid, especially when going from the normal to the fine grid. The velocity near the interface are identical for the three grids, and this shows that either grid are suitable to implement the boundary conditions of the interface between the fluid and the solid (Eq. 3.5). Fig. 3.15 shows that the u -velocity only varies in the x -direction near the piston/fluid boundaries of the channel before the velocity reaches a constant value. This coincides with the results on Fig. 3.16, which shows that there is only a non-zero v -velocity near the boundaries. This means that the flow in the fluid channel can be characterized as one-dimensional in the x -direction and fully developed except near the boundaries. From these results it was concluded that the velocity distribution is not sensitive to the grid and in the following the flow in the fluid channel is determined with the normal grid.

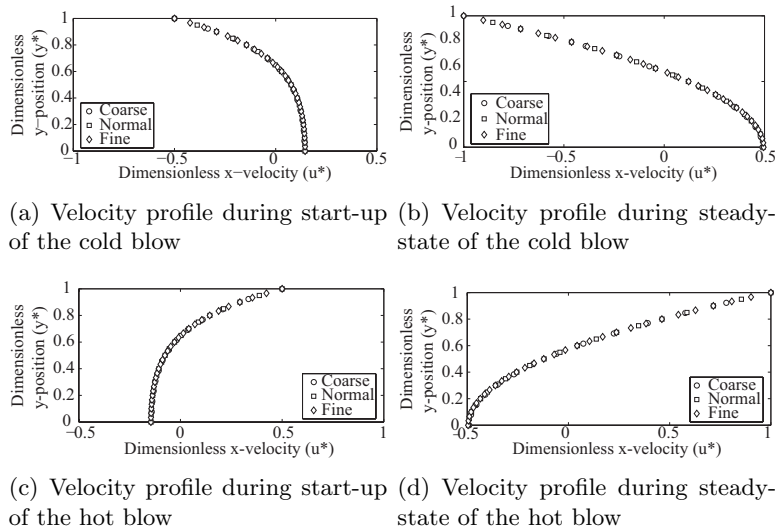
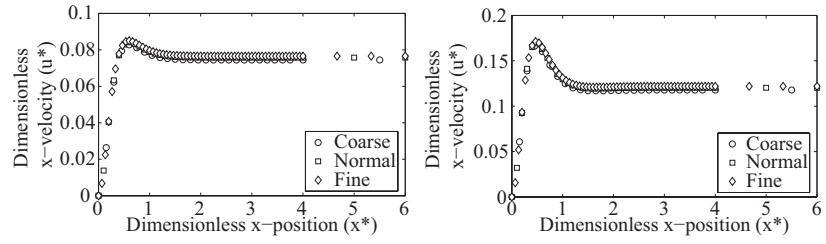
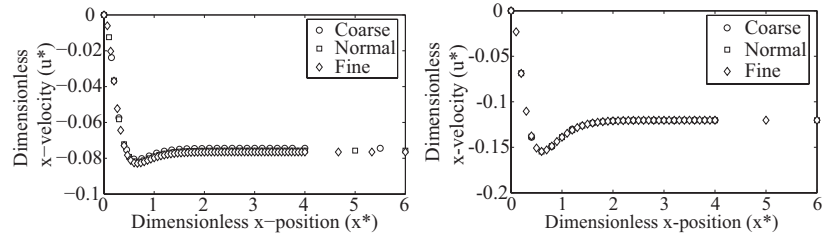


Figure 3.14: Mesh sensitivity analysis of u -velocity in the y -direction.

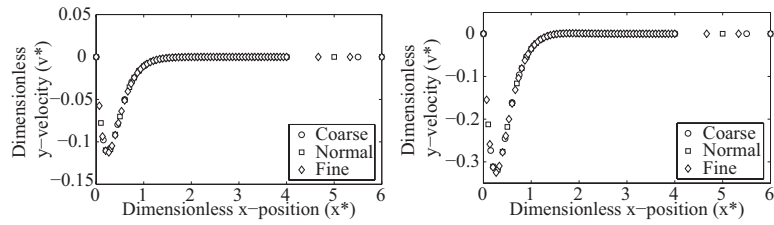


(a) Velocity profile during start-up of the cold blow (b) Velocity profile during steady-state of the cold blow

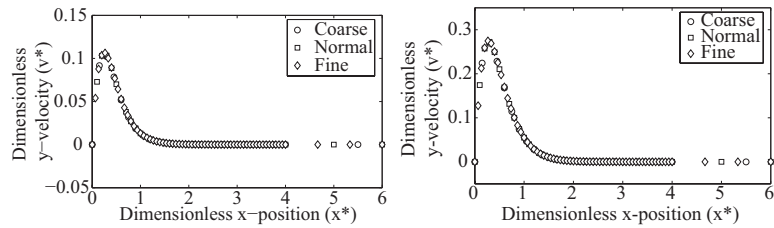


(c) Velocity profile during start-up of the hot blow (d) Velocity profile during steady-state of the hot blow

Figure 3.15: Mesh sensitivity analysis of u -velocity in the x -direction.



(a) Velocity profile during start-up of the cold blow (b) Velocity profile during steady-state of the cold blow



(c) Velocity profile during start-up of the hot blow (d) Velocity profile during steady-state of the hot blow

Figure 3.16: Mesh sensitivity analysis of v -velocity in the x -direction.

Conservation of energy

To analyze the energy conservation of the AMR model a test case was designed in which the specific heat capacity of Gd is constant and the MCE is simplified to a fixed temperature of 5 °C and -4 °C for $\Delta T_{\text{ad}}^{\text{m}}$ and $\Delta T_{\text{ad}}^{\text{dm}}$, respectively. The fixed difference between $\Delta T_{\text{ad}}^{\text{m}}$ and $\Delta T_{\text{ad}}^{\text{dm}}$ result in a magnetic work input, which can be calculated analytically. The analytical magnetic work input per cycle per unit width of the regenerator is

$$w'_{\text{ana}} = \rho c_{\text{p,s}} H_{\text{reg}} L_{\text{reg}} \cdot (\Delta T_{\text{ad}}^{\text{m}} + \Delta T_{\text{ad}}^{\text{dm}}) = 46.41 \text{ J/m}, \quad (3.37)$$

The CHEX was thermally isolated by setting q_c'' to zero, which ensures that only the work applied during the magnetization and the demagnetization is rejected through the HHX and T_{H} was 298 K. If the AMR model has energy conservation, these boundary conditions will result in that Eq. 3.37 is equal to Eq. 3.15 during steady-state. Note, only the magnetic work is compared to Eq. 3.37 since the piston work is determined separately because of the decoupling of the momentum and continuity equations from the energy equation. The conservation of energy test was also subjected to a grid and time step sensitivity analysis using the three grids and time steps. The model was solved with an absolute tolerance of 0.01 K with respect to the temperature distribution, and a total of 600 cycles was simulated to obtain the cyclical steady-state. The results of the conservation of energy analysis are shown in Table 3.7. There is no significant difference between the numerical results from

Table 3.7: Comparison and relative difference (δ) between the numerical and the analytical solution for the three grids and the three time steps.

	Grid			Time step		
	Coarse	Normal	Fine	Coarse	Normal	Fine
$w'_{\text{mag}} (\text{J/m})$	47.07	45.93	46.57	45.85	45.93	45.99
δ (%)	-1.42	1.04	-0.34	1.21	1.04	0.91

the grid sensitivity analysis and the analytical solution. The absolute value of the relative difference was below 1.5% for all three grids. There is a monotonic decrease of the absolute value of the relative difference as the amount of grid elements is increased. This was expected as the discretization error decreases with a decreasing size of the grid element [58]. These results indicate that the model has energy conservation and can accurately determine the energy input during the magnetization and the demagnetization. The low errors further show that the coordinate transformation method used to model the moving boundaries is functioning correctly and is independent of the grid. The time-step sensitivity analysis of the energy conservation also shows a monotonic decrease in the relative difference as the time step is decreased.

3.6.3 Grid and time step sensitivity analysis

Both the specific heat capacity and ΔT_{ad} of a magnetocaloric material are very non-linear in the temperature region where the AMR operates and especially near the Curie temperature

as shown on Fig. 3.10. It is therefore important to chose a spatial grid, which is fine enough to accurately predict the performance of the AMR. To determine the sensitivity of the solution with temperature dependent properties, the AMR model was implemented with the properties shown in Fig. 3.10. Again q_c'' was set to zero and T_H was 298 K and 600 refrigeration cycles was simulated to obtain the steady-state. Because the temperature of the CHEX is unspecified, the temperature will vary over the heat exchanger surface during the cycle. The average T_C per cycle is determined as

$$\bar{T}_C = \frac{1}{\tau \cdot L_{\text{hex}}} \int_0^\tau \int_0^L T_s(x, t) dx dt. \quad (3.38)$$

The results of the grid and time step sensitivity analysis are shown in Table 3.8 in terms of \bar{T}_C and the magnetic work input w'_{mag} . The results again show little difference between the

Table 3.8: The results of the grid and time step sensitivity of the final model with temperature and magnetic field dependent specific heat capacity and ΔT_{ad} .

	Grid			Time step		
	Coarse	Normal	Fine	Coarse	Normal	Fine
\bar{T}_C (K)	287.19	287.16	287.22	287.23	287.16	287.18
w'_{mag} (J/m)	2.57	2.38	2.47	2.30	2.38	2.40

six solutions obtained during the grid and time step sensitivity analysis. The sensitivity analysis was performed for a wide range of both grids and time steps. The fine grid had 5.7 times as many grid points as the coarse grid and the fine time step was four times smaller than the coarse time step. However, the results are almost identical. This shows that the model is robust and not sensitive to the choice of grid or the time step. It was therefore concluded that any combination of the above grids and time steps produces accurate results. In the following the normal grid and time step is used. The final AMR model requires a solution time of about 53 hours on a 3.2 GHz Pentium 4 (Prescott) processor with 2 GB of RAM and uses about 10Mb of storage per simulated cycle.

3.6.4 Independence of initial conditions

To verify that the cyclic steady-state solution is independent of the initial conditions, a test was performed with a linear temperature gradient as the initial condition instead of a uniform temperature. The solution obtained with the new initial conditions was compared to the previously obtained solution (normal grid and time step). The results are shown in Table 3.9, which shows that the two values of \bar{T}_C are equal within the solver tolerance and the two values of w'_{mag} are almost equal. From the results of the initial condition analysis it was concluded that the AMR model is independent of the initial conditions. By using a linear temperature profile as the initial condition the cyclical steady-state was obtained after approximately 470 cycles compared to 600 when using a constant temperature as the initial condition. Therefore, a linear gradient can be used as an initial "guess" to decrease

Table 3.9: The results of the test of the independence of the solution on the initial conditions.

Initial condition	\bar{T}_C	w'_{mag}
Constant temperature	287.16	2.38
Temperature gradient	287.16	2.37
Relative difference	$3.7 \cdot 10^{-4}\%$	0.42 %

the solution time if the transient development of the temperature is not needed.

3.7 Implementation of the AMR model on a cluster

The long solution time of the model is prohibitive for the extensive parameter studies required to determine an optimal AMR design. To address this problem, the AMR model was implemented on a Linux computer cluster with the purpose of performing multiple simulations in parallel. A cluster is a group of multiple, interconnected computers called nodes, which work together and divide a single computational job between the individual nodes. The Cluster is operated by a software system, which connects the nodes and allows them to act in unity. The nodes communicate with each other such that any program running of the Cluster views the multiple nodes as a single multiprocessor computer. The Cluster itself is operated by a central server which manages the nodes and the user only interacts with the server. The job of the server is to run the simulations and to schedule the simulations if the number of requested simulations exceed the number of available nodes. The dataflow from the user PC to the Cluster server to the individual nodes is illustrated on Fig. 3.17.

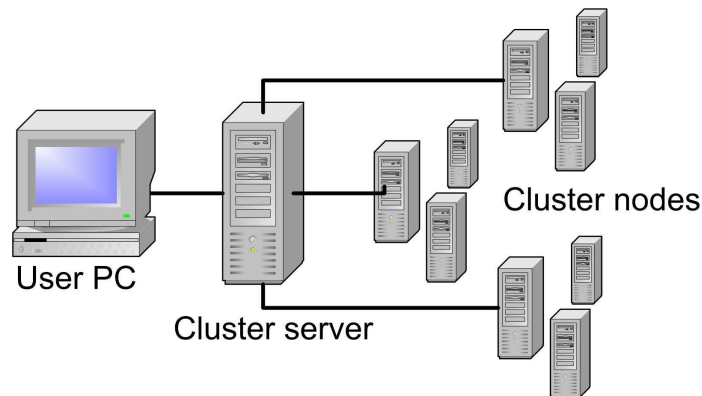


Figure 3.17: Dataflow from the user PC to the central server which operates the nodes of the Cluster.

Presently, COMSOL does not support multiple processors and the use of a cluster does not reduce the simulation time of individual simulations. However, the use of a cluster

does allow multiple simulations with the AMR model to be performed simultaneously and this results in large time savings. Parameter variations, which would previously take weeks can now be achieved within days. Thus allow for more detailed investigations of the AMR behavior to be performed. In addition, the Cluster software allows the individual simulations to be scheduled automatically, which simplify user interaction.

3.8 Summary and final remarks

This chapter described the development of a 2-D mathematical model of a reciprocating AMR with a regenerator made of parallel plates, which were arranged in a stack configuration. The AMR model was developed using the commercial Finite Element software COMSOL Multiphysics, which was customized to allow modelling of the piston displacement of the fluid. The unique modelling methods used in the AMR model made additional verifications of the AMR model necessary. The main conclusions from the verifications was: (1) The methods to model the piston movement works correctly and has energy conservation. (2) From a grid and time step sensitivity analysis it was concluded that the solution of the model is almost independent of both grid and time step and that any combination results in accurate results. (3) From the initial condition analysis it was concluded that the solution of the AMR model is independent of the initial conditions.

The AMR model was previously published in the International Journal of Refrigeration [52]. This paper is included in Appendix D. The implementation of the AMR model on a Cluster was published in a paper presented in 2006 at the Nordic COMSOL Conference in Copenhagen, Denmark [59]. This paper is included in Appendix E.

Chapter 4

Numerical analysis of an Active Magnetic Regenerator

This chapter presents the results obtained with the AMR model. The first part of the chapter contains the initial results of the behavior of the reciprocating AMR, which focus on demonstrating the different capabilities of the AMR model. The initial results illustrate the capabilities of the model to determine both the temperature span (ΔT) of the AMR as well as the temperature distribution within the AMR. The remainder of the chapter presents the results of a series of parameter studies of the AMR performance for different design choices and operating parameters, where the focus is on the behavior of ΔT .

4.1 Initial results

The results in this section were obtained with a magnetic field of 1 T and the basic geometry, operating parameters and boundary conditions showed in Table 3.1, Table 3.3 and on Fig. 3.7, which are summarized on Fig. 4.1.

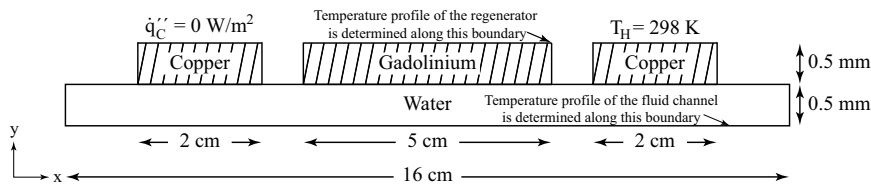


Figure 4.1: The AMR geometry and boundary conditions used to obtain the initial results.

The HHEX had a prescribed temperature of 298 K and there was zero cooling load applied at the CHEX. These boundary conditions were chosen in order to determine the no-load ΔT , which is the maximum temperature difference which may be obtained between the two heat exchangers for a given set of operating conditions. The simulation was performed with 600 cycles, which were sufficient in order to achieve a cyclical steady-state. Fig. 4.2 shows the evolution of \bar{T}_C and the rejected heat as a function of the cycle number.

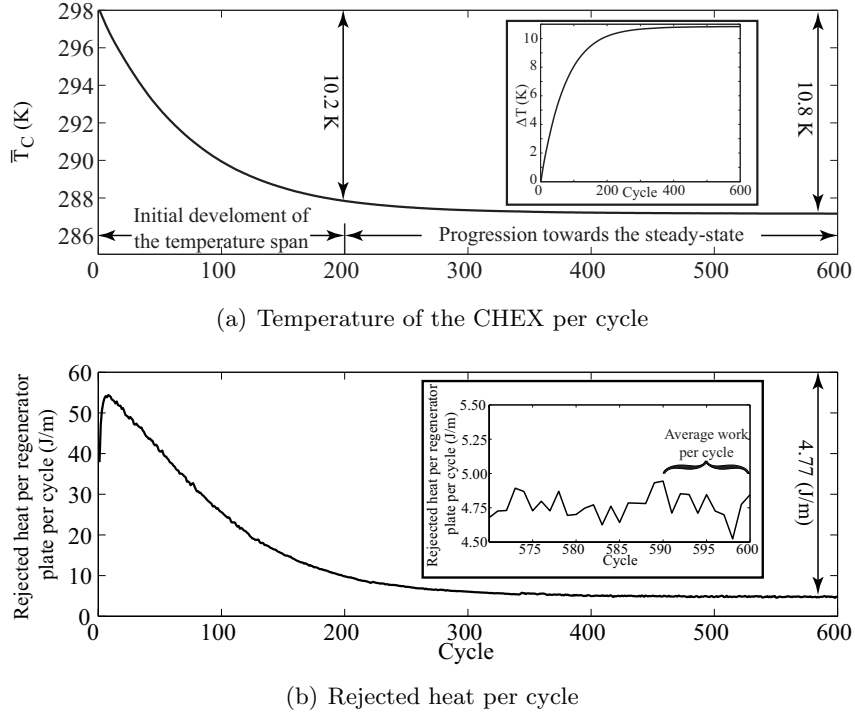


Figure 4.2: (a) The transient evolution of \bar{T}_C from 298.0 K to 287.2 K. The insert shows the corresponding development of ΔT from 0.0 K to 10.8 K. (b) The input work per regenerator plate per cycle. The average rejected heat after 600 cycles is 4.77 Jm^{-1} per plate.

After reaching the steady-state, \bar{T}_C was 287.2 K which gives a ΔT of 10.8 K. As shown on the insert on Fig. 4.2(b) the rejected heat from the HHEX is not constant, even at the cyclical steady-state, but fluctuates from cycle to cycle. This is because the heat flux depends on the temperature gradient and even small temperature variations below the tolerance of the solution results in relative large variations of the magnetic work. At the cyclical steady-state the rejected heat is equal to the magnetic work and to compensate for the fluctuations, w'_{mag} was determined as the average of the rejected heat per cycle over the last 10 cycles. This results in a w'_{mag} of 4.77 J/m per regenerator plate¹ which corresponds to 95.4 kJ per m^3 of Gd. The piston work was determined to be 1.36 mJ per plate. Since the piston work is several orders of magnitude lower than the magnetic work, it was omitted from the total work. The assumption that the piston work is negligible compared to the magnetic work will also be used in the parameter studies described later in this chapter. Fig. 4.2 shows that the transient simulation has an asymptotic convergence towards the cyclic steady-state. This is clearly illustrated by the fact that the change in \bar{T}_C is 10.2 K during the first 200 cycles, while \bar{T}_C only decreases 0.6 K from 200 to 600 cycles. The slow

¹The results for w'_{mag} reported in Table 3.8 are those obtained directly from the model, i.e. for a half plate and fluid channel.

convergence towards the steady-state results in the long solution time of about 53 hours required to complete all 600 cycles. Fig. 4.3 shows the temperature distribution in the AMR and the temperature profiles in the x-direction at various times during the steady-state AMR cycle with the present operating parameters. The temperature profiles are determined at the middle of the regenerator plate and at the middle of the fluid channel (i.e. at the top ($y = H_{\text{fl}} + H_{\text{ref}}$) and bottom ($y = 0$) of the AMR geometry shown in Fig. 4.1). The figures of the temperature distribution of the AMR are illustrated with the pistons moving the fluid even though the AMR is modelled with the regenerator and the heat exchangers as the moving parts and the fluid as the stationary part. This was done to obtain a more intuitive visualization of the movement in the AMR during the cycle. The figures are not shown to scale otherwise it would not be possible to see the temperature variation in the y-direction since the AMR geometry is many times longer than it is high. Fig. 4.3(a) and Fig. 4.3(g) clearly show how the MCE increases and decreases the temperature in the regenerator after the hot blow (Fig. 4.3(k)) and after the cold blow (Fig. 4.3(e)), respectively. After the magnetization and demagnetization Fig. 4.3(c) and Fig. 4.3(i), respectively, show that there are no (perpendicular) temperature differences between the regenerator and fluid before either blow period. Finally, during the blow periods Fig. 4.3(e) and Fig. 4.3(k) show how the velocity distribution in the fluid channel affects the temperature of the fluid and produces a parabolic shaped temperature profile. This was expected since the u -velocity profile in the fluid is also parabolic shaped. From Fig. 4.3(b) and Fig. 4.3(d) it seems as if the temperature of the regenerator does not change the temperature of the fluid significantly during the magnetization period and similarly, during the demagnetization period (Fig. 4.3(h) and Fig. 4.3(j)). This behavior is due to the present AMR geometry which results in that the heat capacity (mc_p) of the fluid is twice that of the average heat capacity of the regenerator. Fig. 4.3(d) and 4.3(j) shows that only a small part (approximately 15%) of the fluid within the regenerator is above T_{H} and below T_{C} after the magnetization and demagnetization periods, respectively. With the chosen process parameters for the present simulation, the pistons displace 40% of the fluid inside the regenerator and 20% of the displacement is used to move the fluid through the gap between the regenerator and the heat exchangers. The consequence might be that fluid colder than T_{H} enters the HHEX or fluid warmer than T_{C} enters the CHEX during the hot and cold blow periods, respectively. This reduces the ΔT by heating the CHEX and cooling the HHEX and will occur if there is insufficient regeneration in the AMR. Fig. 4.3(f) and 4.3(l) show noticeable temperature differences between the regenerator and the fluid after the hot and cold blow. These results indicates that there is indeed insufficient regeneration in the AMR, otherwise the temperatures of the regenerator and the fluid should be almost equal. This means that the piston stroke is too long as discussed above. An additional consequence of the temperature differences between the fluid and the regenerator is that the MCE is not fully utilized. If no temperature differences were present, the temperature in the regenerator would be lower after the hot blow and higher after the cold blow. Thus, the MCE would be able to produce even higher and lower temperatures during magnetization and demagnetization, which should in turn increase the AMR performance. To obtain better regeneration, either the length of the blow periods can be increased or the amount of fluid can be decreased in order to balance the heat capacities of the regenerator and fluid.

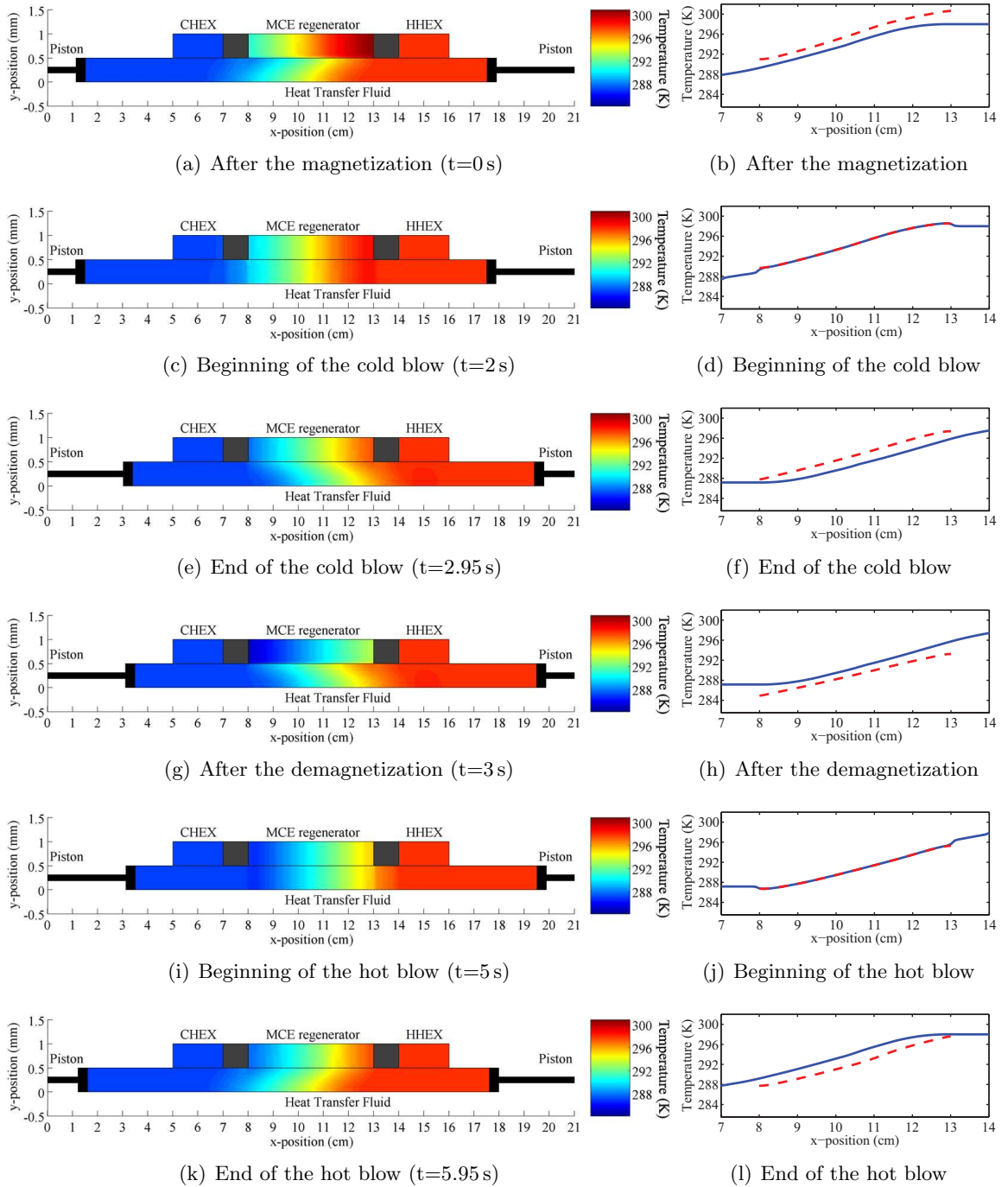


Figure 4.3: The left column shows the temperature distribution in the AMR and the right column shows the temperature profiles in the regenerator (dashed red line) and in the fluid (solid blue line) during the 6 second AMR cycle. (a-b) After the magnetization the temperature of the regenerator is above that of the fluid. There is an almost linear temperature profile in the regenerator whereas the temperature profile in the fluid is non-linear and flat near the right end because of the fluid, which has just entered from the HHEX. (c-d) Before the cold blow there are no temperature differences between the regenerator and the fluid. At the furthest positions to the left and right the temperature is lower than within the regenerator, which is due to the gap between the regenerator and heat exchangers. (e-f) After the cold blow the temperature in the fluid is lower than in the regenerator. (g-h) After the demagnetization the temperature of the regenerator is below that of the fluid. (i-j) Before the hot blow there are again no temperature differences between the regenerator and the fluid. (k-l) After the hot blow the temperature in the fluid is higher than in the regenerator.

Fig. 4.4 shows the temperature profiles in the y -direction at different times after the magnetization (Fig. 4.4(a)) and the demagnetization (Fig. 4.4(b)) with the current operating conditions. The temperature profiles were determined in the middle of the regenerator and the fluid channel in the flow direction. After the magnetization and demagnetization

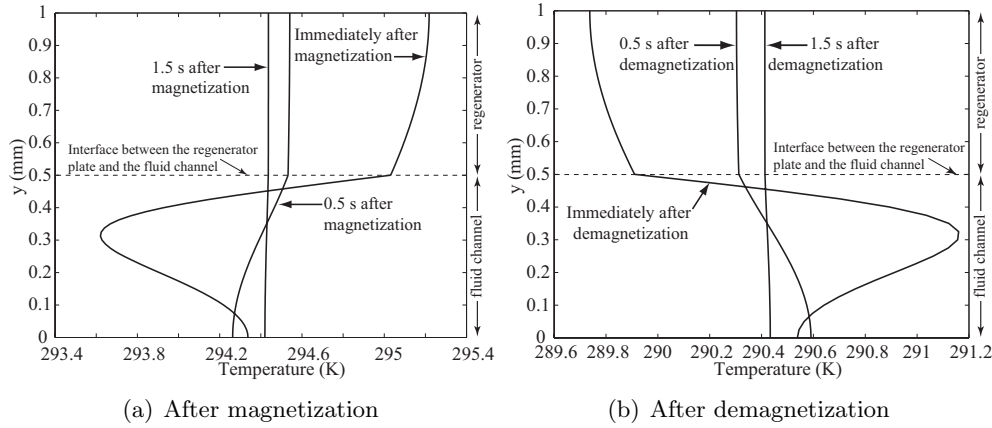


Figure 4.4: The temperature profile in the y -direction of the regenerator and the fluid channel.

periods, the temperature profiles in the regenerator and in the fluid is both found to be non-uniform. This was expected as the fluid is still somewhat in motion after the hot blow and because of the discontinuity caused by the instantaneous temperature change after the magnetization and demagnetization. After 0.5s there is an uniform temperature profile in the regenerator bed while the temperature profile in the fluid is still non-uniform. After 1.5s there is a virtually uniform temperature in both the regenerator and the fluid. Since the MCE manifests itself instantaneously in the regenerator, the majority of the magnetization time is used for heat transfer. Thus the magnetization period can be reduced by at least 0.5s to increase the frequency of the AMR cycle, which in turn increases the AMR performance. The length of the magnetization and demagnetization periods and the overall frequency of the AMR cycle can therefore be optimized to help obtain the maximum performance of the AMR. The results presented in this section shows that the model can evaluate both ΔT and w'_{mag} of an AMR as well as predict the temperature profile through the regenerator and fluid channel. The 2-D approach allowed analysis of the perpendicular heat transfer, which showed noticeable temperature differences between the fluid and regenerator, when a parallel-plate regenerator is used. This justifies the use of a 2-D model and indicates that it is necessary to use such methods when an AMR regenerator with a parallel-plate geometry is modelled. To analyze this issue in more detail, Chapter 6 contains a comparison between the 2-D AMR model developed in this thesis and a 1-D AMR model developed by Engelbrecht et al. [60, 47].

The above results were also included in the paper published in the International Journal of Refrigeration [52] included in Appendix D.

4.2 Introduction to the AMR parameter studies

The performance of an AMR depends on many parameters with a complex interrelationship. Examples include the piston stroke, the ratio between the heat capacity of the regenerator and the fluid as well as the length of the AMR refrigeration cycle. These parameters and others should therefore be subjected to parameter studies to assess the influence of each on the performance of the AMR. The following sections present the results of a series of parameter studies of a reciprocating AMR performed using the 2-D AMR model. The aim of the parameter studies is to achieve a greater understanding of how the AMR works and how the design and operation conditions influences the performance of the AMR. The purpose of this part of the chapter is not to give conclusive results on the optimal parameters, but to illustrate the complex relation between the different operating parameters and discuss the implications for optimal AMR operation. The majority of the parameter studies were performed by changing the value of a single parameter while keeping the rest of the AMR geometry and operating parameters constant with the values shown in Table 3.1 and Table 3.3 and Fig. 4.1. However, in some of the parameter studies two parameters are varied simultaneously to study the combined effect on the AMR performance. It should be noted that this approach does not result in the global optimum value for each parameter but only local optimums. However, as mentioned above these parameter studies are not performed to optimize the AMR. The first parameter study analyzes both ΔT , the refrigeration capacity and the COP to further demonstrate the capabilities of the model. However, due to the time limitations of this project, the subsequent parameter studies only focus on the no-load ΔT , since these results have a direct application in the experimental AMR.

4.3 Influence of the piston stroke

The purpose of this parameter study is to analyze the influence of the stroke on the AMR performance. During steady-state operation of the AMR, theory predicts that there will be a nearly linear temperature profile across the regenerator ranging from T_C to T_H [33]. During the cold and the hot blow, part of the fluid inside the regenerator is displaced to reject or absorbs heat. If the amount of fluid displaced is too small, the performance of the AMR is reduced as only part of the cooling produced by the MCE is utilized. Conversely, if the amount of fluid displaced from the regenerator is too high, fluid colder than T_H or warmer than T_C will flow into the HHEX and CHEX, respectively. The result will be that the CHEX is heated by the fluid and the AMR absorbs heat from the HHEX, which in turn reduces the AMR performance. Thus, there must be an optimal stroke of the pistons. The initial results presented in the previous section indicated that the present operating parameters resulted in a low amount of regeneration in the AMR and that the currently used stroke is too long. Two different sets of AMR operating conditions are considered: (1) The no-load ΔT is determined by setting the cooling load from the CHEX equal to zero. (2) The COP for a ΔT of 10 K is determined by setting T_H equal to 298 K and T_C equal to 288 K. In both cases the stroke was varied so that 5 - 100% of the fluid in the fluid channel was displaced.

4.3.1 Results and discussion

Fig. 4.5(a) shows the transient development of ΔT for selected piston strokes, Fig. 4.5(b) shows the steady-state results in terms of the no-load ΔT and Fig. 4.5(c) show the results in terms of the COP and the refrigeration capacity. The results show that ΔT develops faster for a longer piston stroke than for a shorter piston stroke. In addition, the figure shows that for the present operating conditions the AMR reaches steady-state after less than 600 cycles except for strokes shorter than 2 cm, which required up to 2400 cycles to obtain the cyclical steady-state. On Fig. 4.5(b) the maximum ΔT of 13.9 K is obtained when the stroke displaces 20% of the fluid within the regenerator; this corresponds to a stroke of 1 cm. Conversely, Fig. 4.5(c) shows that a maximum COP of 2.1 is reached when 30% of the fluid is displaced from the regenerator. Finally, a maximum refrigeration capacity of -1.66 W per regenerator plate is obtained when 30% of the fluid is displaced. The maximum of the three curves on Fig. 4.5(b) and Fig. 4.5(c) lies within a narrow range of strokes and this shows that the stroke is an important parameter for the performance of the AMR. Fig. 4.5(b) shows that ΔT rapidly decreases when the pistons displace less than 15% of the fluid. For strokes below 1 cm, the fluid heated and cooled in the regenerator by the MCE does not come into direct contact with the heat exchangers because of the gap between the regenerator and the heat exchangers. This means that the heat transfer can only take place indirectly, by conduction in the fluid, which results in a drastic decrease of ΔT . However, it is interesting that when 17.5% of the fluid is displaced, the resulting ΔT is only 5.3% lower than the maximum ΔT , since the corresponding stroke is only 0.75 cm. The relatively high ΔT indicate that conduction is an efficient mechanism for heat transfer because the observed ΔT should only be obtained indirectly. However, the corresponding COP is only 0.8 which shows that the refrigeration is low. Fig. 4.5(c) shows that only strokes which displace from 15% to 40% of the fluid within the regenerator obtain a usable COP. For the remaining range of strokes, the AMR cannot sustain a ΔT of 10 K by itself; this is in agreement with Fig. 4.5(b). A comparison of Fig. 4.5(b) and Fig. 4.5(c) shows that the stroke which produces the largest COP has a maximum ΔT of 13.2 K. This means that it is possible to obtain a high COP even when the AMR operates close to the maximum obtainable ΔT . The maximum Carnot efficiency is 7.2%, which is low when compared to the previous reports of Carnot efficiencies which are in the range of 30-60% for a reciprocating AMR [19]. The relatively low Carnot efficiency suggests that the AMR geometry or the operating conditions used in the present simulations are not optimal. Fig. 4.6 shows the temperature profiles in the regenerator and the fluid just before and after the blow periods for the optimal fluid displacement of 20%. Before the cold blow, Fig. 4.6(a) shows that only approximately 0.5 cm of the fluid near the hot end is above T_H and a first approximation would be to assume that the optimal stroke should be ≈ 1.5 cm (the stroke must include an additional cm to clear the gap). However, the parabolic velocity profile in the fluid indicates that part of the fluid moves faster than the average velocity of 2 cm/s, which suggests that the stroke should be shorter than the apparent length of 1.5 cm obtained from the figure. This effect can also explain why it is possible to obtain a significant ΔT for a fluid displacement of 17.5% even though none of the fluid heated in the regenerator should reach the HHEX as the stroke is too short to clear the gap. Looking

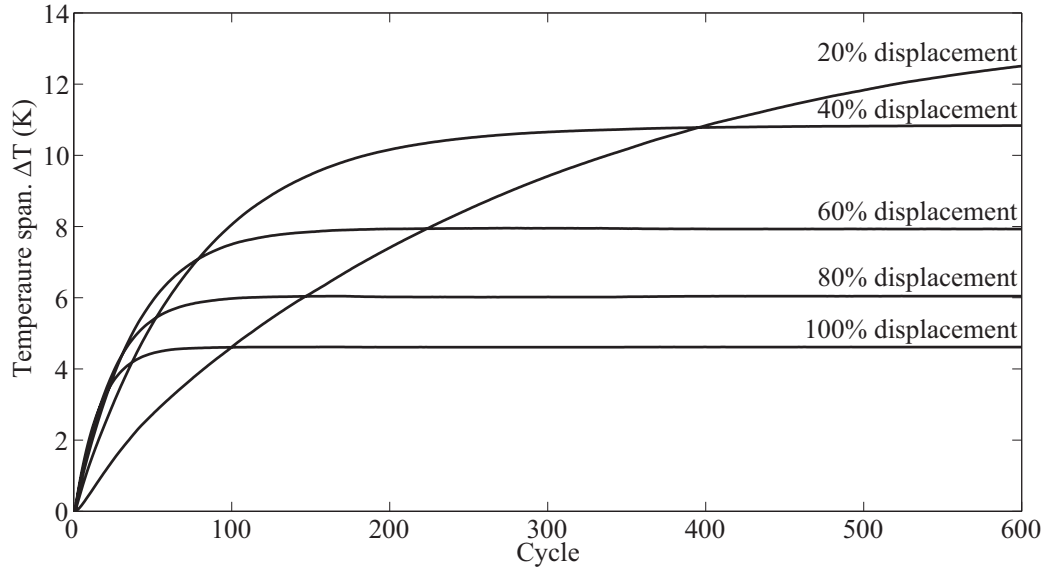
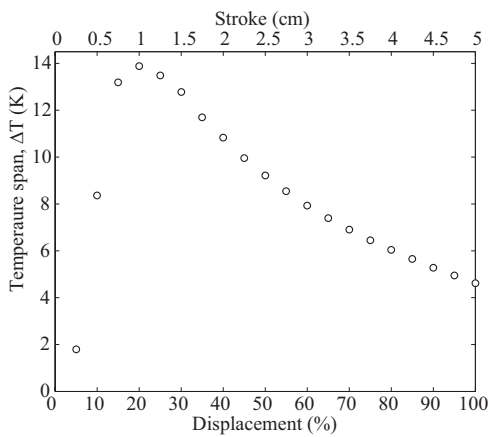
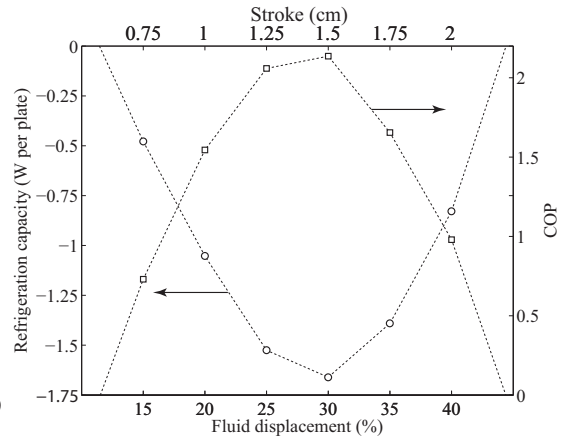
(a) Transient development of ΔT (b) Steady-state no-load ΔT (c) Steady-state refrigeration capacity and COP for $\Delta T=10$ K

Figure 4.5: (a) The evolution of ΔT with no-load boundary conditions as a function of the cycle number for selected piston strokes. (b) ΔT as a function of the fluid displacement with no applied cooling load. (c) COP of the AMR as a function of the piston stroke for a constant ΔT of 10 K. The left y-axis show the refrigeration capacity per regenerator plate and the right y-axis show the corresponding COP. In agreement with Eq. 3.12, the refrigeration capacity is negative and the COP is positive. On (b) and (c) the lower x-axis show the piston stroke as the percentage of the fluid displaced from the regenerator while the upper x-axis show the stroke in centimeters.

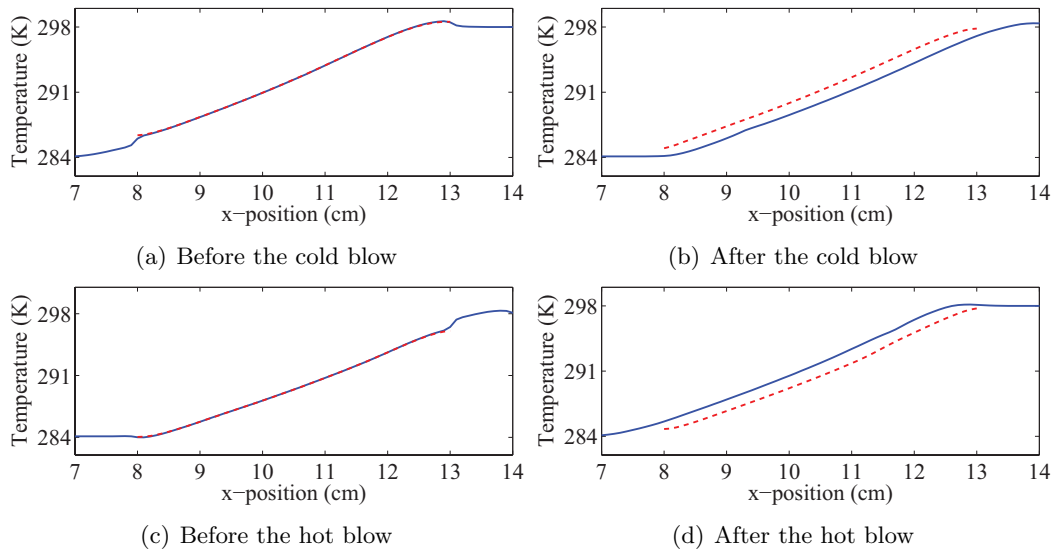


Figure 4.6: Temperature profiles in the regenerator (dashed red line) and in the fluid channel (solid blue line) just before and after the cold blow and the hot blow.

again at Fig. 4.5(b) and Fig. 4.5(c), it is apparent that an AMR with a short stroke is able to achieve a high ΔT but cannot obtain a high refrigeration capacity. A stroke of 0.75 cm is the shortest that can produce a ΔT above 10 K but it only has a relatively low refrigeration capacity and COP because of the small amount of fluid which enters the CHEX. As the stroke increases the refrigeration capacity also increases until the stroke becomes so long that the temperature of the fluid entering the CHEX increases above T_C which in turn decreases the refrigeration capacity. This suggests that the maximum refrigeration capacity is a function of both of the temperature profile and the amount of fluid which enters the CHEX. Fig. 4.6(b) and 4.6(d) show the temperature profiles in the regenerator and the fluid channel after the cold blow and hot blow, respectively. The figures show noticeable temperature differences between the fluid and the regenerator, which is probably due to a limited amount of regeneration as discussed in the previous section.

The results shown in this section was used as the basis of a paper which was presented in 2007 at the Second IIF-IIR International Conference on Magnetic Refrigeration at Room Temperature in Portoroz, Slovenia [61]. This paper is included in Appendix F.

4.4 Influence of the fluid channel height

The previous section indicated that the current geometry limits the regeneration in the AMR, which in turn reduces the performance of the AMR. In theory, an optimal regenerator should heat the fluid exiting the regenerator during the cold blow equal to or above T_H and cool the the fluid exiting the regenerator equal to or below T_C . However, Fig. 4.3 and Fig.

4.6 showed significant temperature differences between the regenerator and fluid after the blow periods. This means that the regenerator does not reject or absorb all the stored heat to and from the fluid. This in turn limits the regeneration and the AMR performance. The hypothesis is that there is too much fluid in the channels between the regenerator plates, which limits the heat transfer between the plates and the excess fluid may also introduce other forms of irreversibilities. To determine the effect of the height flow channels in the regenerator, a parameter study was performed where the flow channel height ($2H_{fl}$) was varied from 0.1 mm to 2 mm while keeping all the other parameters from the reference conditions constant. The stroke is again fixed at 2 cm even though the last parameter study determined that a stroke of 1 cm resulted in the largest ΔT . However, the strokes was reset to the 2 cm value in order to compare the effect of varying the height of the flow channel to the initial results as discussed in the introduction. The boundary conditions for determining the no-load ΔT was used in this simulation and will also be used in the remainder of this chapter.

4.4.1 Results and discussion

Fig. 4.7(a) shows the transient development of ΔT for selected heights of the fluid channel strokes and Fig. 4.7(b) shows the steady-state results of ΔT .

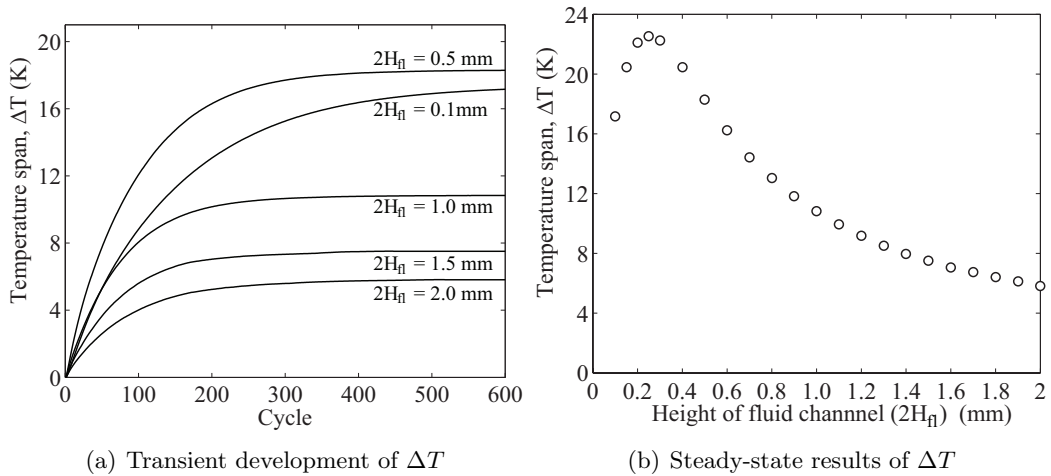


Figure 4.7: (A) The transient evolution of ΔT for different heights of the fluid channel. (b) The no-load ΔT as a function of the variation of the height of the fluid channel ($2H_{fl}$).

The transient development of the ΔT shows that a cyclical steady-state is obtained after approximately 600 cycles except in the situation when the fluid channel height is below 0.4 mm (not shown) where the number of cycles required to reach the steady-state is between 600 and 1200. A maximum ΔT of 22.5 K is obtained with a fluid channel height of 0.25 mm and the optimum fluid channel height lies at the top of a narrow peak. The curve itself is similar to that produced by the pistons stroke parameter study show in Fig. 4.5(b). A possible explanation for the shape of the curves is that as the height of the fluid channel

is decreased the temperature differences between the regenerator and fluid, after the blow periods, decreases and this in turn increases ΔT . However, once the flow channel height has been decreased sufficiently and the temperature differences becomes negligible, any further reduction of the fluid channel height only reduces the fluid flow and thus the amount of heat which is transported to and regenerator. Therefore, at some point there will not be sufficient flow of fluid through the regenerator to transport all the heat generated by the MCE. The temperature profiles in the regenerator and the fluid channel just after the blow periods are determined and the result is shown in Fig. 4.8 for a fluid channel height of 0.25 mm.

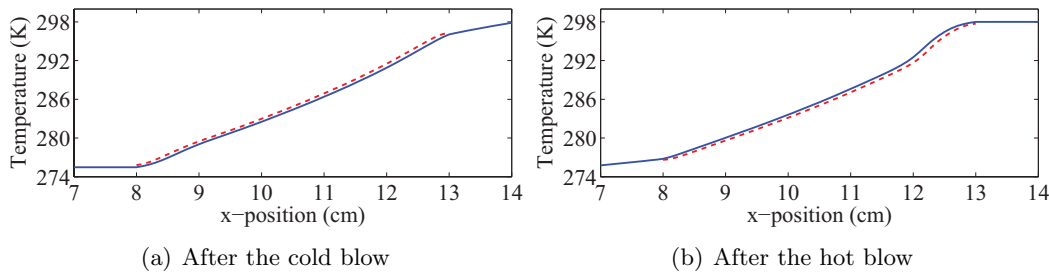


Figure 4.8: Temperature profiles in the regenerator (dashed red line) and in the fluid channel (solid blue line) just after the cold blow and the hot blow.

Fig. 4.8(a) and Fig. 4.8(b) show almost no temperature differences between the regenerator and the fluid after either blow period. These results support the above hypothesis that there should be no temperature differences between the regenerator and fluid in order to obtain optimal AMR performance. In addition, it also suggests that the optimal performance of the AMR depends on both the heat transfer and the flow of fluid through the regenerator. This is indicated by the fact that even for the fluid channel height, which produces the highest ΔT there are still minor temperature differences between the regenerator and fluid. However, a further reduction of the fluid channel does not increase ΔT because the reduction of the height of the flow channel also reduces the mass flow of fluid to below the amount required to sustain the maximum ΔT . To compensate, the stroke could be increased to obtain a higher flow of fluid while still retaining the negligible temperature differences between the regenerator and the fluid. This means that the optimal stroke of the pistons and the optimal height of the fluid channel depends on each other. In order to achieve an even higher ΔT these two parameters should be combined in a parameter study of both. Finally, the frequency of the cycle should also be considered, since if the blow periods are long enough, the temperature differences between the regenerator and the fluid will always be negligible.

4.5 Combined influence of the piston stroke and the fluid channel height

To determine the relationship between the stroke and the fluid channel height and their effect on the no-load ΔT , a parameter study was performed where the fluid channel height ($2H_{\text{fl}}$) was varied from 0.1 mm to 0.3 mm and the stroke was varied from 2 cm to 5 cm. These figures for the length of the stroke are based on the assumption that the piston stroke can be longer with a narrow fluid channel since the increased regeneration allows a larger part of the displaced fluid to be heated or cooled to temperatures above T_{H} and below T_{C} , respectively.

4.5.1 Results and discussion

The results of the parameter study are shown on Fig. 4.9 in terms of the no-load ΔT as a function of the amount of fluid displaced from the regenerator and in terms of the no-load ΔT as a function of the utilization (Φ). The utilization was introduced in Chapter 2 but is repeated here for convenience:

$$\Phi = \frac{\dot{m}_{\text{f}}c_{\text{p,f}}P}{m_{\text{s}}c_{\text{p,s}}}, \quad (4.1)$$

where P is the period of either blow (i.e. τ_2 or τ_4) and $c_{\text{p,s}}$ is the average specific heat capacity of the regenerator material during the cycle. The mass flow of the fluid in the flow channel, \dot{m}_{f} , is determined from the stroke and the flow channel height as:

$$\dot{m}_{\text{f}} = \frac{\Delta x}{P}2H_{\text{fl}}\rho_{\text{f}}, \quad (4.2)$$

where Δx is the stroke. The mass of the regenerator plate, m_{s} , is determined as

$$m_{\text{s}} = 2H_{\text{pl}}L_{\text{reg}}\rho_{\text{s}}, \quad (4.3)$$

The maximum ΔT of 27.2 K is obtained with a fluid channel of 0.1 mm and 100% fluid displacement followed closely by the ΔT of 26.9 K which is obtained with a fluid channel of 0.15 mm and also at 100% fluid displacement. Fig. 4.9(a) shows that as the fluid channel height is decreased, the optimal stroke displaces a larger percentage of the fluid within the regenerator. In addition, it seems that for a fluid channel of 0.1 mm the maximum ΔT has not been obtained, meaning that the pistons should displace more than 100% of the fluid within the regenerator. These results agree with the above assumption that a narrower fluid channel requires a longer stroke to produce the maximum ΔT . The two highest ΔT 's obtained in this parameter study are produced by the two narrowest fluid channels. However, for the remaining results the maximum ΔT for each channel height is non-unique and can also be obtained by reducing the channel height and at the same time increasing the stroke. Essentially, the results show that the same ΔT may be obtained with different operating conditions and hint at the complex relationship between the operating conditions and the AMR geometry. The results shown on Fig. 4.9(b) show that the optimal ΔT for each channel height is obtained with an utilization of approximately 0.27 corresponding to a

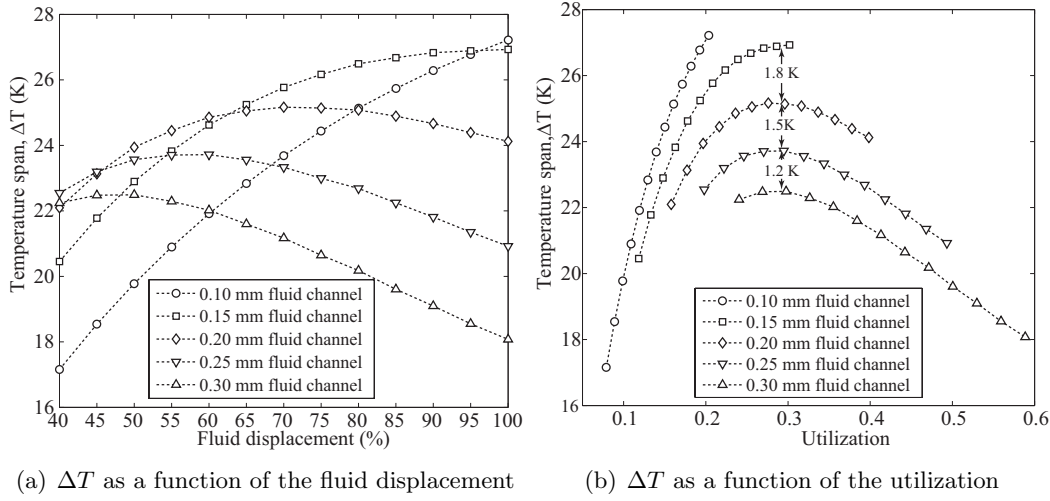


Figure 4.9: Results of the combined parameter study of the fluid displacement and the fluid channel height ($2H_R$).

mass flow of 7.27 g/s per fluid channel with the current geometry and operating conditions. The result is important since it allows the optimal stroke for any channel height to be easily determined once the optimal utilization has been obtained. Whether this tendency is valid for all AMR geometries and operating conditions is currently unknown but is a subject that should be studied in more detail as this behavior would significantly simplify the design and optimization of AMRs. If there exists a global optimum for the utilization it would allow for simple calculation of for example the cycle frequency, the mass flow of the heat transfer fluid, the ratio of regenerator material to the fluid etc. The results on Fig. 4.9(b) shows that at the optimal utilization, the performance of the AMR is increased as the channel height is decreased, and this trend is non-linear since the increase in ΔT is non-proportional to the decrease in channel height as indicated on Fig. 4.9(b). However, it is not possible to determine the optimal mass flow for the narrowest channels as the current geometry only allows the pistons to displace 100% of the fluid within the regenerator. This would be possible in future studies by increasing the length of the flow channel appropriately. Fig. 4.9(b) indicates that it is possible to obtain a much higher ΔT with narrower channels, so this is a subject that should be studied in more detail. Fig. 4.10 shows the temperature profiles in the regenerator and the fluid just before and after the blow periods for the conditions that produced the maximum ΔT , i.e a fluid channel height of 0.1 mm and a stroke of 5 cm. The results on Fig. 4.10(b) and Fig. 4.10(d) again agree with the hypothesis that there should be no temperature differences between the regenerator material and the fluid after the blow periods in order to achieve optimal performance. Fig. 4.10(a) and Fig. 4.10(c) again show that only a small fraction of the fluid temperature profile is above T_H and below T_C before the cold and hot blow, respectively. The theory described in Section 2.3.3 argues that only this fraction of the fluid channel should be displaced during the blow periods. However, the stroke of 5 cm displaces all the fluid in the channel and at the same

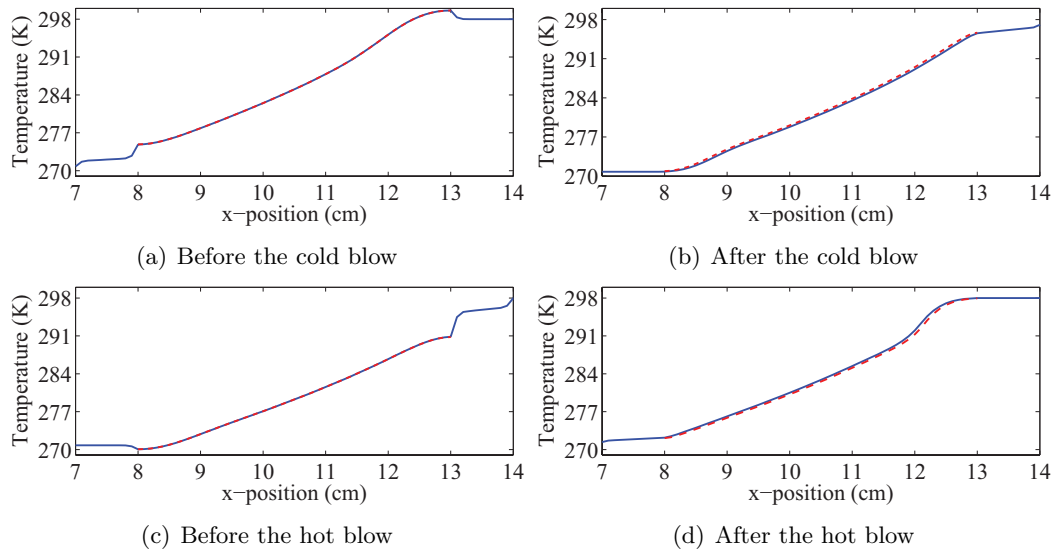


Figure 4.10: Temperature profiles in the regenerator (dashed red line) and in the fluid channel (solid blue line) just before and after the cold blow and the hot blow.

time obtains the highest ΔT . Based on these results it is also concluded that, with sufficient regeneration, the stroke is independent of the temperature profile in the fluid before the blow periods.

4.6 Influence of the heat transfer fluid

In the previous sections, water was utilized as the heat transfer fluid but this is obviously not an option when the cold end of the AMR reaches temperatures below 0°C . In this situation other fluids like ethanol can be used. To determine the influence of the heat transfer fluid, the parameter study of both stroke and the fluid channel height was repeated with three other types of fluids: ethanol, glycerine and mercury. Ethanol was chosen because it represents an option of operation of the AMR below 0°C , mercury was chosen because of its radically different physical properties, which should give additional insights into the behavior of the AMR and, glycerine was chosen to have a reasonable spread in the properties of the fluids. The physical properties are listed in Table 4.1 which in addition to the heat capacity, density, thermal conductivity and viscosity also lists the volumetric heat capacity (C) and the thermal diffusivity (α).

4.6.1 Results and discussion

Fig. 4.11(a) shows the results of the variation of the stroke with the four different heat transfer fluid in terms of the stroke and the fluid displacement and Fig. 4.11(b) shows the results in terms of the utilization. Table 4.2 shows the maximum no-load ΔT for each of

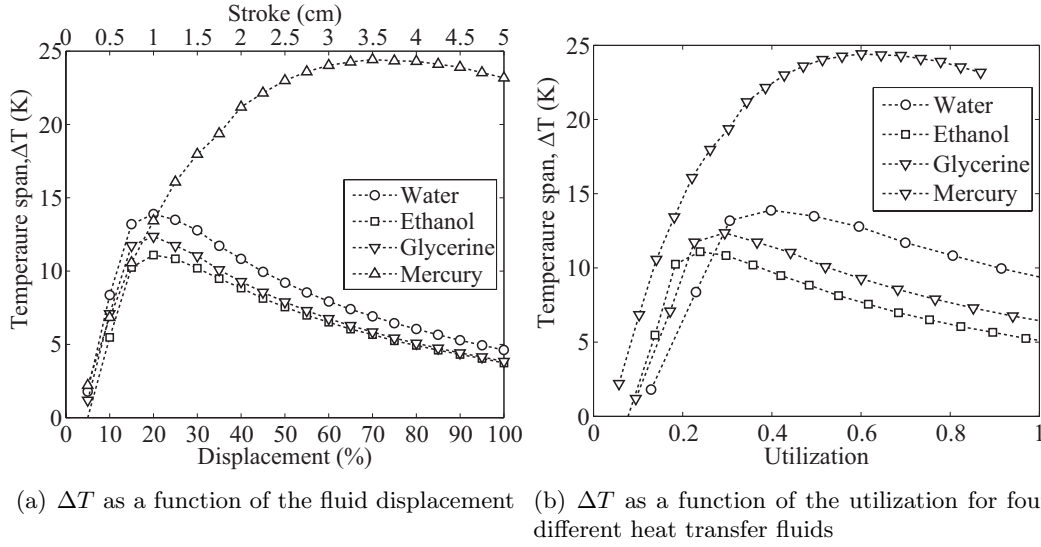


Figure 4.11: The results of the variation of the piston stroke for the four different heat transfer fluids in terms of displaced fluid and the utilization

the four fluids as well as the fluid displacement and the corresponding utilization.

The results show that mercury produces the highest ΔT which is followed by water, glycerine and ethanol, in that order. The maximum ΔT 's for each fluid are ordered in terms of increasing thermal conductivity (and diffusivity) and this supports the theory that there should be no temperature differences between the regenerator and the fluid in order to obtain a good performance. Thus it can be expected that a high thermal conductivity of the transfer fluid allows the AMR to transfer heat between the regenerator and the fluid faster. It is surprising that water, ethanol and glycerine seem to have the same optimal stroke since the different volumetric heat capacities of the three fluids mean that a different amount of heat is transported during the blow periods. However, the optimal stroke for water, ethanol and glycerine all correspond to the gap between the regenerator and the heat exchangers. Therefore a possible explanation of the identical, optimal strokes for water,

Table 4.1: Physical properties of water, ethanol, glycerine and mercury all evaluated at 298 K. The material properties were obtained from the property database in the software program EES [56].

Material	c_p ($\text{Jkg}^{-1}\text{K}^{-1}$)	k ($\text{Wm}^{-1}\text{K}^{-1}$)	ρ (kgm^{-3})	μ ($\text{kgm}^{-1}\text{s}^{-1}$)	C (Jm^{-3})	α (m^2s^{-1})
Water	4183	0.595	997	$8.91 \cdot 10^{-4}$	$4.17 \cdot 10^6$	$1.43 \cdot 10^{-7}$
Ethanol	2513	0.161	786	$1.08 \cdot 10^{-3}$	$1.97 \cdot 10^6$	$8.18 \cdot 10^{-8}$
Glycerine	2416	0.286	1261	$9.93 \cdot 10^{-1}$	$3.05 \cdot 10^6$	$9.39 \cdot 10^{-8}$
Mercury	139.4	8.515	13534	$1.54 \cdot 10^{-3}$	$1.89 \cdot 10^6$	$4.51 \cdot 10^{-6}$

ethanol and glycerine is that the optimal displacement (and the utilization) for each fluid should be lower. However, the effect of the gap distance "hides" this since strokes shorter than 1 cm does not transport a sufficient amount of heat from the regenerator. This is the results of that the fluid in direct contact with the regenerator never flows into either of the two heat exchangers. Therefore it is the AMR geometry that results in the optimal fluid displacement. This could also explain why the optimal utilization for water determined in this analysis is higher than that determined in the previous section. The optimal stroke should be lower and the resulting utilization is also too high. This could also explain why the results for mercury are so dissimilar to the other three fluid and more resembles the results for water shown in Fig. 4.9. Mercury has a much higher thermal conductivity than the other fluids, which results in a better regeneration in the AMR. This in turn means that the pistons can displace a larger fraction of the fluid in the fluid channel compared to the other three heat transfer fluids, exactly as Fig. 4.9 shows. For mercury, the utilization that produces the highest ΔT is higher than that of any of the other fluids, and about twice the optimal utilization for water determined in the previous section. Results from previous studies, like those shown in Fig. 2.13 [43], indicate that a high heat transfer leads to a higher optimal utilization. The results mentioned above are based on a simpler model than the 2-D model used here. However for regenerators in general, it has also been showed that a high heat transfer allows a higher utilization [60]. It is probably this effect that accounts for the higher optimal utilization of mercury. Fig. 4.12(a) shows the results of the variation of the fluid channel height for the four fluids as a function of the fluid channel height ($2H_f$) and the utilization. Table 4.3 shows the maximum ΔT obtained with each of the four fluid along with the corresponding fluid channel height and the utilization.

In this parameter study, water was able to produce the highest ΔT followed by mercury, glycerine and ethanol in that order. The results show that water obtains the highest ΔT in this parameter study while mercury produced the highest ΔT in the previous variation of the stroke. This indicates that the optimal performance of the AMR depends on both the AMR geometry and the material properties and no single parameter dominates the performance. The utilization that corresponds to the maximum ΔT of the four fluids are much lower than those obtained in the previous parameter study. This indicates that the globally optimal utilization for any of the fluids has not been determined in neither parameter study. This is consistent with that neither Fig. 4.11(b) nor Fig. 4.12(b) show the optimal utilization for water determined previously. The results shown in Section 4.5

Table 4.2: The maximum temperature span, ΔT_{\max} and the corresponding fluid displacement and the utilization obtained during the parameter study of the stroke for each of the four fluids.

Fluid	ΔT_{\max} (K)	Fluid displacement (%)	Φ
Water	13.9	20	0.40
Ethanol	11.1	20	0.24
Glycerine	12.4	20	0.30
Mercury	24.4	70	0.60

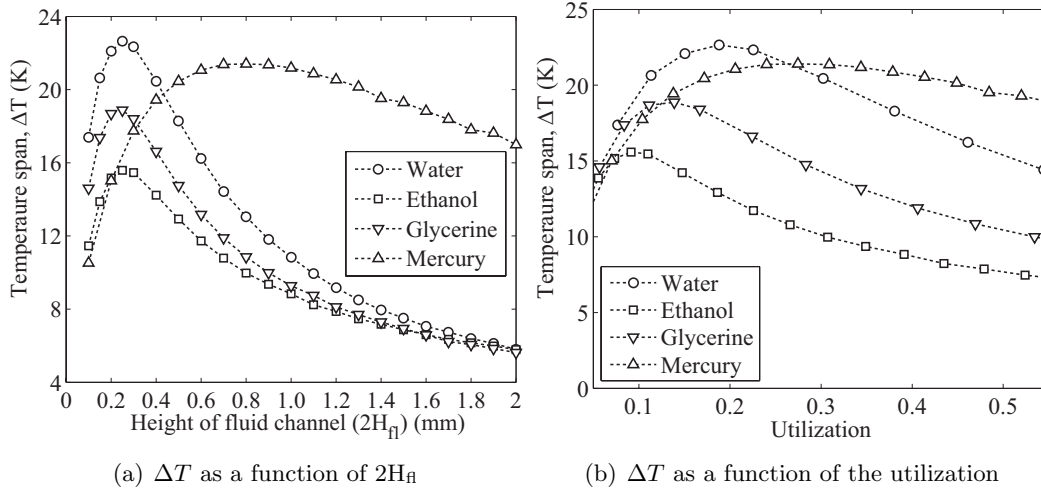


Figure 4.12: The results of the variation of the fluid channel height for the four different heat transfer fluids in terms of $2H_{fl}$ and the utilization.

Table 4.3: The maximum temperature span, ΔT_{max} and the corresponding $2H_{fl}$, and the utilization obtained during the parameters study of the fluid channel height for each of the four fluids.

Fluid	ΔT_{max} (K)	$2H_{fl}$ (mm) (%)	Φ
Water	22.7	0.25	0.19
Ethanol	15.6	0.25	0.09
Glycerine	18.8	0.25	0.14
Mercury	21.4	0.80	0.27

indicated that the the globally optimal utilization is independent of the fluid channel height or stroke. The fact that the utilizations, which correspond to the highest ΔT in the two parameter studies are not equal, clearly indicates that the optimal utilization has not been determined. To determine the true optimum of the utilization, the stroke variation should be performed for at least two fluid channel heights and the resulting utilization should have almost equal values. In addition, the optimal stroke should be larger than the gap distance between the regenerator and heat exchanger to rule out the effect of this part of the AMR geometry. This was not done in the present study due to time limitations, but should be performed in future studies because the existence of a global optimum of the utilization for different types of heat transfer fluids is an important result for the optimization of the AMR.

All fluids except mercury has the same optimal fluid channel height and the results indicate that, except for mercury, the optimal fluid channel height for each fluids allows the AMR to obtain a higher ΔT than that observed during the stroke variation. The narrower fluid channels increases the heat transfer between the fluid and the regenerator plates as

previously discussed in Section 4.4. For example, an AMR with mercury already has good heat transfer characteristics and does not benefit significantly from a narrower fluid channel as the results indicate. But as the results of the stroke variation showed, an AMR with mercury does benefit from an increased stroke. The fluid channel is performed with a constant stroke and the reduction of the fluid channel height also results in a reduced mass flow. This has been shown to have a detrimental effect on the AMR performance in the previous section. For the remaining fluids the increased heat transfer resulting from the narrower fluid channel increases the AMR performance. Although the reduced mass flow also affect the AMR performance, the increased heat transfer is the dominant effect. In fact, it seems that increasing the heat transfer is so important that each fluid keeps benefitting from a narrower fluid channel until the reduced mass flow decreases the performance of the AMR so drastically that the ΔT also starts to decrease. However, the volumetric heat capacities of the water, ethanol and glycerine are different. For example, the difference in volumetric heat capacity between water and ethanol is a factor of two. This means that the reduction of the fluid channel height should be more pronounced for ethanol with its low volumetric heat capacity. This effect cannot be observed as the maximum ΔT for water, ethanol and glycerine all occur for the same fluid channel height. Table 4.1 shows that the thermal conductivity of water, glycerine and ethanol are similar but the thermal conductivity of mercury is much greater compared to any of the other fluids. A reduction in the fluid channel height affects both the heat transfer and the mass flow but the combined effect is unclear. At present, no final conclusion can be made but the results indicate that heat transfer fluids with similar thermal conductivity react similarly to a reduction in the fluid channel height. This theory is supported by that the results for water, ethanol and glycerine show similar trends and the same optimal fluid channel height, whereas mercury with its much higher thermal conductivity has a different trend and optimum. To determine the effect of the properties of the fluid further analysis should be performed where different fluids are subjected to a combined parameter study of the stroke and fluid channel height similar to that performed for water in the previous section. Fig. 4.13 shows the temperature profiles in the regenerator and fluid after the hot blow for the optimal stroke and fluid channel height and each of the four fluids. The results show that during the stroke variation there are noticeable temperature differences between the fluid and the regenerator except for mercury. This supports the hypothesis that there is no significant benefit in narrowing the fluid channel when using mercury, since the heat transfer is already sufficiently high. In this case, it is more beneficial to increase the stroke and mass flow as the results in Fig. 4.11(a) show. Fig. 4.13 shows that for the fluid channel height variation there are almost no temperature differences between the regenerator and the fluid for all the four fluids and that the shapes of the temperature profiles are similar. This again shows that once the temperature differences between the regenerator and the fluid are negligible there is no reason to decrease the channel height further and it is more important to increase the stroke as illustrated by the results for mercury. Since mercury obtains small temperature differences for much higher fluid channels than any of the other fluid, the influence of the decreasing mass flow will manifest itself at longer strokes compared to the other three heat transfer fluids, exactly as the results show.

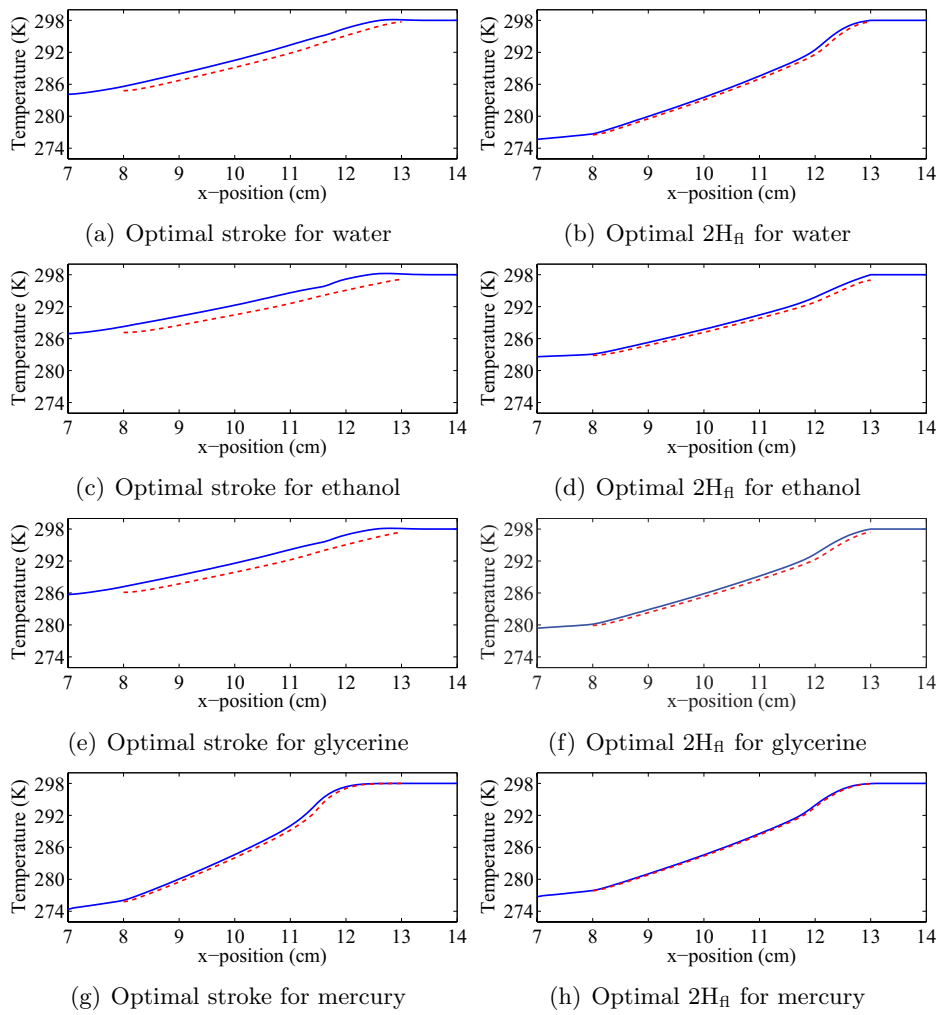


Figure 4.13: Temperature profiles in the regenerator (dashed red line) and in the fluid channel (solid blue line) after the hot blow for the optimal stroke (left column) and the optimal flow channel height (right column) for the four different heat transfer fluids.

4.7 Influence of the frequency of the refrigeration cycle

The results from the previous parameter study showed that the performance of the AMR is very dependent on the heat transfer within the regenerator. The best performance is obtained when there are no temperature differences between the regenerator material and the fluid. For example, the reduction of the height of the fluid channel can increase the no-load ΔT by more than a factor of two. The increased heat transfer offered by the narrower fluid channel could also be obtained by increasing the period of the AMR refrigeration cycle. Another option is to increase the time used for the blow periods (τ_2 and τ_4) by decreasing the time used for heat transfer after the magnetization (τ_1) and the demagnetization (τ_3) for a constant cycle period. This would increase the heat transfer in the AMR since the convective heat transfer during the blow periods is greater than the conductive heat transfer during the magnetization and demagnetization periods. To analyze the influence of each of these two variables, a parameter study was performed where the cycle period was varied from 2 s to 18 s and the length of the magnetization and blow periods was varied so that τ_1/τ_2 (equal to τ_3/τ_4) varied from 1/8 to 8. The latter parameter study also determines the influence of any temperature differences between the regenerator and the fluid before the blow periods. This is interesting since the results shown in Fig. 4.4 indicated that the present length of the magnetization and demagnetization periods could be reduced while still retaining the negligible temperature differences between the regenerator and the fluid. The study of τ_1/τ_2 is also relevant because the results presented in Fig. 4.10 showed that the optimal stroke does not depend on the temperature profile in the fluid before the blow periods. This suggests that the heat transfer period after magnetization and demagnetization may be omitted altogether.

4.7.1 Results and discussion

Fig. 4.14(a) presented the results of the parameter study as a function of the cycle period for constant values of τ_1/τ_2 and Fig. 4.14(b) presents the results as a function of τ_1/τ_2 for constant cycle periods. The maximum ΔT is obtained with a cycle period of 12 s and τ_1/τ_2 equal to 1/8 which results in a ΔT of 18.3 K. The results show that, except for a cycle period of 2 s, the AMR obtains the best performance when τ_1/τ_2 is as low as possible which means that the blow periods should start almost immediately after the regenerator material has been magnetized or demagnetized. These results support the hypothesis that it is important with a high heat transfer during the blow periods. The results also suggest that any temperature differences between the regenerator and the fluid before the blow periods does not affect the AMR performance significantly. This can also be observed from Fig. 4.4 and the curve for a cycle period of 6 s on Fig. 4.14(b). Fig. 4.4 showed that no more than 1.5 s was required to obtain negligible temperature differences between the regenerator and the fluid before the blow periods. However, Fig. 4.14(b) shows that the best performance is obtained for much lower values of τ_1/τ_2 , meaning that the time for heat transfer after the magnetization and demagnetization is significantly below 1.5 s. For example, with a cycle period of 6 s and τ_1/τ_2 equal to 1/8, τ_1 is only 0.33 s but this choice of parameters still obtains the maximum ΔT at this cycle length. For τ_1/τ_2 below 2, a cycle

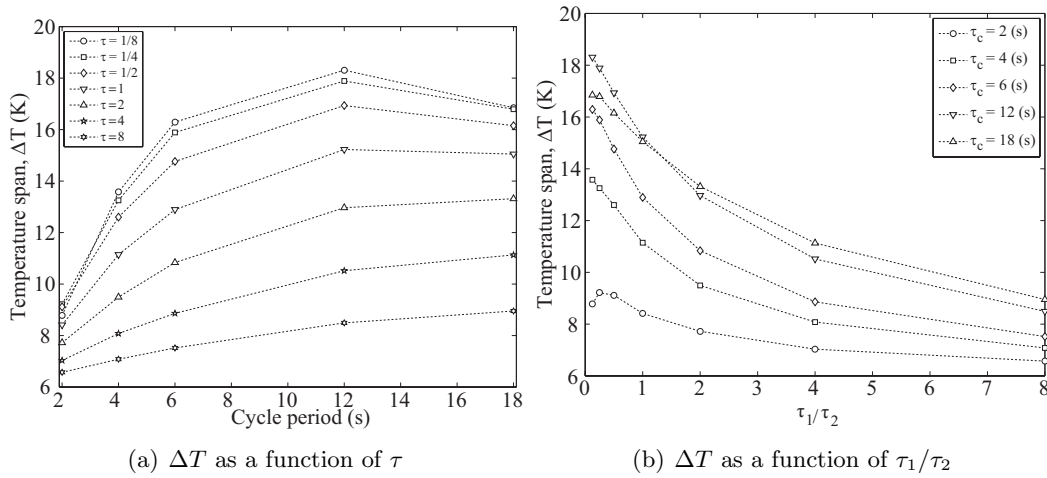


Figure 4.14: The results of the parameter study of the cycle period and the ratio between τ_1 and τ_2 .

period of 12 s produce the highest ΔT otherwise a cycle period of 18 s produces the highest ΔT . These results are somewhat counter-intuitive as a long cycle period should ensure small temperature differences and since the amount of displaced fluid remains constant the utilization should also be almost constant. However, the long cycle period decreases the mass flow in the AMR. Even if the amount of displaced fluid remains constant, the reduced mass flow can limit the heat transfer in the AMR. The effect of the mass flow in isolation has not been investigated separately, however previous results showed that once the temperature differences between the regenerator and the fluid are negligible, deviations in the heat transfer or mass flow can influence the AMR performance adversely. Another possible consequence of a long cycle period could be that there is increased heat conduction from the regenerator to the CHEX and likewise from the HHEX to the regenerator, i.e. "the wrong way". This would only have a slightly negative effect on the AMR performance because the heat conduction is limited due to the low conductivity of water and the thin fluid channel. This effect could also explain the reduced performance at a cycle period of 18 s since this theory is consistent with the above results. For τ_1/τ_2 above 2, the 18 s cycle obtains the highest ΔT because the longer cycle period and thus blow periods results in a higher heat transfer compared to the 12 s cycle. Fig. 4.15 shows the temperature profiles in the regenerator and fluid before and after the hot blow for selected values of τ_1/τ_2 with a cycle period of 12 s. Fig. 4.15 shows that when τ_1/τ_2 is above 1, there are no significant temperature differences between the regenerator and fluid, but there is up to 2 K difference in ΔT compared to τ_1/τ_2 equal to 1/8. This suggests that once the temperature differences between the regenerator and the fluid are negligible, the increased mass flow associated with longer blow periods is more important. This theory is further supported by Fig. 4.16, which shows the temperature profiles in the regenerator and fluid after the hot blow for a cycle period of 12 s and 18 s and τ_1/τ_2 equal to 8. Both cases show similar temperature profiles but the lower mass flow in the 18 s cycle results in a lower ΔT .

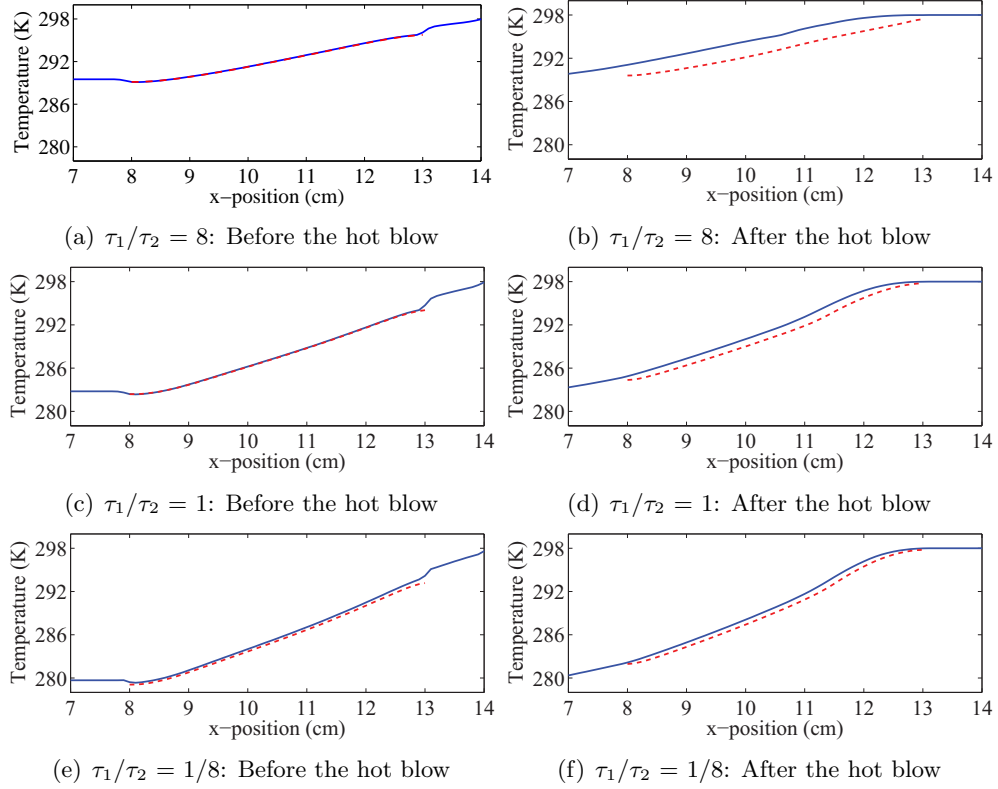


Figure 4.15: Temperature profiles in the regenerator (dashed red line) and in the fluid channel (solid blue line) just before and after the hot blow for selected values of τ_1/τ_2 and a cycle period of 12 s.

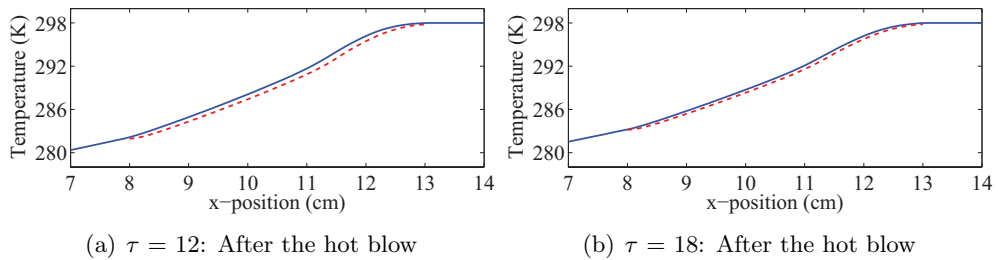


Figure 4.16: Temperature profiles in the regenerator (dashed red line) and in the fluid channel (solid blue line) just before and after the hot blow for selected cycle periods and $\tau_1/\tau_2 = 1/8$.

4.8 Pressure loss in a parallel-plate AMR regenerator

The results obtained from the parameter study of the stroke and fluid channel height are here used to analyze the pressure loss and the piston work in a parallel-plate regenerator geometry. It was previously determined that the piston work was negligible with the initial operating conditions and regenerator geometry. However, since the AMR obtains a better performance with a narrow fluid channel or a long stroke it may be possible that the piston work can no longer be omitted from the total work since both these conditions increase the pressure drop. To analyze whether this is the case, the pressure loss was determined with the AMR model and Eq. 3.16 was used to calculate the piston work as a function of the fluid channel height and the stroke. Because the flow in the majority of the fluid channel is one-dimensional and fully developed, the pressure loss can be compared to the pressure loss predicted by standard fluid mechanical theory. The pressure drop for a fully developed laminar flow in a horizontal pipe can be calculated as [54, 44]

$$\Delta p = \left(\frac{96}{Re} \right) \rho_{\text{fl}} \frac{L_{\text{fl}} \bar{U}^2}{D_{\text{h}}}, \quad (4.4)$$

where where \bar{U} is the mean velocity of an equivalent channel flow, D_{h} is the hydraulic diameter which for a non-circular duct with the current 2-D geometry is defined as two times the total height ($2H_{\text{fl}}$) of the fluid channel [54]

$$D_{\text{h}} = 4H_{\text{fl}} \quad (4.5)$$

The power required for the pistons to displace the fluid is determined as the pressure loss times the volume flow [44]

$$\dot{w}'_{\text{ana}} = 2\Delta p \bar{U} H_{\text{fl}} \quad (4.6)$$

For the AMR model the piston power is \dot{w}'_{piston} divided by the total time of the two blow periods

$$\dot{w}'_{\text{piston}} = \frac{w'_{\text{piston}}}{\tau_2 + \tau_4} \quad (4.7)$$

As a means of comparison, the pressure loss for an equivalent porous bed regenerator is determined using the Ergun equation which has been previously used in one-dimensional AMR models [60]:

$$\Delta p = \left(\frac{A\alpha\mu}{d_{\text{h}}^2} \cdot \epsilon \bar{U} + \frac{B\beta\rho_{\text{fl}}}{d_{\text{h}}} \cdot (\epsilon U_0)^2 \right) \cdot L_{\text{reg}} \quad (4.8)$$

where A,B, α and β are constants and d_{h} is the hydraulic diameter of the particles in the porous bed. The term $\epsilon \bar{U}$ represents the open area fluid velocity which is determined as the fluid velocity inside the regenerator and corrected for the porosity. The constants A and B are 180 and 1.8 and d_{h} is equal to $200 \mu\text{m}$ [60]. and α and β is determined as:

$$\alpha = \frac{(1 - \epsilon)^2}{\epsilon^2} \quad \text{and} \quad \beta = \frac{1 - \epsilon}{\epsilon^3} \quad (4.9)$$

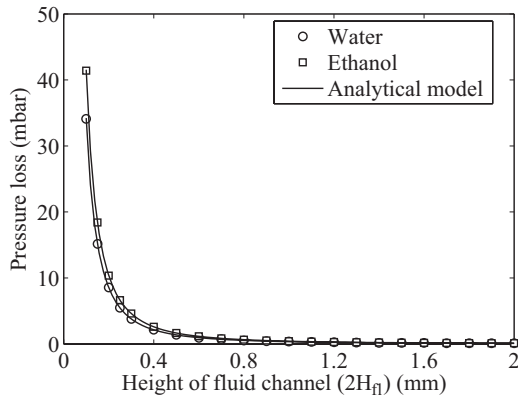
The equivalent porosity for a parallel-plate regenerator is determined as:

$$\epsilon = \frac{H_{\text{fl}}}{H_{\text{fl}} + H_{\text{reg}}} \quad (4.10)$$

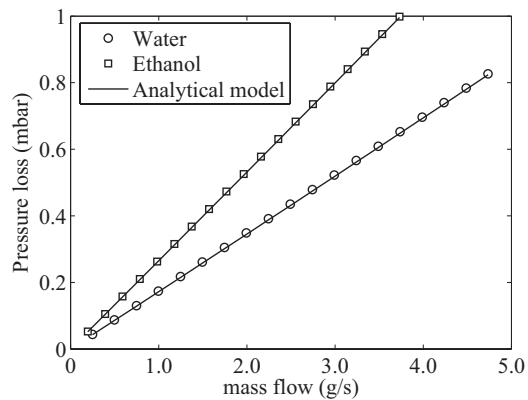
The piston power required to push the fluid through the porous bed regenerator is determined using Eq. 4.6 with the same range of volume flows ($\bar{U} \cdot 2H_{\text{fl}}$) as for the parallel-plate regenerator in order to compare the pressure drop under similar conditions.

4.8.1 Results and discussion

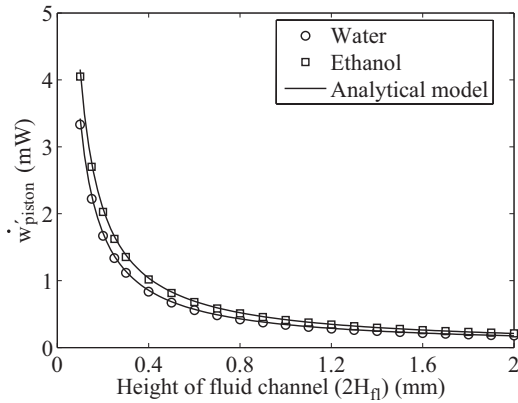
Fig. 4.17(a) shows the pressure loss in the regenerator as a function of the fluid channel height for a constant stroke and Fig. 4.17(b) shows the pressure loss as a function of the mass flow (equivalent to the stroke) for a constant fluid channel height. Figs. 4.17(c) and 4.17(d) show the corresponding pump work for the two cases. The four figures also show the pressure loss and work determined by the analytical model. The pressure loss and piston work was determined for both water and ethanol. However, the flow is determined with a dimensionless model and therefore these results should apply for all the fluids considered in this chapter. The results presented in Fig. 4.17(c) and Fig. 4.17(d) show that the pistons power is in the mW range even with the narrowest fluid channel or the longest stroke. This shows that it is also a valid assumption to neglect the piston work under these conditions. In addition, the increased performance obtained using the narrow channel and long stroke means that the piston work becomes an even smaller fraction of the total work. The figures also show an excellent agreement between the analytical and the model results for the pressure drop and pistons work. This means that future analysis of the pressure drop in the regenerator may be performed using the simple models shown in Eq. 4.4 to Eq. 4.6. Fig. 4.17(e) and Fig. 4.17(f) shows the pressure loss in a corresponding porous bed regenerator using water as the fluid. A comparison with the pressure drop and the piston work in the porous bed regenerator shows that in a porous bed regenerator the pressure loss and pistons work are in the range of bars and watts, respectively, while the pressure drop and piston work for a parallel-plate regenerator are in the range of mbar and mW, respectively. This means that for a porous bed regenerator the piston work will be a significant parasitic loss, which is not the case for a parallel-plate regenerator. However, a porous bed has a better heat transfer due to a larger surface area which in turn results in a higher performance. This may partly offset the parasitic load of the pistons. But if the porosity is decreased (i.e. due to an optimal ratio between the regenerator material and the fluid) the pressure loss starts to increase significantly and a parallel-plate regenerator can achieve a lower equivalent porosity before the pressure loss start to reduce the AMR performance.



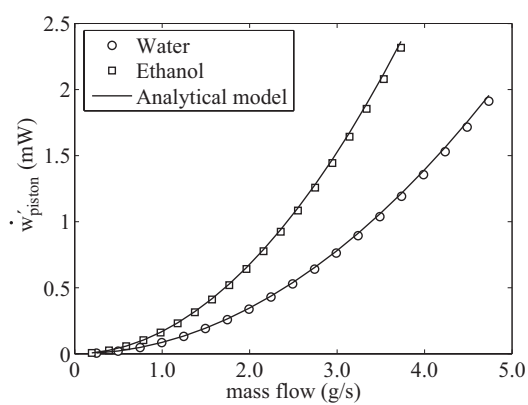
(a) Pressure loss as a function of the fluid channel height



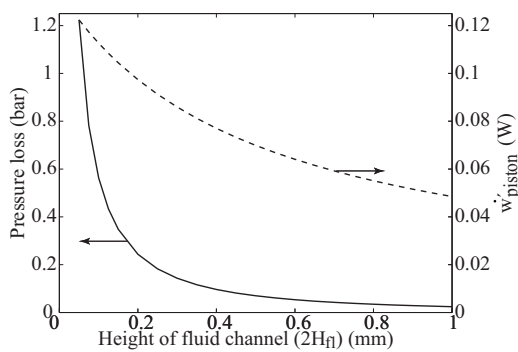
(b) Pressure loss as a function of the mass flow



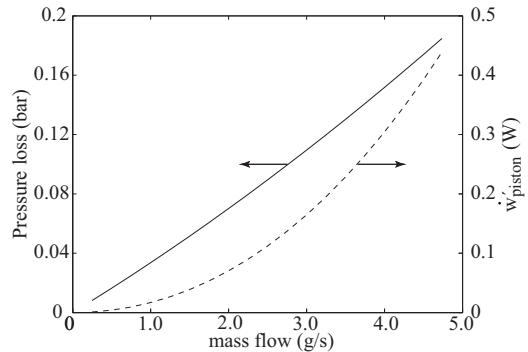
(c) Piston work as a function of the fluid channel height



(d) Piston work as a function of the mass flow



(e) Pressure loss and work as a function of the fluid channel height



(f) Pressure loss and work as a function of the mass flow

Figure 4.17: The pressure loss in the regenerator with water and ethanol. (a) Pressure loss for an increasing height of the fluid channel and a fixed mass flow (stroke). (b) Pressure loss for an increasing mass flow (stroke) with a fixed height of the fluid channel. (c-d) The corresponding piston work for the two cases. (e-f) The pressure loss and piston work for the two cases for a corresponding porous bed regenerator and water as the heat transfer fluid..

Since the pressure loss in the fluid channel can be determined analytically it may also be possible to determine the velocity profile analytically. The steady-state 1-D momentum equation with constant viscosity can be written as [44]:

$$\mu \left(\frac{\partial^2 u}{\partial y^2} \right) = \frac{\partial p}{\partial x} \quad (4.11)$$

The solution to the velocity profile is obtained by integrating twice:

$$u(y) = \frac{1}{2\mu} \frac{\partial p}{\partial x} y^2 + C_1 y + C_2, \quad (4.12)$$

where C_1 and C_2 are the constants of the integration. By applying the boundary conditions:

$$\left. \frac{\partial u}{\partial y} \right|_{y=0} = 0 \quad \text{and} \quad u(H_{\text{fl}}) = U_{\text{P}} \quad (4.13)$$

the two constants are determined as:

$$C_1 = 0 \quad \text{and} \quad C_2 = U_{\text{P}} - H_{\text{fl}}^2 \frac{1}{2\mu} \frac{\partial p}{\partial x} \quad (4.14)$$

Introducing C_1 and C_2 into Eq. 4.12 results in the following expression for the velocity profile

$$u(y) = -\frac{H_{\text{fl}}^2}{2\mu} \frac{\partial p}{\partial x} \left(1 - \frac{y^2}{H_{\text{fl}}^2} \right) + U_{\text{P}} \quad (4.15)$$

Fig. 4.18 compares the velocity profile obtained with the FE model and the velocity profile obtained with the analytical solution where Eq. 4.4 was used to obtain $\partial p/\partial x$.

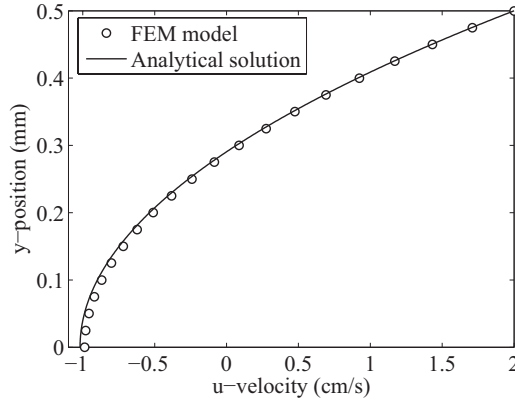


Figure 4.18: Comparison between the steady-state u -velocity profile in the y -direction determined with the FE model (symbols) and the analytical solution (solid line) during the hot blow .

As the results on the figure show, there is an excellent agreement between the two models. As a consequence, the analytical model can be used to determine the velocity profile in the fluid in future developments of the AMR model. This would simplify the AMR model and eliminate any numerical errors associated with the FE solution of the flow in the fluid channel.

4.9 Summary and final remarks

The results presented in this chapter showed that the AMR model is able to determine the no-load ΔT , the refrigeration capacity and the COP of an AMR for a range of operating conditions and regenerator geometries. In addition, the model can determine the temperature profiles in both the x- and y-direction of the regenerator and fluid channel. There was significant temperature variations in the y-direction of the fluid channel for some choices of operating conditions and regenerator geometries. This shows that a 2-D approach is required when an AMR with a parallel-plate regenerator is modelled. The AMR model was used to perform a number of parameter studies where basic operating parameters as well as parts of the AMR geometry was varied to determine the influence of each. The parameter studies mainly demonstrated the capabilities of the AMR model and obtained results directly applicable to the experimental AMR, but did not focus on explaining the overall behavior of the AMR. This was due to the time limitations of this project. However, a number of the results from the parameter studies seemed to apply generally for AMRs, which can be summarized as follows:

- Both the stroke and the height of the fluid channel have a significant impact on the AMR performance. The initial results from the AMR model predicted a ΔT of ≈ 11 K while the optimal values of the both stroke and the fluid channel height resulted in a ΔT of ≈ 27 K. With a narrow fluid channel the piston stroke must be longer to obtain the highest ΔT . In some cases, the piston stroke must displace more than 100% of the fluid inside the channel. The AMR should therefore be designed to accommodate this. The stroke which produced the maximum ΔT for a number of different heights of the fluid channel, all resulted in the same utilization and thus also the same mass flow. This means that once the optimal utilization has been determined it can be used to determine optimal piston stroke for other heights of the fluid channel. However, this only seem to apply when the fluid channel is sufficiently narrow. Here, the ratio between the thickness of the regenerator plate and the height of the fluid channel varied from 3.33 to 10, which seemed to be sufficient to determine the optimal utilization. Using water as the heat transfer fluid the optimal utilization was 0.27 but the results also indicate that different fluids may have different optimal utilizations. An additional benefit of having a narrow fluid channel is that the long stroke required for the optimal utilization also allows the AMR to reach the steady-state faster. In general, the results showed that it is possible to obtain significant ΔT 's with a parallel-plate regenerator and a 1 T magnetic field but that there is still room for improvement before the AMR is comparable to conventional refrigeration.
- All the results indicate that any perpendicular temperature differences between the regenerator and the fluid after the blow periods should be negligible in order to obtain the optimal AMR performance. The different operating conditions and regenerator geometries, which resulted in the highest ΔT 's all showed virtually no perpendicular temperature differences between the regenerator and the fluid. The small temperature differences allows the AMR to fully utilize the MCE and can be obtained by designing the AMR with good heat transfer characteristics. Examples include, nar-

row fluid channels, sufficiently long cycle period, using a heat transfer fluid with a good conductivity etc. However, once the perpendicular temperature differences are negligible, the utilization and mass flow in the AMR become more important. Finally, the results suggest that any temperature differences between the regenerator and the fluid before the blow periods are unimportant. The heat transfer periods after the magnetization and demagnetization in the AMR refrigeration cycle, should therefore be minimized.

- For a given combination of regenerator geometry and AMR operating conditions, water seems to be the best heat transfer fluid due to its high thermal conductivity. Therefore water with a suitable antifreeze that does not reduce the thermal conductivity significantly is a good candidate for use in AMRs.
- Because of the length of the fluid channel, the flow in the AMR during the blow periods is 1-D in the x-direction, and fully developed. An analysis of the flow and pressure drop determined by the AMR model shows that both the pressure drop and the steady-state velocity profile can be determined using analytical methods. This allows for easy analysis of the pressure drop in the regenerator. Future versions of the AMR model should could also use an analytical solution to determine the velocity profile in the flow channels directly in order to reduce the solution time.
- Another subject that has not yet been discussed is that the solution time of the model seems to increase with the no-load ΔT . To simulate an AMR with good performance can require up to 250+ hours. This is especially evident for AMRs with narrow fluid channels, which had some of the longest solution times. This may be problematic in future parameter studies. The current implementation of the model may prove to be too slow even with the computational resources of a cluster. An important improvement of the AMR model would be to include methods to directly determine the cyclical steady-state thus reducing the solution time of the model significantly. An example of this approach is a shooting method developed by Andersen [62], which was applied to different models of cyclic machines similar to the AMR. This method obtained good results and may offer a solution to the long solution time of the AMR model.

Chapter 5

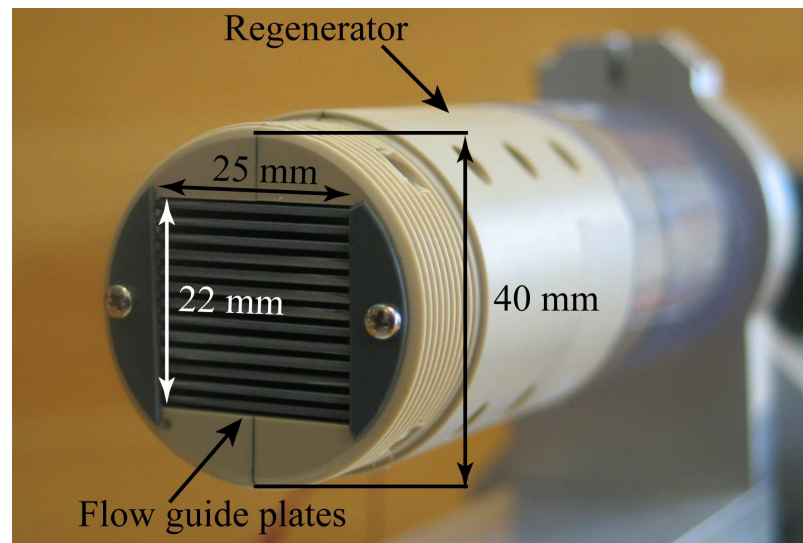
Experimental validation of the Active Magnetic Regenerator model

This chapter presents the results of an experimental verification of the AMR model. The results of a laboratory-scale AMR were compared to the results from the AMR model which was configured to simulate the operating conditions of the experimental AMR. The comparison was performed on the basis of two parameter studies.

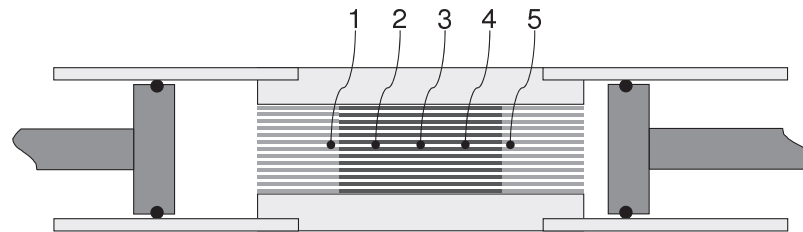
The experiments described in this chapter were not part of the work covered by this thesis and were performed by Christian Bahl from the Risø National Laboratory. The results described in this chapter will be published in a paper currently under preparation.

5.1 The Experimental Active Magnetic Regenerator

The experimental AMR consists of a 40 mm long cylinder with an outer diameter of 40 mm in which a rectangular regenerator block 25 mm wide and 22 mm high is situated. The regenerator block has slits at either side, which hold flat plates of a magnetocaloric material. The heat transfer fluid flows through the channels between the regenerator plates and at both ends of the regenerator, 20 mm long plastic flow guide plates are placed in the direction of the flow to ensure a laminar flow in the channels. Fig. 5.1(a) show a cross section of the regenerator with the cylinder, the regenerator block and the position of the flow guides and the regenerator plates. The heat transfer fluid is forced through the channels by two pistons placed in perspex tubes with an inside diameter of 34 mm. The two tubes are affixed to either end of the cylinder surrounding the regenerator block, as illustrated in Fig. 5.1(b). The two pistons are rigidly fixed to each other ensuring that they always move in phase. The distance and the velocity of the piston movement is controlled by a stepper motor and the whole AMR assembly is moved in and out of a magnetic field using a drive shaft controlled by a second stepper motor. To measure the temperature profile in the AMR, five type E thermocouples are placed equidistantly along the fluid channel



(a) Cross section of the experimental AMR



(b) Schematic representation of the experimental AMR

Figure 5.1: (a) The cross section of the cylindrical AMR enclosure with the rectangular regenerator block and shows the position of the regenerator plates as well as the flow guides. (b) In the middle of the schematic the regenerator sheets are shown in dark grey and the plastic flow guides are shown in paler grey. At both ends of the regenerator the two tubes which holds the pistons are placed. The positions of the five thermocouples which are indicated by the numbers 1 to 5.

adjacent to the central regenerator plate. Each thermocouple protrudes about 1 mm into the channel. The three central thermocouples are placed between the regenerator plates to measure the temperature inside the regenerator. The outer thermocouple in either end is placed between the plastic flow guides and measure the temperature at the hot and cold ends of the AMR. The position of the thermocouples are indicated on Fig. 5.1(b). The above dimensions of the experimental AMR are different from the model geometry used in Chapter 3 and 4 because of design changes which occurred during the development of the experimental AMR. The geometry used in the previous chapters was based on the original design of the experimental AMR. The changes was due to that the experimental AMR was redesigned to fit an electromagnet to make the device more versatile. The limited gap of the electromagnet made it necessary to shorten the regenerator and due to a lack of space in the electromagnet, the heat exchangers had to be omitted. Because of time

constraints, there was no time to update the model to reflect the design changes. However, the difference between the original design and the new design are minor. In the modelling geometry, the regenerator plates are simply shortened by 1 cm and the AMR enclosure was shortened by 4 cm. There are also fewer plates, but this have no impact of the model. The omission of the heat exchangers is handled by modelling the plastic flow guide plates as very inefficient heat exchangers. The details of these approximations are described later. In the present experiments the AMR is loaded with 13 plates of 99.9% pure gadolinium obtained from China Rare Metal Material Co. Each plate is 0.9 mm thick, 25 mm wide and 40 mm long in the flow direction, giving a total mass of Gd of 92 g. The resulting channels in the regenerator are 0.8 mm high. The magnetic field for the experimental AMR is applied by a LakeShore EM7 electromagnet capable of giving a maximum applied field of $\mu_0 H = 1.4 \text{ T}$ for a gap of 40 mm. The experimental AMR executes the conventional four steps of the AMR cycle: magnetization, cold blow, demagnetization and hot blow. The time spent for each of these steps as well as the total cycle time was controlled by varying the acceleration and velocity of the stepper motors. Similar to the AMR model, the time spent on magnetizing is set to be identical to the time for demagnetization and referred to as τ_1 and τ_3 , respectively. Likewise, the hot and the cold blows also are set to take the same time, referred to as τ_2 and τ_4 , respectively. The total cycle time, τ , is thus twice the sum of τ_1 and τ_2 (or τ_3 and τ_4). The perspex tube at the "cold end" of the AMR is insulated with insulating foam. Due to geometrical limitations of the electromagnet, the perspex tube at the "hot end" could not be insulated. The electromagnet applied a magnetic force of about 120 N on the regenerator, which limits how fast the AMR can be moved out of the magnetic field. The result is that the magnetic field is removed gradually during the demagnetization period and since τ_1 and τ_3 are equal, the magnetic field is also applied gradually during the magnetization periods. This limits both τ_1 and τ_3 to about 1.2 s. Fig. 5.2 shows how the field inside the regenerator increases and decreases during the refrigeration cycle and the figure also shows the movement of the pistons.

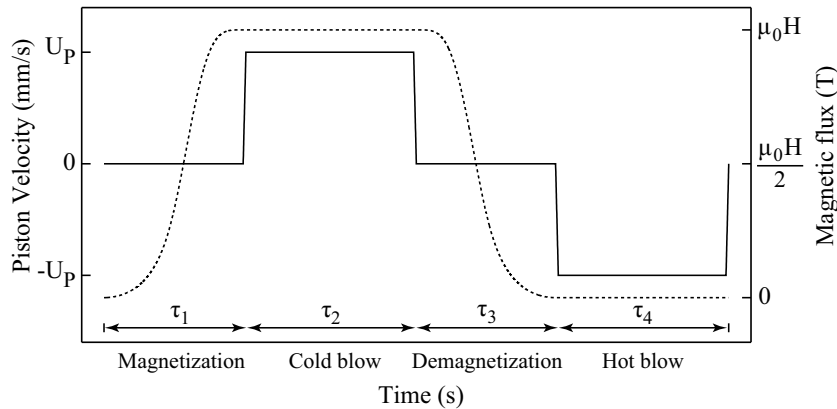


Figure 5.2: Application of the magnetic field and the piston movement during the refrigeration cycle in the experimental AMR.

5.2 Numerical modelling of the experiment

The AMR model was configured to the physical dimensions of the experimental machine by using the data shown in Table 5.1. In the model, the regenerator was separated from the flow guide plates by a small gap of 2 mm, again to ensure that all heat transfer between the regenerator and the surroundings occurs through the flow channel. The magnetocaloric

Table 5.1: Dimensions of the repeating unit in the AMR model.

Part	Length (mm)	Height (mm)
Regenerator	40	0.45
Flow guides	18	0.45
Fluid channel	120	0.4

properties of Gd was implemented using the WDS model. Greater accuracy should be obtained by determining the actual magnetocaloric properties of the supplied Gd plates. But due to limited time, experimental data of the magnetocaloric properties of the actual regenerator material could not be applied in this study. The model assumes that the AMR includes two heat exchangers in contact with a cooling load and the surroundings. This is not the case in the experimental AMR. However, the experimental AMR includes two flow guides at the positions of the heat exchangers in the model which are in contact the perspex tube. The heat conduction through the assembly should be low because of the low conductivity of both the perspex and the plastic flow guides but were included in the AMR model to simulate the heat exchangers. An effective thermal conduction of the HHEX in the model was estimated with a simple steady-state FE model illustrated on Fig. 5.3. The model analyzes the heat flux from the interior of the flow guides to the surroundings

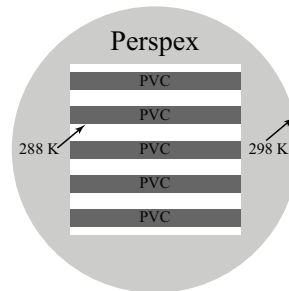


Figure 5.3: Determination of the effective thermal conductivity on the flow guide plates.

with a constant temperature difference between the fluid channel and the surroundings. This analysis determines the total heat transfer from the perspex tube, estimates the heat flow from a single flow guide plate and translates this to an effective thermal conductivity for the HHEX in the model using the dimensions given in Table 5.1. Using the relevant material properties supplied by the manufacturer of the perspex and the plastic flow guides,

this results in an effective thermal conduction of $k_{\text{eff}} = 2.54 \cdot 10^{-3} \text{Wm}^{-1}\text{K}^{-1}$. The specific heat capacity of the plastic guides was estimated to $1500 \text{Jkg}^{-1}\text{K}^{-1}$ and the density was 1300kgm^{-3} . An ambient temperature of 298K was assumed at the hot end and since the cold end of the experimental AMR was insulated with additional foam, the model assumed no-load conditions at the cold end (i.e. perfect insulation). To compare the experimental results and the numerical results, the AMR model evaluate ΔT by determining the temperature at the positions in the fluid channel that corresponds to thermocouples 1 and 5.

5.3 The parameter studies

Two sets of experiments were performed. In the first experiment the AMR was operated at a range of piston strokes using four different heat transfer fluids inside the AMR. These parameter variations were based on the results presented in Section 4.6. In the second set of experiments, the value of τ_1/τ_2 was varied along with the total time period of the cycle itself. These parameter variations were based on the results presented in Section 4.7. In each experiment, ΔT is determined by measuring the temperature at the cold end (thermocouple 1) and the hot end of the AMR (thermocouple 5). The electromagnet is set to a field of $\mu_0 H = 1.0 \text{T}$ at the center of the pole gap. However, due to the size of the AMR the average effective field is $\mu_0 H = 0.97 \text{T}$ when the regenerator is centered in the electromagnet. When the AMR is outside the the magnetic field 130mm from the center of the electromagnet, the stray field of the electromagnet still gives a field of $\mu_0 H = 0.16 \text{T}$ within the regenerator. Fig. 5.4 shows the variation of the magnetic field from the center of the electromagnet to the furthest position of the regenerator outside the electromagnet.

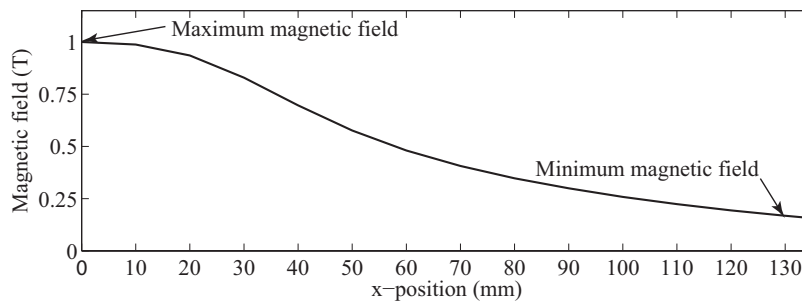


Figure 5.4: Profile of the magnetic field inside and outside the electromagnet.

The minimum and maximum magnetic fields in the regenerator during the AMR cycle were used as input to the WDS model to determine the magnetocaloric properties of the regenerator. It should be noted that the model does not simulate the gradual increase and decrease of the magnetic field observed in the experimental AMR. Instead the model assumes that the magnetic field is applied instantaneously at the beginning of the magnetization and

likewise removed instantaneously. Due to time limitations, the model was not changed to simulate a time dependent variation of the magnetic field.

5.3.1 Piston stroke variation

The magnetic refrigeration machine was run using piston strokes from 0.5 mm to 10 mm. Each piston stroke length is equivalent to moving a specific fraction of the heat transfer fluid through the regenerator. Due to the difference between the cross sectional area of the perspex tubes in which the pistons move and the cross section area of the fluid channel, a piston stroke of 1 mm is equivalent to a fluid displacement of 9.5%. As the piston stroke length is changed, the piston velocity is changed accordingly to ensure a constant τ_2 . The variation of the piston stroke was performed with number four different heat transfer fluids in the AMR. The first heat transfer fluid tested was demineralized water, together with 10% ethanol (WE). Ethylene glycol (Ethane-1,2-diol) (EG) and Propylene glycol (Propane-1,2-diol) (PG) were also used in the AMR since these are both industrially relevant heat transfer fluids but with heat transfer parameters significantly different from those of water. Finally an Extra Virgin Olive Oil (OO) was also used as the heat transfer fluid because olive oil was previously used in an earlier experimental AMR [63]. The properties of each of the heat transfer fluids are given in Table 5.2. In these experiments τ_1 and τ_2 are both been kept at 3s, resulting in a total cycle time of 12s and a τ_1/τ_2 of 1.

Table 5.2: Density, specific heat capacity, thermal conductivity, viscosity and thermal diffusivity for the four heat transfer fluid tested in the experimental AMR.

Material	c_p ($\text{Jkg}^{-1}\text{K}^{-1}$)	k ($\text{Wm}^{-1}\text{K}^{-1}$)	ρ (kgm^{-3})	μ ($\text{kgm}^{-1}\text{s}^{-1}$)	α (m^2s^{-1})	Ref.
Water/ethanol	4330	0.52	981	$1.60 \cdot 10^{-3}$	$1.23 \cdot 10^7$	[64]
Ethylene glycol	2406	0.25	1115	$17.5 \cdot 10^{-3}$	$0.94 \cdot 10^7$	[44]
Propylene glycol	2508	0.20	1036	$40.4 \cdot 10^{-3}$	$0.77 \cdot 10^7$	[55]
Olive oil	2000	0.17	915	$84 \cdot 10^{-3}$	$0.93 \cdot 10^7$	[65]

5.3.2 Cycle timing variation

In the second set of experiments, the cycle parameters was varied, while keeping the total cycle time and piston stroke length constant. The ratio τ_1/τ_2 was varied from approximately 0.34 to 4.5 with cycle times of both 12s and 18s. The variation of τ_1/τ_2 was done by introducing a "wait" period after the magnetization and demagnetization to prolong τ_1 and adjusting the piston velocity in order to vary τ_2 . The water and ethanol mixture was used as the heat transfer fluid and 50% of the fluid inside the regenerator was displaced.

5.4 Results and discussion

5.4.1 Piston stroke variation

Fig. 5.6 shows a comparison between the experimental results and model results of the steady-state ΔT as a function of the fluid displacement for each of the four fluids. The experimental results are shown together on 5.5(a). The corresponding model results are shown in Fig. 5.5(b). Table 5.3 shows the maximum ΔT for each fluid and the corresponding fluid displacement obtained with the experimental AMR and predicted by the model.

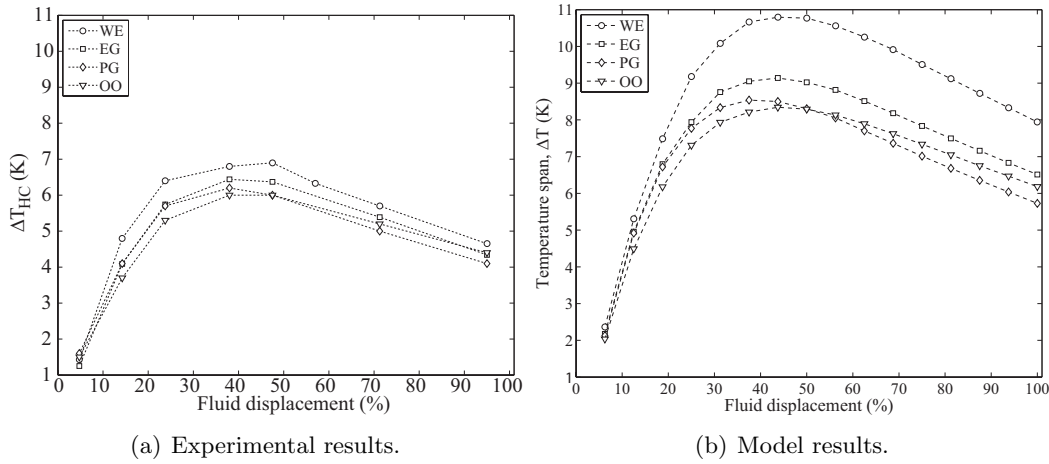
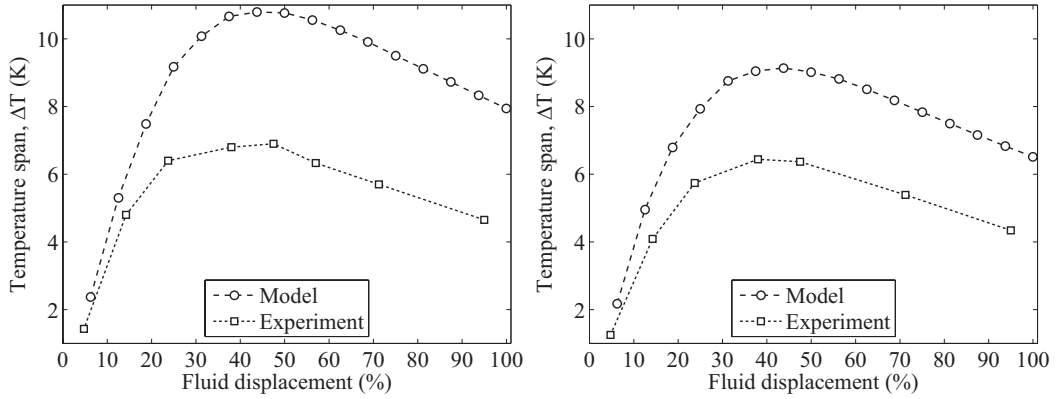


Figure 5.5: Model and experimental AMR results for the ΔT as a function of the stroke for each of the four heat transfer fluids.

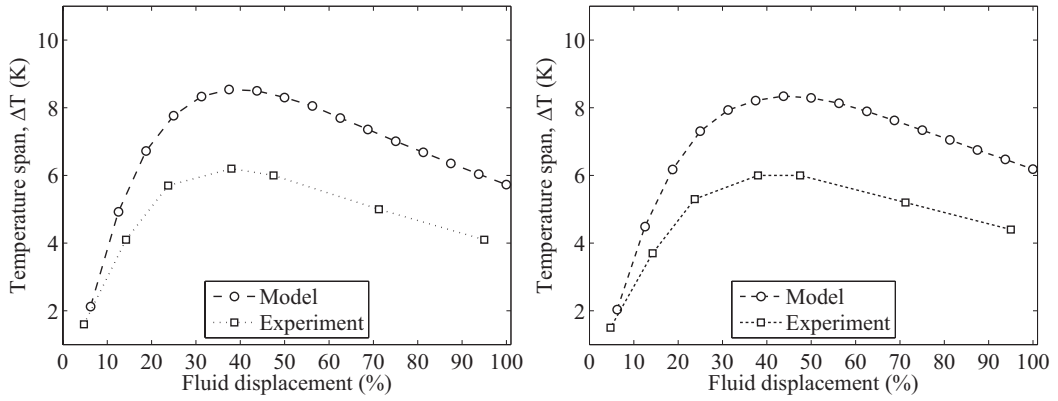
Table 5.3: Experimental and model results of the maximum temperature span, ΔT_{\max} , and the corresponding fluid displacements for each of the four fluids.

Fluid	Experimental ΔT_{\max} (K)	Experimental displacement (%)	Model ΔT_{\max} (K)	Model displacement (%)
Water/ethanol	6.9	48	10.8	44
Ethylene glycol	6.4	38	9.1	44
Propylene glycol	6.2	38	8.5	38
Olive oil	6.0	48	8.3	44

The experimental results show that the WE mixture produces the highest ΔT followed by EG, PG and OO, in that order. For fluid displacements between 14% and 48%, the ΔT 's of the fluids are ordered in terms of increasing thermal conductivity. However, above 48% the curve for OO crosses that of PG and the ΔT 's are now ordered in order of increasing thermal diffusivity. The results of the AMR model show the same behavior as the experimental results, where WE obtain the highest ΔT followed by EG, PG and OO.



(a) Experimental and model results for the water/ethanol mixture. (b) Experimental and model results for ethylene glycol.



(c) Experimental and model results for propylene glycol. (d) Experimental and model results for olive oil.

Figure 5.6: Comparison of experimental and model results for the AMR with different strokes and heat transfer fluids.

The model predicts that the maximum ΔT 's occur at slightly different strokes compared to the experimental results. The AMR model also predicts that the ΔT 's of the fluids are ordered in terms of increasing thermal conductivity at short stroke lengths and in terms of increasing thermal diffusivity at longer stroke lengths. The AMR model predicts that the ΔT of OO exceeds that of PG at 52% fluid displacement, which is slightly above the 48% obtained experimentally. The comparison between the experiment and the model for each of the four fluids in Fig. 5.6 also shows a good qualitative agreement for all the four fluids. Both the model and the experimental behavior of ΔT have the same shape and show a rapid initial increase of ΔT until the maximum is obtained, which is followed by a slower decrease of ΔT until the maximum fluid displacement is reached. The above results show that the AMR model is able to accurately predict the trends of the AMR and is able to estimate the optimal operating conditions with good precision. This is an important result

that shows that the model can be used for reliable optimization of the experimental AMR. There is also a fairly good quantitative agreement between the models and the experiment. Table 5.4 shows the mean and maximum absolute and relative error of the model compared to the experimental AMR. The difference in the values of ΔT between the experiment and

Table 5.4: Mean and maximum absolute (δ_{abs}) and relative error (δ_{rel}) of the model for the four fluids. All the maximum errors occurred at 95% fluid displacement.

Fluid	Mean δ_{abs} (K)	Max δ_{abs} (K)	Mean δ_{rel} (%)	Max δ_{rel} (%)
Water/ethanol	2.9	4.2	50	78
Ethylene glycol	2.0	2.7	38	56
Propylene glycol	1.8	2.4	36	46
Olive oil	1.7	2.3	35	46

the model was expected since the experimental AMR has heat losses to the surroundings which are not included in the model. The heat loss increases with the thermal conductivity of the fluid and the temperature difference between the inside of the AMR and the surroundings. This temperature difference must increase with ΔT and this helps to explain why WE has the largest errors since the thermal conductivity of WE is more than twice as high compared to the other fluids. In addition, Table 5.4 also shows that both the absolute and the relative error decreases for fluids with lower thermal conductivity, which in general also results in lower ΔT 's. This indicates that it is important to insulate the AMR and it may be possible to obtain better performance with the experimental AMR by increasing the insulation. Finally, the results of the stroke parameter study shows that for a given set of operating conditions and a specific regenerator geometry, a water based heat transfer fluid is the preferable choice. Since water cannot be used below 0 °C without an antifreeze, the above results show that the antifreeze itself should be chosen carefully or it may reduce the AMR performance by lowering the thermal conductivity. Both ethanol, ethylene glycol and propylene glycol are commonly used antifreeze agents [64]. However, all three have a low thermal conductivity compared to using a salt like NaCl as an antifreeze [64]. If NaCl does not react with the regenerator material it would be a good antifreeze agent.

5.4.2 Refrigeration cycle variation

Fig. 5.7 shows the experimental results of the temperature span as a function of τ_1/τ_2 for cycle periods of 12s and 18s. The corresponding results from the AMR model are also shown on the figure. Table 5.5 shows the maximum ΔT obtain for each cycle period and the corresponding value of τ_1/τ_2 for both the experimental AMR and the model. The experimental results show that the maximum ΔT is obtained with a cycle period of 12s at the minimum τ_1/τ_2 of 0.51 followed by the cycle period of 18s again at the lowest ratio of τ_1/τ_2 of 0.34. Compared to this, the results from the model show similar results where the maximum ΔT is obtained at a cycle period of 12s followed by the cycle period of 18s. For both periods, the largest ΔT was obtained at the lowest τ_1/τ_2 ratio. Looking at the trends of the curves, both the experiment and the model show that ΔT increases for decreasing values

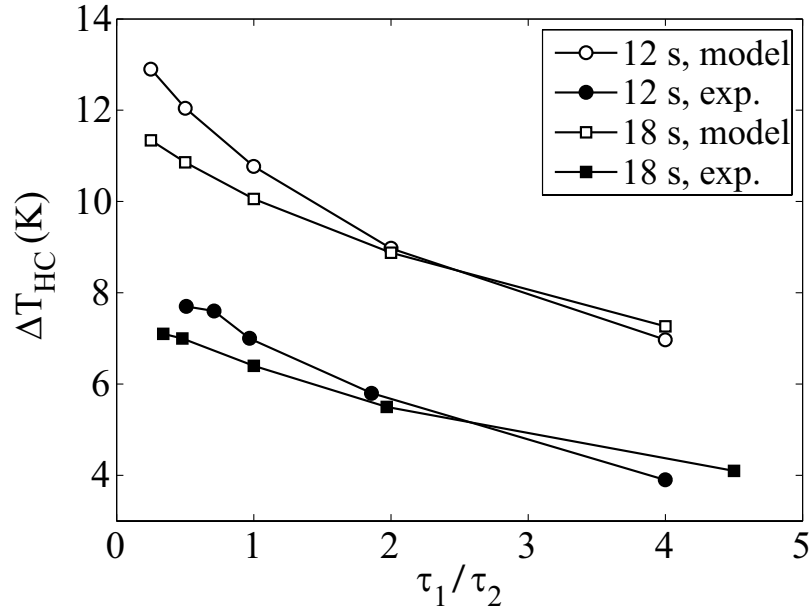
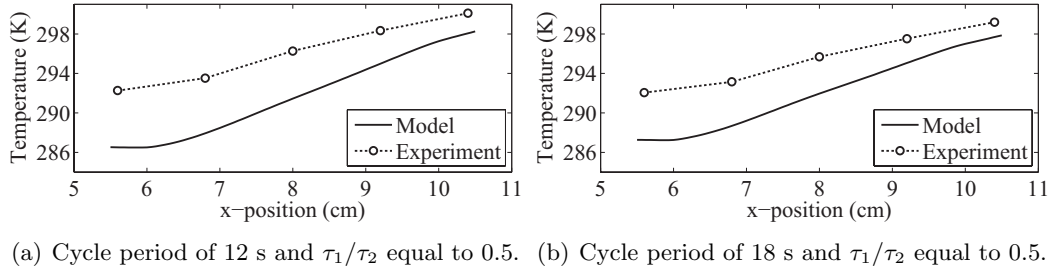


Figure 5.7: Model and experimental ΔT as a function of τ_1/τ_2 for cycle periods of 12 s and 18 s.

of τ_1/τ_2 similar to the results presented in Chapter 4. These results clearly show that it is detrimental for the AMR performance to wait after the magnetization and demagnetization periods and the majority of the cycle time should be used for the blow periods. This was also concluded previously in Chapter 4. Comparing the experimental and model results again show that the model is able to reproduce the qualitative trends of the experimental AMR. The experimental results show that a cycle period of 12 s generally has the largest ΔT except for the highest τ_1/τ_2 ratio of 4. The same trend is predicted by the model, which shows that a cycle period of 12 s obtains the highest ΔT 's in the parameter study except for τ_1/τ_2 equal to 4. This is again similar to the results in Chapter 4 which showed that a cycle of 18 s obtains a higher ΔT at high values of τ_1/τ_2 compared to a cycle of 12 s. In this parameter study, there is a good quantitative agreement of the resulting ΔT . For a cycle period of 12 s, the mean error of the model is 60% and the maximum error is 79% which occurs for τ_1/τ_2 equal to 0.51. For the cycle period of 18 s, the mean error is 61% and the maximum

Table 5.5: Experimental and model results of the maximum temperature span, ΔT_{\max} , and the corresponding τ_1/τ_2 for each of the two cycle periods at a fluid displacement of 50%.

Cycle periods	Experimental ΔT_{\max} (K)	Experimental τ_1/τ_2	Model ΔT_{\max} (K)	Model τ_1/τ_2
12 s	7.7	0.51	12.9	0.25
18 s	7.1	0.34	11.3	0.25



(a) Cycle period of 12 s and τ_1/τ_2 equal to 0.5. (b) Cycle period of 18 s and τ_1/τ_2 equal to 0.5.

Figure 5.8: Comparison of the experimental results of the temperature profile in the fluid after the cold blow for (a) a cycle period of 12 s and τ_1/τ_2 equal to 0.5 and (b) a cycle period of 18 s and τ_1/τ_2 equal to 0.5

error is 71% which occur at τ_1/τ_2 equal to 0.34. The mean errors are larger than those obtained in the stroke parameter study which is probably due to the fact that the average ΔT is larger in this parameter variation. In the above comparison, the AMR model was able to predict the behavior of the experimental AMR with good accuracy and obtained a good agreement with the experimental performance. This again show the validity of the AMR model for simulation of the experimental AMR. Fig. 5.8 show the temperature profile in the fluid after the cold blow at τ_1/τ_2 equal to 0.5 for a cycle period of both 12 s and 18 s, which were obtained from both the experiment and the model. The temperature profiles of the experimental AMR and the model are in good agreement and both show an almost linear trend. The model underestimates the temperatures of the experimental AMR and there is a ≈ 2 K difference at the hot end and a 4 – 5 K difference at the cold end. The differences are due to the fact that the model does not predict the temperature span obtained by the experimental AMR. The above results show that the model can accurately predict the temperature profiles in the AMR and this further validates the AMR model.

5.5 Summary and final remarks

This section has shown that the AMR model is able to predict both the trends and the performance of the experimental AMR. The results showed an excellent qualitative and a good quantitative agreement between the experiment and the model. These results verify that the model includes all the important physical phenomena occurring inside the AMR. This means that the model can be used to predict the behavior of the AMR for a range of operating conditions. The good agreement between the experiments and the model is even more impressive when the differences between the experimental AMR and the model is taken into consideration. The model uses a MCE based on a theoretical model and all other properties are estimated from standard references and there is a difference in how the magnetic field is applied in the model and in the experimental AMR. In addition, the model does not include heat losses to the surroundings which can explain some the quantitative discrepancies between the model and the experimental results. As the model is further developed to properly address these issues, the model should be able to obtain results even

closer to those of the experimental AMR. From the experimental comparison in this chapter it was concluded that the developed AMR model has been validated and is able to provide a good estimates of both the behavior and the performance of an AMR. These results show that the model is a useful tool which may be used for both analysis, design and optimization of the experimental AMR.

Chapter 6

Comparison of the 2-D AMR model to a 1-D AMR model

This chapter compares the 2-D model developed in this thesis to a 1-D AMR model developed by Engelbrecht et al. [60, 47]. The initial results presented in Section 4.1 showed significant temperature differences in the heat transfer fluid when modelling a parallel-plate regenerator. This justified the use of a 2-D model. However, the subsequent results also showed that the solution time of the 2-D model can be more than 250 hours. The comparison of the two models are used to analyze whether the additional complexity and long solution time required by the 2-D model is necessary for accurate simulation of an AMR with a parallel-plate regenerator.

The study presented in this chapter was performed in collaboration with Kurt Engelbrecht from the University of Wisconsin-Madison. The work and results described in this chapter will be published in a paper currently under preparation.

6.1 Description of the one-dimensional AMR model

The 1-D model solves the coupled one-dimensional partial differential equations of the space and time dependent temperature profiles in the regenerator and in the fluid to determine the performance of the AMR. The model is flexible with respect to operating conditions, geometry, and material and fluid properties. The modelling geometry of the 1-D model is simpler compared to the 2-D model and only considers the regenerator material and the fluid within the fluid channels. The equipment external to the regenerator bed (e.g., pistons, heat exchangers, magnet, etc.) is not explicitly modeled; their effect on the regenerator is implemented through an imposed time variation of the mass flow of the fluid and the magnetic field as well as through the boundary conditions. The 1-D model assumes uniform fluid flow in the regenerator and assumes that the fluid and solid temperature varies only in the x-direction (flow direction). The 1-D model uses established correlations to determine important regenerator parameters such as the Nusselt number and the friction factor and accounts for temperature gradients in the solid by scaling the Nusselt number.

6.1.1 Governing equations

The temperatures of the regenerator and fluid are derived from the energy balances on the fluid and regenerator. After some simplification, the energy balance on the fluid is [47]:

$$\dot{m}_f c_{p,f} \frac{\partial T_f}{\partial x} + \frac{Nu k_f a_s}{D_h} A_c (T_f - T_s) + \rho_f A_c \epsilon c_{p,f} \frac{\partial T_f}{\partial t} - k_{\text{disp}} A_c \frac{\partial^2 T_f}{\partial x^2} = \left| \frac{f_f \dot{m}^3}{2 \rho_f^2 A_c^2 D_h} \right|. \quad (6.1)$$

From left to right, the terms represent the enthalpy change of the flow, heat transfer from the fluid to the regenerator material, energy storage, energy transfer due to axial dispersion associated with mixing in the fluid, and viscous dissipation. The governing equation for the regenerator is [47]:

$$\frac{Nu k_f a_s}{D_h} (T_f - T_s) + k_{\text{eff}} \frac{\partial^2 T_s}{\partial x^2} = (1 - \epsilon) \rho_s T_s \left(\frac{\partial s}{\partial \mu_0 H} \right)_T \frac{\partial \mu_0 H}{\partial t} + (1 - \epsilon) \rho_s c_{p,s} \frac{\partial T_s}{\partial t} \quad (6.2)$$

where the terms represent heat transfer from the fluid to the regenerator, non-dispersive or static axial conduction through the composite of the regenerator and fluid, magnetic work transfer, and energy storage. In Eq. 6.2, k_{eff} is the effective static thermal conductivity of the regenerator/fluid composite, k_{disp} is an effective conductivity which accounts for the axial dispersion caused by eddy mixing of the fluid in the direction of flow. The overall size of the AMR is specified according to its length (L_{reg}) and cross-sectional area (A_c).

The magnetic work in the 1-D model is time dependent and during the refrigeration cycle the magnetic field is ramped from 0 T to 1 T over a period of time. The magnetic field field is aligned with the cycle period so that the middle of the total period of time where the magnetic field is applied, occurs at the middle of the magnetization and cold blow periods. This is illustrated on Fig. 6.1 which shows the variation of the mass flow and the magnetic field used in the 1-D model. As boundary conditions, the 1-D model assume no heat loss to

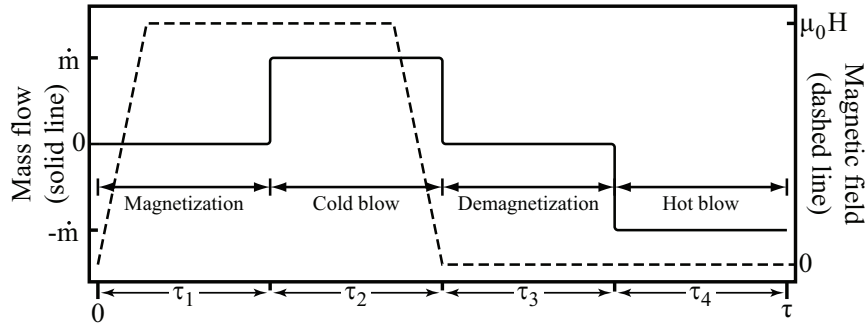


Figure 6.1: The variation of the mass flow (solid line) and the magnetic field (dashed line) in the 1-D model during the AMR refrigeration cycle.

the surroundings and the edges of both the fluid and solid ($x=0$, and $x=L_{\text{reg}}$) are adiabatic except during the blow periods where the fluid enters the regenerator with the prescribed temperature of the CHEX and the HHEX (T_C and T_H).

6.1.2 Heat transfer between the regenerator and the fluid

The regenerator on the 1-D model is characterized by the hydraulic diameter (D_h), the porosity (ϵ), and the specific surface area (a_s), which can be determined from the dimensions of the regenerator, which is shown schematically on Fig. 6.2. The regenerator is assumed to consist of N plates and channels.

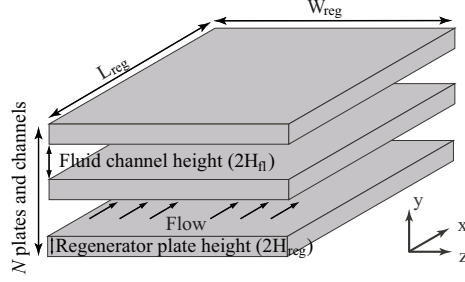


Figure 6.2: Definition of the dimensions of AMR regenerator used to determine the hydraulic diameter, the porosity and the specific surface area.

The porosity is defined as the flow area (i.e. the channel area) divided by the total area

$$\epsilon = \frac{N \times 2H_{fl}}{N \times 2 \cdot (H_{fl} + H_{reg})} \Rightarrow \frac{H_{fl}}{H_{fl} + H_{reg}} \quad (6.3)$$

The hydraulic diameter is defined as four times the flow area divided by the total wetted perimeter of the fluid channels [44]:

$$D_h = \frac{4 \times N \times 2H_{fl} \times W_{reg}}{N \times 2(2H_{fl} + W_{reg})} \Rightarrow \frac{4H_{fl}}{1 + 2\frac{H_{fl}}{W_{reg}}} \quad (6.4)$$

It can be assumed that $W_{reg} \gg H_{fl}$ such that $H_{fl}/W_{reg} \approx 0$ leading to the following definition of D_h which corresponds to the hydraulic diameter for infinite parallel plates [54]:

$$D_H = 4H_{fl} \quad (6.5)$$

The specific heat transfer area is the total heat transfer area of the regenerator divided by the volume of the regenerator

$$a_s = \frac{2 \times N \times W_{reg} \times L_{reg}}{N \times 2(H_{fl} + H_{reg}) \times W_{reg} \times L_{reg}} \Rightarrow \frac{1}{H_{fl} + H_{reg}} \quad (6.6)$$

The heat transfer between the regenerator and fluid is determined from the Nusselt number. Here the theoretical correlation suggested by Nickolay and Martin [66] for heat transfer between parallel plates is used to determine the local Nusselt number as

$$Nu_x = Nu - \frac{1}{3} \left(\frac{Nu_2 - b}{Nu} \right)^{n-1} Nu_2 \quad (6.7)$$

where Gz is the Graetz number and Nu is the average Nusselt number defined as

$$Nu = (Nu_1^n + b^n + (Nu_2 + b)^n)^{1/n}, \quad (6.8)$$

with

$$Nu_1 = 7.541 \quad Nu_2 = 1.841Gz^{1/3} \quad b = 0 \quad n = 3.592. \quad (6.9)$$

The Graetz number is determined as:

$$Gz = \frac{D_h}{x} Re Pr. \quad (6.10)$$

where x is positive in direction of the flow. Re is the Reynolds number and Pr is the Prandtl number defined as

$$Re = \frac{\bar{U} D_h \rho_f}{\mu_f} \quad Pr = \frac{c_{p,f} \mu_f}{k_f} \quad (6.11)$$

where \bar{U} is the mean velocity of the fluid. The friction factor for flow between parallel plates is equal to [44]:

$$f = \frac{96}{Re}. \quad (6.12)$$

6.1.3 Solution method of the 1-D model

The solution for the cyclical steady fluid and regenerator temperatures from Eq. 6.1 and Eq. 6.2 are obtained on a equidistant numerical grid that extends from 0 to L_{reg} in space and from 0 to τ in time. These equations are linearized and discretized using finite differences, and the resulting set of algebraic equations is solved. The numerical model starts from an initial temperature distribution and takes implicit time steps forward in time until the cyclical steady state has been achieved. To determine when the cyclical steady-state has been reached, the absolute value of the change in total energy of the regenerator and the fluid between the beginning and end of each cycle is evaluated and this quantity is compared to the maximum change in the total energy of the bed and fluid during the cycle. The cyclical steady state is assumed to be achieved when this dimensionless value of the absolute change in energy of the regenerator from cycle to cycle is less than a specified tolerance.

6.1.4 Evaluation of the AMR performance

The two models evaluate the performance in much the same way. The 1-D model determines the heat absorbed from the cooling load from the net convective heat flux exiting from the cold end of the regenerator during the hot blow. The rejected heat is likewise determined from the net convective heat flux exiting from the hot end of the regenerator during the cold blow. The magnetic work at steady-state operation is determined from the 1st law of thermodynamics as the difference between the rejected heat and the refrigeration capacity since the 1-D model assumes no heat loss from the AMR enclosure. The COP is then determined as the refrigeration capacity divided by the magnetic work.

6.1.5 Key modeling differences between the 1-D and the 2-D model

Both models were developed to simulate an AMR but the approaches used by the two models are quite different. Aside from the difference in dimensions, the list below show central differences between the two models

- The 2-D model assumes an instantaneous and adiabatic magnetization and demagnetization, where the 1-D model uses a ramped magnetic field and treats the magnetic work as an energy input to the governing equations of the regenerator material. In other words, the 2-D model uses ΔT_{ad} of the magnetocaloric material directly, while the 1-D model uses Δs_M . The two methods result in slightly different refrigeration cycles. There is heat transfer to the fluid during magnetization and demagnetization in the 1-D model, while the processes are adiabatic in the 2-D model. The consequences of this difference are described below in more detail.
- The 1-D model calculates the cooling capacity from the heat flux into the CHEX, while the 2-D model includes a CHEX and assumes very good contact with the cooling load. This difference is assumed to be of minor consequence.
- The 1-D model assumes constant temperatures at the CHEX and HHEX, but the 2-D model includes the two heat exchangers in the model geometry and accounts for temperature gradients in both. This difference between the models are minimized by choosing a modelling geometry for the 2-D model which emulate the boundary conditions of the 1-D model. This is described in more detail later in this chapter.

6.2 Implementation of the two models

The regenerator geometry used for the initial comparison between the 1-D and 2-D models consists of flat plates of Gd with a length of 50 mm in the flow direction and the flow channel of the 2-D model was 130 mm long with 20 mm heat exchangers. In the 2-D model the gap between the regenerator and the heat exchangers was reduced to 1 mm. This was done in order to emulate the boundary conditions of the 1-D model more accurately by placing the heat exchangers closer to the regenerator. This placement helps to ensure that the fluid flowing into the regenerator is very close to the temperature of the heat exchangers. This change was necessary since the results in Chapter 4 showed that the temperature of the fluid in the gap can be different from the temperature in the heat exchangers. The height of the both the regenerator plates and the flow channels were varied during the comparison of the two models as explained in the following analysis. The material properties of the different parts of the AMR geometry are equal to those shown in Table 3.2 and the WDS model was used to implement magnetocaloric properties of the regenerator material in both models. The properties used by the 1-D model to implement the MCE are the specific entropy as a function of the temperature and the magnetic field which is used to derive the specific heat capacity and Δs_M . Table 6.1 shows the AMR cycle parameters used in the comparison except for the mass flow, which is varied during the comparison of the two models. The

Table 6.1: Process parameters for the AMR cycle

Parameter	Value	Unit
Cycle period (τ)	6	s
τ_1 and τ_3	0.6	s
τ_2 and τ_4	2.4	s
Ramp period	0.3	s
$\mu_0 H$	1	T
Stroke	3.5	cm

refrigeration cycle was kept at 6 s, but τ_1 to τ_4 were changed such that τ_1/τ_2 was equal to 1/4 in order to obtain a better AMR performance.

6.2.1 The implementation of the magnetocaloric effect in the two models

A notable difference between the two models is the implementation of the magnetic work of the MCE. In the 2-D model the MCE is implemented using ΔT_{ad} whereas the 1-D model implements the MCE on the basis of Δs_M . To test whether the two methods of implementing the MCE yield the same results, a comparison was performed where the 1-D model was used to simulate an adiabatic magnetization. The resulting temperature change in the regenerator was compared to the ΔT_{ad} directly obtained from the WDS model. To simulate an adiabatic magnetization with the 1-D model, the Nusselt number and the axial conduction in the regenerator were both set to zero. The ramping of the magnetic field from 0 T to 1 T was implemented with 50 to 200 time steps to determine the required number of time steps to obtain sufficient accuracy. The results are shown on Fig. 6.3.

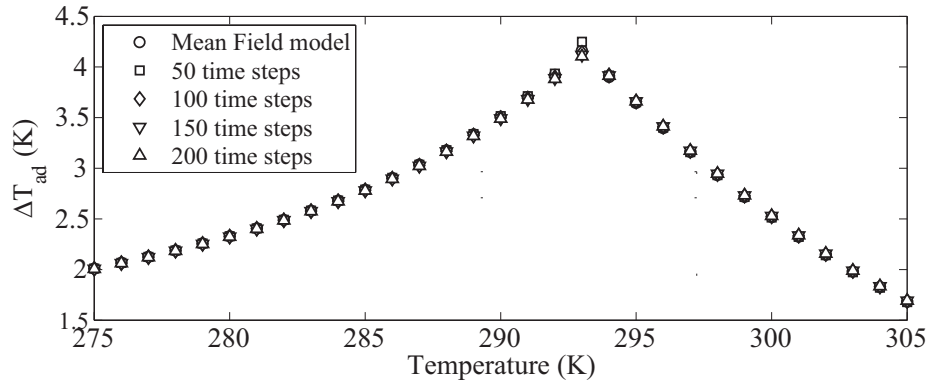


Figure 6.3: Simulation of the adiabatic magnetization with the 1-D model.

As the figure shows, determination of ΔT_{ad} using Δs_M results in almost identical values to those directly obtained with the WDS model. In addition, the ΔT_{ad} determined with the 1-D model is not sensitive to the number of time steps used during the ramping of the

magnetic field. Increasing the number of time steps from 50 to 200 decreases the maximum error between the 1-D model and the WDS model from 0.09 K to 0.06 K. In the following comparison, 100 time steps were used during the ramping of the magnetic field. This requires a total of 2000 time steps for a total cycle since the ramping period of 0.3 s is equal to 1/20 of the total cycle time. Since the MCE is highly temperature dependent the 1-D model was also subjected to a grid sensitivity analysis where the amount of grid points was varied from 30 to 120. The results are shown on Fig. 6.4, which shows that both the refrigeration capacity and the COP of the 1-D model are not very sensitive to the number of grid points. In the following comparison 90 grid points were therefore used.

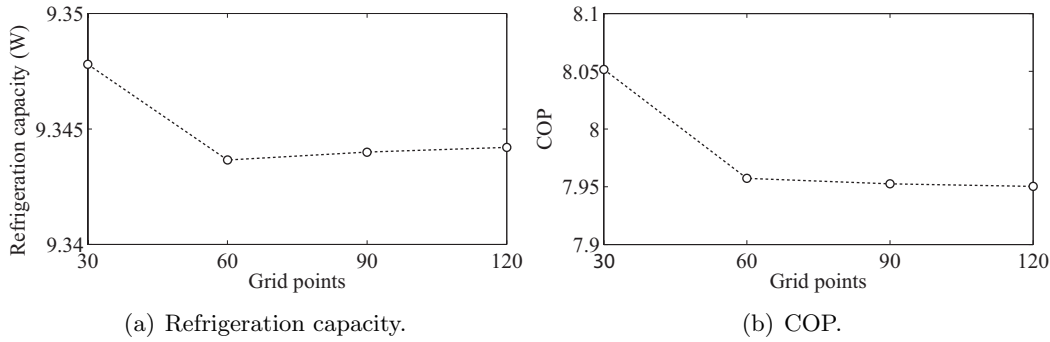


Figure 6.4: The results of the grid sensitivity analysis (2000 time steps).

6.3 Comparison of the 1-D and 2-D model

Important model outputs are the refrigeration capacity, the rejected heat, the magnetic work, the COP and the temperature profiles at various points in the cycle. These four parameters are used to compare the two models. To properly compare the temperature profiles from the two models, the results of the temperature in the fluid channel from the 2-D model were averaged in the direction perpendicular to flow. The average fluid temperature profile of the 2-D model then corresponds to the bulk fluid temperature obtained from the 1-D model. The difference between the 1-D and the 2-D models is determined by the root mean square error (RMSE) between the temperatures profiles in the fluid channel predicted by the two models. The RMSE is determined as

$$RMSE = \sqrt{\frac{1}{N} \sum_{i=1}^N (T_{2D,i} - T_{1D,i})^2} \quad (6.13)$$

where T_{2D} is the temperature profile obtained from the 2-D model at the i^{th} grid point, T_{1D} is the temperature profile obtained from the 1-D model at the i^{th} grid point and N is the number of grid points. Since the two models do not have an equal number of grid points, interpolation was used to perform the comparison. The RMSE is determined before the

cold and the hot blow periods. The temperature profiles at these points of the refrigeration cycle were chosen for the comparison, because they are important for the performance of the AMR. The temperature profile before the hot blow affects the refrigeration capacity and similarly, the temperature profile before the cold blow affects the heat rejected to the surroundings. The 1-D and 2-D models are compared for plate thicknesses going from 0.1 mm to 3 mm with a constant porosity of 33.3%, i.e. the fluid channel height was half the value of the plate thickness. The mass flow was varied such that the utilization was kept constant (by assuming a constant specific heat capacity of Gd) at approximately 0.27 with the corresponding mass flow of 7.27 gs^{-1} for a 1 mm plate. This utilization corresponds to the optimal value for water determined in Chapter 4. To determine the mass flow for the other thicknesses of the regenerator plate the above mass flow was scaled linearly. In general, it would be expected the two models should have better agreement as the plate thickness and the height of the fluid channel are decreased. This is because the smaller distances in in plate and channel results in smaller temperature gradients ($\partial T/\partial y$) and should approach 1-D conditions.

6.4 Results and discussion

6.4.1 Refrigeration capacity, rejected heat and the COP

The results of the comparison are presented in terms of the refrigeration capacity on Fig. 6.5(a), the rejected heat on Fig. 6.5(b), the magnetic work (difference between the rejected heat and the refrigeration capacity) on Fig. 6.5(c) and the COP on Fig. 6.5(d). The two models obtain virtually identical results for the refrigeration capacity and the rejected heat for plate thicknesses of 1 mm and below. Above 1 mm plate thickness the curves of the two models start to diverge and in absolute terms the 1-D model consistently underestimates both the refrigeration capacity and the rejected heat compared to the 2-D model. Notice that the positive values of the refrigeration capacity and the negative values of the rejected heat have no physical meaning and should only be viewed as a numerical comparison. These results agree with the hypothesis that thinner regenerator plates and narrow fluid channels results in better agreement between the two models. In addition, the two models have similar trends on both Fig. 6.5(a) and Fig. 6.5(b), which show a parabolic shape of both the refrigeration capacity and the rejected heat. Both peak at 1 mm plate thickness and start to decline for both decreasing and increasing plate thickness. The reduced performance for decreasing plate thickness can be explained by that that the thinner plate produce less cooling because a less amount of material is available and the refrigeration capacity should decrease to zero at a infinitesimal regenerator plate thickness. For increasing plate thickness, the decrease in performance is probably due to increasing temperature differences between the plates and fluid since the increased plate thickness and fluid channel height limits the heat transfer. Compared to the 2-D model, the 1-D model overestimates the magnetic work for plate thicknesses above 1 mm and underestimates the magnetic work for plate below 1 mm in thickness. There does not seem to be a better agreement of the magnetic work as the plates get thinner although the difference of the magnetic work estimate by the two models is lowest for thin plates. This also affects the determination of the COP. Fig. 6.5(d)

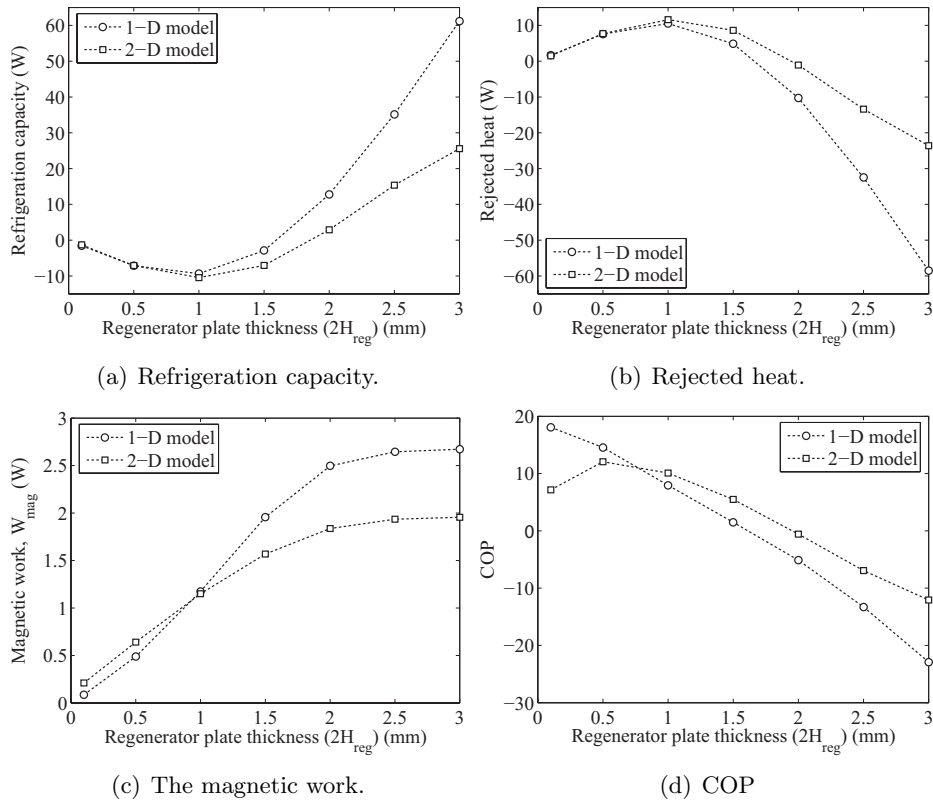


Figure 6.5: Comparison between the 1-D and 2-D models in terms of (a) refrigeration capacity, (b) rejected heat, (c) the magnetic work and (d) the COP.

shows that the two models obtain similar values of the COP for regenerator plates between 0.5 mm and 1.5 mm and difference increases as the thickness of the regenerator plates is increased. Again the negative COP's have no physical meaning. The trends of the COP of the two models are also different. The 2-D model shows a parabolic shape the COP which has a maximum at a plate thickness of 0.5 mm. Compared to this, the 1-D predicts an increasing COP for a decreasing plate thickness and Fig. 6.5(d) shows no optimum of the COP. These results can be explained from the results of the magnetic work. Since the magnetic work of the 1-D model decreases below that of the 2-D model for plates thinner than 1 mm but the the refrigeration capacity of the two models are almost equal, the COP of the 1-D must be higher compared to the 2-D model. However, the results are somewhat surprising given the good agreement of the refrigeration capacity and the rejected heat. But since the magnetic work is a derived value determined from the refrigeration capacity and the rejected heat, small differences between the two models can lead to large differences in both the magnetic work and the COP. The magnetic work and COP may therefore not be the best method of comparing the two models although they are both important parameters for an AMR. To obtain a better evaluation of the COP, an alternative method

of determining the magnetic work should be used. This could for example be by using Δs_M to implement the MCE in the 2-D model as well. The magnetic work could then be determined explicitly in both models by integrating the source term that represent the magnetic work. This was not done in the present study due to time limitations, but should be performed in future studies in order to compared the two model directly.

6.4.2 Fluid temperature profiles, RMSE and temperature gradients

Fig. 6.7 shows the actual fluid temperatures profile for the 1-D model and the 2-D model before the cold and hot blow for selected values of the plate thickness. The average RMSE between the temperature profiles in the fluid channel of the two models before the blow periods is showed on Fig. 6.6(a). On Fig. 6.7 there is an excellent agreement between

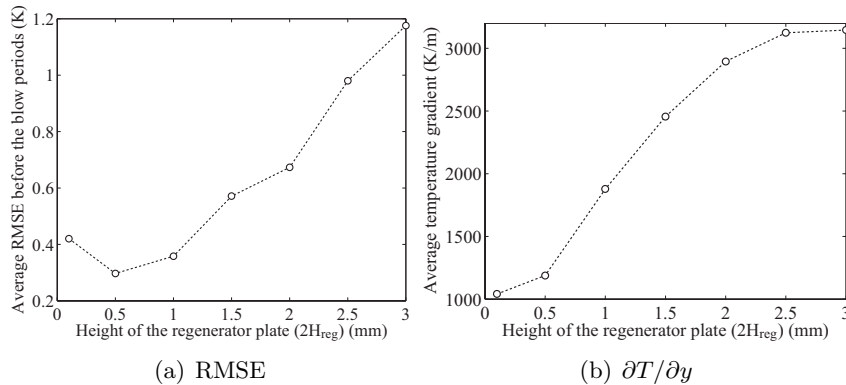


Figure 6.6: Comparison between the 1- D and 2-D models in terms of (a) the RMSE and (b) the average $\partial T/\partial y$ in the fluid.

the temperature profiles predicted by the two models for plate thicknesses of 1 mm or less with virtually no difference between the temperature profiles determined. This is an important result since the AMR will often be designed with thin plates and fluid channels, because of the increased specific heat transfer are such a regenerator geometry results in. There is also a good qualitative and quantitative agreement since the two models predict the same shape of temperature profile. The 2-D model predicts a higher and lower temperatures in the fluid, before the cold blow and the hot blow, respectively, for an increasing thickness of the regenerator plate. There is a good agreement between the two models near the regenerator edges which is because the fluid entering the regenerator from the heat exchangers has an almost constant temperature. Fig. 6.6(a) shows that the RMSE before the blow periods decreases with decreasing plate thickness except for a plate thickness of 0.1 mm, which show a slight increase on the RMSE. The RMSE shows that thinner plates and flow channels do not unanimously result in a better agreement between a 1-D and 2-D model. This partly contradicts the hypothesis that thinner plates and flow channels yield better agreement between the two models due to smaller values of $\partial T/\partial y$. To analyze the influence temperature gradients further, Fig. 6.6(b) shows the average $\partial T/\partial y$ in the

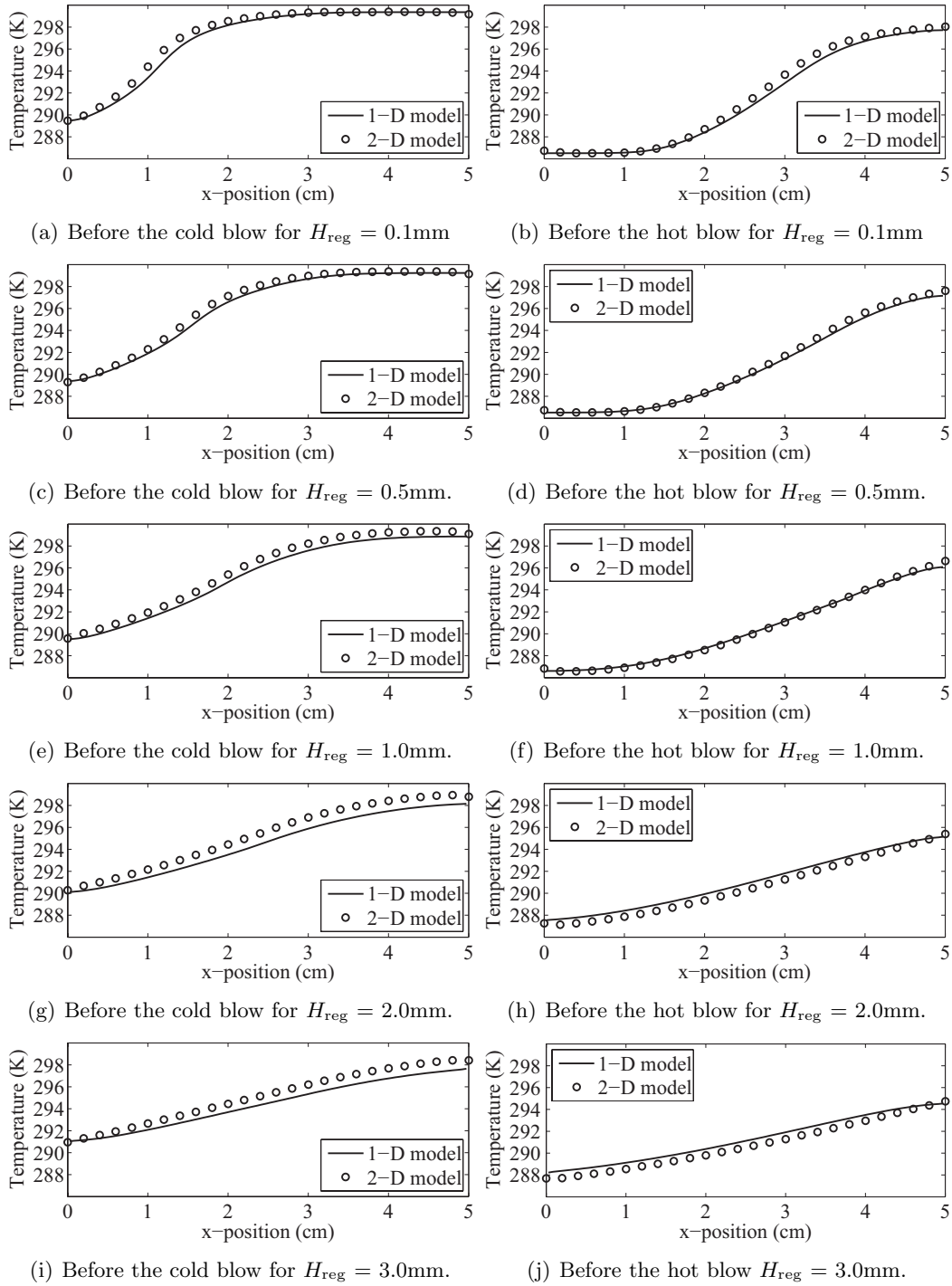


Figure 6.7: The average temperature profiles in the fluid predicted by the two models before the cold blow (left column) and the hot blow (right column).

fluid during the AMR. The fluid channel will exhibit the largest temperature differences because of the low thermal conductivity of the fluid compared to the regenerator material and because of the influence of convection. The fluid channel will therefore also have the largest values of $\partial T/\partial y$. Fig. 6.6(b) shows that $\partial T/\partial y$ decreases as the plate thickness and flow channel height becomes thinner as expected. However, when the results of $\partial T/\partial y$ is compared to Fig. 6.6(a), the results show that smaller values of $\partial T/\partial y$ do not result seem to results in a better agreement between a 1-D and a 2-D model. However, $\partial T/\partial y$ decreases with decreasing plate thickness where there is also good agreement between the models of both the refrigeration capacity and the rejected heat. This indicates that the increase in the RMSE at a regenerator plate of 0.1 mm is not representative of a good agreement between the two models. The is probably because the RMSE is only determined at two specific two points during the refrigeration cycle, which may not show a general tendency for the AMR models. However, it is not possible to determine an average RMSE for the entire refrigeration cycle since the two models have different behavior during the magnetization and demagnetization. The MCE should be implemented using identical methods in order to compared the two models more fairly using the RMSE, but this could not be done in this study due to time limitations.

6.5 Summary and final remarks

This chapter compared the results of a 1-D and a 2-D numerical model of an AMR with a parallel-plate regenerator. An important difference between the two models were that the 1-D model implements the MCE on the basis of the Δs_M where 2-D model uses the ΔT_{ad} . However, a comparison showed virtually no difference between the two methods of implementing the MCE. Using Δs_M to implement the MCE in future versions of the 2-D model would allow the MCE to be time dependent. This would make the 2-D model able to more accurately simulate the physical conditions in the experimental AMR. Furthermore, by implementing the MCE as a heat source allows the magnetic work to determined directly. The 1-D model and 2-D model were configured to obtain as identical operating conditions as possible and the two models were compared for a range of plate thicknesses. The comparison showed excellent agreement between the refrigeration capacity and the rejected heat for regenerator plates of 1 mm or less. However, the corresponding COP only showed a reasonable agreement for regenerator plates between 0.5 mm to 1 mm. In addition, the predicted trend of the COP of the two models was different. The reason for the bad agreement of the COP was attributed to differences in the magnetic work predicted by the two models. Small differences in the magnetic work between the two models results in large differences in the COP. The temperature profile in the fluid channel determined by the two models were also compared. The temperature profiles of the two models had the same shape but there were differences in the temperatures predicted by the two models as the thickness of the plates and channel increased. But for plates below 1 mm there was excellent agreement between the fluid temperature profiles, which coincided with the best agreement of the refrigeration capacity and the rejected heat between the two models. These results support the hypothesis that thinner plates and fluid channel have smaller temperature gradients

in the y-direction and therefore more 1-D like conditions. The RMSE between the models increased slightly as the plate thickness was decreased below approximately 0.5 mm where there was a minimum in the RMSE. This result did not agree with the hypotheses that thinner plates and flow channels have smaller temperature gradients. However, a subsequent analysis of the 2-D model showed that the temperature gradients does indeed decrease for decreasing plate thicknesses. Since there was good agreement between the refrigeration capacity and the rejected heat between the two models, it was concluded that the RMSE at a single point during the refrigeration cycle it not representative of a fit between the models. From the results in this chapter it was concluded that both a 1-D model and a 2-D model can both accurately predict both the refrigeration capacity and the temperature profiles in an AMR with a parallel-plate regenerator provided that the plate and the fluid channel are sufficiently small. However, for thicker plates and fluid channels, or where it is suspected that the temperature gradient in the y-direction is significant, a 2-D model must be used to accurately simulate the performance of an AMR with a regenerator of parallel plates.

This page was intentionally left blank.

Chapter 7

Conclusion

The purpose of the work described in this thesis was to develop a mathematical model of a laboratory-scale, reciprocating AMR, which was constructed at Risø National Laboratory. The experimental AMR operates around room temperature and is based on a regenerator made of a stack of parallel plates separated by channels of heat transfer fluid. The time-dependent, two-dimensional model solves the momentum and continuity equations for the flow in the fluid channels and the coupled energy equations for the heat transfer in the regenerator material and in the fluid channels. The AMR model was implemented in a commercial software package using the standard implementations of the governing equations. During the development of the AMR model it was necessary to develop specialized methods to model the special characteristics of a reciprocating AMR. This made extensive, additional verification of the AMR model necessary. The main conclusions from the verification was (1) that the methods used to model the AMR works correctly, (2) that the AMR model has energy conservation, (3) that the solution of the model is almost independent of both the applied grid and time step and finally (4) that the solution is independent of the initial conditions. These results indicate that the model can correctly simulate an reciprocating AMR and that the model can be used to study both transient and steady-state phenomena. The performance of the AMR can be evaluated in terms of the no-load temperature span, the refrigeration capacity, and the COP. In addition, the model can be used to determine the temperature profiles in both the regenerator material and the fluid channel. The model requires a solution time from 50 to 250 hours on a 3.2 GHz Pentium 4 (Prescott) processor. To perform parameter studies, the AMR model was implemented on a computer cluster, which allows multiple simulations to be performed simultaneously.

The results from the AMR model showed significant temperature differences in the heat transfer fluid for certain operating conditions, which show that two-dimensional methods are justified when an AMR based on a parallel-plate regenerator is modelled. The AMR model was validated by comparing the results of the model to measurement obtained from the experimental AMR at several different operating conditions. The validation showed excellent agreement between the behavior of the AMR model and the behavior of the experiments as well as a good agreement between the measured and the simulated temperature spans of the AMR. In addition, the AMR model could accurately predict the optimal operating conditions of the AMR. These results indicate that the model includes all the

important physical phenomena occurring inside the AMR and that the model can be used to simulate the behavior of the AMR for a wide range of operating conditions.

The developed AMR model is flexible and was used to perform several parametric studies of the AMR performance. The results from these studies showed that the AMR model is able to determine the performance of an AMR for a wide range of boundary conditions, choice of materials, operating conditions and regenerator geometries. The parameter studies demonstrated the capabilities of the AMR model and obtained results directly applicable to the experimental AMR but did not focus on explaining the general behavior of the AMR. However, a number of results from the parameter studies seemed to apply more generally for AMRs. For example, the results indicated that there should be no perpendicular temperature differences between the regenerator and the fluid after the blow periods in order to obtain the optimal AMR performance. Therefore, the AMR should initially be designed with good heat transfer characteristics. A high heat transfer may be obtained by using a heat transfer fluid with a high thermal conductivity, using narrow fluid channels between the regenerator plates and having a sufficiently long refrigeration cycle. During the initial parameter studies the best AMR performance was obtained with narrow fluid channels. However, thin channels require that the pistons displace more fluid in order to obtain the maximum temperature span. In some cases the pistons displaced all of the fluid inside the regenerator channels, and the AMR should therefore be designed to accommodate high flow rates. The piston strokes, which obtained the best performance for different heights of the fluid channel, all resulted in the same utilization. For example, using water as the heat transfer fluid gave an optimal utilization of 0.27. This is a very important result, since it indicates the existence of a global optimum of the utilization, which can be used to simplify the design and optimization of an AMR. The results from the parameter studies also showed that the blow periods of the AMR refrigeration cycle should start almost immediately after the magnetization and demagnetization, and that introducing a "wait" period after the application or removal of the magnetic field is not required. Based on the the initial parameter studies it was concluded that it is possible to obtain a significant temperature span in an AMR with a parallel-plate regenerator and an 1 T magnetic field. However, there is still room for improvements, and future work should concentrate on more detailed studies, both to understand the fundamental behavior of the AMR, but also to increase the performance to a level where the AMR is comparable to conventional refrigeration.

From results presented in this thesis it was concluded that the developed AMR model may be used to perform accurate and reliable simulations of an reciprocating AMR operating at room temperature. The AMR model can therefore be used for analysis, design and optimization of the experimental AMR. The model will be an important tool in the development of magnetic refrigeration into an efficient, environmentally friendly and commercial alternative to conventional refrigeration.

Bibliography

- [1] C. Zimm, A. Jastrab, A. Sternberg, V. Pecharsky, K. Gschneider, M. Osborne, and I. Anderson, “Description and performance of a near-room temperature magnetic refrigerator,” *Advances in Cryogenic Engineering* **43**, 1759–1766 (1998).
- [2] B. Yu, Q. Gao, B. Zhang, X. Meng, and Z. Chen, “Review on research of room temperature magnetic refrigeration,” *International Journal of Refrigeration-Revue Internationale du Froid* **26**, 622–636 (Sept. 2003).
- [3] S. Russek and C. Zimm, “Potential for cost effective magnetocaloric air conditioning systems,” *International Journal of Refrigeration* doi:10.1016/j.ijrefrig.2006.07.019, – (2006).
- [4] V. K. Pecharsky and J. K. A. Gschneidner, “Advanced magnetocaloric materials: What does the future hold?,” *International Journal of Refrigeration* **29**, 1239–1249 (2006).
- [5] E. Warburg, “Magnetische untersuchungen,” *Ann.Phys.(Leipzig)* **13**, 141–164 (1881).
- [6] P. Weiss and A. Piccard, “A new thermomagnetic phenomenon,” *Comptes Rendus Hebdomadaires des Seances de l’Academie des Sciences* **166**, 352–354 (1918).
- [7] W. Giaque and D. MacDougall, “Production of temperatures below 1 degrees K by adiabatic demagnetisation of gadolinium sulphate,” *Journal of the American Chemical Society* **57**, 1175–1185 (1935).
- [8] P. Debye, “Einige bemerkungen zur magnetisierung bei tiefer temperatur,” *Annalen der Physik* **81**, 1154–1160 (1926).
- [9] W. Giaque, “A thermodynamic treatment of certain magnetic effects. a proposed method of producing temperatures considerably below 1 degrees absolute,” *Journal of the American Chemical Society* **49**, 1864–1870 (1927).
- [10] S. Collins and F. Zimmerman, “Cyclic adiabatic demagnetization,” *Physical Review* **90**(5), 991–992 (1953).
- [11] C. Heer, C. Barnes, and J. Daunt, “The design and operation of a magnetic refrigerator for maintaining temperatures below 1-Degrees-K,” *Review of Scientific Instruments* **25**(11), 1088–1098 (1954).

- [12] G. Brown, "Magnetic heat pumping near room temperature," *Journal of Alloys and Compounds* **47**, 3673–3680 (Aug. 1976).
- [13] J. Barclay and W. Steyert, "Active magnetic regenerator," (1982).
- [14] V. Pecharsky and K. Gschneidner, "Giant magnetocaloric effect in $\text{Gd}_5(\text{Si}_2\text{Ge}_2)$," *Physical Review Letters* **78**, 4494–4497 (June 1997).
- [15] K. Gschneidner, V. Pecharsky, and A. Tsokol, "Recent developments in magnetocaloric materials," *Reports on Progress in Physics* **68**, 1479–1539 (June 2005).
- [16] T. F. Petersen, N. Pryds, A. Smith, S. Linderoth, S. Jeppesen, and H.-J. H. Knudsen, "Magnetic refrigeration and the magnetocaloric effect," in *Proceedings of the Danske K oledage conference in Odense, Denmark*, (2006).
- [17] A. Tishin and Y. Spichkin, *The Magnetocaloric Effect and its Applications*, Institute of Physics Publishing, Temple Back, Bristol BS1 6BE, UK (2003).
- [18] E. Bruck, "Developments in magnetocaloric refrigeration," *Journal of Physics D-Applied Physics* **38**, R381–R391 (Dec. 2005).
- [19] V. Pecharsky and K. Gschneidner, "Magnetocaloric effect and magnetic refrigeration," *Journal of Magnetism and Magnetic Materials* **200**, 44–56 (Oct. 1999).
- [20] A. Tishin, "Magnetocaloric effect in the vicinity of magnetic phase transition," *Journal of Magnetism and Magnetic Materials* **184**, 62–66 (Apr. 1998).
- [21] A. Kitanovski and P. W. Egolf, "Thermodynamics of magnetic refrigeration," *International journal of refrigeration* **29**, 3–12 (2005).
- [22] A. Morrish, *The Physical Principles of Magnetism*, John Wiley & Sons, Inc. (1965).
- [23] N. Ashcroft and N. Mermin, *Solid State Physics*, Saunders College Publishing, London (1976).
- [24] A. R. Dinesen, *Magnetocaloric and magnetoresistive properties of $\text{La}_{0.67}\text{Ca}_{0.33-x}\text{Sr}_x\text{MnO}_3$* . PhD thesis, Technical University of Denmark (2004).
- [25] A. Dinesen, S. Linderoth, and S. Morup, "Direct and indirect measurement of the magnetocaloric effect in a $\text{La}_{0.6}\text{Ca}_{0.4}\text{MnO}_3$ ceramic perovskite," *Journal of Magnetism and Magnetic Materials* **253**, 28–34 (Dec. 2002).
- [26] Y. Bingfeng, Z. Yan, G. Qiang, and Y. Dexi, "Research on performance of regenerative room temperature magnetic refrigeration cycle," *International Journal of Refrigeration* **29**, 1348–1357 (2006).
- [27] E. Schroeder, G. Green, and J. Chafe, "Performance predictions of a magnetocaloric refrigerator using a finite element model," *Advances in Cryogenic Engineering* **35**, 1149–1155 (1990).

- [28] R. Nielsen, “Det magnetiske køleskab,” *Risønyt* **1**, 26–28 (2003).
- [29] J. Barclay, “The theory of an active magnetic regenerativ refrigerator,” *NASA STI/Recon Technical Report N* **83**, 34087 (1982).
- [30] R. M. V. C. G. Chen, F.C.; Murphy, “Thermodynamic analysis of four magnetic heat-pump cycles,” *Journal of Engineering for Gas Turbines and Power* **114**, 715–720 (1992).
- [31] J. Barclay and S. Sarangi, “Selection of regenerator geometry for magnetic refrigerator applications,” *American Society of Mechanical Engineers* **dec**, 9–13 (1984).
- [32] A. DeGregoria, “Modeling the active magnetic regenerator,” *Advances in Cryogenic Engineering* **37**, 867–873 (1991).
- [33] V. K. Pecharsky and J. Gschneidner, “Magnetocaloric effect and magnetic refrigeration,” *Journal of Magnetism and Magnetic Materials* **200**, 44–56 (Oct. 1999).
- [34] M. Richard, A. Rowe, and R. Chahine, “Magnetic refrigeration: Single and multi-material active magnetic regenerator experiments,” *Journal of Applied Physics* **95**, 2146–2150 (Feb. 2004).
- [35] J. Hall, C. Reid, I. Spearing, and J. Barclay, “Thermodynamic considerations for the design of active magnetic regenerative refrigerators,” *Advances in Cryogenic Engineering* **41b**, 1653–1664 (1996).
- [36] T. E. W. Schumann, “Heat transfer: A liquid flowing through a porous prism,” *J. Franklin Institute* **208**, 405–416 (1929).
- [37] J. Hu and J. Xiao, “New method for analysis of active magnetic regenerator in magnetic refrigeration at room-temperature,” *Cryogenics* **35**, 101–104 (Feb. 1995).
- [38] F. Allab, A. Kedous-Lebouc, J. Fournier, and J. Yonnet, “Numerical modeling for active magnetic regenerative refrigeration,” *Ieee Transactions on Magnetics* **41**, 3757–3759 (Oct. 2005).
- [39] F. Shir, C. Mavriplis, L. Bennett, and E. la Torre, “Analysis of room temperature magnetic regenerative refrigeration,” *International Journal of Refrigeration-Revue Internationale du Froid* **28**, 616–627 (June 2005).
- [40] A. Sarlah, A. Kitanovski, A. Poredos, P. Egolf, O. Sari, F. Gendre, and C. H. Besson, “Static and rotating active magnetic regenerators with porous heat exchangers for magnetic cooling,” *International Journal of Refrigeration* **29**, 1332–1339 (2006).
- [41] K. Matsumoto and T. Hashimoto, “Thermodynamic analysis of magnetically active regenerator from 30 to 70-K with a Brayton-like cycle,” *Cryogenics* **30**, 840–845 (Oct. 1990).

- [42] A. Smäili and R. Chahine, “Thermodynamic investigations of optimum active magnetic regenerators,” *Cryogenics* **38**, 247–252 (Feb. 1998).
- [43] P. Li, M. Gong, G. Yao, and J. Wu, “A practical model for analysis of active magnetic regenerative refrigerators for room temperature applications,” *International Journal of Refrigeration* **29**, 1259–1266 (2006).
- [44] F. P. Incropera and D. P. DeWitt, *Introduction to Heat transfer 3rd ed.*, vol. 3rd, John Wiley & Sons (1996).
- [45] F. Shir, L. Bennett, E. la Torre, C. Mavriplis, and R. Shull, “Transient response in magnetocaloric regeneration,” *Ieee Transactions on Magnetics* **41**, 2129–2133 (June 2005).
- [46] K. Engelbrecht, G. Nellis, and S. Klein, “The effect of internal temperature gradients on regenerator matrix performance,” *Journal of Heat Transfer* **12**, 1060–1069 (2006).
- [47] K. Engelbrecht, G. Nellis, and S. Klein, “Comparing modelling predictions to experimental data for active magnetic regeneration refrigeration systems,” in *Proceedings of the Second IIF-IIR International Conference on Magnetic Refrigeration at Room Temperature Portoroz, Slovenia, 11-12 April 2007*, (2007).
- [48] J. Dikeos, A. Rowe, and A. Tura, “Numerical analysis of an active magnetic regenerator (AMR) refrigeration cycle,” *AIP Conference Proceedings* **823**, 993–1000 (2006).
- [49] K. L. Engelbrecht, G. F. Nellis, S. A. Klein, and C. B. Zimm, “Recent developments in room temperature active magnetic regenerative refrigeration,” *HVAC&R research* **13**, 525–542 (2007).
- [50] COMSOL, *Comsol Multiphysics User’s guide Version 3.2b*. COMSOL AB, COMSOL AB, Chalmers Teknikpark 412 88 Göteborg, 3.2 ed. (2005).
- [51] A. M. Rowe and J. A. Barclay, “Ideal magnetocaloric effect for active magnetic regenerators,” *Journal of applied physics* **93** (2003).
- [52] T. Petersen, N. Pryds, A. Smith, J. Hattel, H. Schmidt, and H. J. Knudsen, “Two-dimensional mathematical model of a reciprocating room-temperature active magnetic regenerator,” *Accepted by the International Journal of Refrigeration*, – (2007).
- [53] F. M. White, *Viscous Fluid flow*, McGraw-Hill, Inc. (1991).
- [54] R. W. Fox and A. T. McDonald, *Introduction to Fluid Mechanics*, John Wiley and Sons, Inc. (1994).
- [55] D. Lide, *CRC Handbook of chemistry and physics*, vol. 85, CRC Press (2004).
- [56] S. Klein, “EES - engineering equation solver,” (2004).
- [57] COMSOL, *Comsol Multiphysics Model Library guide*. COMSOL AB, COMSOL AB Chalmers Teknikpark 412 88 Göteborg, 3.2b ed. (2005).

- [58] J. H. Ferziger and M. Peric, *Computational Methods for Fluid Dynamics*, Springer, 3 ed. (2002).
- [59] T. F. Petersen, N. Pryds, and A. Smith, "Using a linux cluster for parallel simulations of an active magnetic regenerator refrigerator," in *Proceedings of the 2006 Nordic COMSOL Conference in Lyngby, Denmark*, L. Gregersen, ed., **1**, COMSOL A/S, COMSOL A/S (2006).
- [60] K. Engelbrecht, G. Nellis, and S. Klein, "A numerical model of an active magnetic regenerator refrigeration system," Tech. Rep. ARTI-21CR/612-10075, University of Wisconsin-Madison (2005).
- [61] T. F. Petersen, N. Pryds, and A. Smith, "A numerical analysis of a reciprocating active magnetic regenerator with a parallel-plate regenerator geometry," in *Proceedings of the Second IIF-IIR International Conference on Magnetic Refrigeration at Room Temperature in Portoroz, Slovenia*, **1**(1) (2007).
- [62] S. Andersen, *Numerical Simulation of Cyclic Thermodynamic Processes*. PhD thesis, Technical University of Denmark, Dept. of Mech. Eng., Energy (2005).
- [63] X. Bohigas, E. Molins, A. Roig, J. Tejada, and X. Zhang, "Room-temperature magnetic refrigerator using permanent magnets," *Ieee Transactions on Magnetics* **36**, 538–544 (May 2000).
- [64] Å. Melinder, ed., *Thermophysical Properties of Liquid Secondary Refrigerants*, International Institute of Refrigeration - Institut International du Froid (1997).
- [65] "Olive oil information and products." <http://www.oliveoilsource.com/> (2007).
- [66] M. Nickolay and H. Martin, "Improved approximation for the nusselt number for hydrodynamically developed laminar flow between parallel plates," *International Journal of Heat and Mass Transfer* **45**, 3263–3266 (2002).
- [67] S. Y. Dankov and A. M. Tishin, "Magnetic phase transitions and the magnetothermal properties of gadolinium," *Physical review B* **57**, 3478–3490 (1998).

This page was intentionally left blank.

Appendix A

The Weiss, Debye and Sommerfeld model of the magnetocaloric effect

The specific heat capacity, the specific entropy, Δs_M and ΔT_{ad} of a magnetocaloric material can be calculated using a combination of the Weiss mean field theory, the Debye theory and the Sommerfeld theory. The combined model is in this thesis referred to as the WDS model.

A.1 The Weiss mean field theory

The Weiss molecular mean field model is a well-established approximate theory for the magnetism of solids which is treated in e.g. [22]. The classical relations are here adapted to the SI formulation using the approach described by Dinesen [24]. The magnetic contribution to the total specific heat capacity is determined as

$$c_{\text{mag}} = -\mu_0 H \frac{\partial \sigma}{\partial T} - \frac{1}{2} N_{\text{int}} \frac{(\partial \sigma)^2}{\partial T}. \quad (\text{A.1})$$

where N_{int} is the mean field constant defined as

$$N_{\text{int}} = \frac{3k_B \Theta_C}{N_s g^2 \mu_B^2 J(J+1)}, \quad (\text{A.2})$$

where k_B is the Boltzmann constant, Θ_C is the Curie temperature, N_s is the number of magnetic spins per unit mass, g the Landé factor, J the total angular momentum in units of \hbar and μ_B is the Bohr magneton. The specific magnetization can be determined as:

$$\sigma = N_s g J \mu_B B_J(\chi). \quad (\text{A.3})$$

where $B_J(\chi)$ is the Brillouin function defined as

$$B_J(\chi) = \frac{2J+1}{2J} \coth\left(\frac{2J+1}{2J}\chi\right) - \frac{1}{2J} \coth\left(\frac{1}{2J}\chi\right). \quad (\text{A.4})$$

and χ is defined as

$$\chi = \frac{gJ\mu_B\mu_0H}{k_bT} + \frac{3\theta_C J}{T(J+1)} B_J(\chi). \quad (\text{A.5})$$

Equation A.4 and Eq. A.5 must be solved simultaneously by iteration. The magnetic part of the total specific entropy can either be determined by integrating Eq. A.1 or directly as [17]

$$s_{\text{mag}} = \frac{N_A}{M} k_B \left(\ln \left(\frac{\sinh(\frac{2J+1}{2J}\chi)}{\sinh(\frac{\chi}{2J})} \right) - \chi B_J(\chi) \right), \quad (\text{A.6})$$

where N_A is Avogadro's number and M is the molar mass of the material. Equation A.6 can be used to determine Δs_M directly but also ΔT_{ad} as

$$s_{\text{mag}}(H_f, T + \Delta T_{\text{ad}}) = s_{\text{mag}}(H_i, T), \quad (\text{A.7})$$

where H_i, H_f are the initial and final magnetic field, respectively.

A.2 The Debye theory

The lattice contribution to the total specific heat capacity is determined as [23]

$$c_{\text{lat}} = 9k_B \frac{N_A}{M} \left(\frac{T}{\Theta_D} \right)^3 \int_0^{\Theta_D/T} \frac{x^4 e^x}{(e^x - 1)^2} dx, \quad (\text{A.8})$$

where Θ_D is the Debye temperature which is a material dependent constant. The lattice part of the total specific entropy part is determined as [17]

$$s_{\text{lat}} = k_B \frac{N_A}{M} \left(-3 \ln \left(1 - e^{-\frac{\Theta_D}{T}} \right) + 12 \left(\frac{T}{\Theta_D} \right)^3 \int_0^{\Theta_D/T} \frac{x^3 dx}{(e^x - 1)} \right) \quad (\text{A.9})$$

A.3 The Sommerfeld theory

The Sommerfeld model is based on the theory for the thermal properties of conduction electrons which are treated in more detail in ref. [23]. The electronic part of the total specific heat capacity can be calculated as

$$c_{\text{ele}} = \gamma_e T, \quad (\text{A.10})$$

where γ_e is the Sommerfeld constant. The electronic contribution to the total specific entropy is determined as

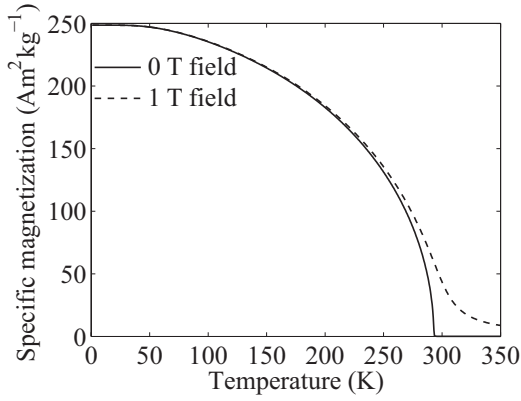
$$s_{\text{ele}} = \int \frac{c_{\text{ele}}}{T} dT = \gamma_e T \quad (\text{A.11})$$

A.4 The magnetocaloric effect of gadolinium

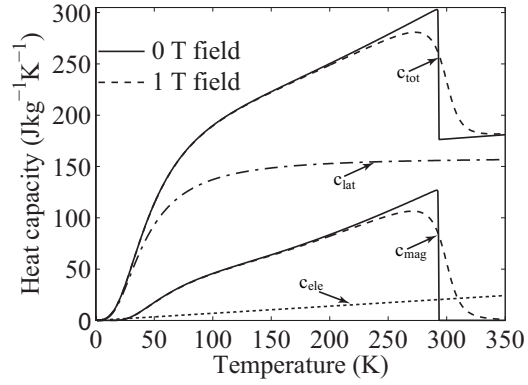
As an example the WDS model is used to model the MCE of gadolinium (Gd) using the material properties shown in Table A.1. The resulting specific magnetization, specific heat capacity, Δs_M and ΔT_{ad} of Gd are shown in Fig. A.1.

Table A.1: Magnetic properties of Gd used to determine the magnetocaloric effect using the WDS model [55, 17].

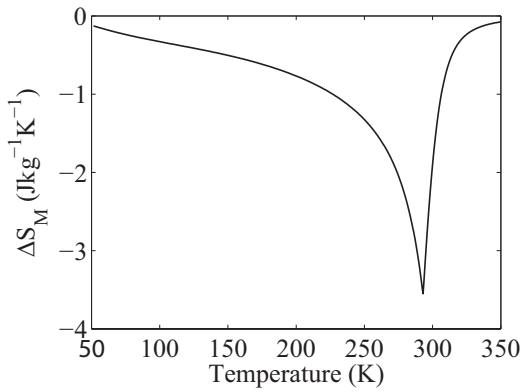
Parameter	Value	Unit
M	0.157	kgmol^{-1}
Θ_D	169	K
Θ_C	293	K
γ_e	$6.93 \cdot 10^{-2}$	$\text{Jkg}^{-1}\text{K}^{-2}$
g_J	2	-
J	3.5	\hbar



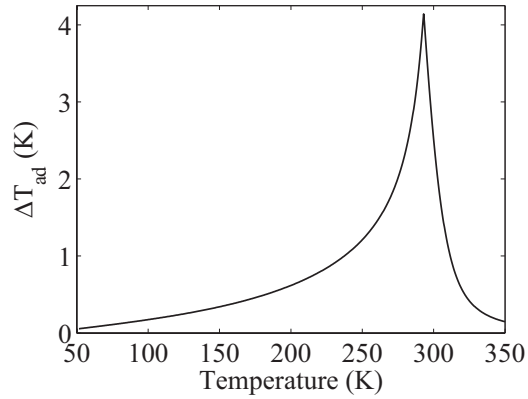
(a) Specific magnetization of Gd at 0 and 1 T



(b) Specific heat capacity of Gd.



(c) Δs_M of Gd.



(d) ΔT_{ad} of Gd.

Figure A.1: The specific magnetization, specific heat capacity, Δs_M and ΔT_{ad} for Gd in magnetic fields of 0 T and 1 T.

The WDS model is commonly used to model magnetocaloric material and gives reasonable estimates of the specific heat capacity, Δs_M and ΔT_{ad} . Fig. A.2 shows a comparison of the experimental and Weiss model data for the magnetic specific heat capacity of Gd [67]. Fig. A.3 shows a similar comparison of the specific heat capacity, Δs_M and ΔT_{ad} of the magnetocaloric ceramic $\text{La}_{0.67}\text{Ca}_{0.275}\text{Sr}_{0.055}\text{MnO}_3$, which is another candidate for room temperature magnetic refrigeration [24]. The comparison for Gd shows a reasonable good agreement between the experimental and the theoretical specific heat capacity. The agreement is less good near the Curie temperature where the mean field model fail to model the anomaly at the magnetic phase transition adequately. For $\text{La}_{0.67}\text{Ca}_{0.275}\text{Sr}_{0.055}\text{MnO}_3$ there is a good agreements between the experimental and theoretical maximum values for both Δs_M and ΔT_{ad} . The WDS model overestimates the MCE below the Curie temperature, but in general there is a good agreement between experiment and the WDS model. Below the Curie temperature the WDS model consistently underestimates the experimental values of the specific heat capacity of $\text{La}_{0.67}\text{Ca}_{0.275}\text{Sr}_{0.055}\text{MnO}_3$. However, far above or below the Curie temperature there is good agreement between experiment and model similar to the results obtained for Gd. These results shows that the WDS model is able to provide good qualitative results of the behavior of the MCE and a reasonable estimate of the qualitative values of the MCE.

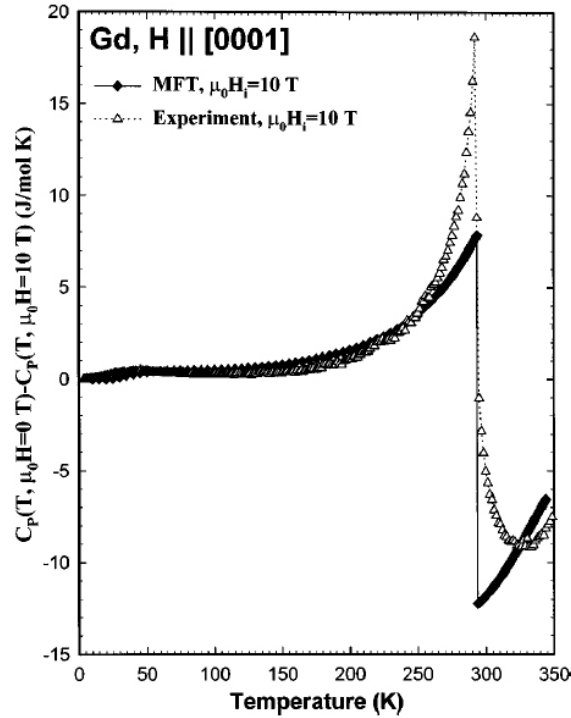


Figure A.2: The experimental values of the magnetic specific heat capacity of Gd compared to the theoretical values determined by the Weiss mean field model [67]. The specific heat capacity is shown as the difference between the zero-field specific heat capacity and the specific heat capacity at 10 T.

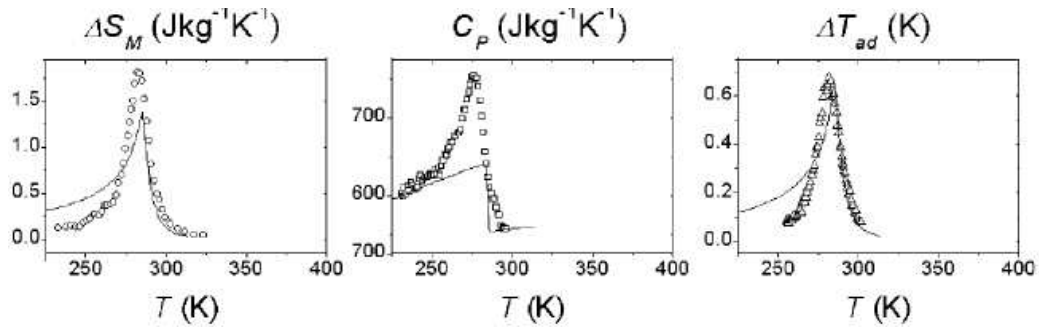


Figure A.3: The experimental values of the specific heat capacity, Δs_M and ΔT_{ad} of $\text{La}_{0.67}\text{Ca}_{0.275}\text{Sr}_{0.055}\text{CaMnO}_3$ and the theoretical values determined the WDS model. The data was obtained from ref. [24].

This page was intentionally left blank.

Appendix B

Further verification of the AMR model

This appendix contains additional tests used to verify the AMR model which were not included in Chapter 3. The first part describes how the coordinate transformation method is implemented in COMSOL. The second part contains a test of the dimensionless formulation of the momentum and continuity equations used to determine the flow in the fluid channel. The third and final part explains how the cyclical steady-state of the flow in the fluid channel is obtained.

B.1 Implementation and test of the coordinate transformation method

The coordinate transformation method is used to model the displacement of the fluid in the regenerator channels by the reciprocating pistons and was developed specifically for the AMR model. The theory of the coordinate transformation method is explained in Section 3.3. This section explains the practical implementation of the coordinate transformation method in COMSOL by using the method to perform a basic verification test. The basic test is performed without moving boundaries but it is subsequently explained how to introduce the moving boundaries.

B.1.1 Basic test of the coordinate transformation method

The basic test of the coordinate transformation method is performed by using the method to solve a heat transfer problem with an analytical solution and then comparing the two solutions. Fig. B.1 shows two semi-infinite solids in contact along a common boundary and with different initial temperatures. This transient heat transfer problem is well-known in the literature and the temperature in the two solids as a function of position and time can be determined as [44]:

$$\frac{T(x, t) - T_s}{T_i - T_s} = \operatorname{erf}\left(\frac{x}{2\sqrt{\alpha t}}\right), \quad (\text{B.1})$$

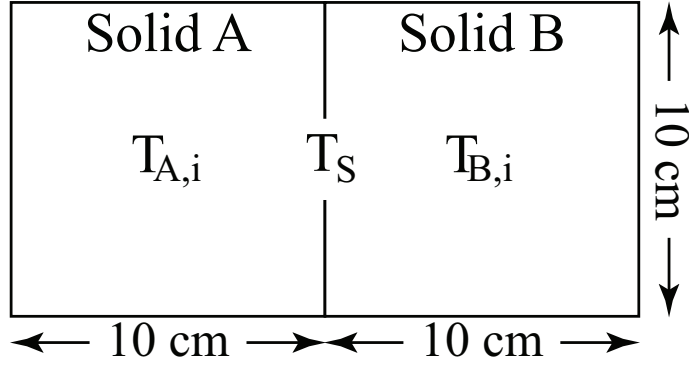


Figure B.1: Illustration of heat transfer problem of two semi-infinite solids, which is used to test the coordinate transformation method.

where T_i is the initial temperature of the solid, T_s is the common temperature of the boundary between the solids and α is the thermal diffusivity defined as:

$$\alpha = \frac{k}{\rho c_p}. \quad (\text{B.2})$$

The temperature of the boundary, T_s , between the solids is determined as [44]:

$$T_s = \frac{(\sqrt{k\rho c_p})_A T_{A,i} + (\sqrt{k\rho c_p})_B T_{B,i}}{(\sqrt{k\rho c_p})_A + (\sqrt{k\rho c_p})_B} \quad (\text{B.3})$$

In order to compare the analytical solution to the numerical solution, the final time of the simulation must be short enough to ensure that the temperature at the left and right boundary of solid A and solid B remains constant at T_A and T_B , respectively. This ensures that the assumption of a semi-infinite solid is valid in the numerical model. Each solid was 10 cm \times 10 cm large and solid A was made of copper while solid B was made of iron. The material properties and initial temperatures of the two solids are shown in Table B.1.

Table B.1: Material properties and initial temperature of solid A and solid B [50].

Solid	Material	c_p	k ($\text{Jkg}^{-1}\text{K}^{-1}$)	ρ ($\text{Wm}^{-1}\text{K}^{-1}$)	α (kgm^{-3})	T_i (m^2s^{-1})	K
A	Copper		385	400	8700	$1.19 \cdot 10^{-4}$	0
B	Iron		440	76.2	7870	$2.20 \cdot 10^{-5}$	10

B.1.2 Implementation of the coordinate transformation method in Comsol Multiphysics

This section describes the practical implementation of the coordinate transformation method in COMSOL. The description is mostly based on screen shots and this section can therefore

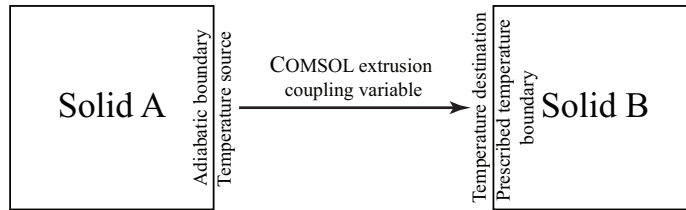


Figure B.2: Approach used to implement the coordinate transformation method in COMSOL to solve the heat transfer problem in Fig. B.1.

also be used as a basis of implementing the coordinate transformation method for other applications. The method used to implement the coordinate transformation method in COMSOL and obtain the correct boundary conditions is called "extrusion coupling variables". The extrusion coupling variables makes variables from a source available at a non-local destination and also allows a coordinate transformation of said variables. To implement the method in COMSOL, the two domains are modelled separately and the temperatures of the interfacing boundaries are coupled together with the extrusion coupling variables. The source for the extrusion coupling variables is the temperature of the right boundary of solid A and the destination is the left boundary of solid B. The boundary condition for the source boundary is adiabatic conditions and the boundary condition for the destination boundary is a prescribed temperature (the temperature of the right boundary of solid A). A schematic of the approach is shown on Fig. B.2 It may seem counterintuitive to use an adiabatic condition on the right boundary of solid A. However, the extrusion coupling variables "override" the adiabatic setting and the result is that the physically correct heat flow is obtained. However, this only works when the weak formulation of the FE method is used. If any of the other formulations available in COMSOL is used to implement the extrusion coupling variables the method will not work. In these cases there will only be heat flow from solid A to solid B as the adiabatic condition is enforced by COMSOL. Fig. B.3 shows how the temperatures of the source and destination boundaries are defined in COMSOL to apply the extrusion coupling variables. In the "source transformation" box in Fig. B.3(a) and "destination transformation" box Fig. B.3(b) "y" is entered in both, as it is the temperatures in the y-direction of the solids that must be mapped with the extrusion coupling variables. Fig. B.4 show the application of the boundary conditions for the source and destinations boundaries. The temperature profile in the two solids was solved with a grid of 10×10 elements ($N_x \times N_y$) and the time step was 0.01 s. The model was solved with an absolute tolerance of 1×10^{-3} K and a relative tolerance of 10^{-10} .

B.1.3 Results

Fig. B.5 shows the solutions of obtained with the coordinate transformation method and the analytical solution. Since there are virtually no differences between the two solutions, it was concluded that the coordinate transformation method is conceptually valid.

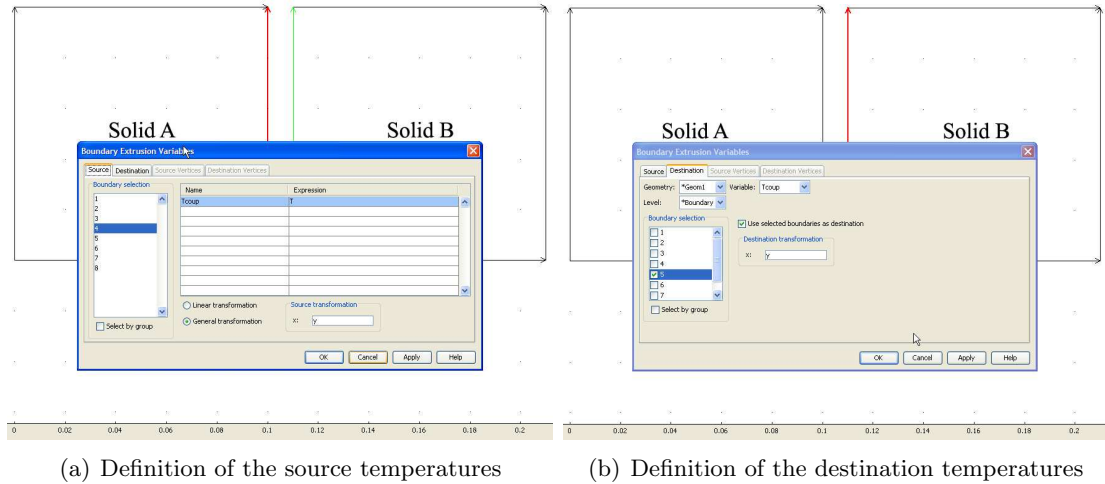


Figure B.3: Application of the source and destination temperature for the extrusion coupling variables used to implement the coordinate transformation method in COMSOL. The temperatures at the source boundary is referred to as "Tcoup" in the two figures.

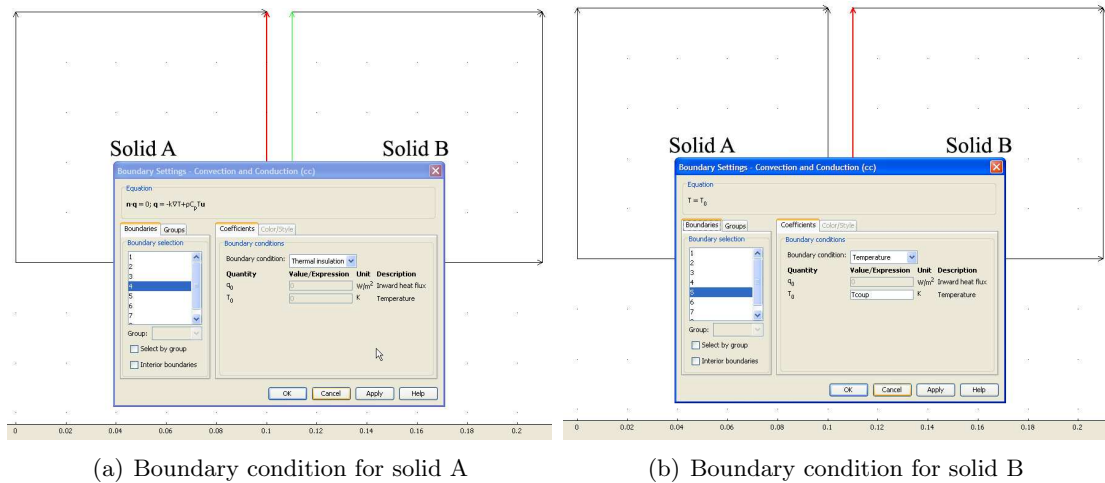


Figure B.4: Application of the boundary conditions of solid A and solid B to implement the coordinate transformation method.

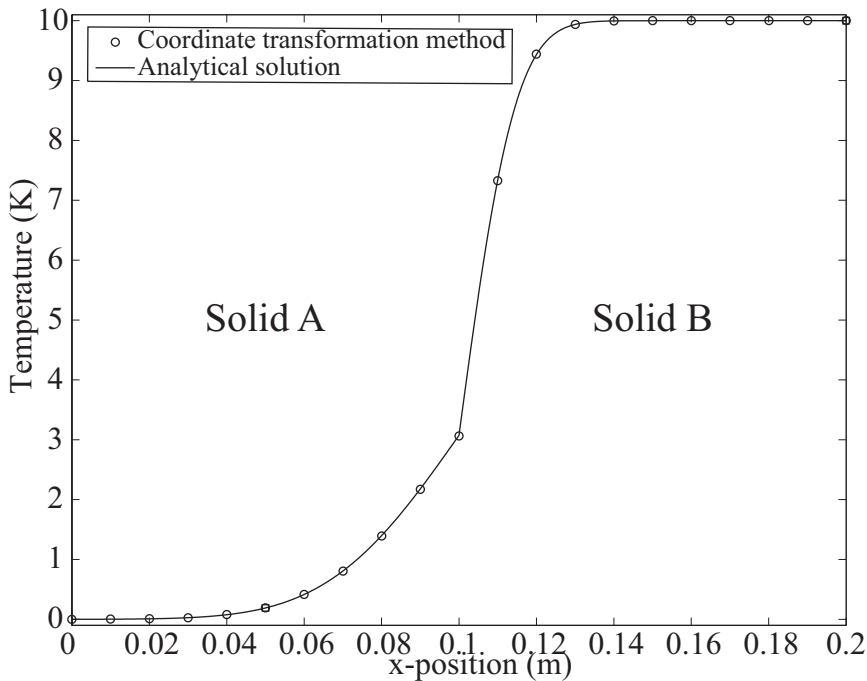


Figure B.5: Comparison of the solutions of the heat transfer in two semi-infinite solids using the coordinate transformation method and the analytical solution. The two solids had an initial temperature difference of 10 K and the figure shows the temperature profile after three (3) seconds. As the figure shows, the temperature of right and left boundary of solid A and B, respectively, remains equal to the initial temperatures.

B.1.4 Implementation of moving boundaries using the coordinate transformation method

Using the coordinate transformation method to model moving boundaries is done by adding a transformation of the coordinates when defining the extrusion coupling variables. The modelling geometry of the AMR is used to describe how to model moving boundaries with the coordinate transformation method. The AMR modelling geometry is shown on Fig. B.6 and the source for the extrusion coupling variables is the upper boundary of the fluid channel and the destinations are the lower boundary of the CHEX, regenerator plate and the HHEX. The boundary conditions are again adiabatic conditions for the source boundary and a prescribed temperature at the destination boundaries. With these setting the extrusion coupling variable method results in heat transfer between the solids (CHEX, regenerator plate and HHEX) and the fluid where there is overlap between the domains. However, on the parts of the interface of the fluid with no contact between the fluid domain and the solid domains the fluid have an adiabatic conditions. As described in Chapter 3, the coordinate transformation method can be used to model the moving boundaries of the

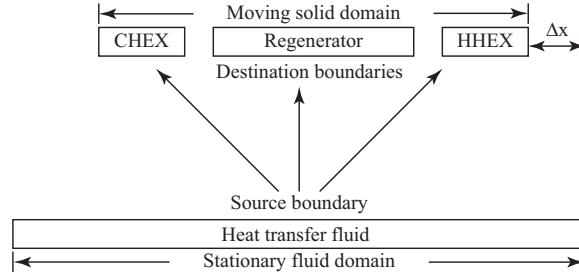


Figure B.6: Definition of the source and destination boundaries for the extrusion coupling variables to implement the coordinate transformation method when modelling moving boundaries.

AMR model by expressing the temperatures of the solid/fluid boundary as

$$T_s(x_f - \Delta x) = T_f(x_f). \quad (\text{B.4})$$

where Δx is the displacement of the pistons during the cycle. Fig. B.6 shows how the extrusion coupling variables are used to implement the coordinate transformation method with a relative movement between the solid and fluid domains. In the definition of the destination for the extrusion coupling variables, Eq. B.4 is implemented using the "destination transformation" box as shown on Fig. B.8(b). Fig. B.7 shows the results from the verification test of the coordinate transformation method first presented in the Chapter 3. The figures show how the solid domain changes position during the cycle. From these figures it was concluded that the coordinate transformation method is a valid approach to modelling a relative movement between the solid and the fluid.

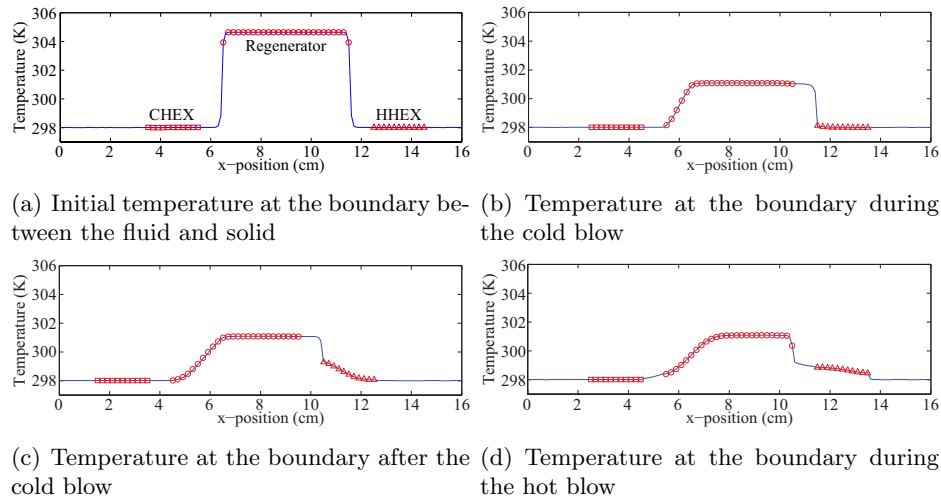
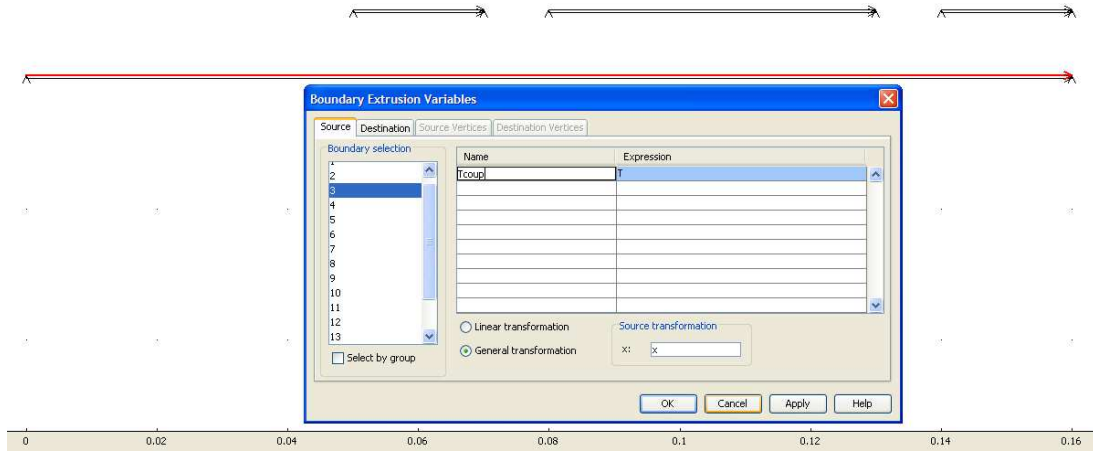
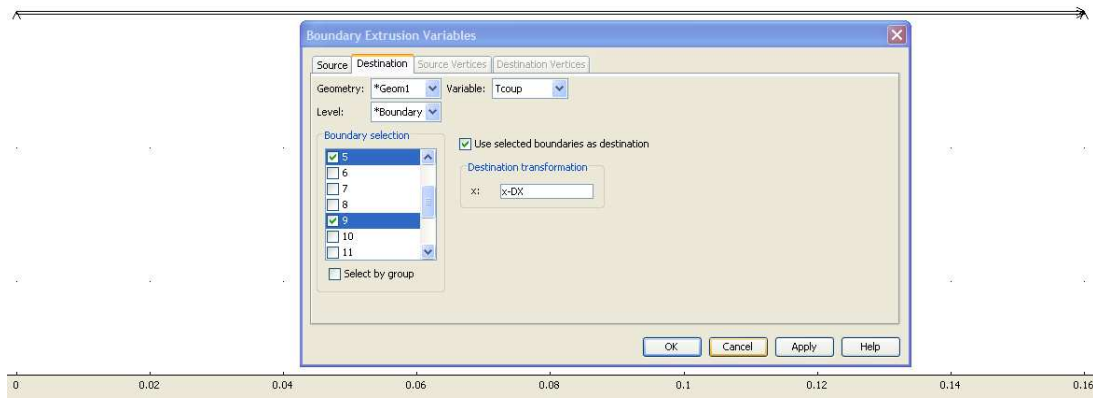


Figure B.7: Results of using the coordinate transformation method to simulate moving boundaries.



(a) Source definition



(b) Destination definition

Figure B.8: Definition of the source and destination of the extrusion coupling variables COMSOL to implement the coordinate transformation method to solve moving boundaries in the AMR model.

B.2 Verification of the solution of the fluid channel flow

In Section 3.4 the velocity profiles in the fluid was determined with a dimensionless formulations of the momentum and continuity equations. However, the dimensionless equations used in this theses are different from the standard dimensionless momentum and continuity equations used in fluid mechanics [53]. The difference is that the period of the AMR refrigeration cycle is used as the characteristic time scale to make the time dimensionless. It is more conventional to base the characteristic time scale on the characteristic velocity and the characteristic length. A test was therefore performed to determine whether the dimensionless and the non-dimensional formulations of the momentum and continuity equations results in identical solutions of the velocity field. Both formulations were used to determine the velocity profile in the x-direction of the fluid channels. The results were compared both by graphically and by determination of the correlation coefficient (R^2). Fig. B.9 shows the velocity profiles at selected times during the cold blow (upper row) and hot blow (lower row). In all cases the two formulations of the momentum and continuity equations yields virtually identical velocity profiles and the R^2 values of unity also show the equality of the two different solutions. It was therefore concluded that the dimensionless momentum and continuity equations determine the flow in the fluid channels correctly.

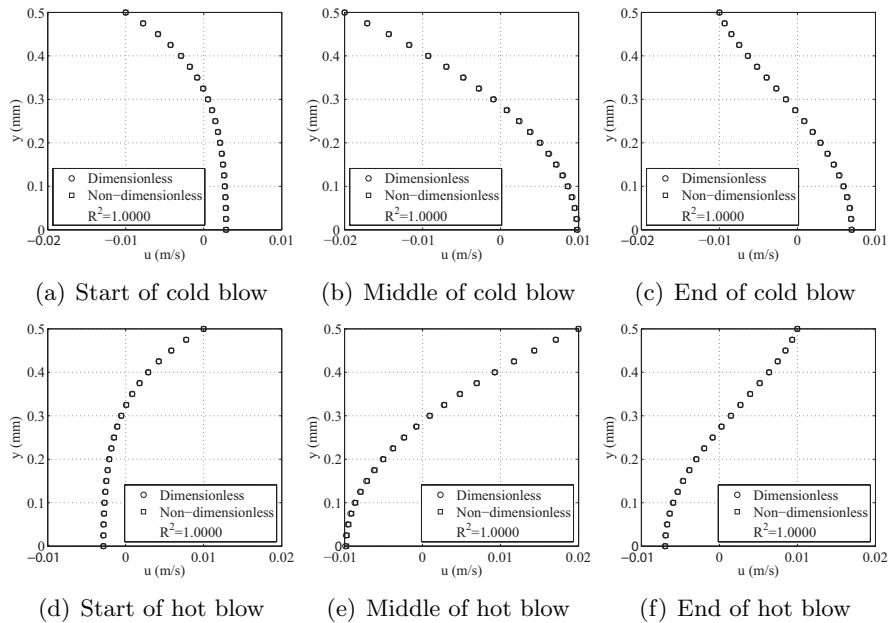


Figure B.9: Comparison between the non-dimensional and a dimensional solution of the flow in the fluid channel. The velocity at the solid-fluid interface ($y=0.5$ mm) is negative during the cold blow where the regenerator and heat exchangers moves from right to left. This corresponds to the pistons moving the fluid from the CHEX toward the HHEX. During the hot blow the regenerator and heat exchangers move from left to right and the velocity at the interface is in this case positive.

B.3 Determination of the cyclical steady-state of the flow in the fluid channel

The flow in the fluid channel reaches a cyclical steady-state within a single cycle. This is illustrated on Fig. B.10 and which shows the dimensionless velocity profile in the x-direction during the cold blow of the first cycle. Because the flow is either staving or stopping the flow the max velocity is only 50% of the piston velocity. After a dimensionless time period of $1/60$, Fig. B.10(c) shows that there is zero movement in the flow. Because of the symmetry of the AMR cycle these results also apply during the hot blow period. Therefore the initial conditions for either blow periods will always be zero velocity in the fluid. This means that the velocity profiles does not change from cycle to cycle as long as the dimensionless value of τ_2 is above $1/60$. This condition applies for ratios of τ_1/τ_2 below 29 and the maximum τ_1/τ_2 used in this thesis is 8. Fig. B.10(d) shows a comparison of the velocity profiles at the start the cold blow during cycle 1 and 2, which shows no difference in the velocity profile. These results will obviously change with the Reynolds number, but the time period for obtaining zero movement in the fluid is so low, that the assumption of a cyclical steady-state within a single cycle will almost certainly apply for all the simulations presented in this thesis. In any case, it is only for simulations when the density of the fluid is very high or the cycle period and τ_1/τ_2 are very low that this theoretically could be an issue. In addition, any changes to the initial conditions caused by residual movement of the fluid when the next blow period starts only has an effect during the start-up of the blow periods. This is because the steady-state velocity profile depends only on the boundary conditions and is therefore not affected by the initial conditions. Therefore, there will be virtually no effect on the results should the assumption of a cyclical steady-state within a single cycle be invalid in any of the presented simulations. Based on these results, it was concluded that it is valid to assume a cyclical steady-state of the flow on the fluid channel within the first refrigeration cycle.

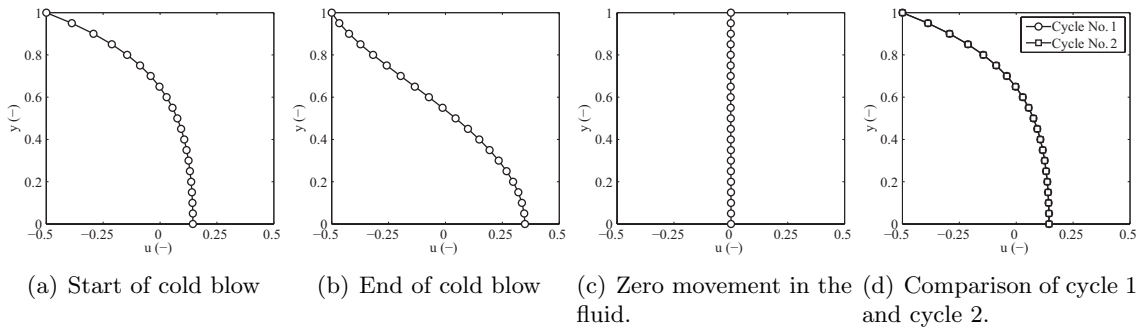


Figure B.10: (a) velocity profile at the beginning of the cold blow in the first AMR cycle and (b) the end of the cold blow in the first AMR cycle. (c) There is zero movement in the fluid almost immediately after the end of the blow period. (d) The velocity profiles at the start of the cold blow in cycle 1 and 2 are identical meaning that the cyclical steady-state is obtained within the first cycle.

This page was intentionally left blank.

Appendix C

Paper presented at the Danske
Køledage Conference, 2006

This page was intentionally left blank.

Magnetic Refrigeration and the Magnetocaloric Effect

Thomas Frank Petersen¹
Risø National Laboratory,
Materials Research Department,
Frederiksborgvej 399, P.O. 49, DK-4000 Roskilde.
and
Technical University of Denmark,
Department of Mechanical Engineering,
Nils Koppels Allé 403, DK-2800 Lyngby

Nini Pryds, Anders Smith, Søren Linderøth and Stinus Jeppesen
Risø National Laboratory,
Materials Research Department,
Frederiksborgvej 399, P.O. 49, DK-4000 Roskilde.

Hans-Jørgen Høgaard Knudsen
Technical University of Denmark,
Department of Mechanical Engineering,
Nils Koppels Allé 403, DK-2800 Lyngby

Abstract

Magnetic refrigeration at room temperature is an emerging technology for refrigeration, which promises low energy consumption and is environmentally friendly. Magnetic refrigeration is based on the magnetocaloric effect, which manifests itself as a reversible increase in temperature when magnetic materials are placed in a magnetic field. This paper introduces and describes magnetic refrigeration cycles and the magnetocaloric effect, and shows how magnetic refrigeration can be an alternative to vapour-compression refrigeration. A review of the Danish research on magnetic refrigeration at Risø National Laboratory is also provided.

Keywords: Magnetocaloric Effect, Magnetic Refrigeration, Active Magnetic Regenerator, AMR

¹ Corresponding author: Phone:+45 4677 5720, Fax:+45 4677 5758, thomas.frank.petersen@risoe.dk

1 Introduction

Magnetic refrigeration at room temperature is an interesting alternative to conventional refrigeration due to its numerous benefits, among other that, magnetic refrigeration systems are effective and have low energy consumption, the systems are compact and virtually silent and the refrigerants are environmentally friendly.

Magnetic refrigeration uses the magnetocaloric effect (MCE) to provide cooling. The MCE can be observed as an increase in temperature when a magnetic material, kept in thermal isolation (adiabatic conditions), is placed in a magnetic field. This is called the adiabatic temperature change (Figure 1.).

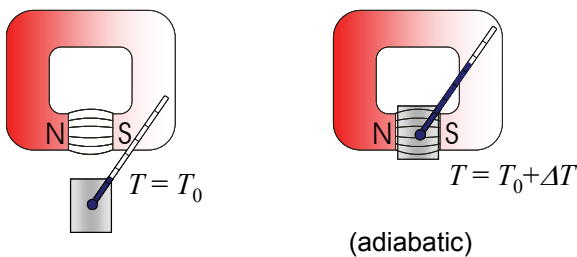


Figure 1: The adiabatic temperature change. The sample has the initial temperature T_0 , and is thermally isolated from the surroundings. When the sample is placed in a magnetic field the temperature increases to $T=T_0+\Delta T_{ad}$, illustrated by the thermometer. When the sample is removed from the magnetic field the temperature decreases to T_0 (Dinesen 2004).

Magnetic refrigeration at room temperature is a relatively new field of research, but the MCE has been used in specialized areas of refrigeration since the 1930s. The MCE was discovered in 1881 by Warburg who observed the adiabatic temperature change in iron and in 1918 Weiss and Piccard explained the MCE theoretically. In 1926-1927 Debye and Giauque suggested that the MCE be used to obtain extremely low temperatures (<1 K) using a method called *adiabatic demagnetization* and in 1933 MacDougall verified the method by cooling a sample from 1.5 K to 0.25 K. Giauque was awarded the Nobel price for his research in 1949. Since MacDougall's experiment adiabatic demagnetization has been a standard technique in experimental physics to obtain temperatures from a few kelvin down to a few nano kelvin. In 1976 Brown constructed the first magnetic refrigerator operating at room temperature,

using gadolinium as refrigerant and a superconducting magnet. The refrigerator obtained a temperature difference of 51 K (Brown 1976). Subsequently a number of magnetic refrigerators have been build with the most notable development being the magnetic refrigerator constructed in 2001 by the Astronautics Corporation in the USA. This refrigerator uses permanent magnets and eliminates superconducting magnets; an important step for making magnetic refrigeration ready for commercial applications.

Magnetic refrigeration uses the MCE by taking a solid refrigerant through repeated "heat pump" cycles; the general principle is comparable to conventional vapour-compression refrigeration (Figure 2).

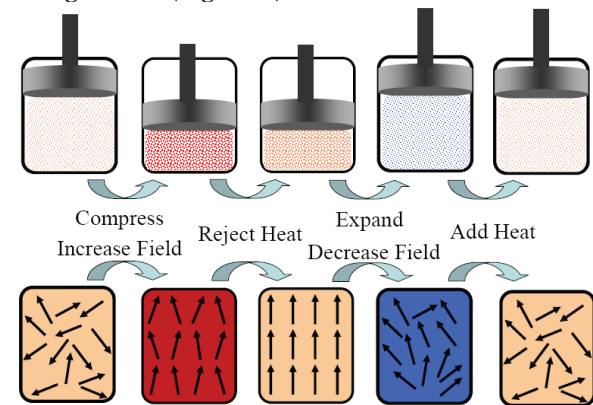


Figure 2: Similarities between vapour-compression and magnetic refrigeration. In the first step the refrigerant (vapour or magnetic solid) is initially at ambient temperature and experiences either a compression or an increased magnetic field to increase the temperature. In the second step the refrigerant rejects heat to the surroundings, and returns to ambient temperature. In the third step the temperature of the refrigerant decreases as it is expanded or the magnetic field is removed. In the fourth step, the refrigerant absorbs heat from the cooling load until it reaches ambient temperature and the cycle can start over. By repeating the cycle the cooling load is continuously cooled (figure from (Nellis et al. 2004)).

The above cooling cycle cannot be used for actual refrigeration because it is limited by the adiabatic temperature change. This is one of the major issues with magnetic refrigeration; even with superconducting magnets, the adiabatic temperature change in gadolinium (the most commonly used material) is approximately 20 K,

and with permanent magnets the change it is approximately 6 K. To increase the MCE, much research is focused towards improving the materials. For the MCE to be used for practical purposes, a magnetic refrigeration system must employ a regenerative cycle, and the AMR (Active Magnetic Regeneration) cycle is the most commonly used today which is explained in detail in section 4. The AMR cycle has been realized in a number of experimental magnetic refrigerators, and virtually all new magnetic refrigerators are based on the AMR cycle.

In the next part of the paper a short review of the research on magnetic refrigeration at Risø in Denmark is presented and in the remainder of the paper magnetic refrigeration cycles and the MCE is described in detail.

2 Magnetic refrigeration at Risø

The Materials Research Department at Risø National Laboratory has investigated the MCE since 2001. The research team currently consists of seven persons, where two are PhD students. The main focus in this research has been the development of new ceramic materials for magnetic refrigerator applications. Recently an AMR refrigerator has also been constructed in order to directly testing the materials suitability for magnetic refrigeration directly. To study and optimize the experimental AMR refrigerator a two-dimensional mathematical model of the AMR is also currently being developed. In the following sections, the three areas of research are described in further detail.

2.1 Materials research

All magnetic materials, to a greater or lesser degree, exhibit the MCE. However, some materials, by virtue of their unique electronic structure or physical nanostructure, display a significantly enhanced MCE, and can potentially be used for magnetic refrigeration. The large magnetic entropy changes at the Curie temperature of certain ceramics (perovskite manganites) have been the focus of much research interests in recent years. The ferromagnetic transition of the $A_{1-x}B_xMnO_3$ type perovskites is accompanied by significant lattice changes at the Curie temperature. The simultaneous occurrence of structural and magnetic transitions can strongly influence the

magnetic entropy change. The Curie temperature of these materials covers the entire temperature range from very low temperatures to near 300 K and some show sufficient MCE to be used as magnetic refrigerants. This behaviour indicates that the MCE in these ceramics is high and tuneable and suitable for magnetic refrigerants in a wide temperature interval.

The adiabatic temperature change for $La_{0.67}Ca_{0.33-x}Sr_xMnO_3$ ($x=0.0-0.33$) was investigated experimentally, and it was found that the Curie temperature can be tuned from 267 K to 369 K, with a corresponding maximum adiabatic temperature change of 1.5 K to 0.5 K respectively (Figure 3).

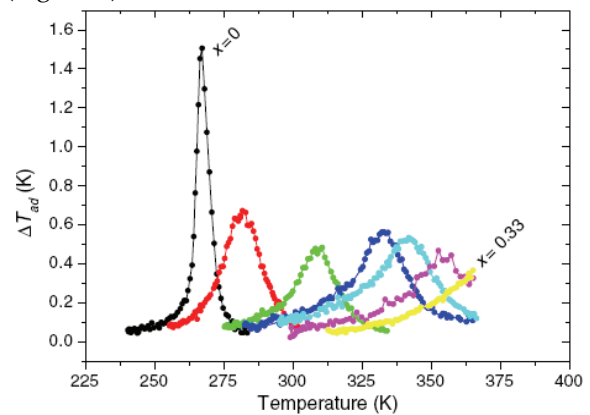


Figure 3: The adiabatic temperature change in $La_{0.67}Ca_{0.33-x}Sr_xMnO_3$ ($x=0-0.33$) in a magnetic field of 0.7 Tesla. The peak of each curve is centred on the Curie temperature and illustrates that the Curie temperature can be adjusted by changing the composition (Dinesen et al. 2005)

The experimental results show that these ceramics are potential candidates for magnetic refrigeration over a wide temperature range. This work is described in detail in (Dinesen 2004) and (Dinesen et al. 2005). Presently, the materials research has resulted in two scientific articles and a PhD report, and Risø is currently pursuing patents. The materials research is currently continued through a PhD project.

2.2 Experimental active magnetic regenerator refrigerator

Risø has designed, fabricated, and is currently testing a proof-of-concept, magnetic refrigerator based on the concept in Figure 8. The experimental AMR refrigerator uses a linear motion of the refrigerant situated within an electromagnet with a maximum field of about 0.8

T. The motion of the refrigerant is arranged to pass through a gap in the magnet where the magnetic field is concentrated. As it passes through the field, the refrigerant exhibits a MCE and heats up. After entering the field, a stream of water is pushed through the refrigerant to draw the heat out of the material by means of pistons. When the refrigerant leaves the magnetic field, it cools down due to the MCE. A second stream of water is then cooled by the refrigerant. Heat exchangers in each end of the AMR refrigerator provide a heat sink and a cooling load.

2.3 Mathematical modelling of an Active Magnetic Regenerator

The experimental AMR refrigerator executes a complex thermodynamic cycle which cannot be analysed in a simple way. To understand and analyze the AMR cycle it is necessary to use numerical methods, and mathematical modelling has been the subject of several projects in recent years. As part of a PhD project, Risø has developed a two-dimensional model to analyze the experimental AMR refrigerator. The model accounts for the coupled problem of heat transfer and periodic fluid flow under alternating magnetization and demagnetization. The finite element method was used to implement and solve the problem numerically. The model is able to predict the magnetic refrigerator performance at many conditions and will be used to optimize geometry, choice of materials, operating frequency etc. The model is currently used to study the design of the proof-of-concept AMR in detail and publications are forthcoming.

3 Magnetic refrigeration cycles

Magnetic refrigeration can be realized with different thermodynamic cycles; in the following the magnetic Carnot, Brayton, Eriksson and AMR cycles are explained in detail. There are three new types of thermodynamic processes, used in magnetic refrigeration:

- Isothermal magnetization, where the refrigerant is magnetised while the temperature is kept constant; during this process the MCE manifests as a change in entropy (see section 4)
- Adiabatic magnetization, where the temperature of the refrigerant increases due to the adiabatic temperature change.

- The isofield process, where the magnetic field is kept constant.

For a cyclic process the 1st law of thermodynamics is written as:

$$\oint du = \oint dw + \oint dq = 0 \quad (2.1)$$

where dw refers to the external or technical work. Using the 2nd law of thermodynamics the cyclic work can also be written as:

$$w = -\oint Tds \quad (2.2)$$

The coefficient of performance (COP) is used to evaluate the effectiveness of a magnetic refrigeration cycles.

$$COP = \frac{q_c}{w} \quad (2.3)$$

where q_c is the cooling load.

3.1 The Carnot cycle

In magnetic refrigeration cycles the Carnot cycle can be considered the reference cycle. The cycle consists of two isothermal and two adiabatic processes and can be illustrated in a schematic T-S diagram between two isofield lines (Figure 4)

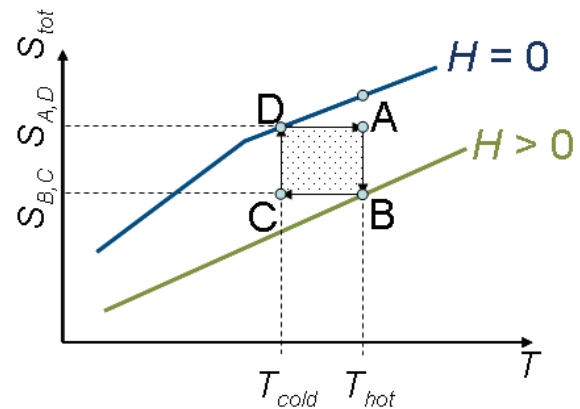


Figure 4: The magnetic Carnot cycle consists of four steps; isothermal magnetization from A to B, adiabatic demagnetization from B to C, isothermal demagnetization from C to D and finally adiabatic magnetization from D to A.

Although the Carnot cycle looks simple, it is complex to realize, and it will be explained in further detail. The cycle starts at point A at the temperature of the hot heat exchanger and a partial magnetic field. From point A to B there is isothermal magnetization as the refrigeration rejects heat while the magnetic field is increased to its maximum strength. From point B to C the temperature of the refrigerant is reduced by

partial adiabatic demagnetization. From point C to D there is isothermal demagnetization as the magnetic field is removed while the refrigerant adsorbs heat from the cold heat exchanger. Finally, from point D to A the refrigerant undergoes partial adiabatic magnetization as the magnetic field is increased until the refrigerant reaches the initial state. The work (the area ABCD) can be calculated from equation (2.2):

$$w = -\oint Tds = -\int_A^B Tds - \int_C^D Tds \quad (2.4)$$

$$= T_{hot}(s_A - s_B) - T_{cold}(s_D - s_C)$$

The cooling load is the heat absorbed during process CD, which can be calculated as:

$$q_c = \int_C^D Tds = T_{cold}(s_D - s_C) \quad (2.5)$$

The COP is then:

$$COP = \frac{q_c}{w} = \frac{T_{cold}(s_D - s_C)}{T_{hot}(s_A - s_B) - T_{cold}(s_D - s_C)} \quad (2.6)$$

Since the adiabatic process AB and CD have the same entropy difference, equation (2.6) can be further simplified, which leads to the following well known result for the COP of a Carnot cycle:

$$COP = \frac{T_{cold}}{T_{hot} - T_{cold}} \quad (2.7)$$

For practical refrigeration, the temperature span between the hot and cold sink is limited by the high and low isofield curves. Consequently, the hot and cold temperature cannot be chosen freely. Furthermore, the cycle uses a varying magnetic field, as each of the four points experiences a unique magnetic field. This requires an electromagnet or superconducting magnet where the field can be manipulated; this is energy inefficient and makes the Carnot cycle unsuitable for normal refrigeration.

3.2 The Ericsson cycle

For magnetic refrigeration to be used under normal conditions, it is necessary to make the temperature span independent of the cycle. This can be accomplished with regeneration. The Ericsson cycle consists of two isotherms and two isofields and uses regeneration (Figure 5).

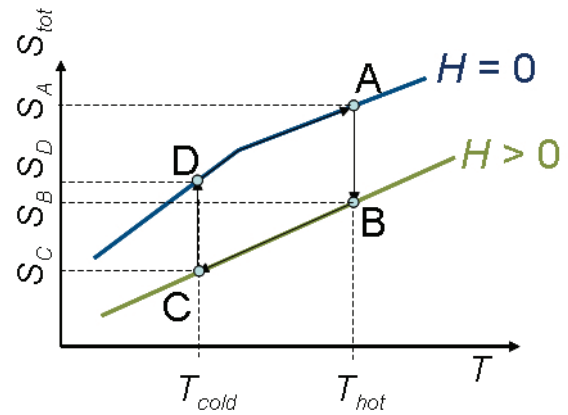


Figure 5: The Ericsson cycle. From A to B there is isothermal magnetization and heat rejection, from B to C isofield cooling and regeneration, from C to D isothermal demagnetization and heat absorption and from D to A isofield heating with regeneration.

Brown used the Ericsson cycle when he built his magnetic refrigerator; as regenerator he used a cylinder filled with a water/alcohol mixture, and the refrigerant, gadolinium, was formed as concentric cylinders, which could slide up and down the length of the regenerator. In each end of the regenerator a heat reservoir was placed to provide isothermal conditions (Figure 6).

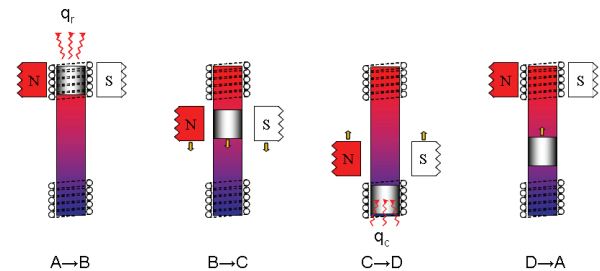


Figure 6: The use of a regenerator in the Ericsson refrigeration cycle. The position of the magnet and refrigerant inside the regenerator during the four steps of the Ericsson cycle shown on Figure 5 is illustrated on the four figures from left to right.

At steady-state there is a temperature gradient along the regenerator and the machine starts with the gadolinium and the magnet positioned at the hot reservoir of the generator. The gadolinium is magnetized and the produced heat is rejected to the hot reservoir which provides isothermal conditions. The gadolinium and the magnet is simultaneously moved down through the regenerator at constant magnetic field during which the gadolinium rejects heat to the regenerator until it reaches the temperature of the cold reservoir. The magnet is moved up to the hot reservoir and the gadolinium is

demagnetized while the gadolinium absorbs heat from the cold reservoir. Finally, the gadolinium is moved up through the regenerator and absorbs heat until it reaches the temperature of the hot reservoir. The regenerator is used to bring the refrigerant from the temperature of the cold heat reservoir to the temperature of the hot reservoir and vice versa. However, because regeneration is driven by temperature differences, it is an irreversible process which decreases the efficiency of the cycle.

The absorbed heat can be determined as:

$$q_c = \int_C^D T ds = T_{cold} (s_D - s_C) \quad (2.8)$$

The rejected heat can likewise be determined as:

$$q_r = \int_A^B T ds = T_{hot} (s_B - s_A) \quad (2.9)$$

Finally, the work can be determined as:

$$w = -q_r - q_c = T_{hot} (s_A - s_B) - T_{cold} (s_D - s_C) \quad (2.10)$$

The COP can be calculated from equation (2.8) and (2.10) :

$$COP = \frac{T_{cold} (s_D - s_C)}{T_{hot} (s_A - s_B) - T_{cold} (s_D - s_C)} \quad (2.11)$$

By letting T_{cold} go to T_{hot} the limit of the COP for the Ericsson cycle becomes that of the Carnot cycle (Kitanovski and Egolf 2005):

$$\lim_{T_{cold} \rightarrow T_{hot}} COP = \frac{T_{cold}}{T_{hot} - T_{cold}} \quad (2.12)$$

3.3 The Brayton cycle

The Brayton cycle is a regenerative cycle similar to the Ericsson cycle; the only difference being that it uses adiabatic instead of isothermal magnetization and demagnetization (Figure 7).

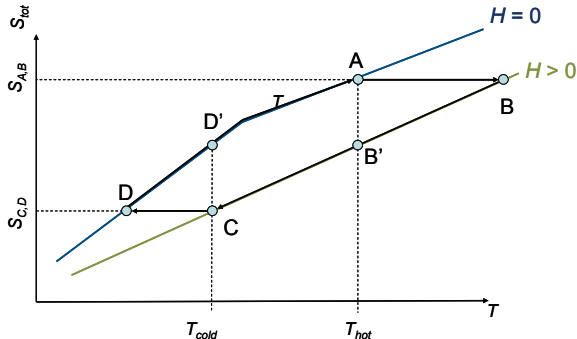


Figure 7: The Brayton cycle: From A to B there is adiabatic magnetization, from B to C isofield heat rejection, and regeneration, from C to D adiabatic demagnetization and from D to A isofield heat absorption with regeneration.

The Brayton cycle uses adiabatic magnetization and demagnetization and heat rejection and absorption must occur during process BC and process DA; this is illustrated on the figure as process BB' and DD'.

The absorbed heat from the cooling load can be determined as:

$$q_c = \int_D^A T ds \quad (2.13)$$

The rejected heat can likewise be determined as:

$$q_r = \int_B^C T ds \quad (2.14)$$

The work is determined from the conservation of energy:

$$w = -q_r - q_c = -\left(\int_B^C T ds + \int_D^A T ds\right) \quad (2.15)$$

The COP is calculated from equation (2.15) :

$$COP = \frac{\int_D^A T ds}{-\left(\int_B^C T ds + \int_D^A T ds\right)} \quad (2.16)$$

3.4 The Active Magnetic Regenerator cycle

The AMR cycle consists of adiabatic magnetization and demagnetization and two isofield processes, which make the AMR cycle identical to the Brayton cycle. However, in the AMR the refrigerant provides both refrigeration and regeneration. The essential part of an AMR is a porous regenerator "bed" made of the magnetocaloric refrigerant. Heat exchangers integrated with the refrigerator transport heat from the regenerator to the surroundings and from the cooling load to the regenerator. Because the refrigerant is a solid, the AMR includes a "heat transfer fluid" which couples the refrigerant to the heat exchangers. The regenerator bed is immersed in the heat transfer fluid and by means of pistons or pumps the heat transfer fluid can move back and fourth through the regenerator. A refrigerator based on the AMR cycle is best explained with a graphic illustration (Figure 8).

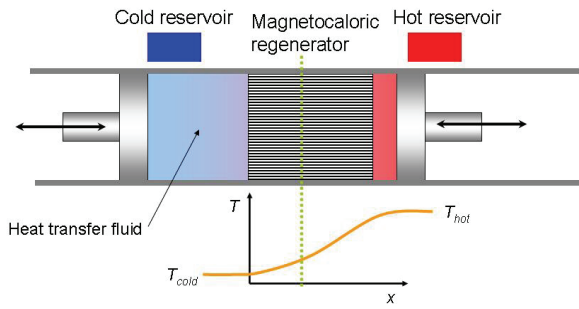


Figure 8: Magnetic refrigerator based on the AMR cycle. The magnetocaloric regenerator is placed in the middle of the refrigerator surrounded by heat transfer fluid. In one end of the regenerator bed a cold reservoir is placed and a hot reservoir is placed in the other end. Pistons in each end can move the heat transfer fluid through the regenerator. The figure inserted at the bottom show the temperature profile through the refrigerator at steady-state.

The AMR cycle starts with the refrigerator in the position shown on Figure 8, with a given temperature gradient through the regenerator bed. The magnetic field is applied which heats the regenerator bed which in turn rejects heat to the heat transfer fluid within the regenerator bed. This results in a new temperature profile. Subsequently the heat transfer liquid is displaced from the cold reservoir towards the hot reservoir (the cold blow). The displacement moves all the heat transfer fluid with a temperature higher than the hot reservoir from the regenerator bed and replace it with cold heat transfer fluid. At the hot reservoir, the heat transfer fluid rejects heat to the surroundings which results in new temperature gradient in the regenerator. The regenerator bed is cooled by demagnetization and absorbs heat from the heat transfer liquid. Finally, the heat transfer liquid is displaced from the hot reservoir to the cold reservoir (the hot blow). The heat transfer fluid with a lower temperature than the cold reservoir is replaced with warm fluid and the cold heat transfer fluid absorbs heat from the cold reservoir (i.e. the cooling load). This returns the temperature gradient to its original level. The essential action of the AMR is the manipulation of the temperature gradient in the regenerator bed to produce liquid with a temperature, which is higher or lower than the temperature of the hot and cold reservoirs respectively. A simplified temperature gradient throughout the cycle can be illustrated in four steps (Figure 9).

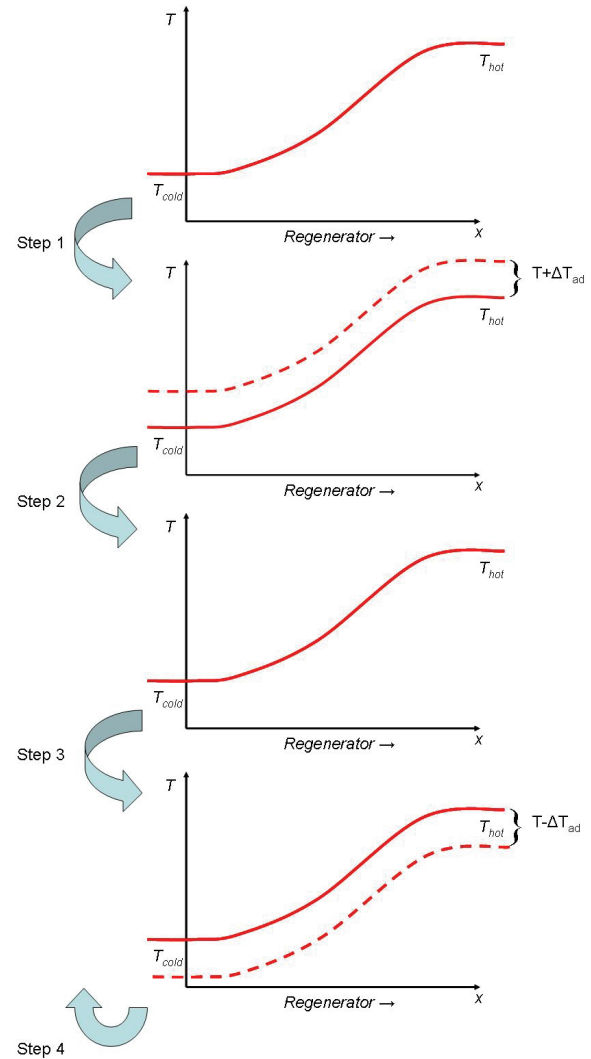


Figure 9: Temperature profile in an AMR during operation, starting from the top. The cycle starts with a temperature gradient along the regenerator. In step 1 the AMR is magnetized, the temperature in the regenerator is increased and the gradient is “lifted” upwards. In step 2 the fluid is shifted from left to right and the hot fluid is moved out to the hot reservoir where heat is rejected, resulting in a new temperature distribution. In step 3 the AMR is demagnetized shifting the gradient “downwards”. Finally, in step 4 the fluid is shifted from right to left letting the cold fluid absorb heat from the cold reservoir; this returns the AMR to its original temperature distribution.

The AMR cycle cannot be illustrated by in a T-S diagram as each part of the regenerator bed executes an individual thermodynamic cycle, which is linked to each other through the heat transfer liquid. The AMR is a complex cycle, but offers the optimal utilization of the MCE.

4 Theory of the magnetocaloric effect

The magnetocaloric effect is intrinsic to all magnetic materials and is caused by changes of the entropy of the material. In general, the magnetocaloric effect itself manifests as either absorption or emission of heat when a magnetic material (e.g. iron) is placed in a magnetic field (Tishin and Spichkin 2003). This is caused by the coupling between the magnetic spin system and the thermal properties. The MCE is most easily observed as the adiabatic temperature change, ΔT_{ad} , but can also be measured indirectly as the isothermal entropy change, ΔS_M . The latter is obtained when the sample is magnetized under isothermal conditions. The relationship between the two properties can be illustrated using a schematic T-S diagram (Figure 10).

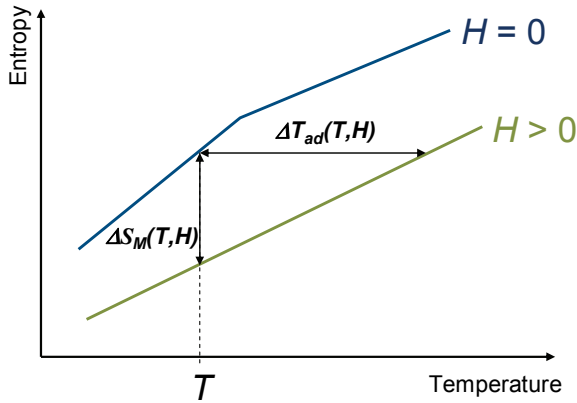


Figure 10: The adiabatic temperature change and the isothermal entropy change. The first occurs when entropy is kept constant, while the second occur when the temperature is kept constant.

If hysteresis² is neglected, the magnetization can be assumed reversible, i.e. the magnetic spin system returns to its initial alignment when the magnetic field is removed; this assumption is used in the remainder of the paper.

To explain the isothermal entropy change consider a magnetic sample with a given magnetic spin system under isothermal conditions. When an external magnetic field is applied, the magnetic spin system become aligned with the field, which increase the magnetic ordering and decrease the magnetic entropy (Figure 11).

² Hysteresis is an effect, which occurs if a ferromagnetic sample retains some remnant magnetization even when removed from the magnetic field.

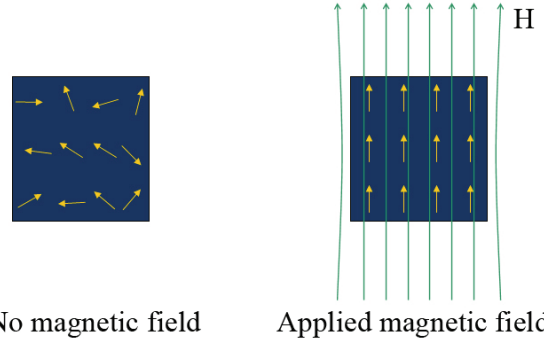


Figure 11: The ordering of the magnetic spin system of an isothermal sample before and after a magnetic field is applied. The individual magnetic moments become aligned with the external field which decreases the magnetic entropy of the sample. If the magnetic field is removed the magnetic spin system reverts to its original alignment

The adiabatic temperature change can be explained in a similar fashion. The total entropy of the sample can be split into three sources; the *magnetic entropy* from the magnetization of the material; the *lattice entropy* from the lattice vibrations of the material and the *electronic entropy* from the free electrons of the material (denoted s_m , s_l and s_e respectively) (Dinesen 2004). The lattice and the electronic entropy can be regarded as independent of the magnetic field and only depends on temperature, but the magnetic entropy is strongly dependent on both the magnetic field and the temperature. The total entropy can be written as a sum of entropy functions:

$$s_{tot}(H, T) = s_m(H, T) + s_l(T) + s_e(T) \quad (3.1)$$

If the magnetic field is applied under adiabatic conditions, the total entropy remains constant during the magnetization process. Thus, when the magnetic entropy is decreased, the lattice and electronic entropy must increase along with the temperature to compensate. When the external field is removed, the magnetic spin system reverts to its original alignment, which decreases the thermal entropy and returns the sample to its original temperature.

4.1 Thermodynamic theory of the magnetocaloric effect

The thermodynamic system used to develop the thermodynamics of the MCE consists of a magnet and a ferromagnetic sample (Figure 12).

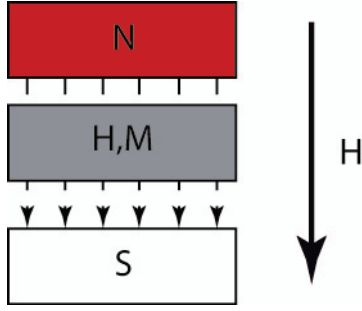


Figure 12: The thermodynamic system consists of the magnetic sample (grey area) and the magnet (red and white area), the arrow denotes the direction and strength of the magnetic field. Within the sample the total magnetic field is increased due to the magnetization of the sample.

From the 1st law of thermodynamics the change in internal energy is defined as the sum of the changes in heat and work:

$$du = dq + dw \quad (3.2)$$

However, two different systems can be defined as either the magnet *and* the magnetic sample or the magnetic sample alone. Here only the sample is considered and the correct definition is (Adib 2002):

$$du = Tds + \mu_0 Hd\sigma \quad (3.3)$$

where μ_0 is the permeability of free space, H the external magnetic field and σ the specific magnetization. The infinitesimal change in internal entropy can be written in the general form:

$$ds = \left(\frac{\partial s}{\partial T} \right)_H dT + \left(\frac{\partial s}{\partial H} \right)_T dH \quad (3.4)$$

For an isobaric process at constant magnetic field the 2nd law of thermodynamics yields the entropy dependence on temperature:

$$\left(\frac{\partial s}{\partial T} \right)_H = \frac{c_H}{T} \quad (3.5)$$

where c_H is the total heat capacity at constant pressure and magnetic field. The entropy dependence on the magnetic field can be expressed in terms of the magnetization according to (Morrish 1965):

$$\left(\frac{\partial s}{\partial H} \right)_T = -\mu_0 \left(\frac{\partial \sigma}{\partial T} \right)_H \quad (3.6)$$

Equation (3.5) and (3.6) are introduced into equation (3.4) to obtain an expression for the entropy:

$$ds = \frac{c_H}{T} dT + \mu_0 \left(\frac{\partial \sigma}{\partial T} \right)_H dH \quad (3.7)$$

The total specific heat capacity at constant field can be written as:

$$c_H = \left(\frac{\partial q}{\partial T} \right)_H \quad (3.8)$$

Using the 2nd law of thermodynamics and equation (3.8) this leads to the following relation:

$$\begin{aligned} c_H &= T \left(\frac{\partial s}{\partial T} \right)_H = T \left(\frac{\partial}{\partial T} (= s_m + s_l + s_e) \right) \\ &\Rightarrow T \left(\frac{\partial s_m}{\partial T} \right)_H + T \left(\frac{\partial s_l}{\partial T} \right)_H + T \left(\frac{\partial s_e}{\partial T} \right)_H \\ &\Rightarrow c_m + c_l + c_e \end{aligned} \quad (3.9)$$

Thus, like the specific entropy, the specific heat capacity is also the sum of the magnetic³, lattice and electronic contributions.

For isothermal magnetization the entropy change can be determined from equation (3.7) by setting dT equal to zero. Integrating over the change in the magnetic field results in the following expression:

$$\Delta s_M = -\mu_0 \int_{H_1}^{H_2} \left(\frac{\partial \sigma}{\partial T} \right)_H dH \quad (3.10)$$

For a ferromagnetic material the magnetization decreases with temperature and $(\partial \sigma / \partial T)$ is negative, which means that an increased magnetic field reduces the entropy as expected.

The adiabatic temperature change can be determined from equation (3.7) by setting ds to zero and integrating over the change in the magnetic field.

$$\Delta T_{ad} = -\mu_0 \int_{H_1}^{H_2} \frac{T}{c_H} \left(\frac{\partial \sigma}{\partial T} \right)_H dH \quad (3.11)$$

The adiabatic temperature change is directly proportional to the temperature and inversely proportional to the heat capacity. Since $(\partial \sigma / \partial T)$ is negative, an increase in the magnetic field results in a positive adiabatic temperature change as both the temperature and heat capacity are positive, again as expected.

From equation (3.10) and (3.11) it can be concluded that the MCE will be large if:

- The magnetic field change is large

³ The subscript, m , denotes that c_m , is the magnetic contribution to the total heat capacity. This should not be confused with the total heat capacity at constant magnetization.

- The magnetization changes rapidly with temperature (i.e. $|\partial\sigma/\partial T|$ is large)
- The heat capacity is small

From the second point one can expect a large MCE near the Curie temperature of ferromagnetic materials, where the material changes phase from an ordered ferromagnetic spin system to a random paramagnetic spin system. This transition is associated with a large reduction of magnetization, and thus a large MCE (Figure 13).

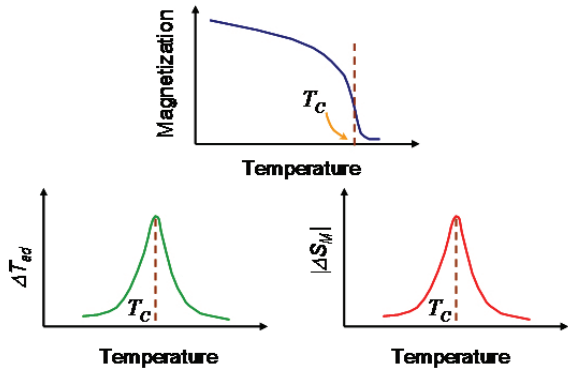


Figure 13: The relationship between the temperature dependence of the magnetization and the magnetocaloric effect. The magnetocaloric effect is largest around the Curie temperature where the material experiences a phase transition. The adiabatic temperature change will have a positive peak and the isothermal entropy change will have a negative peak.

4.2 Materials for magnetic refrigeration

For a material to be suitable for magnetic refrigeration it must have a Curie temperature in the vicinity of the temperature regime where the refrigerator will operate. Furthermore, for magnetic refrigeration system commercially usable the material must be chemically stable to avoid corrosion and be “cheap enough”.

The magnitude of the MCE in real materials has not yet been discussed, i.e. how large a temperature difference is it possible to achieve in different magnetic fields. The “prototype” material is gadolinium, which has been used since the 1970s. The adiabatic temperature change for gadolinium in different magnetic fields is shown as an example (Figure 14).

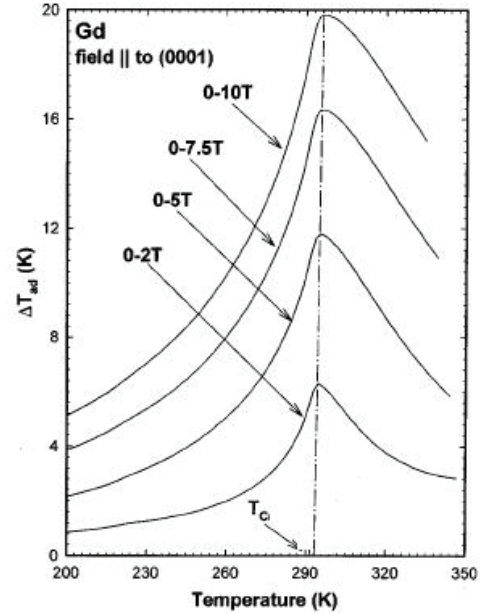


Figure 14: The adiabatic temperature change in gadolinium as a function of temperature in magnetic fields ranging from 2 to 10 T. Magnetic fields above approximately 2 T can only be achieved from superconducting magnets (Tishin et al. 1999)

The figure reveals one of the greatest problems when using the MCE for refrigeration; the obtainable temperature difference is small. It is only around 20 K even in a magnetic field of 10 T, which can only be obtained using superconducting magnets. For permanent magnets it is only possible to obtain magnetic field changes of approximately 2 T, the temperature difference is approx. 6 K. This is one of the primary reasons for the need for regeneration in magnetic refrigeration; the MCE cannot directly obtain the temperature span needed for conventional household refrigeration.

Finally, it should be mentioned that it is possible to model the magnetocaloric effect using a phenomenological model of magnetism as the one presented in (Dinesen 2004). The model may be used with the equations presented in this paper for basic investigations of the MCE and magnetic refrigeration cycles.

5 Conclusion and outlook

Magnetic refrigeration offers a more energy effective alternative to vapour-compression based refrigeration. This is because magnetic refrigeration uses the magnetocaloric effect, a virtually reversible thermodynamic process, which occurs when a magnetic material is placed

in a magnetic field. However, it is not possible to use the magnetocaloric effect directly for refrigeration. Specialized refrigeration cycles with regeneration are required for magnetic refrigeration to be used for conventional refrigeration. Experimental refrigerators have been constructed to demonstrate the concept.

Risø National Laboratory has investigated the magnetocaloric effect in ceramics since 2001, and the results are promising. The research activities have recently been extended into two new areas: Risø has constructed a proof-of-concept magnetic refrigerator to test the ceramics suitability for magnetic refrigeration and a detailed finite element model was developed to optimize the design of the magnetic refrigerator. Publications on these new research areas are forthcoming.

It is the aim of Risø that the old and new research areas complement each other and produce knowledge and patents which help magnetic refrigeration become commercial.

6 Nomenclature

Symbol	Unit
c_H	$\text{Jkg}^{-1}\text{K}^{-1}$
c_m	$\text{Jkg}^{-1}\text{K}^{-1}$
c_l	$\text{Jkg}^{-1}\text{K}^{-1}$
c_e	$\text{Jkg}^{-1}\text{K}^{-1}$
H	Am^{-1}
μ_0	NA^{-2}
q	W
T	K
T_c	K
ΔT_{ad}	K
σ	Am^{-1}
ΔS_m	$\text{JK}^{-1}\text{kg}^{-1}$
s	$\text{JK}^{-1}\text{kg}^{-1}$
S_m	$\text{JK}^{-1}\text{kg}^{-1}$
S_l	$\text{JK}^{-1}\text{kg}^{-1}$
S_e	$\text{JK}^{-1}\text{kg}^{-1}$

7 Acknowledgements

The authors would like to thank Louise Theil Kuhn, and Frank Petersen for proof-reading the manuscript, Kristian Nim Sørensen for technical support during construction of the AMR and

Toke Henriksen for LabView support for the AMR control and data acquisition software.

8 References

- Adib, A. B. (2002). "Free energies for magnetic systems."
- Brown, G. V. (1976). "Magnetic heat pumping near room temperature." *Journal of Alloys and Compounds*, 47(8), 3673-3680.
- Dinesen, A. R., Linderoth, S., and Morup, S. (2005). "Direct and indirect measurement of the magnetocaloric effect in $\text{La}_{0.67}\text{Ca}_{0.33-x}\text{Sr}_x\text{MnO}_3$ +/-delta (x is an element of [0; 0.33])." *Journal of Physics-Condensed Matter*, 17(39), 6257-6269.
- Dinesen, A. R. (2004). "Magnetocaloric and magnetoresistive properties of $\text{La}_{0.67}\text{Ca}_{0.33-x}\text{Sr}_x\text{MnO}_3$." Risø National Laboratory, August 2004, 103 p., ISBN 87-550-3224-9.
- Kitanovski, A., and Egolf, P. W. (2005). "Thermodynamics of magnetic refrigeration." *International journal of refrigeration*, 29(3-12), 3-21.
- Morrish, A. H. (1965). *The Physical Principles of Magnetism.*, John Wiley & Sons, Inc..
- Nellis, G., Engelbrecht, K., Klein, S., Zimm, C., and Russek, S.(2004). "Model and Evaluation Tools for Assessing Magnetocaloric Effect for Space Conditioning and Refrigeration Applications."
- Tishin, A. M., Gschneidner, K. A., and Pecharsky, V. K. (1999). "Magnetocaloric effect and heat capacity in the phase-transition region." *Physical Review B*, 59(1), 503-511.
- Tishin, A., and Spichkin, Y. (2003). *The Magnetocaloric Effect and its Applications.*, Institute of Physics Publishing.

This page was intentionally left blank.

Appendix D

Paper published in the
International Journal of
Refrigeration

This page was intentionally left blank.

available at www.sciencedirect.comjournal homepage: www.elsevier.com/locate/ijrefrig

Two-dimensional mathematical model of a reciprocating room-temperature Active Magnetic Regenerator

Thomas Frank Petersen^{a,b,*}, Nini Pryds^b, Anders Smith^b, Jesper Hattel^c,
Henrik Schmidt^c, Hans-Jørgen Høgaard Knudsen^a

^aDepartment of Mechanical Engineering, Technical University of Denmark, Nils Koppels Allé, Building 402, DK-2800 Lyngby, Denmark

^bDepartment of Fuel Cells and Solid State Chemistry, Risø National Laboratory, Technical University of Denmark, Frederiksborgvej 399, DK-4000 Roskilde, Denmark

^cDepartment of Manufacturing Engineering and Management, Technical University of Denmark, Produktionstorvet, Building 425, DK-2800 Lyngby, Denmark

ARTICLE INFO

Article history:

Received 14 November 2006

Received in revised form

25 May 2007

Accepted 23 July 2007

Published online ■

Keywords:

Magnetic regenerator

Regenerator

Geometry

Flat plate

Modelling

Simulation

Performance

Temperature

ABSTRACT

A time-dependent, two-dimensional mathematical model of a reciprocating Active Magnetic Regenerator (AMR) operating at room-temperature has been developed. The model geometry comprises a regenerator made of parallel plates separated by channels of a heat transfer fluid and a hot as well as a cold heat exchanger. The model simulates the different steps of the AMR refrigeration cycle and evaluates the performance in terms of refrigeration capacity and temperature span between the two heat exchangers. The model was used to perform an analysis of an AMR with a regenerator made of gadolinium and water as the heat transfer fluid. The results show that the AMR is able to obtain a no-load temperature span of 10.9 K in a 1 T magnetic field with a corresponding work input of 93.0 kJ m⁻³ of gadolinium per cycle. The model shows significant temperature differences between the regenerator and the heat transfer fluid during the AMR cycle. This indicates that it is necessary to use two-dimensional models when a parallel-plate regenerator geometry is used.

© 2007 Elsevier Ltd and IIR. All rights reserved.

Modèle mathématique bidimensionnel d'un régénérateur de réfrigérateur magnétique alternatif fonctionnant à température ambiante

Mots clés : Réfrigérateur magnétique ; Régénérateur ; Géométrie ; Plaque plane ; Modélisation ; Simulation ; Performance ; Température

* Corresponding author. Department of Fuel Cells and Solid State Chemistry, Risø National Laboratory, Technical University of Denmark, Frederiksborgvej 399, DK-4000 Roskilde, Denmark.

E-mail address: thomas.frank.petersen@risoe.dk (T.F. Petersen).

0140-7007/\$ – see front matter © 2007 Elsevier Ltd and IIR. All rights reserved.

doi:10.1016/j.ijrefrig.2007.07.009

Nomenclature

Variables

c_p	heat capacity ($\text{J kg}^{-1} \text{K}^{-1}$)
ΔT_{ad}	adiabatic temperature change (K)
ΔT	temperature span (K)
Δx	piston stroke (m)
g	Landé factor
h	heat transfer coefficient ($\text{W m}^{-2} \text{K}^{-1}$)
H_{fl}	height of the pistons (m)
H	magnetic field strength (A m^{-1})
J	total angular momentum (\hbar)
k	thermal conductivity ($\text{W m}^{-1} \text{K}^{-1}$)
k_B	Boltzmann constant ($1.38 \times 10^{-23} \text{J kg}^{-1}$)
L	heat exchanger length (m)
N	Number of atoms per unit mass (kg^{-1})
N_s	Number of magnetic spins per unit mass (kg^{-1})
p	pressure (Pa)
q'	transferred energy per unit width (W m^{-1})
q''_c	heat flux (W m^{-2})
t	time (s)
T	temperature (K)
U_P	piston velocity (m s^{-1})
u	x-direction velocity (m s^{-1})
v	y-direction velocity (m s^{-1})
w'	work input per unit width (J m^{-1})

Greek

δ	relative difference (%)
μ_0	vacuum permeability ($4\pi \times 10^{-7} \text{N A}^{-2}$)
μ_B	Bohr magneton ($9.27 \times 10^{-24} \text{A m}^2$)
μ_f	viscosity ($\text{kg m}^{-1} \text{s}^{-1}$)
γ_e	Sommerfeld constant ($\text{J kg}^{-1} \text{K}^{-2}$)
ρ	density (kg m^{-3})
τ	AMR cycle length (s)
σ	Specific magnetization ($\text{Am}^2 \text{kg}^{-1}$)
θ_C	Curie temperature (K)
θ_D	Debye temperature (K)

Subscript

C	cold heat exchanger
c	absorbed heat
f	fluid
H	hot heat exchanger
mag	magnetic work
piston	piston work
r	rejected heat
s	solid

Superscript

dm	demagnetization
m	magnetization

1. Introduction

Magnetic refrigeration (MR) has for decades been used to obtain extremely low temperatures ($<4 \text{K}$) but recent developments in materials science have made MR a candidate for room-temperature refrigeration (Gschneidner et al., 2005). Room-temperature MR has the potential to reduce the energy consumption significantly when compared to vapour-compression refrigeration. Experiments have obtained a Coefficient Of Performance (COP) of 10, corresponding to a Carnot efficiency of 75%, while typical COPs for conventional refrigeration are between 2 and 4 (Gschneidner et al., 2005). Magnetic refrigeration is based on the magnetocaloric effect (MCE), which occurs when a magnetic material is subjected to a magnetic field. The MCE can be observed as an adiabatic temperature change (ΔT_{ad}). During adiabatic magnetization the total entropy is constant. Because the magnetic field reduces the spin entropy of the magnetic material, the lattice entropy must increase to keep the total entropy constant, leading to a temperature change of ΔT_{ad} . The MCE is virtually reversible in a number of materials, thus when the magnetic field is removed the material reverts to its initial temperature. The temperature change depends on the magnetic field and increases with the field. Typical values of ΔT_{ad} are 1–8 K in fields of 1–2 T (Gschneidner et al., 2005). To achieve a temperature span comparable to conventional refrigeration regeneration is therefore required. For a detailed review of the MCE, see (Tishin and Spichkin, 2003).

The most common design for MR today is the Active Magnetic Regenerator (AMR) (Pecharsky and Gschneidner, 1999). The AMR is based on a solid regenerator of a magnetocaloric material that allows a fluid to flow through. Examples of regenerator geometries are parallel plates, perforated plates or a packed bed of particles (Barclay and Sarangi, 1984). The regenerator is immersed in an inert heat transfer fluid (e.g. water, alcohol or helium) inside an enclosure and the fluid transport heat to and from the solid regenerator. Heat is absorbed from a cooling load and transferred to the fluid through a cold heat exchanger (CHEX) placed in one end of the regenerator, while a hot heat exchanger (HHEX), placed in the opposite end, rejects heat from the fluid to the surroundings. Pistons or pumps are used to move the fluid through the regenerator and into the heat exchangers. A typical AMR cycle consists of four sequential steps: (1) magnetization; the AMR is subjected to a magnetic field and the MCE increases the temperature of the regenerator while the fluid is heated by heat transfer from the regenerator, (2) the cold blow; fluid flows through the regenerator from the CHEX to the HHEX and heat is rejected to the surroundings through the HHEX, (3) demagnetization; the AMR is removed from the magnetic field and the MCE reduces the temperature of the regenerator while the fluid is cooled by heat transfer to the regenerator and (4) the hot blow; fluid flows through the regenerator from the HHEX to the CHEX where heat is absorbed from the cooling load through the CHEX. When the steady-state is reached, there is a nearly linear temperature

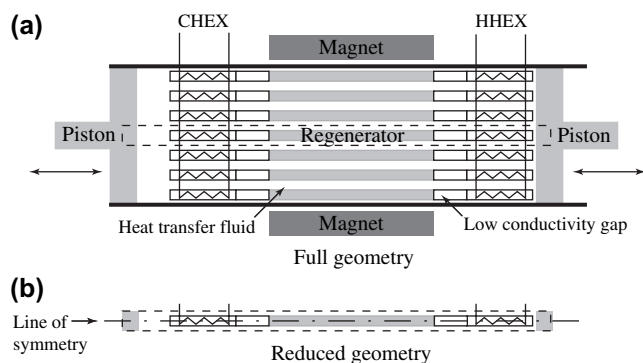


Fig. 1 – (a) The regenerator is made of parallel plates separated by channels of fluid. By neglecting effects in the transversal direction the geometry can be confined to two dimensions. The repeating design of the regenerator allows the model geometry to be reduced to a single repeating unit. (b) The repeating unit consists of a single regenerator plate surrounded by half a channel of fluid on either side with heat exchangers and pistons on either side of the plate. The line in (b) (- · - ·) illustrates the symmetry line of the repeating unit.

profile through the regenerator going from the CHEX (T_C) to the HHEX (T_H). The AMR constitutes a thermodynamic system which can neither be represented by analogies to regenerative vapour-compression refrigeration cycles nor as a composite of cascaded sub-cycles (Hall et al., 1996). Each infinitesimal element of the regenerator experiences a unique thermodynamic cycle where a solid produces the refrigeration while a fluid transfers heat between the regenerator elements. In addition, there is a possible overlap between the thermodynamic cycles of adjacent elements. These issues make analytical analysis of AMRs difficult because of the coupled physical effects of fluid flow, heat transfer and magnetism. To overcome these issues, numerical modelling techniques are used to allow design and optimization of AMRs.

Previous numerical models of room-temperature AMRs (Hu and Xiao, 1994; Engelbrecht et al., 2005a,b; Allab and Kedous-Lebouc, 2005; Siddikov et al., 2005; Shir et al., 2005) use a modelling approach which was originally developed for cryogenic AMRs (Barclay, 1982; Schroeder et al., 1990; DeGregoria, 1991). The existing room-temperature models consider a AMR with a packed bed as the regenerator and water or helium as the fluid. The 1-D heat transfer equation is used to determine the temperature distribution in the regenerator and in the fluid, while empirical correlations are used to determine the heat transfer between the regenerator and the fluid. In some cases the heat transfer equations are simplified to increase numerical efficiency by, for example, neglecting axial conduction or the heat loss to the surroundings. The 1-D approach is suitable for a bed of packed particles where the temperature gradient tangential to the regenerator bed is negligible (Schumann, 1929). Comparisons between modelling and experimental results have also been published (Allab and Kedous-Lebouc, 2005; Shir et al., 2005). These investigations show that the models are able to reproduce the general shape

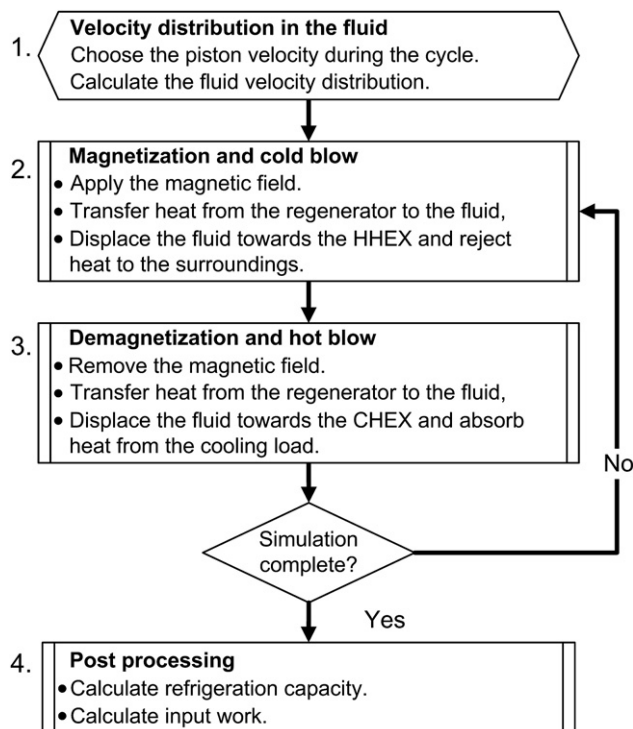


Fig. 2 – The AMR cycle is modelled by grouping the four physical steps into two repeating stages: (1) magnetization and the cold blow and (2) the demagnetization and the hot blow. The two stages are repeated until convergence. The AMR simulation is preceded by an initialization stage and concluded with an evaluation stage.

of the transient temperature evolution at the hot and cold ends of the regenerator but over-predict the temperature span (ΔT) between the heat exchangers. The discrepancy is contributed to the neglecting of axial conduction and because parasitic losses are not included in the model (Allab and Kedous-Lebouc, 2005; Shir et al., 2005). It is also suggested that the tangential temperature gradient should be taken into consideration (Engelbrecht et al., 2005a).

The motivation for the present study was to aid in the development of an experimental reciprocating room-temperature AMR by using numerical modelling. To overcome some of the limitations of the 1-D models a time-dependent, 2-D mathematical model was developed. The model accounts for all major fundamental physical phenomena by directly solving the coupled partial differential equations for the fluid flow and heat transfer.

2. Modelling the Active Magnetic Regenerator refrigerator

Fig. 1a shows the geometry considered in the present study which is based on the reciprocating linear AMR design (Pecharsky and Gschneidner, 1999). The geometry consists of a regenerator made of flat parallel plates arranged in a stack configuration with heat exchangers and pistons placed on

either side. By neglecting boundary effects, the repetitive design of the regenerator allows the full geometry to be reduced to a repeating unit. The geometry of the repeating unit can be simplified due to symmetry as illustrated on Fig. 1b.

The gap between the regenerator and the heat exchangers ensure that the heat transfer to and from the regenerator only occurs through the fluid. The gap is considered to be thermally insulated and omitted from the model geometry. Likewise, the pistons are also omitted from the model geometry as heat conduction in the pistons is neglected.

2.1. Governing equations of the AMR model

The model must account for the flow of the fluid, the MCE of the regenerator material, the heat transfer between the regenerator and the fluid and the heat transfer between the fluid and the heat exchangers. The simulation of the AMR cycle is performed in four stages: (1) the initial stage determines the velocity profile in the fluid, (2) the second stage models the magnetization and the cold blow, (3) the third stage models the demagnetization and the hot blow; the two latter stages are repeated until convergence and finally (4) the postprocessing stage evaluates the performance in terms of temperature span, cooling capacity and work input. A schematic diagram of the model and the different stages are shown in Fig. 2.

2.1.1. Stage 1 – the velocity distribution in the fluid

The velocity distribution in the fluid is determined by solving the momentum and continuity equations for an incompressible fluid (subscript f) with constant (temperature independent) properties (White, 1991)

$$\rho_f \left(\frac{\partial \mathbf{U}}{\partial t} + (\mathbf{U} \cdot \nabla) \mathbf{U} \right) - \mu_f \nabla^2 \mathbf{U} + \nabla p = 0, \tag{1}$$

$$\nabla \cdot \mathbf{U} = 0, \tag{2}$$

where ρ_f is the density of the fluid, μ_f is the dynamic viscosity of the fluid, \mathbf{U} is the 2-D velocity field (u, v) in the fluid and p is the pressure. Eqs. (1) and (2) can be solved independently of the temperature. Using a predetermined piston movement, the transient velocity distribution in the fluid is determined by solving Eq. (1) with the boundary conditions described in Section 2.2, until a cyclic steady-state is reached.

2.1.2. Stage 2 – magnetization and cold blow

During the magnetization, the MCE occurs almost instantaneously throughout the entire regenerator (Tishin and

Spichkin, 2003). The magnetization is therefore assumed adiabatic and is modelled by increasing the temperature in the regenerator by ΔT_{ad}

$$T = T_i + \Delta T_{ad}^m(T_i, \mu_0 H_0), \tag{3}$$

where T is the local temperature of the regenerator bed after the magnetization, T_i is the initial local temperature of the regenerator, $\Delta T_{ad}^m(T, \mu_0 H_0)$ is a function that describes ΔT_{ad} as the magnetic field is increased from zero to H_0 , and μ_0 is the vacuum permeability. Immediately after the magnetization the hot regenerator rejects heat to the fluid, and part of the heated fluid is then removed by the pistons and rejects its heat to the HEX. To determine the temperature distribution in the AMR, the coupled heat transfer equations for the solid domains (the regenerator and the two heat exchangers) and the fluid are solved. For the solid domain (subscript s) the temperature distribution is determined by the heat transfer equation

$$\rho_s c_{p,s} \frac{\partial T_s}{\partial t} + \nabla \cdot (-k_s \nabla T_s) = 0, \tag{4}$$

where $c_{p,s}$ is the heat capacity of the solid, T_s is the temperature of the solid and $k_{p,s}$ is the thermal conductivity of the solid. For compactness the generic subscript s is used for all the solid domains, but each domain is modelled with unique thermal properties. The temperature distribution in the fluid is determined by the heat transfer equation for an incompressible fluid with convective terms

$$\rho_f c_{p,f} \left(\frac{\partial T_f}{\partial t} + (\mathbf{U} \cdot \nabla) T_f \right) + \nabla \cdot (-k_f \nabla T_f) = 0, \tag{5}$$

where $c_{p,f}$ is heat capacity of the fluid, T_f is the temperature of the fluid and k_f is the thermal conductivity of the fluid. The velocity distribution previously determined from Eqs. (1) and (2) is used as an input value for Eq. (5) to determine the convective heat transfer. All thermodynamic properties, except the heat capacity of the magnetocaloric material which is temperature dependent, are evaluated at T_H . The solid and fluid are assumed in perfect thermal contact with the following boundary condition

$$\left(k_f \frac{\partial T_f}{\partial y} \right) = \left(k_s \frac{\partial T_s}{\partial y} \right). \tag{6}$$

When Eq. (6) is used as the boundary condition between the solid and fluid, Eqs. (1) and (2) must be solved with a sufficiently fine mesh to determine the full development of the

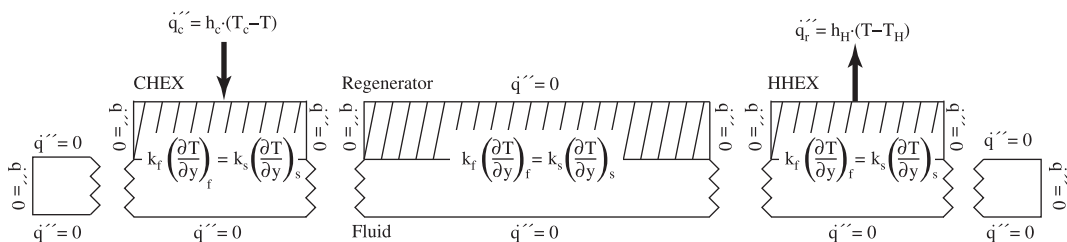


Fig. 3 – The boundary conditions used in the AMR model.

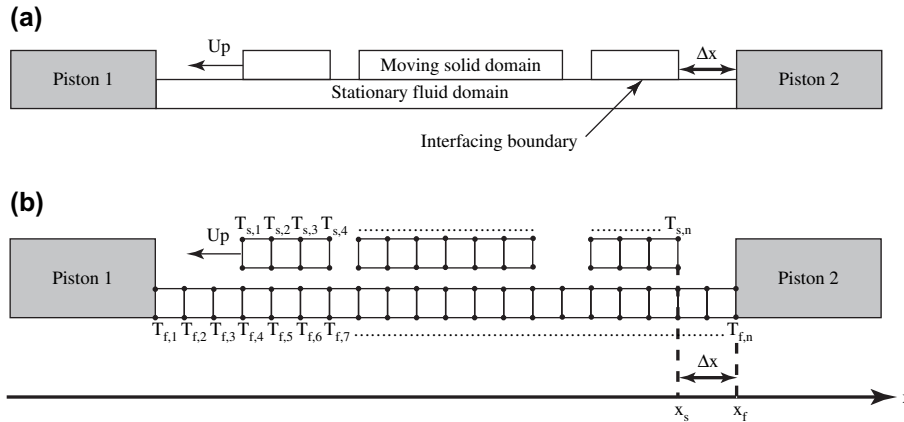


Fig. 4 – The conceptual approach used to model the thermal conduction between a moving and the stationary domain. (a) The piston displacement of the fluid is converted to a situation where the solid domain drags along the top of the fluid domain. (b) The solid and the fluid domains are modelled separately and the piston movement is modelled with a coordinate transformation of the temperature along the interface. As an example, consider the situation in (b) where the solid domain has moved a distance (Δx) relative to the fluid. In this case, the part of the solid domain with the temperature $T_{s,1}$, is equal to $T_{f,4}$, $T_{s,2}$, is equal to $T_{f,5}$ and so on. This relation is used to implement the boundary condition given by Eq. (6).

velocity boundary layer. The rate of heat rejected from the HHEX to the surroundings is determined by a convection boundary condition

$$\dot{q}_r'' = h_H \cdot (T - T_H), \quad (7)$$

where \dot{q}_r'' is the rate of rejected heat per area, h_H is the heat transfer coefficient of the HHEX and T_H is temperature of the HHEX. Both h_H and T_H are input parameters. The heat transfer coefficient depends on the geometry of the heat exchanger and can be determined by standard heat transfer analysis (Incropera and DeWitt, 1996). The temperature distribution and the rate of rejected heat are determined by solving Eqs. (4)–(7). The temperature distribution at the end of stage 2 is then used as the initial conditions in stage 3.

2.1.3. Stage 3 – demagnetization and hot blow

During stage 3 the adiabatic demagnetization reduces the temperature of the regenerator by the local ΔT_{ad}

$$T = T_i + \Delta T_{ad}^{dm}(T_i, \mu_0 H_0), \quad (8)$$

where $\Delta T_{ad}^{dm}(T_i, \mu_0 H_0)$ describes ΔT_{ad} when the magnetic field is decreased from H_0 to zero. The two functions ΔT_{ad}^{dm} and ΔT_{ad}^m are related by the following equation

$$\Delta T_{ad}^m(T, \mu_0 H_0) = -\Delta T_{ad}^{dm}(T + \Delta T_{ad}^m(T, \mu_0 H_0), \mu_0 H_0). \quad (9)$$

The regenerator absorbs heat from the fluid. Part of the cooled fluid is then removed by the pistons and absorbs heat from the cooling load. The rate of heat absorbed through the CHEX is determined by a convective boundary condition

$$\dot{q}_c'' = h_C \cdot (T_C - T), \quad (10)$$

where \dot{q}_c'' is the prescribed cooling load per area of the heat exchanger, h_C is the heat transfer coefficient of the CHEX, and T_C is the temperature of the CHEX. Again both h_C and T_C are input parameters. The temperature distribution and the rate of absorbed

heat is determined by solving Eqs. (4)–(6) along with Eq. (10). The remaining boundaries are considered adiabatic as they are either insulated or symmetry lines in the model geometry

$$\dot{q}'' = 0. \quad (11)$$

The overall boundary conditions for the heat transfer equations are illustrated in Fig. 3.

The temperature distribution at the end of the stage 3 is used as initial conditions for stage 2 in the following cycle. Stage 2 and 3 are repeated for a user-specified number of cycles or until the cyclic steady-state is reached. Steady-state occurs when the temperature distribution at the end of stage 3 is equal to the temperature distribution at the beginning of stage 2.

2.1.4. Stage 4 – evaluation of AMR performance

The amount of cooling absorbed per width of the CHEX per cycle is determined by integration of Eq. (10)

$$q_c' = \int_0^\tau \int_0^L \dot{q}_c'' dx dt, \quad (12)$$

where τ is the cycle period and L is the length of the heat exchanger. The rejected heat per width of the HHEX per cycle is similarly determined by integration of Eq. (7)

Table 1 – Geometrical dimensions used to validate the AMR model

Part	Material	Length (cm)	Height (mm)
Regenerator	Gadolinium	5	0.5
Heat exchangers	Copper	2	0.5
Fluid	Water	16	0.5
Gap between heat exchangers and regenerator	–	1	0.5

Table 2 – Material properties evaluated at 298 K (Lide, 2004; Klein, 2004)

Material	c_p ($J kg^{-1} K^{-1}$)	k ($W m^{-1} K^{-1}$)	ρ ($kg m^{-3}$)	μ ($kg m^{-1} s^{-1}$)
Gadolinium	235	10.5	7900	n.a.
Copper	385	401	8933	n.a.
Water	4183	0.595	997	8.91×10^{-4}

$$q'_r = \int_0^\tau \int_0^L \dot{q}''_r dx dt. \quad (13)$$

The total work input per width of the AMR is the sum of the work required to magnetize the regenerator and the work required to move the pistons:

$$w' = w'_{mag} + w'_{piston}. \quad (14)$$

The work required to magnetize and demagnetize the regenerator bed cannot be calculated directly, but since there are no losses in the AMR, the 1st law of thermodynamics can be used to determine the total work input per cycle as

$$w'_{mag} = q'_r - q'_c. \quad (15)$$

The work required to move the fluid is not included in Eq. (15), because of the decoupling between the momentum equation and the heat transfer equations. The work required to displace the fluid during the two blow periods is evaluated from the pressure induced forces acting on the ends of the pistons

$$w'_{piston} = \int_0^\tau \left(U_p(t) \cdot \int_0^{H_p} \Delta p(y, t) dy \right) dt, \quad (16)$$

where U_p is the velocity of the pistons, t is the time, H_p is the height of the pistons and Δp is the pressure difference between the two pistons.

2.2. Modelling the piston displacement

The displacement of the heat transfer fluid constitutes a moving boundary problem as the pistons move position during the cycle. To model the stroke of the pistons, the model geometry is divided into a solid domain (the two heat exchangers and the regenerator) and a fluid domain. The situation where the pistons displace the fluid below the solid domain is equal to

Table 3 – Magnetic properties of gadolinium used to determine the magnetocaloric effect

Parameter	Value
N (kg^{-1})	3.83×10^{24}
N_s (kg^{-1})	3.83×10^{24}
θ_D (K)	169
θ_C (K)	293
γ_e ($J kg^{-1} K^{-2}$)	6.93×10^{-2}
g_j	2
J (\hbar)	3.5

Data taken from Lide (2004) and Tishin and Spichkin (2003).

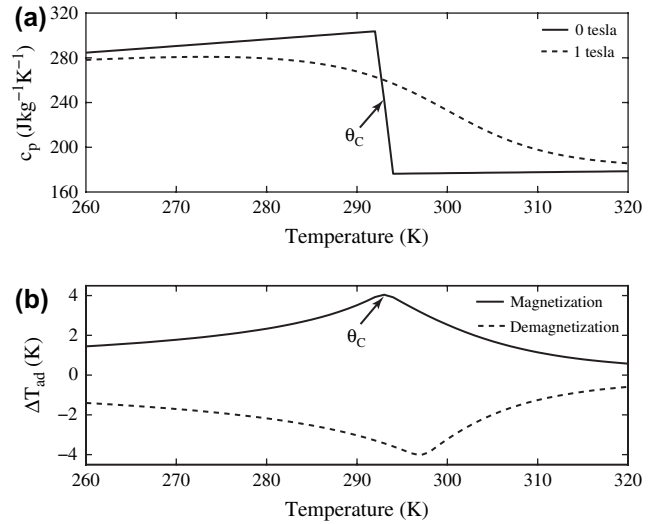


Fig. 5 – (a) The heat capacity of gadolinium as a function of temperature in zero magnetic field and in a magnetic field of 1 T. As shown on the figure there is a sharp decrease at the Curie temperature with zero field, whereas an applied magnetic field smoothes the transition. (b) The ΔT_{ad} of gadolinium during both magnetization and demagnetization is a function of temperature. During magnetization, ΔT_{ad} peaks at the Curie temperature with a maximum of 4.1 K, whereas ΔT_{ad} during demagnetization peaks at a higher temperature in agreement with Eq. (9).

a situation where the fluid domain is stationary while the solid domain slides along the upper boundary of the fluid. This approach allows both the solid and the fluid domains to be modelled as stationary, while the relative movement is simulated using the coordinate transformation illustrated on Fig. 4.

To implement the coordinate transformation let x_s be the x-coordinate of the solid domain boundary, x_f be the

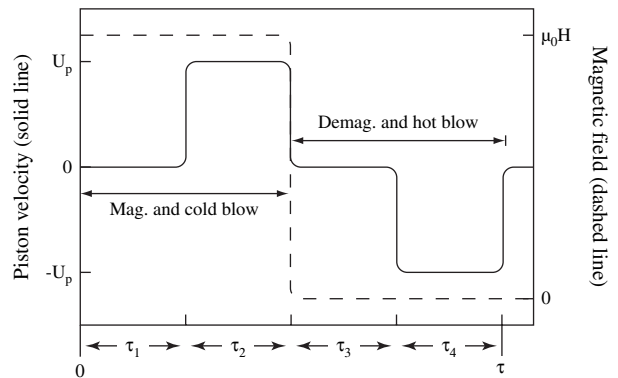


Fig. 6 – The variation of the piston velocity (solid line) and the magnetic field (dashed line) during the AMR cycle. The pistons are stationary during the magnetization period (τ_1) and demagnetization period (τ_3) and move with a constant velocity during the cold blow (τ_2) and hot blow (τ_4). The magnetic field is applied at the beginning of the cycle (0 and τ) and removed at the end of the cold blow.

Table 4 – Process parameters for the AMR cycle

Parameter	Value and unit
Piston stroke	2 cm
Cycle period (τ)	6 s
τ_1 and τ_3	2 s
τ_2 and τ_4	1 s
$\mu_0 H$	1 T
T_H and initial temperature	298 K
h_H	$10^6 \text{ W m}^{-2} \text{ K}^{-1}$
h_C	$0 \text{ W m}^{-2} \text{ K}^{-1}$

x -coordinate of the fluid domain boundary, and Δx denote the displacement of the solid domain relative to the fluid. The two coordinates are related by the following expression

$$x_f = x_s + \Delta x(t). \quad (17)$$

Since Δx is equal to the stroke of the pistons, it can be determined by integration of the piston velocity

$$\Delta x(t) = \int_0^t U_p(t') dt'. \quad (18)$$

If $T_s(x_s)$ is the temperature of the solid and $T_f(x_f)$ is the temperature of the fluid, both along the interfacing boundary, then x_s can be substituted by Eq. (17) and $T_s(x_s)$ can be expressed in terms of x_f

$$T_s(x_f - \Delta x) = T_f(x_f). \quad (19)$$

The corresponding temperatures determined by Eq. (19) are used in Eq. (6) to couple the two domains.

The solution of the velocity distribution in the fluid must also account for the coordinate transformation. This is done by specifying the appropriate boundary conditions for Eqs. (1) and (2). The interface between the fluid and the pistons is a no-slip boundary where

$$\begin{pmatrix} u \\ v \end{pmatrix} = \begin{pmatrix} 0 \\ 0 \end{pmatrix}. \quad (20)$$

The interface between the fluid and the solid has a prescribed velocity equal to the velocity of the pistons as shown in Fig. 4, where

$$\begin{pmatrix} u \\ v \end{pmatrix} = \begin{pmatrix} U_p(t) \\ 0 \end{pmatrix}. \quad (21)$$

The symmetry line is modelled as a slip boundary where the

Table 5 – The grids used for the grid sensitivity analysis

	Coarse grid	Normal grid	Fine grid
	$N_x \times N_y$	$N_x \times N_y$	$N_x \times N_y$
Regenerator	33×6	50×10	75×15
Heat exchangers	13×6	20×10	30×15
Fluid	106×6	160×10	240×15

N_x denotes the number of elements in the x -direction and N_y denotes the number of elements in the y -direction. The normal grid correspond to an element size of $1 \text{ mm} \times 0.05 \text{ mm}$ in all parts of the geometry.

normal component of the velocity is zero

$$v = 0, \quad (22)$$

and the tangential component of the viscous force is zero

$$\mu_f \left(\frac{\partial u}{\partial y} \right) = 0. \quad (23)$$

2.3. Modelling the magnetocaloric effect

The total heat capacity of a magnetocaloric material, $c_{p,s}$ is the sum of the magnetic, lattice and electronic heat capacities, denoted c_m , c_l and c_e , respectively (Tishin and Spichkin, 2003)

$$c_{p,s} = c_m + c_l + c_e. \quad (24)$$

ΔT_{ad} is calculated as

$$\Delta T_{ad} = -\mu_0 \int \frac{T}{c_p} \left(\frac{\partial \sigma}{\partial T} \right)_H dH, \quad (25)$$

where μ_0 the vacuum permeability and σ is the specific magnetism. Eq. (25) is integrated over the change in magnetic field strength to determine the resulting ΔT_{ad} . In this paper the magnetic heat capacity and the specific magnetism is determined using the Weiss mean field model, the lattice heat capacity is determined with the Debye model and the electronic heat capacity is determined using the Sommerfeld model. These models are presented in Appendix A. However, it should be noted that the numerical AMR model can also use experimental data of the MCE.

3. Model validation

The model was discretized with the weak formulation of the Finite Element Method which solves the PDEs on integral form, and implemented in the commercial software Comsol Multiphysics. The Comsol Multiphysics code has previously been validated through a number of NAFEMS¹ benchmark studies (Comsol, 2005a). However, because the presented model use an uncommon method to solve the moving boundary problem, the model is further validated through a series of tests. Three tests are performed: (1) a validation that the model has energy conservation, (2) a verification that the steady-state is independent of the initial conditions and (3) an analysis of the grid and time step sensitivity of the final model.

3.1. Implementation detail

To perform the validation, the AMR model was implemented with the system geometry shown in Table 1, and the material properties² shown in Table 2. Gadolinium was chosen as the regenerator material as it is regarded as a benchmark material for MR because of its high MCE near room temperature. The material properties used to model the MCE of gadolinium

¹ National Agency for Finite Element Methods and Standards.

² The constant value of the heat capacity of gadolinium shown in Table 3 is only used in the validation of the conservation of the energy validation, otherwise the heat capacity depends on both the temperature and the magnetic field.

Table 6 – The time steps used for the time step sensitivity analysis

Time step	Number of time steps
Fine	240
Normal	120
Coarse	60

are shown in Table 3 and the resulting heat capacity and ΔT_{ad} are shown in Fig. 5.

Fig. 6 shows a schematic representation of the velocity of the pistons and the application of the magnetic field during a typical AMR cycle.

The process parameters of the AMR cycle used in the present calculation are shown in Table 4. Perfect thermal contact between the HHEX and the surroundings was used as a first assumption and obtained with a high value of h_H . The CHEX was thermally isolated, by setting h_C to zero, to ensure that all the work applied during the magnetization and the demagnetization is rejected through the HHEX. The spatial discretization of the geometry consists of a grid of rectangular elements, and the temporal discretization of the AMR cycle consists of a number of time steps of equal length. The grid sensitivity analysis is performed on three grids where each grid has at least 50% more elements in each direction than the previous, see Table 5. Similarly, the time step sensitivity analysis is performed with the number of time steps shown in Table 6. The grid sensitivity analysis is performed with the normal time step, and the time step sensitivity analysis is performed on the normal grid. During all the calculations the velocity distribution in the fluid is determined with the fine grid and the fine time step to ensure sufficient detail of the velocity boundary layer as discussed previously.

3.1.1. Conservation of energy

To analyze the energy conservation, a test case is designed where the heat capacity of gadolinium is taken to be constant and the MCE is simplified to a fixed temperature of 5 °C and –4 °C for ΔT_{ad}^m and ΔT_{ad}^{dm} , respectively. The fixed difference between ΔT_{ad}^m and ΔT_{ad}^{dm} result in a net total work input which can be calculated analytically. The magnetic work input per cycle per unit width of the regenerator is

$$w'_{mag} = \rho c_p \Omega \cdot (\Delta T_{ad}^m + \Delta T_{ad}^{dm}) = 46.41 \text{ J/m}, \quad (26)$$

where Ω is the volume of one half of a regenerator plate. During steady-state the result of Eq. (26) should be equal to the result from Eq. (15). To test energy conservation the steady-state

Table 7 – Comparison and relative difference (δ) between the numerical and the analytical solution for the three grids and the three time steps

	Grid			Time step		
	Coarse	Normal	Fine	Coarse	Normal	Fine
$w' \text{ (J/m)}$	46.33	46.35	46.41	46.39	46.35	46.45
$\delta \text{ (%)}$	0.18	0.13	0.011	0.057	0.13	–0.082

Table 8 – The results of the grid and time step sensitivity of the final model with temperature and magnetic field dependent heat capacity and ΔT_{ad}

	Grid			Time step		
	Coarse	Normal	Fine	Coarse	Normal	Fine
$\bar{T}_C \text{ (K)}$	287.17	287.14	287.14	287.14	287.14	287.14
$w' \text{ (J/m)}$	2.48	2.32	2.34	2.30	2.32	2.35

must be obtained. In numerical terms, the steady-state is reached when the maximum difference between the temperature profiles in the regenerator in two subsequent cycles are below the absolute tolerance of the solution. The conservation of energy test is subjected to a grid and time step sensitivity analysis using the three grids and time steps shown in Tables 5 and 6. The model was solved with an absolute tolerance on the temperature of 0.01 K, and a total of 600 cycles was simulated to obtain the numerical steady-state. The results of the conservation of energy analysis are shown in Table 7.

The numerical values for the grid sensitivity analysis are found to be very close to the analytical solution with a relative difference below 0.2% for all three grids. There is a monotonic decrease of the relative difference as the amount of grid elements is increased, which is expected as the discretization error decreases with a decreasing size of the grid element. These results show that the model has energy conservation and can accurately determine the energy input during the magnetization and the demagnetization. The low error further shows that the moving mesh algorithm is functioning correctly and independently of the mesh. The time step sensitivity analysis of the energy conservation shows a decrease in the relative difference as the time step is decreased, but in absolute terms the coarse time step has the lowest difference between the analytical and the numerical solution. It may seem counterintuitive that largest time step results in the smallest deviation. However, the time-dependent terms are solved with a backwards differentiation formula (BDF) which uses a variable-order, variable-time step scheme (Comsol, 2005b). The BDF method ensures that an accurate solution is achieved by adapting the time step to actual problem, but as a result, the time step used during the simulation may be significantly different from the specified time step.

3.2. Independence of initial conditions

To verify that the cyclic steady-state solution is independent of the initial conditions, a simulation was performed with a linear temperature gradient as the initial condition. The solution obtained with the new initial conditions is compared to

Table 9 – Comparison between the solution for two different initial conditions for the AMR model

Initial temperature	w'	$\delta \text{ (%)}$	$T_C \text{ (K)}$	$\delta \text{ (%)}$
Uniform	46.35	–	292.0	–
Gradient	46.35	7.7×10^{-3}	292.0	3.9×10^{-4}

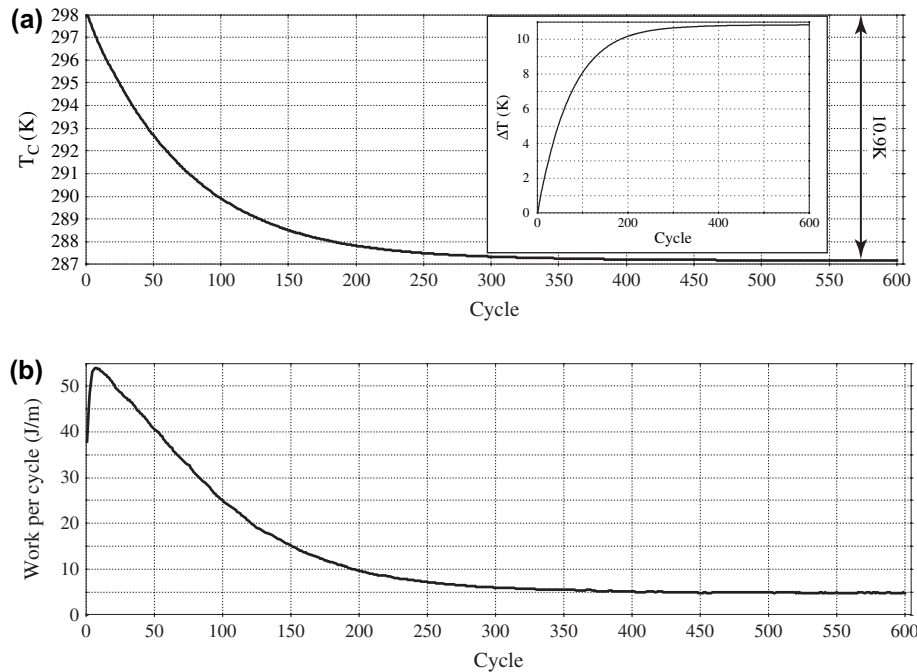


Fig. 7 – (a) The transient evolution of \bar{T}_C from 298.0 K to 287.1 K. The inset shows the corresponding development of ΔT from 0.0 K to 10.9 K. (b) The input work per regenerator plate per cycle for all the simulated refrigeration cycles. The steady-state work input obtained after 600 cycles is 4.65 J/m.

the previously obtained solution (constant heat capacity and MCE, normal grid and time step) and the results are shown in Table 9. The results obtained with the two types of initial conditions show that two values of w' are almost equal and the two values of T_C are equal within the solver tolerance.

3.3. Grid and time step sensitivity analysis

As Fig. 5 shows, both the heat capacity and the ΔT_{ad} of a magnetocaloric material are very non-linear in the temperature region where the AMR operates and especially near the Curie temperature. It is therefore important to choose a grid which is fine enough to accurately predict the performance of the AMR. To determine the sensitivity of the solution to the grid and the time step, the model was implemented with a temperature and magnetic field dependent heat capacity and the performance of the AMR was simulated with the three different grids and time steps. The results of the grid and time step sensitivity analysis of the model with non-linear heat capacity and ΔT_{ad} are given in Table 8 in terms of T_C and the total work input w' . However, because the temperature of the CHEX is unspecified, the temperature will vary over the heat exchanger surface during the cycle. The average temperature of the CHEX per cycle is determined as

$$\bar{T}_C = \frac{1}{\tau \cdot L} \int_0^\tau \int_0^L T_s(x, t) dx dt. \quad (27)$$

Both \bar{T}_C and w' , decrease as the grid becomes finer. However, it seems as if the value of w' increases slightly when the grid is changed from normal to fine. This is because the heat flux depends on the temperature and even small temperature variations below the solver tolerance results in variations of w' . For

the time step analysis, the values of \bar{T}_C are equal within the solver tolerance and there is a monotonic increase of w' as the time step decreases. These results indicate that all three grids are “fine enough” to yield similar solutions, and that further refinement of the grid will bring the solution successively closer to a grid-independent solution (Ferziger and Peric, 2002). However, increasing the number of grid elements increases the computation time. Compared to the coarse grid, the normal grid increases the solution time by a factor of 1.9 while using the fine grid increases the solution time by a factor of 4.3.

3.4. Final remarks on the validation

The main conclusions from the validation is that the model has energy conservation and from the grid and time step sensitivity analysis it was shown that the solution is almost independent of both grid and time step and that any combination results in accurate results. In the remainder of the paper the normal grid and the normal time step is therefore used. From the initial condition analysis it was concluded that the AMR model is independent of the initial conditions. This means that a linear gradient can be used as an initial “guess” to decrease the solution time if the transient development of the temperature is not required.

4. Results

The mean field model was used to evaluate ΔT_{ad} and the heat capacity of gadolinium as functions of the magnetic field and the temperature as discussed in Section 2.3 and the MCE data

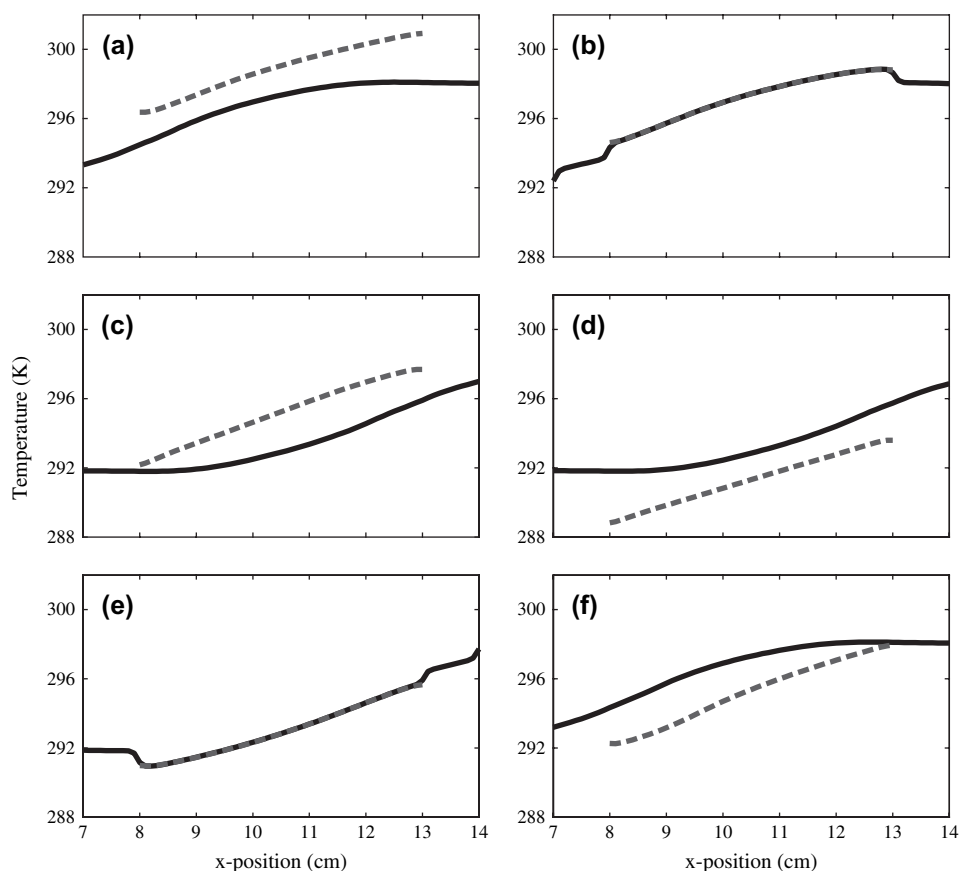


Fig. 8 – The temperature distribution in the regenerator (dotted line) and the fluid (solid line) at various points during the AMR cycle. (a) After the magnetization the temperature of the regenerator is above that of the fluid. There is an almost linear temperature profile in the regenerator whereas the temperature profile in the fluid is non-linear and flat near the right end because of the fluid, which has just entered from the HHEX. (b) Before the hot blow there is thermal equilibrium between the regenerator and the fluid. At the furthest positions to the left and right the temperature is lower than within the regenerator. This corresponds to the gap between the regenerator and the heat exchangers. (c) After the hot blow the temperature in the fluid is must lower than in the regenerator. At left end of the regenerator, the temperature of the fluid is almost constant which corresponds to the fluid, which has just entered from the CHEX. (d) After the demagnetization the temperature of the regenerator is below that of the fluid. (e) Before the cold blow there is thermal equilibrium between the regenerator and the fluid. (f) After the cold blow the temperature in the fluid is higher than in the regenerator.

were implemented in the AMR model. No cooling load was applied at the CHEX in order to determine the maximum obtainable temperature span between the CHEX and the HHEX ($\Delta T = T_H - T_C$). Fig. 7a shows the evolution of \bar{T}_C and w' as a function of the cycle number. After 600 cycles, \bar{T}_C is found to be 287.1 K which results in a ΔT of 10.9 K (T_H was kept constant at 298.0 K). The total work input per cycle, w' , is found to be 4.65 J/m per regenerator plate³ corresponding to 93.0 kJ m⁻³ of gadolinium. Since the piston work is several orders of magnitude lower than the magnetic work it was neglected. Fig. 7 shows that the transient simulation has an asymptotic convergence towards the cyclic steady-state. This is clearly illustrated by the fact that the change in \bar{T}_C is 10.2 K during the first 200 cycles, while \bar{T}_C only decreases 0.7 K from 200 to 600 cycles. The slow convergence towards the steady-state

³ The results for w' reported in Table 8 are those obtained directly from the model, i.e. for a half plate and fluid channel.

results in a long solution time of the model. The 600 cycles used to obtain the results above required a total solution time of about 53 h on a 3.2 GHz Pentium 4 (Prescott) processor with 2 GB of RAM.

Fig. 8 shows the temperature in the x-direction at various times during the steady-state AMR cycle. The temperature profiles are determined at the middle of the regenerator plate and at the middle of the fluid channel (i.e. at the top and bottom of the AMR geometry shown in Fig. 3). During the magnetization period (Fig. 8a,b) and the demagnetization period (Fig. 8d,e) it seems as if the temperature of the regenerator does not change the temperature of the fluid significantly. This behavior is probably due to that the thermal mass (mc_p) of the fluid is twice that of the average thermal mass of the regenerator. Fig. 8b and e shows that only a small part (approximately 15%) of the fluid within the regenerator is above T_H and below T_C after the magnetization and demagnetization periods, respectively. With the chosen process parameter for

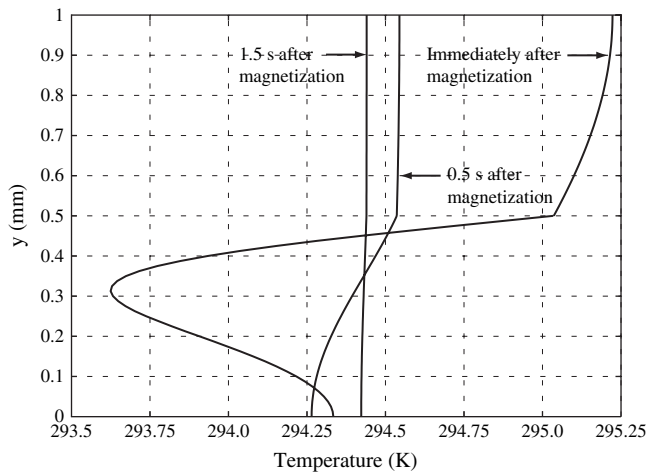


Fig. 9 – The temperature in the y -direction through the regenerator at 0.0 s, 0.5 s and 1.5 s after the magnetization.

the current simulation, the pistons displace 40% of the fluid inside the regenerator where 20% of the displacement is used to clear the gap between the regenerator and the heat exchangers. This might result in that fluid colder than T_H enters the HHEX or fluid warmer than T_C enters the CHEX during the hot and blow periods, respectively. This behavior reduces the performance of the AMR and will occur if there is insufficient regeneration in the AMR. Fig. 8c and f shows that there are significant temperature differences between the regenerator and the fluid after the hot and cold blow. This indicates that there is insufficient regeneration in the AMR, otherwise there should be thermal equilibrium between the regenerator and the fluid. This has two consequences: (1) that the piston stroke is too long as discussed above and (2) that the MCE is not fully utilized. In the case of thermal equilibrium the temperature in the regenerator would be lower after the hot blow and higher after the cold blow. This means the MCE would be able to produce higher and lower temperatures during magnetization and demagnetization, respectively, and this would in turn increase the AMR performance. To obtain better regeneration either the length of the blow periods should be increased or the amount of fluid should be decreased. Since the model is 2-D it is interesting also to examine the temperature distribution in the y -direction. Fig. 9 shows the temperature in the y -direction at the middle of the regenerator at different times after the magnetization.

After the magnetization period, the temperature distribution in both the regenerator and the fluid is found to be non-linear. This is expected as the fluid is still in motion after the hot blow. After 0.5 s, there is a uniform temperature profile in the regenerator bed while the temperature profile in the fluid is still non-linear. After 1.5 s, there is a virtually uniform temperature in both the regenerator and the fluid, indicating that a thermal equilibrium is reached. The magnetization occurs instantaneously which means that the majority of the magnetization period is used for heat transfer. This result shows that the magnetization period can be reduced by at least 0.5 s to increase the frequency of the AMR cycle which in turn increases the AMR performance. The length of the magnetization and demagnetization periods as well as the

overall frequency of the AMR cycle must be optimized to obtain the maximum performance of the AMR.

The above results show that the performance of an AMR is complex and depends on the piston stroke, the ratio between the thermal mass of the regenerator and the fluid as well as the length of the AMR refrigeration cycle. All these parameters should therefore be subjected to an optimization study. These issues will be addressed in a future paper.

5. Conclusion and outlook

A 2-D model of a reciprocating AMR with a regenerator consisting of parallel plates arranged in a stack configuration was developed and verified. The model is designed to be flexible, i.e. it is possible to vary all essential parameters like the dimensions of the regenerator and choice of materials of both regenerator and fluid. Preliminary results show that the model can predict the temperature profile through the regenerator and has the ability to evaluate both the temperature span and the input work of an AMR. The 2-D approach allows analysis of the tangential heat transfer which shows that there are significant temperature differences between the fluid and the regenerator, when a parallel-plate regenerator is used. This justifies the use of a 2-D model and indicates that it is necessary to use 2-D methods when regenerator geometries, which are different from a packed bed of particles, are modelled. Future work will concentrate on using the present model for optimization studies of reciprocal AMRs. In addition, the model will be further validated by comparison with an experimental reciprocal AMR currently under development at Risø National Laboratory.

Acknowledgments

The authors thank Thure Ralfs and Lars Gregersen from Comsol A/S for computational resources and modelling assistance and Christian Bahl for useful discussions.

Appendix A. The Weiss, Debye and Sommerfeld models

5.1. The Weiss mean field model

The magnetic contribution to the heat capacity is determined from the Weiss mean field model (Morrish, 1965; Dinesen et al., 2002)

$$c_m = -\mu_0 H \frac{\partial \sigma}{\partial T} - \frac{1}{2} N_{\text{int}} \frac{(\partial \sigma)^2}{\partial T}, \quad (28)$$

where N_{int} is the mean field constant which is determined as

$$N_{\text{int}} = \frac{3k_B \Theta_C}{N_s g^2 \mu_B^2 J(J+1)}, \quad (29)$$

where k_B is the Boltzmann constant, Θ_C is the Curie temperature, N_s is the number of magnetic spins per unit mass, g is the Landé factor, J is the total angular momentum in units of \hbar , and μ_B is the Bohr magneton. The specific magnetism which is calculated as

$$\sigma = N_s g J \mu_B B_f(\chi) \quad (30)$$

where $B_f(\chi)$ is the Brillouin function defined as

$$B_f(\chi) = \frac{2J+1}{2J} \coth\left(\frac{2J+1}{2J}\chi\right) - \frac{1}{2J} \coth\left(\frac{1}{2J}\chi\right). \quad (31)$$

The quantity χ is the solution to the equation

$$\chi = \frac{gJ\mu_B\mu_0 H}{k_B T} + \frac{3\theta_C J}{T(J+1)} B_f(\chi), \quad (32)$$

where Eq. (32) must be solved by iteration.

5.2 The Debye model

The lattice contribution to the total heat capacity can be calculated from the Debye theory as (Ashcroft and Mermin, 1976)

$$c_l = 9Nk_B \left(\frac{T}{\Theta_D}\right)^3 \int_0^{\Theta_D/T} \frac{x^4 e^x}{(e^x - 1)^2} dx, \quad (33)$$

where N is the number of atoms per unit mass and Θ_D is the Debye temperature.

5.3 The Sommerfeld model

The electronic contribution to the total heat capacity can be calculated from the Sommerfeld theory as (Ashcroft and Mermin, 1976)

$$c_e = \gamma_e T, \quad (34)$$

where γ_e is the Sommerfeld constant.

REFERENCES

- Allab, F., Kedous-Lebouc, A., 2005. Numerical modeling for active magnetic regenerative refrigeration. *IEEE Trans. Magn.* 41, 3757–3759.
- Ashcroft, N., Mermin, N., 1976. *Solid State Physics*. Saunders College Publishing, London.
- Barclay, J.A., 1982. The theory of an active magnetic regenerative refrigerator. NASA STI/Recon Technical Report N 83, p. 34087.
- Barclay, J.A., Sarangi, S., 1984. Selection of Regenerator Geometry for Magnetic Refrigerator Applications. *American Society of Mechanical Engineers*, pp. 9–13.
- Comsol, 2005a. *Comsol Multiphysics Model Library*, third ed. COMSOL AB, Chalmers Teknikpark 412 88 G.
- Comsol, 2005b. *Comsol Multiphysics User's guide Version 3.2b*.
- DeGregoria, A., 1991. Modeling the active magnetic regenerator. *Adv. Cryog. Eng.* 37, 867–873.
- Dinesen, A.R., Linderth, S., Mørup, S., 2002. Direct and indirect measurement of the magnetocaloric effect in a $\text{La}_{0.6}\text{Ca}_{0.4}\text{MnO}_3$ ceramic perovskite. *J. Magn. Magn. Mater.* 253, 28–34.
- Engelbrecht, K., Nellis, G., Klein, S., 2005a. A numerical model of an active magnetic regenerator refrigeration system. *Tech. Rep. ARTI-21CR/612-10075*, University of Wisconsin-Madison.
- Engelbrecht, K., Nellis, G., Klein, S., Boeder, A., 2005b. Modeling active magnetic regenerative refrigeration systems. In: *Proceedings of the First IIF-IIR International Conference on Magnetic Refrigeration at Room Temperature* Montreux, Switzerland, 27–30 September 2005, pp. 265–274.
- Ferziger, J.H., Peric, M., 2002. *Computational Methods for Fluid Dynamics*, third ed. Springer.
- Gschneidner, K., Pecharsky, V., Tsokol, A., 2005. Recent developments in magnetocaloric materials. *Rep. Prog. Phys.* 68, 1479–1539.
- Hall, J., Reid, C., Spearing, I., Barclay, J., 1996. Thermodynamic considerations for the design of active magnetic regenerative refrigerators. *Adv. Cryog. Eng.* 41b, 1653–1664.
- Hu, J.C., Xiao, J.H., 1994. New method for analysis of active magnetic regenerator in magnetic refrigeration at room-temperature. *Cryogenics* 35, 101–104.
- Incropera, F., DeWitt, D., 1996. *Introduction to Heat Transfer*, third ed. John Wiley and Sons.
- Klein, S.A., 2004. *Computer code, Engineering Equation Solver Version V7.174-3D*.
- Lide, D.R. (Ed.), 2004. *CRC Handbook of Chemistry and Physics*, 85th ed. CRC Press.
- Morrish, A., 1965. *The Physical Principles of Magnetism*. Wiley Inc., New York.
- Pecharsky, V., Gschneidner, K., 1999. Magnetocaloric effect and magnetic refrigeration. *J. Magn. Magn. Mater.* 200, 44–56.
- Siddikov, B.M., Wade, B.A., Schultz, D.H., 2005. Numerical simulation of the active magnetic regenerator. *Comput. Math. Appl.* 49, 1525–1538.
- Shir, F., Mavriplis, C., Benneth, L., Torre, E., 2005. Analysis of room temperature magnetic regenerative refrigeration. *Int. J. Refrigeration* 28, 616–627.
- Schroeder, E., Green, G., Chafe, J., 1990. Performance predictions of a magnetocaloric refrigerator using a finite element model. *Adv. Cryog. Eng.* 35, 1149–1155.
- Schumann, T.E.W., 1929. Heat transfer: a liquid flowing through a porous prism. *J. Franklin Inst.* 208, 405–416.
- Tishin, A., Spichkin, Y., 2003. *The Magnetocaloric Effect and its Applications*. Institute of Physics Publishing.
- White, F.M., 1991. *Viscous Fluid Flow*, second ed. McGraw-Hill Inc.

Appendix E

Paper presented at the Nordic
Comsol Conference, 2006

This page was intentionally left blank.

Using a Linux Cluster for Parallel Simulations of an Active Magnetic Regenerator Refrigerator

T. F. Petersen^{*1}, N. Pryds¹ and A. Smith¹

¹Risø National Laboratory, Fuel Cells and Solid State Chemistry Department, Frederiksborgvej 399, P.O. Box 45, DK-4000 Roskilde, Denmark

*Corresponding author: email:thomas.frank.petersen@risoe.dk

Abstract: This paper describes the implementation of a Comsol Multiphysics model on a Linux computer Cluster. The Magnetic Refrigerator (MR) is a special type of refrigerator with potential to reduce the energy consumption of household refrigeration by a factor of two or more. To conduct numerical analysis of an experimental MR, a mathematical model was developed. The model solves the coupled Navier-Stokes and heat transfer equations which describe the physical phenomenon occurring within the MR. The MR performs a cyclic process, and the model must be time-dependent to determine the steady-state conditions. The coupled set of equations and the transient convergence towards the final steady state means that the model has an excessive solution time. To make parametric studies practical, the developed model was implemented on a Cluster to allow parallel simulations, which has decreased the solution time significantly.

Keywords: Magnetic refrigeration, Active Magnetic Regenerator, Linux computer Cluster.

1 Introduction

Magnetic refrigeration (MR) is an uncommon form of refrigeration, traditionally used for cryogenic applications. However, recent advances in materials science have made MR an alternative candidate for refrigeration at room-temperature. When magnetic materials are subjected to a magnetic field under adiabatic conditions, the field forces the spins of the electrons in the material to align. As a result, the magnetic entropy of the material is reduced and because the total entropy is constant, the temperature increases by the adiabatic temperature change (ΔT_{ad}). This effect is known as the magnetocaloric effect (MCE) and is the basis for MR. Compared to conventional refrigeration MR has two main advantages: (1) Magnetic refrigeration is an energy efficient technology with the potential to reduce the

energy consumption of household refrigeration by a factor of two or more [1]. (2) Because MR uses a solid refrigerant, gaseous refrigerants, which may be hazardous and/or contribute to the global warming, are eliminated. Risø National Laboratory has conducted research on MR for several years, and is currently developing a proof-of-concept MR system called an Active Magnetic Regenerator (AMR). To aid in the design of the experimental AMR, a transient two-dimensional mathematical model was developed in Comsol Multiphysics (CM). Due to a long solution time, the model was implemented on a Linux computer Cluster. This has allowed parallel simulations which are used to perform large scale parameter variations. The main purpose of the present paper is to describe the methods used to implement the model in a Cluster environment. Secondly, a method for solving sliding boundary problems is described.

2 The Principle of Magnetic Refrigeration

The MCE is a material dependent property, but even with the most advanced materials and in high magnetic fields, ΔT_{ad} is of a relatively small magnitude (<22 K) [1]. To obtain temperature spans which are comparable to conventional refrigeration the AMR utilizes regeneration.

The AMR developed by Risø is based on the design shown in Figure 1.

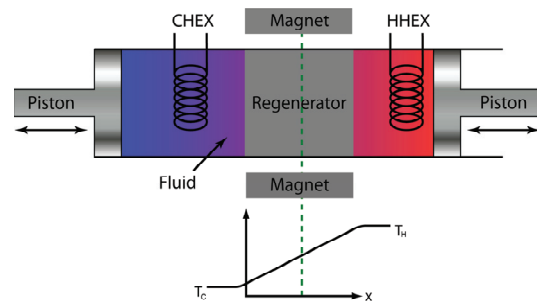


Figure 1: The AMR developed by Risø is based on the linear reciprocating design. At steady-state there is temperature profile across the regenerator.

The AMR is based on a regenerator made of a magnetocaloric solid that allow a fluid to flow through. Examples of regenerator geometries include parallel plates, wire screens or a packed bed of particles. The regenerator is called active because it acts as the refrigerant in the AMR. The regenerator is immersed in a fluid inside an enclosure and pistons in both ends of the enclosure can displace the fluid through the regenerator. The purpose of the fluid is to act as a heat transfer medium to transport heat to and from the regenerator. A heat exchanger placed in one end of the regenerator (CHEX) absorbs heat from a cooling load while a heat exchanger in the other end (HHEX) rejects heat to the ambient. The AMR can move in and out of a magnetic field to produce the MCE. The AMR produces refrigeration in a cyclic process. After a certain amount of cycles, a steady-state is reached and a linear temperature profile is developed across the regenerator from the position of the CHEX (temperature T_C) to the position of the HHEX (temperature T_H), see Figure 1. The AMR refrigeration cycle consists of four sequential steps:

1. The AMR is moved into the magnetic field and the temperature of the regenerator increases by ΔT_{ad} . The fluid is heated by heat transfer from the regenerator.
2. Fluid flows into the regenerator from the cold end and displaces all the fluid in the regenerator with a temperature between T_H and $T_H + \Delta T_{ad}$. The hot fluid rejects heat to the surroundings through the HHEX.
3. The AMR is removed from the magnetic field and the temperature of the regenerator decreases by ΔT_{ad} . The fluid is cooled by heat transfer to the regenerator.
4. Fluid at T_H flows into the regenerator from the hot end, and displaces all the fluid in the regenerator with a temperature between T_C and $T_C - \Delta T_{ad}$. The cold fluid absorbs heat from the cooling load through the CHEX.

3 Modelling approach

This paper does not provide a detailed description of the complete AMR model and this section only contains a summary description of the AMR model. The emphasis is put on the equations essential to understand the methods described in the remainder of this paper. For a complete description see reference [2].

3.1 Model geometry

Figure 2 (A) shows the geometry considered in the model. The repetitive design of the regenerator (parallel plates) allows the full geometry to be simplified, see Figure 2 (B). The gaps between the regenerator plates and the heat exchangers are thermally insulated to ensure that the heat transfer between the regenerator and the heat exchangers only occurs through the fluid.

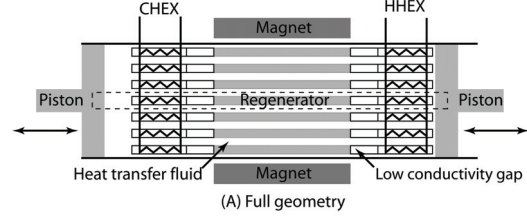


Figure 2: (A) The AMR geometry considered here consists of a regenerator made of parallel plates separated by channels of fluid. Heat exchangers and pistons are placed on at both ends of the plate. (B) By neglecting boundary effects, the full geometry can be reduced to a single repeating unit which consists of a single regenerator plate surrounded by half a channel of fluid on either side. The symmetry allows the geometry of the repeating unit to be further simplified.

3.2 Governing Equations

The velocity distribution in the fluid (f) is determined by solving the Navier-Stokes and continuity equations for an incompressible fluid with constant properties:

$$\rho_f \left(\frac{\partial \mathbf{U}}{\partial t} + (\mathbf{U} \cdot \nabla) \mathbf{U} \right) - \mu_f \nabla^2 \mathbf{U} + \nabla p = 0 \quad (1.1)$$

$$\nabla \cdot \mathbf{U} = 0, \quad (1.2)$$

where ρ_f is the density, μ_f is the viscosity, \mathbf{U} is the velocity field (u, v) and p is the pressure.

The temperature distributions in the regenerator and the heat exchangers (s), are determined by the heat transfer equation:

$$\rho_s c_{p,s} \frac{\partial T_s}{\partial t} + \nabla \cdot (-k_s \nabla T_s) = 0, \quad (1.3)$$

where $c_{p,s}$ is the heat capacity, $\rho_{p,s}$ is the density, T_s is the temperature and $k_{p,s}$ is the thermal conductivity.

The temperature distribution in the fluid is determined by the heat transfer equation with convective terms:

$$\rho_f c_{p,f} \left(\frac{\partial T_s}{\partial t} + (\mathbf{U} \cdot \nabla) T_f \right) + \nabla \cdot (-k_f \nabla T_f) = 0, \quad (1.4)$$

where $c_{p,f}$ is heat capacity, T_f is the temperature and k_f is the thermal conductivity.

During magnetization and demagnetization, the regenerator temperature is changed by ΔT_{ad} according to the following expression:

$$T = T_i + \Delta T_{ad}(T, \Delta B), \quad (1.5)$$

where T_i is the initial temperature in the regenerator and $\Delta T_{ad}(T, \Delta B)$ is a function which describes ΔT_{ad} as a function of temperature for a change in the magnetic field (ΔB). During magnetization ΔB is positive and during demagnetization ΔB is negative.

Comsol Multiphysics does not support direct manipulation of the temperature, and Eq. (1.5) must be implemented using the initial conditions of a transient model. The AMR simulation is therefore performed in two stages; the first stage to implement Eq. (1.5) during the magnetization and the second stage to implement Eq. (1.5) during the demagnetization see Figure 3.

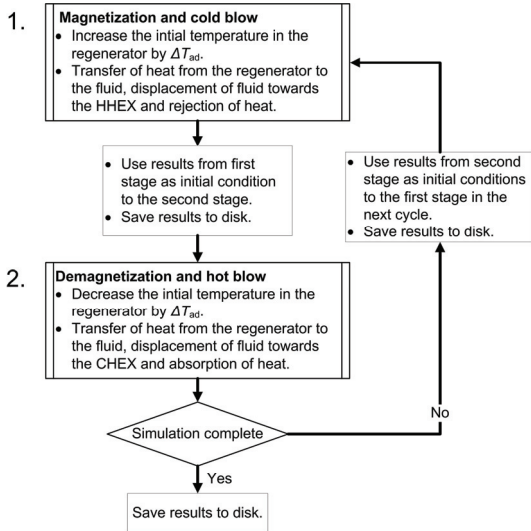


Figure 3: The AMR cycle is modelled by grouping the four physical steps into two repeating stages namely: (1) the magnetization and the cold blow and (2) the demagnetization and the hot blow. Each stage uses the solution from the last time step of the previous stage as initial conditions. The initial temperature in the regenerator is then either increased or decreased by using Eq. (1.5). The two stages are repeated for a user-specified amount of cycles.

The boundary condition between the solid and the fluid is:

$$\left(k_f \frac{\partial T_f}{\partial y} \right) = \left(k_s \frac{\partial T_s}{\partial y} \right). \quad (1.6)$$

The boundary conditions for the heat exchangers are a prescribed temperature, namely T_H and T_C .

4 Methods

This section describes the modelling of the piston displacement and the implementation of the AMR model on a Linux Cluster.

4.1 Modelling the piston displacement

The situation where the pistons displace the fluid between the regenerator plates is equal to a situation where the fluid and pistons are stationary while the regenerator and the heat exchangers slide along the top of the fluid see Figure 4 (A). The movement of the pistons is a sliding boundary problem which is solved using a coordinate transformation. To model the stroke of the pistons, the total geometry is divided into a solid geometry (the two heat exchangers and the regenerator) and a fluid geometry (pistons and fluid), see Figure 4 (B).

To use the coordinate transformation method, let x_s be the x-coordinate of the solid, let x_f be the x-coordinate of the fluid and let Δx be the displacement of the solid domain relative to the fluid. The two coordinates are related by the following expression:

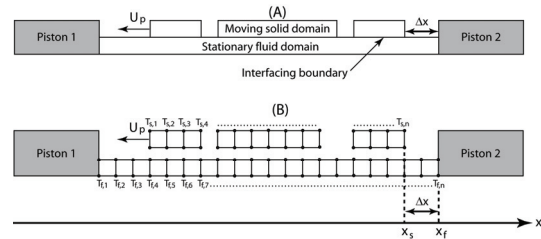


Figure 4: (A): The movement of the pistons is converted to a situation where the solid drags along the top of the fluid. (B): The solid and the fluid domains are modelled as separate geometries, and the piston displacement is modelled with a coordinate transformation. To understand how the coordinate transformation works, consider the situation where the solid has moved a distance (Δx) relative to the fluid. In this case, the temperature of the solid at $T_{s,1}$, $T_{s,2}$, $T_{s,3}$, $T_{s,4}$, is equal to $T_{f,4}$, $T_{f,5}$, $T_{f,6}$, $T_{f,7}$. This coupling can be achieved by knowing the temperature distribution of the solid and fluid along the interface and Δx .

$$x_s = x_f + \Delta x(t), \quad (1.7)$$

where Δx is the displacement of the solid relative to the fluid. Since Δx is equal to the stroke of the pistons, it can be determined by integration of the piston velocity

$$\Delta x(t) = \int_0^t U_p(t') dt', \quad (1.8)$$

where U_p is the velocity of the pistons and t is the time. As shown on Figure 4, $T_s(x_s)$ is the local temperature of the solid and $T_f(x_f)$ is the local temperature of the fluid along the interface. By substituting x_s at the right hand side of Eq.(1.7), $T_s(x_s)$ can be expressed in terms of x_f :

$$T_f(x_f) = T_s(x_f - \Delta x). \quad (1.9)$$

Eq. (1.9) together with Eq. (1.6) are used to couple the two domains. The CM implementation of the coordinate transformation is performed with boundary extrusion coupling variables; a method first described in a generator included in the CM Electromagnetics model library. The implementation of the method for the piston displacement of the fluid is explained in Figure 5.

Although the upper boundary of the fluid domain is defined as adiabatic, the extrusion coupling variables “overrides” this setting, which results in a heat flow between the solid and fluid that corresponds to Eq. (1.6).

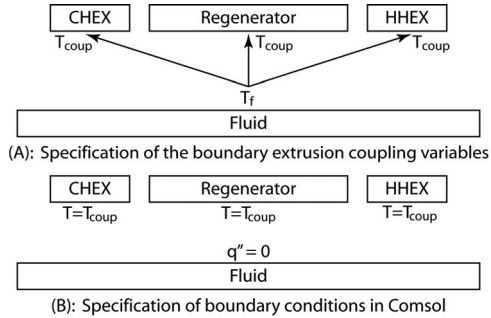


Figure 5: The implementation of the coordinate transformation method in CM is achieved with boundary extrusion coupling variables. (A): The source for the extrusion coupling variable is the temperature of the upper boundary of the fluid with no source transformation. The destinations for the temperature are the lower boundary of the CHEX, HHEX and the regenerator. A destination transformation of “ $x-\Delta x$ ” is used to implement the coordinate transformation given by Eq. (1.9). (B): The boundary condition of the lower boundaries of the CHEX, HHEX and the regenerator are a prescribed temperature equal to the temperature of the fluid. The upper boundary of the fluid is adiabatic.

In order for the model to be consistent, the boundary conditions of Eqs. (1.1) and (1.2) must also account for the stationary pistons and for the sliding of the solid along the top of the fluid.

4.2 Implementation on a Linux Cluster

Implemented in CM, the AMR model requires a solution time of about 53 hours per simulation. The long solution time is prohibitive for the extensive parameter variations required to determine an optimal AMR design. To solve this problem, the AMR model was implemented on a Linux computer Cluster with the purpose of allowing parallel simulations. A Cluster is a group of coupled computers which work together and divide a single computational job between multiple individual computers (nodes). In this respect, a Cluster allows the individual nodes to work as single multiprocessor computers. Presently, CM does not support multiple processors. Thus, the use of a Cluster does not reduce the simulation time of individual simulations, but allows parameter variations to be performed in the time of a single simulation. The Cluster is operated by a central server which manages the nodes, and the user only interacts with the server, as shown on Figure 6.

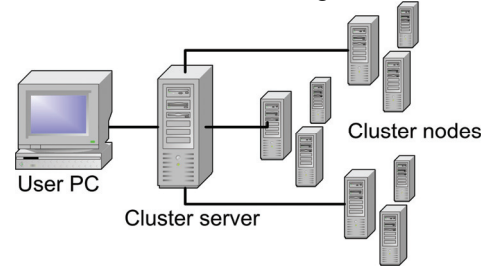


Figure 6: Dataflow from the user PC to the central server which operates the nodes of the Cluster.

The central server schedules the individual simulations and runs them on the nodes. This allows the user to start more simulations than there are nodes in the Cluster. As the simulations are completed and the nodes become available, the server starts the remaining simulations.

In addition to hardware, the following are required to run a CM model on a Cluster:

- A software system for operating a Cluster.
- Converting the CM model to a script.
- A display system for graphics.
- A Comsol license for each simulation.

The purpose of the Cluster software is to interconnect the nodes and allow them to act as

whole. The Cluster software allows the nodes to communicate with each other, such that any program running on the Cluster sees the nodes as single computer. The software is also used to schedule the simulations. In this study, the Linux based OSCAR software is used [3]. The Cluster must be able to start simulations automatically. The simplest way to achieve this is to export the CM model as a Matlab script which can be solved by CM in batch mode. Comsol Multiphysics must have access to a display system even if graphics are not used. In this implementation, the nodes access a Virtual Network Computing (VNC) server which provides the display. The license manager regards each computer in the Cluster as an individual computer; therefore a license is required for each concurrent simulation.

5 Numerical Model

The AMR model was implemented with the typical geometrical dimensions shown in Table 1 and the material properties shown in Table 2.

Table 1: Geometrical data of the AMR model

Part	Material	Length	Height
Regenerator	Gadolinium ¹	5 cm	0.5 mm
CHEX	Copper	2 cm	0.5 mm
HHEX	Copper	2 cm	0.5 mm
Fluid	Water	16 cm	0.5 mm

Table 2: Material properties evaluated at 298 K [3, 4].

	Gadolinium	Copper	Water
c_p (J/(kg·K))	235 ²	385	4186
k (W/(m·K))	10.9	401	0.595
ρ (kg/m ³)	7900	8933	997
μ (kg/(m·s))	-	-	$8.91 \cdot 10^{-4}$

The pistons are stationary during the periods which the AMR is in and out of the magnetic field and move with a constant velocity during the displacement periods. The process parameters of the AMR cycle used in the present simulations are given by Table 3.

Table 3: The process parameters used in the implementation of the numerical AMR model.

Parameter	Value
Magnetic field	1T
Piston stroke (Δx)	2 cm
Cycle period (τ)	6 s
Time in and out of the magnetic field	2 s
Time used to displace the fluid	1 s

5.1 Test of the sliding boundary method

Using a boundary extrusion coupling variable to solve the sliding boundary problems is non-trivial and a test was performed to determine whether the method obeys energy conservation. The test consists of simulating a single AMR cycle with no heat flux through the CHEX and the HHEX. In addition, the MCE is not implemented in the test; instead the regenerator is simply given a 5 K higher temperature than the rest of the AMR system. The heat capacity of Gadolinium is regarded as constant with the value given by Table 2. The energy conservation of the model is tested with the following equation:

$$\delta_{abs} = \int_0^\tau \left| \sum_{i=1}^N \rho_i c_{p,i} \Omega_i \cdot \frac{\partial T}{\partial t} \right| dt, \quad (1.10)$$

where N is the number of domains, Ω is the volume, $\partial T / \partial t$ is the derivative of the temperature with respect to time and δ_{abs} is the absolute residual. The relative residual is determined as:

$$\delta_{rel} = \frac{\delta_{abs}}{\sum_{i=1}^N \rho_i c_{p,i} \Omega_i \cdot T_i} \cdot 100\%. \quad (1.11)$$

If the model obeys energy conservation both the residuals are (approximately) zero. The test is performed for three cases where each test increases the complexity of the model. (1) No piston displacement and no velocity in the fluid. (2) Piston displacement but no velocity in the fluid. (3) Both piston displacement and velocity distribution in the fluid. The results of the test cases are shown in Table 4.

Table 4: The results of the energy conservation test of the coordinate transformation method

Test case	δ_{abs} (J)	δ_{rel} (%)
1	$7.16 \cdot 10^{-8}$	$5.34 \cdot 10^{-11}$
2	$9.98 \cdot 10^{-3}$	$7.45 \cdot 10^{-6}$
3	$1.96 \cdot 10^{-2}$	$1.46 \cdot 10^{-5}$

¹ The ferromagnetic metal Gadolinium is considered a benchmark material for MR.

² The heat capacity of Gadolinium is not constant, but dependent on both the temperature and the magnetic field.

The low absolute and relative results in the first test case show that the coordinate transformation method obeys energy conservation. The relative movement between the domains increases the residual by five orders of magnitude and the addition of the movement of the fluid increases the residual by a factor of ~ 2 . However, the relative residual are in all the test cases low enough to conclude that the coordinate transformation method obeys energy conservation.

6 Results

Figure 7 shows an example of a typical parameter variation. In each simulation T_H was 298 K while T_C was decreased from 298 K in steps of 2 K. For each simulation the Coefficient Of Performance (COP) is determined as:

$$COP = \frac{q_C}{w}, \quad (1.12)$$

where q_C is the heat absorbed from the cooling load per cycle, and w in the work per cycle.

The work is calculated from the 1st law of thermodynamics:

$$w = q_H - q_C, \quad (1.13)$$

where q_H is the rejected heat per cycle.

The COP is a measure of the energy efficiency of a given refrigerator. A typical COP value for conventional household refrigerators is no larger than 2 [1], and as Figure 7 shows, the AMR has a much higher value.

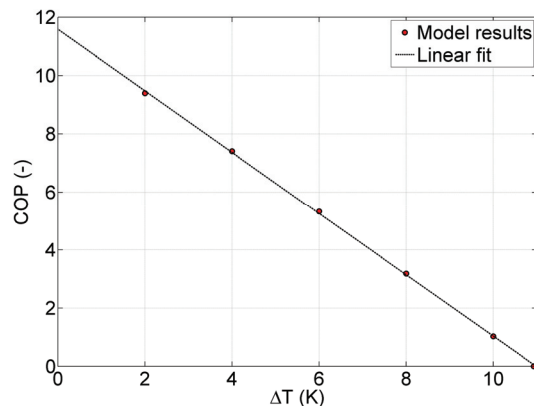


Figure 7: The parameter variation shows a linear decrease of the COP as ΔT ($T_H - T_C$) increases. This was expected because as ΔT increases, a larger fraction of the energy produced by the MCE is used to sustain the ΔT which in turn reduces the amount of heat which can be absorbed from the cooling load.

7 Discussion

The use of a Cluster to solve the AMR model presented here results in large time savings. Parameter variations which would previously take weeks can now be achieved within days. A Cluster implementation has several advantages over running a series of simulations on individual computers. The Cluster allows individual simulations to be scheduled automatically which simplify user interaction. In addition, the Cluster allows the individual nodes to act as a multiprocessor computer for parallel computations. The latter possibility is important, as the forthcoming version of CM includes a new solver which supports multiprocessors and parallel processing. This will allow other types of CM models to take advantage of a Cluster and reduce the solution time of simulations significantly.

8 Conclusion

To determine an optimal AMR design numerous parameter variation studies are required or a large set of experiments are needed. Numerical studies were previously unpractical due to the long solution time of the AMR model presented here. The Cluster implementation of the AMR model has made parallel simulations possible, and allowed for detailed investigations of AMR behavior. At present, only parameter variation studies will benefit from a Cluster, but the use of Clusters will be more important in the future as new versions of Comsol Multiphysics include solvers designed for parallel computations. This development will allow many other types of numerical studies to benefit from a Cluster implementation.

9 References

- [1] Gschneidner, K. A., Pecharsky, V. K., and Tsokol, A. O. Recent developments in magnetocaloric materials, *Reports on Progress in Physics*, **68**, 1479-1539 (2005)
- [2] Petersen, T. F., Pryds, N., Smith, A., Hattel, J., Schmidt, H., and Knudsen, H. H. Two-dimensional Mathematical Model of a Reciprocating Room-Temperature Active Magnetic Regenerator, submitted to the *International Journal of Refrigeration* (2006).
- [3] Open Source Cluster Application Resources, <http://oscar.openclustergroup.org> (2005)
- [4] Lide, D. R. *CRC Handbook of chemistry and physics*, 85th edition (2004).
- [5] Klein, S. A. *EES - Engineering Equation Solver* (2004).

Appendix F

Paper presented at The Second
IIF-IIR International Conference
on Magnetic Refrigeration at
Room Temperature, 2007

This page was intentionally left blank.

A NUMERICAL ANALYSIS OF A RECIPROCATING ACTIVE MAGNETIC REGENERATOR WITH A PARALLEL-PLATE REGENERATOR GEOMETRY

T.F. PETERSEN*, N. PRYDS, A. SMITH, C.R.H. BAHL

Risø National Laboratory, Fuel Cells and Solid State Chemistry Department, Frederiksborgvej
399, P.O. Box 49, DK-4000 Roskilde, Denmark

*Corresponding author: *e-mail address*: thomas.frank.petersen@risoe.dk

ABSTRACT

We have developed a two-dimensional model of a reciprocating Active Magnetic Regenerator (AMR) with a regenerator made of parallel plates arranged in a stack configuration. The time-dependent, two-dimensional model solves the Navier-Stokes equations for the heat transfer fluid and the coupled heat transfer equations for the regenerator and the fluid. The model is implemented using the Finite Element Method. The model can be used to study both transient and steady-state phenomena in the AMR for any ratio of regenerator to fluid heat capacity. Results on the AMR performance for different design choices and operating parameters are presented and the implications for optimal AMR operation are discussed.

INTRODUCTION

Recently, we have developed a two-dimensional mathematical model of an AMR based on the linear reciprocating configuration [1]. The purposes of this model are: (1) to analyze different design options for an experimental AMR, (2) to determine the optimal operating conditions for an AMR and (3) to help understand the physical phenomena which occur inside the AMR. **Figure 1(A)** shows a schematic illustration of the AMR considered in the present study, which consists of an enclosure where a magnetocaloric regenerator, immersed in a fluid, is situated. Pistons are mounted at both ends of the enclosure to move the fluid through the regenerator and into contact with two heat exchangers also placed in either end. One of the heat exchangers (CHEX) is connected to a cold heat source and the other heat exchanger (HHEX) is connected to a hot heat sink. The magnetocaloric effect (MCE) is generated in the regenerator by moving the AMR enclosure in and out of a static magnetic field. **Figure 1(B)** shows a close-up of the geometry of the regenerator that consists of flat parallel plates arranged in a stack configuration and separated by channels of fluid.

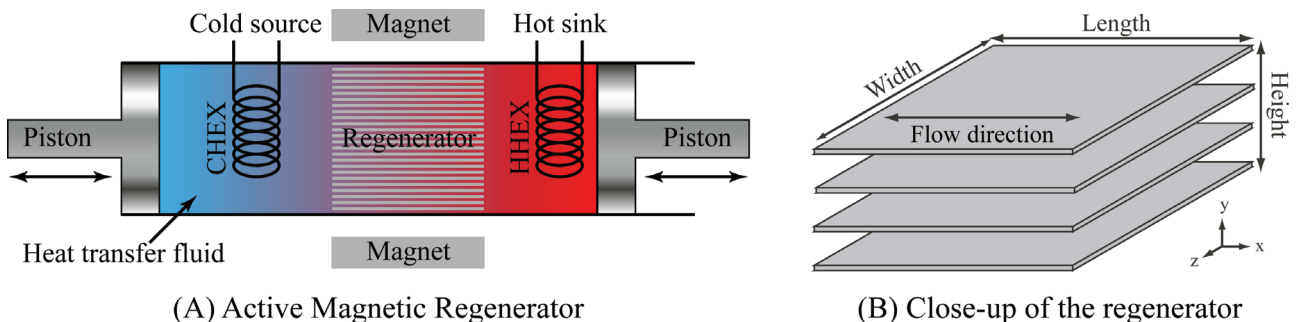


Figure 1: (A) Schematic illustration of the reciprocating AMR. (B) The geometry of the regenerator consists of parallel plates separated by channels of fluid.

The AMR performs a refrigeration cycle with four steps: (1) Magnetization where the temperature of the regenerator increases and heat is transferred to the fluid, (2) the cold blow with displacement of fluid from the regenerator towards the HHEX and rejection of heat to the hot sink, (3) demagnetization which results in the reduction of both the temperature of the regenerator and the temperature of the surrounding fluid and (4) the hot blow with displacement of the fluid from regenerator towards the CHEX and absorption of heat from the cold source [2]. The first part of this paper gives a short presentation of the numerical model followed by the second part which presents the results of a numerical optimization study for selected operating parameters of the AMR.

1 THE TWO-DIMENSIONAL AMR MODEL

This section only contains a summary description of the AMR model, for a comprehensive description see ref. [1]. To determine the performance of the AMR system, the model solves the Navier-Stokes equations for the heat transfer fluid, and the coupled heat transfer equations of the regenerator and the fluid. The model is time-dependent allowing a study of both the transient phenomena in the AMR and the cyclic steady-state performance,

1.1 Model geometry

Figure 2(A) shows a schematic illustration of the AMR geometry considered in the modelling. By neglecting boundary effects, the periodicity of the regenerator allows the full geometry to be simplified to a repeating unit, which consists of a single regenerator plate with half a channel of fluid on either side, see **Figure 2(B)**. The regenerator and the heat exchangers are separated by a small gap with low thermal conductivity to ensure that all heat transfer between the two occurs through the fluid.

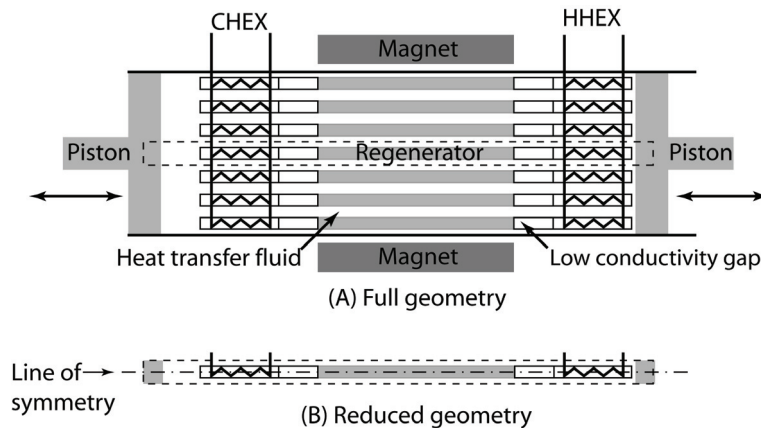


Figure 2: (A) A schematic representation of the geometry considered in the numerical AMR model. (B): Using the periodicity of the regenerator the full geometry can be simplified to a single repeating unit. The symmetry allows the repeating unit to be further simplified.

1.2 Governing equations

The velocity field in the fluid (subscript f) is determined by solving the momentum and continuity equations for an incompressible fluid, with constant temperature independent properties:

$$\rho_f \left(\frac{\partial \mathbf{U}}{\partial t} + (\mathbf{U} \cdot \nabla) \mathbf{U} \right) - \mu_f \nabla^2 \mathbf{U} + \nabla p = 0, \quad (1)$$

$$\nabla \cdot \mathbf{U} = 0, \quad (2)$$

where ρ_f is the density of the fluid, μ_f is the viscosity of the fluid, \mathbf{U} is the velocity field (u,v) in the fluid and p is the pressure in the fluid. The temperature distributions in the solids (regenerator and the heat exchangers) (subscript s) are determined by separate heat transfer equations for each solid:

$$\rho_s c_{p,s} \frac{\partial T_s}{\partial t} - \nabla \cdot (k_s \nabla T_s) = 0, \quad (3)$$

where $c_{p,s}$ is the heat capacity of the relevant solid, ρ_s is the density of the solid, T_s is the temperature of the solid and k_s is the thermal conductivity of the solid. The temperature distribution in the fluid is determined by the heat transfer equation with convective terms:

$$\rho_f c_{p,f} \left(\frac{\partial T_f}{\partial t} + (\mathbf{U} \cdot \nabla) T_f \right) - \nabla \cdot (k_f \nabla T_f) = 0, \quad (4)$$

where $c_{p,f}$ is heat capacity, T_f is the temperature and k_f is the thermal conductivity of the fluid respectively. During magnetization and demagnetization it is assumed that the magnetically induced temperature change (ΔT_{ad}) generated by the MCE occurs instantaneously and adiabatically in the regenerator:

$$T = T_i + \Delta T_{ad}(T, \Delta B) \quad (5)$$

where T_i is the initial temperature in the regenerator and $\Delta T_{ad}(T, \Delta B)$ is a function of the temperature and the magnetic field (ΔB). During magnetization, ΔB and ΔT_{ad} are positive while during demagnetization ΔB and ΔT_{ad} are negative.

1.3 Boundary conditions

Figure 3 shows the overall boundary conditions for the various parts of the AMR. At the interface between the solid and the fluid, heat is only transferred through thermal conduction because of the no-slip momentum boundary condition [3]. This is expressed as:

$$\left(k_f \frac{\partial T_f}{\partial y} \right) = \left(k_s \frac{\partial T_s}{\partial y} \right) \quad (6)$$

The boundary condition for the CHEX is defined as a convective heat flux:

$$\dot{q}_C'' = h_C \cdot (T_C - T), \quad (7)$$

where \dot{q}_C'' is the heat flux absorbed from the cold source, h_C is the heat transfer coefficient of the CHEX and T_C is the temperature of the cold source. The boundary condition for the HHEX is:

$$\dot{q}_H'' = h_H \cdot (T - T_H), \quad (8)$$

where \dot{q}_H'' is the heat flux rejected to the hot sink, h_H is the heat transfer coefficient of the HHEX and T_H is the temperature of the hot sink. The heat transfer coefficients depend on the geometry and flow of the heat exchangers and can be determined by standard heat transfer analysis. The remaining boundaries of the AMR geometry are considered to be adiabatic as they are either insulated or a symmetry line.

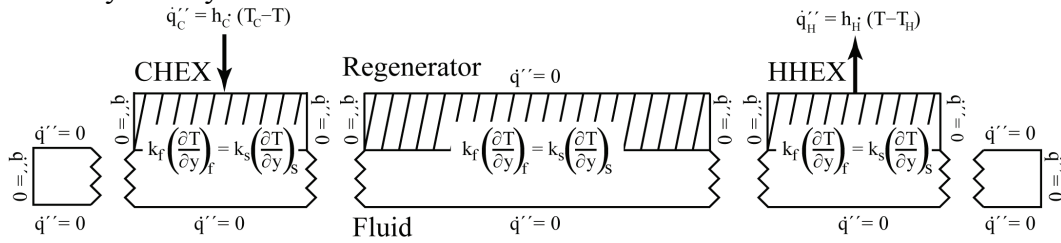


Figure 3: The boundary conditions used in the AMR model.

1.4 Evaluation of the AMR performance

The Coefficient Of Performance (COP) for the AMR refrigerator is defined as:

$$COP = \frac{q'_C}{w'_{tot}}, \quad (9)$$

where q'_C is the absorbed heat from the cold source and w'_{tot} is the total work input, both are per unit width of the AMR per refrigeration cycle. The amount of heat absorbed from the cold source per cycle is determined as:

$$q'_C = \int_0^\tau \int_0^{L_C} q''_C dx dt, \quad (10)$$

where τ is the cycle period and L_C is the length of the CHEX. Likewise the amount of heat rejected to the hot sink per cycle, q'_H is determined as:

$$q'_H = \int_0^\tau \int_0^{L_H} q''_H dx dt, \quad (11)$$

where L_H is the length of the HHEX. The total work input is the sum of the work required to magnetize and demagnetize the regenerator and the work required to displace the fluid. Since there are no losses in the AMR the magnetic work per cycle can be calculated from the 1st law of thermodynamics as the difference between the absorbed and rejected heat:

$$w'_{mag} = q'_C - q'_H. \quad (12)$$

The piston work is not included in Eq. (12) due to the decoupling between the momentum equation and the heat transfer equations. However, it has previously been shown that for the present regenerator geometry, the piston work is much smaller than the magnetic work and can be neglected [1]. The Carnot efficiency (ε) is defined as:

$$\varepsilon = \frac{COP}{COP_{Carnot}}, \quad (13)$$

where COP_{Carnot} is the COP of the corresponding Carnot cycle defined as:

$$COP_{Carnot} = \frac{T_C}{T_H - T_C}. \quad (14)$$

1.5 Implementation of the AMR model

The AMR model was implemented using the software COMSOL Multiphysics, and the resulting numerical model has been validated in a previous study [1]. The geometrical dimensions and the material properties used in the present calculations are given in **Table 1**.

Table 1: Geometrical data and material properties (at 298 K and 1 atm) of the AMR model.

Part	Material	Length (cm)	Height (mm)	c_p ($Jkg^{-1}K^{-1}$)	k ($Wm^{-1}K^{-1}$)	ρ (kgm^{-3})	μ ($kgm^{-1}s^{-1}$)
Regenerator plate	Gadolinium	5	1	see text	10.5	7900	-
CHEX	Copper	2	1	385	401	8933	-
HHEX	Copper	2	1	385	401	8933	-
Fluid channel	Water	16	1	4186	0.595	997	$8.91 \cdot 10^{-4}$

The properties of gadolinium depend on both the temperature and the magnetic field. The mean field model was therefore used to determine both the heat capacity and ΔT_{ad} [4]. **Figure 4** shows the different steps of the motion of the pistons and the application of the magnetic field during an AMR cycle. **Table 2** shows the AMR cycle parameters used in the present study.

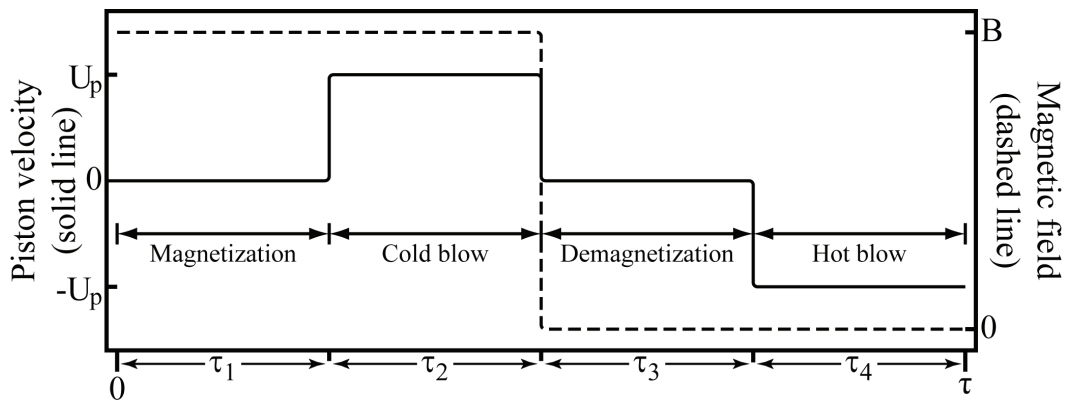


Figure 4: The variation of the piston velocity (solid line) and the magnetic field (dashed line) during the four steps of the AMR refrigeration cycle.

Table 2: The parameters of the AMR cycle used in the parameter variations.

Parameter	Value
Magnetic field (B)	1 T
Cycle period (τ)	6 s
Magnetization and demagnetization periods (τ_1 and τ_3)	2 s
Cold and hot blow periods (τ_2 and τ_4)	1 s

2 ANALYSIS AND OPTIMIZATION OF THE PISTON STROKE

During steady-state operation of the AMR a nearly linear temperature profile across the regenerator ranging from T_C to T_H is established [2]. During the cold and hot blow, part of the fluid inside the regenerator is displaced to reject or absorb heat. It is thus important that only fluid warmer than T_H or colder than T_C is displaced. If the amount of the liquid which is displaced is too small the performance of the AMR is reduced as only part of the cooling produced by the MCE is utilized. Conversely, if the amount of fluid which is displaced from the regenerator is too high the cold source will be heated by the fluid and the AMR will absorb heat from the hot sink; this results in a reduction of the performance. Thus, there is an optimal stroke of the pistons. To determine the effect of the stroke on the performance, the model is used to perform a parameter variation of the fraction of fluid displaced from the regenerator. Two different sets of AMR operating conditions are considered: (1) the maximum temperature span between the two heat exchangers is determined by setting the cooling load from the cold source equal to zero, and (2) the variation of the COP for an AMR with a fixed temperature span of 10 K between the source and sink is determined. In both cases the stroke is varied so that 5-95% of the fluid in the regenerator is displaced. In both cases 600 cycles were simulated. **Table 3** shows the heat exchangers parameters used for the two cases.

Table 3: Heat exchanger data used in the two parameter variations.

Parameter variation	h_H ($\text{Wm}^{-2} \text{K}^{-1}$)	h_C ($\text{Wm}^{-2} \text{K}^{-1}$)	T_H (K)	T_C (K)
1. No-load conditions	10^6	0	298	-
2. Constant temperature span	10^6	10^6	298	288

Perfect thermal contact between the source and sink and the heat exchangers is assumed. This is achieved by using the artificially high values for the heat transfer coefficients show in **Table 3**.

2.1 Results

Figure 5 shows the results of the parameter variations for the two operating conditions. For the first parameter variation a maximum temperature span of 13.2 K is obtained when the stroke displaces 25% of the fluid within the regenerator. For the second parameter variation a maximum COP of 2.1, with a corresponding Carnot efficiency of 7.2% is also obtained when 25% of the fluid is displaced from the regenerator. **Figure 6** shows the transient development of the temperature span for selected piston strokes. These results show that the temperature span develops faster for a longer piston stroke than for a short piston stroke. In addition, the figure shows that the AMR reaches steady-state after less than 600 cycles except for the shortest stroke. The limit for when the steady-state is obtained are strokes of 1 cm or longer (not shown).

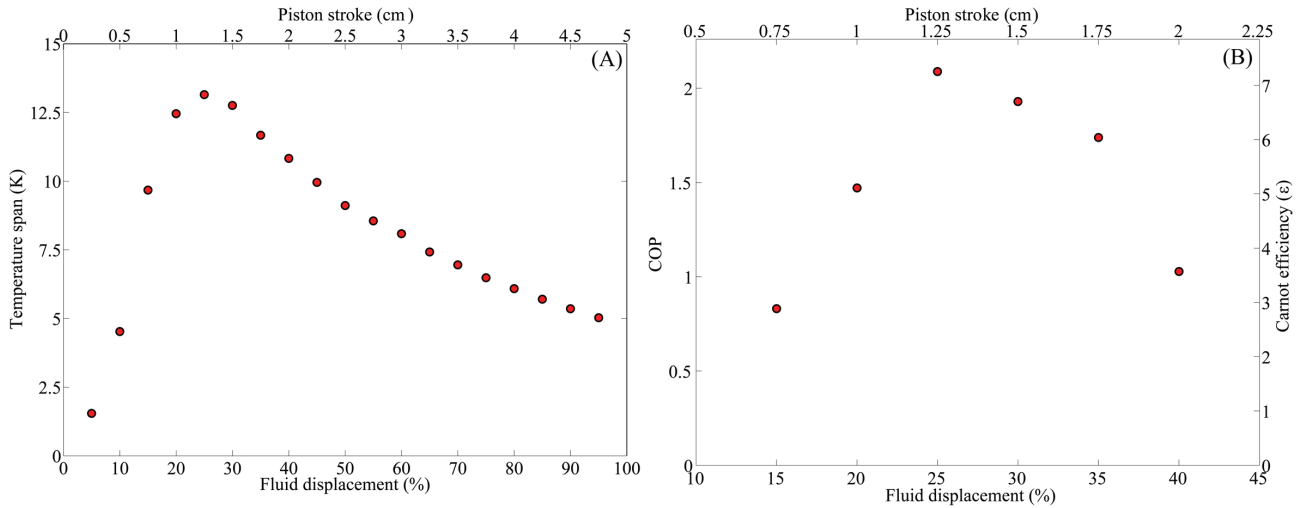


Figure 5: (A) the temperature span as a function of the stroke without an applied cooling load. (B) COP of the AMR as a function of the piston stroke for a fixed temperature span of 10 K. The left y-axis show the COP and the right y-axis show the corresponding Carnot efficiency. The lower x-axis show the piston stroke as the percentage of the fluid displaced from the regenerator and the upper x-axis show the stroke in centimeters.

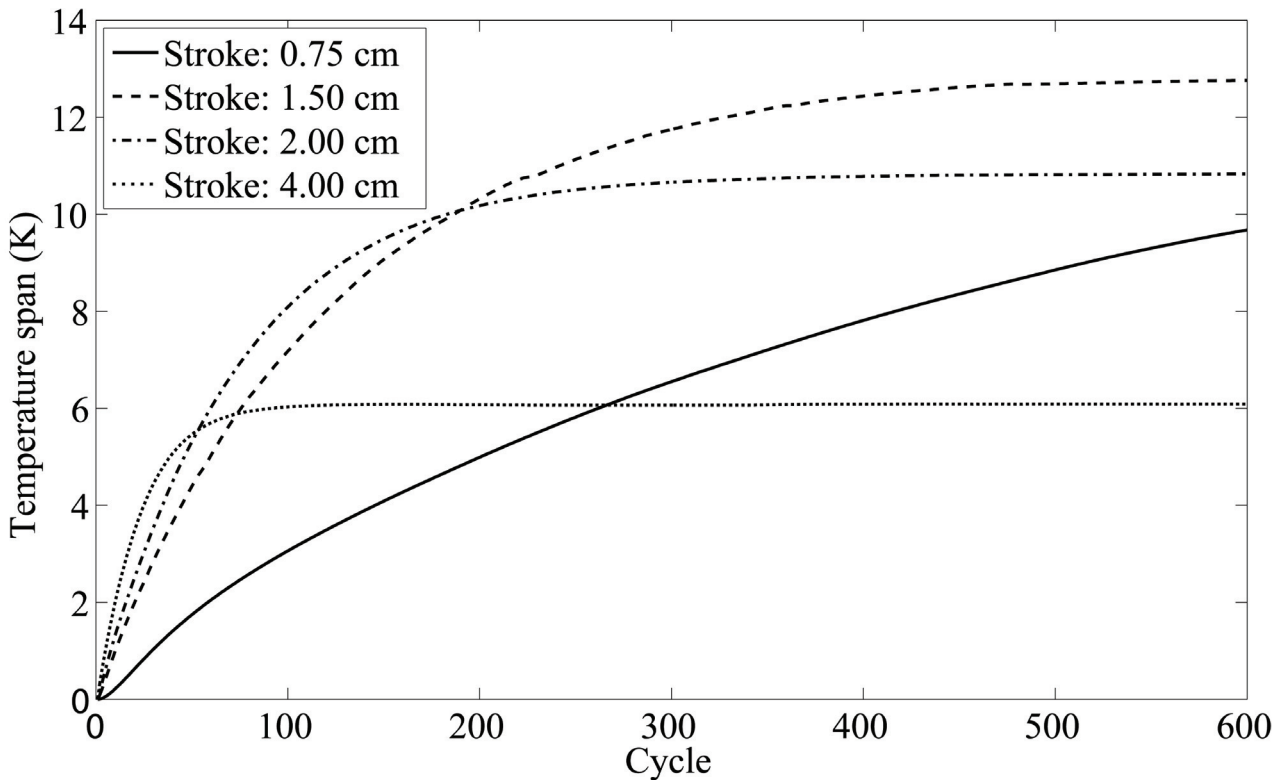


Figure 6: The evolution of the temperature span between the CHEX and the HHEX under no-load conditions as a function of the number of AMR cycles for selected piston strokes.

3 DISCUSSION

The results presented on **Figure 5(A)** show that the temperature span drops off rapidly when the pistons displace less than 20% of the fluid corresponding to the 1 cm gap between the regenerator and the heat exchangers. Hence, at least this amount of fluid must be displaced from the regenerator for the fluid heated or cooled by the MCE to come into contact with the heat exchangers. The observed development of a temperature span with less than 20% of fluid displacement is due to indirect heat transfer by convection and conduction. When exactly 20% of fluid is displaced, the resulting temperature span is only 5.3% lower than the maximum temperature span. This suggests that convection and conduction are efficient methods of heat transfer since the relatively high temperature span can only be obtained indirectly through these two mechanisms. **Figure 5(B)** shows that only piston strokes which displace from 15% to 40% of the fluid within the regenerator produce a usable COP. For the remaining range of strokes, the AMR cannot sustain the 10 K temperature span by itself, in agreement with **Figure 5(A)**. Notice that **Figure 5(A)** shows a temperature span below 10 K for a stroke of 0.75 cm whereas **Figure 5(B)** shows that it is possible to obtain a COP of 0.8 at the same stroke. This is because in case (1) the AMR did not completely obtain steady-state. By comparing **Figure 5(A)** and **Figure 5(B)**, we see that the stroke which produces the largest COP has a maximum temperature span of 13.2 K. This shows that that it is possible to obtain a high COP even when the AMR operates close to the maximum obtainable temperature span. The maximum Carnot efficiency of 7.2% is low when compared to the previous reports of Carnot efficiencies which are in the range of 30-60% for a reciprocating AMR [2]. Thus, the current operating conditions for the AMR may not be optimal.

CONCLUSION

A two-dimensional mathematical model of a linear reciprocating AMR has been developed which can predict both transient and steady-state behavior. The model is able to determine the AMR performance both in terms of the maximum temperature span and in terms of the COP. In the present study the model was used to perform two parameter variations to determine the correlation between the amount of fluid displaced from the regenerator during the refrigeration cycle and the AMR performance. The first parameter variation showed that with no cooling load, a maximum temperature span of 13.2 K can be obtained when 25% of the fluid is displaced from the regenerator. The second parameter variation indicates that for an AMR with a fixed temperature span of 10 K a maximum COP of 2.1 could be obtained when 25% of fluid is displaced from the regenerator. However, the corresponding Carnot efficiency is relatively low, with a value of 7.2%, which suggests that the AMR geometry or the operating conditions used in the present simulations may not be optimal. In addition, the simulations showed that a long stroke allows the temperature span to develop faster but yields a lower temperature span compared to a shorter stroke. Finally, the simulations showed the usefulness of the AMR model for the optimization of a linear reciprocating AMR under various operating conditions.

NOMENCLATURE

Symbol	Name and unit	Symbol	Name and unit
B	Magnetic field (T)	\dot{q}''	Absorbed/ rejected heat flux (Wm^{-2})
c_p	Specific heat capacity ($\text{Jkg}^{-1}\text{K}^{-1}$)	q'	Absorbed/rejected heat per cycle (Jm^{-1})
COP	Coefficient Of Performance (-)	T	Temperature (K)
ε	Carnot efficiency (-)	τ	AMR cycle period (s)
ρ	Density (kgm^{-3})	τ_1	Magnetization period (s)
μ	Kinematic viscosity ($\text{kgm}^{-1}\text{s}^{-1}$)	τ_2	Cold blow period (s)
h	heat transfer coefficient ($\text{Wm}^{-2}\text{K}^{-1}$)	τ_3	Demagnetization period (s)
k	Thermal heat conductivity ($\text{Wm}^{-1}\text{K}^{-1}$)	τ_4	Hot blow period (s)
L	Length of heat exchanger (m)	W	input work per cycle (Jm^{-1})

Sub- and superscript	Meaning	Sub- and superscript	Meaning
C	CHEX	mag	Magnetic work
f	Fluid	s	solid
H	HHEX	tot	total work

REFERENCES

- Petersen, T. F., Pryds, N., Smith, A., Hattel, J., Schmidt, H., and Knudsen, HJ. H. (2006), *Two dimensional Mathematical Model of a Reciprocating Room-Temperature Active Magnetic Regenerator*, Submitted to the International Journal of Refrigeration.
- Pecharsky, V. K., and Gschneidner, K. A. (1999), *J. Magn. Mater.*, 200 (1-3), 44-56.
- White, F. M. (1991), *Viscous Fluid Flow*, 2nd ed., McGraw-Hill, Inc.
- Dinesen, A. R. (2004), *Magnetocaloric and magnetoresistive properties of $\text{La}_{0.67}\text{Ca}_{0.33-x}\text{Sr}_x\text{MnO}_3$* , PhD Thesis, Risø National Laboratory.

This page was intentionally left blank.

Risø's research is aimed at solving concrete problems in the society.

Research targets are set through continuous dialogue with business, the political system and researchers.

The effects of our research are sustainable energy supply and new technology for the health sector.

